Molecular Mechanisms of Aortic Aneurysms

Moleculaire mechanisme van aorta aneurysmata

Joyce Burger

ISBN
978-94-6380-783-8

Cover:
Joyce Burger en Kirsten Peerdeman, Atelier Indrukwekkend, Delft

Inside:
Bregje Jaspers, ProefschriftOntwerp.nl, Nijmegen

Print
ProefschriftMaken | www.proefschriftmaken.nl

Financial support for printing this thesis by Stichting Lijf en Leven and the Dutch Heart Foundation is gratefully acknowledged.

Molecular Mechanisms of Aortic Aneurysms

Moleculaire mechanisme van aorta aneurysmata

Proefschrift

ter verkrijging van de graad van doctor aan de
Erasmus Universiteit Rotterdam
op gezag van de rector magnificus
Prof.dr. R.C.M.E. Engels
en volgens het besluit van het College voor Promoties.
De openbare verdediging zal plaatsvinden op

dinsdag 16 juni 2020 om 13.30 uur

Joyce Burger

Geboren te Alkmaar

Erasmus University Rotterdam

Promotoren
Prof. dr. R. Kanaar
Prof. dr. R.M.W. Hofstra

Overige leden
Prof. dr. H.J.M. Verhagen
Prof. dr. D.F.E. Huylebroeck
Prof. dr. B. Callewaert

Copromotoren
Dr. J. Essers
Dr. I. van der Pluijm

Financial support by the Dutch Heart Foundation for the publication of this thesis is gratefully acknowledged.

TABLE OF CONTENTS

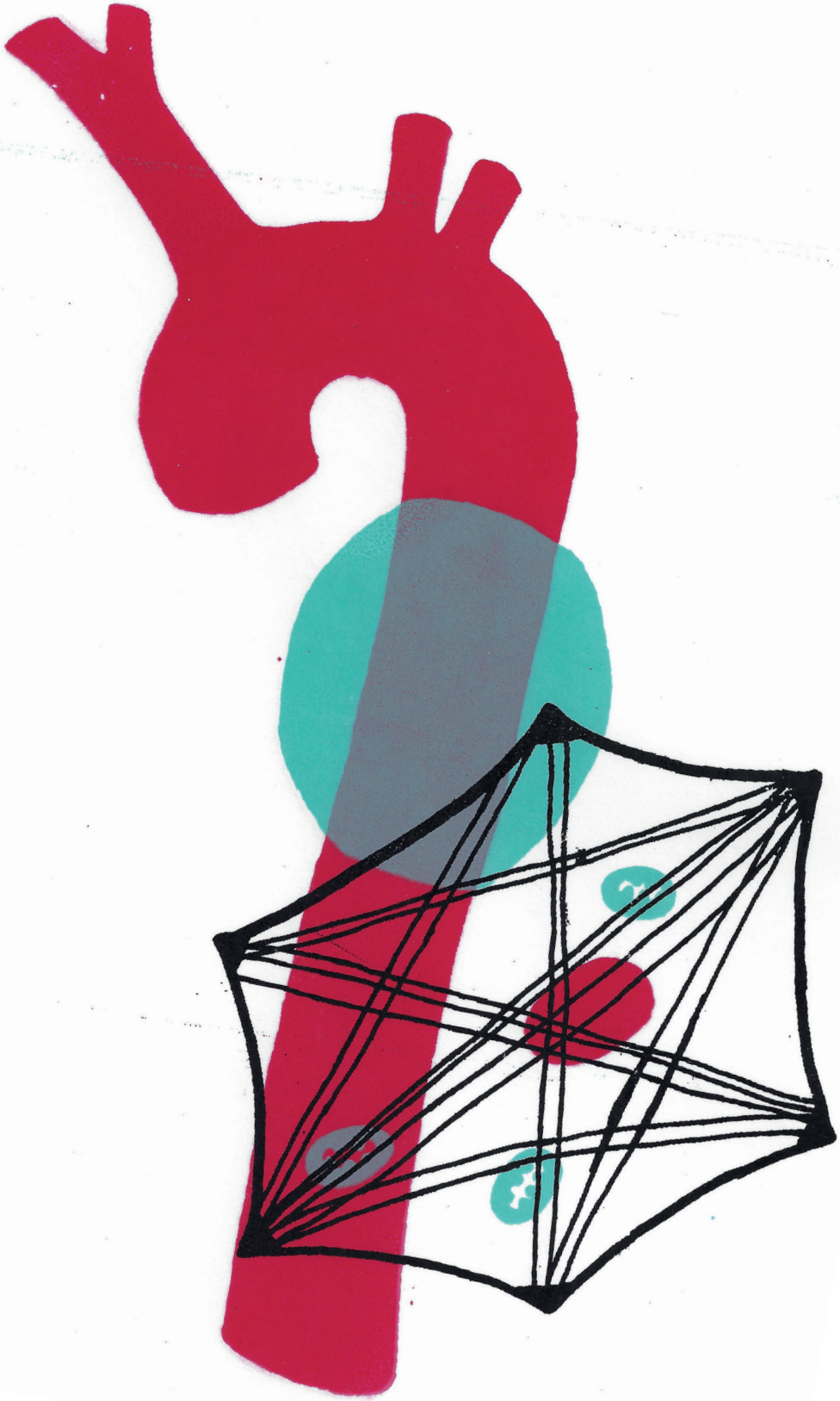

CHAPTER 1

GENERAL INTRODUCTION

STRUCTURE OF THE AORTIC WALL

The aorta is the largest artery in the human body and facilitates oxygenated blood flow from the pumping heart to the rest of the body. The aorta is built to resist high pressure and propagate blood flow, especially in the ascending aorta and aortic arch. Elasticity and rigidness are provided by the three layers that make up the aorta; the intima, the media and the adventitia (Fig. 1). The intimal layer (intima) consists of a single layer of endothelial cells that are lined along the inside of the artery and its connective tissue. This layer also contains an internal elastic membrane that separates the intimal layer from the medial layer (media). The medial layer is built up of vascular smooth muscle cells surrounded by extracellular matrix and a defined number of elastin layers. The media is often called the muscular layer of the artery as it provides the aorta the ability to contract and relax, thereby regulating blood pressure. While the elastin layers present in the media appear as single layers in histological cross-sections of the aorta, they are composed of continuous elastin sheets that are circumferentially oriented in the medial layer of the artery and separated by the vascular smooth muscle cells. The adventitial layer (adventitia) mainly consists of fibroblasts and collagen giving the aorta strength and stability. The adventitia also harbors the vasa vasorum; small blood vessels that supply nutrients to the adventitia and the outer region of the medial layer. These small blood vessels are needed since the layers are too thick to receive nutrients by diffusion from the lumen.

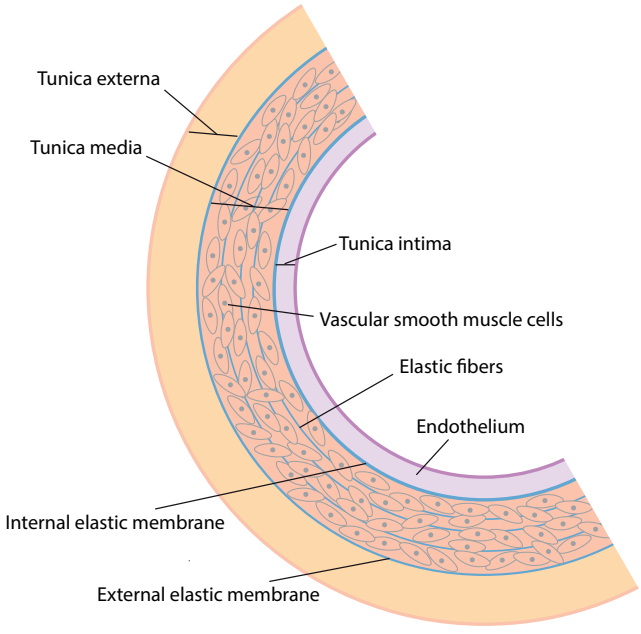

Figure 1. Schematic overview of the aortic wall layers

Cross-section of the aortic wall displaying the tunica intima, tunica media and tunica externa and an overview of their main components.

The aorta can be divided into different regions: the thoracic part, which originates from the heart, and the abdominal part, which starts below the diaphragm. The thoracic aorta can be further subdivided into the ascending aorta, the arch and the descending aorta. The abdominal aorta can be subdivided into a suprarenal region, above the renal artery, and the infrarenal region, below the renal artery (Fig. 2).

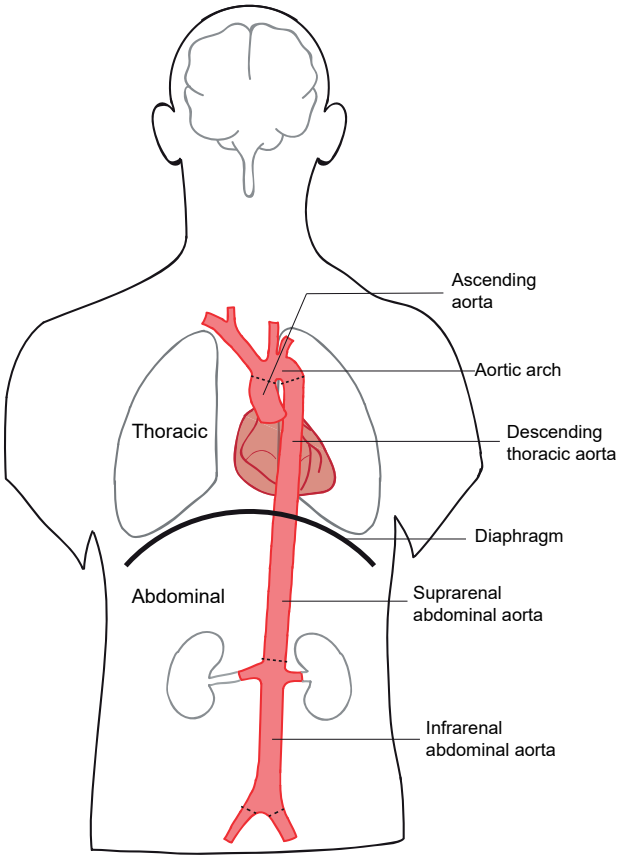

Figure 2. Schematic overview of the aortic regions

The aorta can be divided into a thoracic part and an abdominal part, these are anatomically separated by the diaphragm. The thoracic aorta can be subdivided into the ascending aorta, the aortic arch and the descending aorta. The abdominal aorta can be further divided into the suprarenal abdominal aorta and the infrarenal abdominal aorta. The aortic regions are separated by a dotted lines in this figure.

VASCULAR PATHOLOGIES OF THE AORTA

Genetic variants and/or cardiovascular risk factors, such as high blood pressure, smoking, obesity and advanced age, can cause a variety of pathologies of the aorta, including aortic aneurysms. The aortic wall becomes thinner when aneurysms occur, which can lead to dissections or a complete rupture of the aorta. Dissections can be divided into different types depending on the location of the tear. During an aortic dissection the intima is often injured which results in accumulation of blood between the intima and media of the aorta. The most common symptom of an aortic dissection is sudden pain on the chest and/or back, depending on the location of the dissection. An aortic dissection can be defined as acute (within two weeks of onset of pain), subacute (two-six weeks after onset) or as chronic (more than six weeks after the onset). Classification of aortic dissections occurs via two systems, the DeBakey and the Stanford systems (Fig. 3). The DeBakey system classifies into three types (I, II and III) according to the first entry site and extent of the dissection in the aorta. Type I has an initial entry in the ascending aorta and the dissection continues into the descending aorta. In type II, the dissection originates and is confined to the ascending aorta. Type III has an initial entry in the descending aorta and can propagate to the ascending aorta (IIIa) or further into the descending aorta (IIIb) [1, 2]. The Stanford system classifies the region of the aorta that is affected by the dissection, the ascending aorta (type A) or the descending aorta (type B) [2, 3]. The Stanford system is a simplification of the DeBakey system and is based on the clinical course and prognosis of patients who had dissections involving the ascending aorta as opposed to those in whom the disease did not extend proximal to the left subclavian artery [3, 4]. Symptoms of a full wall rupture also include acute chest and/or back pain. A full wall rupture results in severe hypotension which can lead to a deep coma or death [2].

Aortic aneurysms can occur in different regions along the aorta, abdominal aortic aneurysms (AAA) below the diaphragm and thoracic aortic aneurysms (TAA) above the diaphragm. The TAA group can be further subdivided into ascending TAA (directly subsequent to the heart), aortic arch TAA and descending TAA (subsequent to the aortic arch) [5-7]. If an AAA is localized above the kidneys it is referred to as an suprarenal AAA, below the kidneys it is referred to as a infrarenal AAA. When an aneurysm encompasses the thoracic and abdominal region, crossing through the diaphragm, it is called a thoracoabdominal aneurysm. Figure 4 shows a schematic overview of the locations of these different aneurysms.

During development the aorta originates from distinct embryological origins: the endoderm, the mesoderm and the ectoderm. The ectoderm is the exterior layer and is responsible for the formation of the neural tube and gives rise to neural crest cells in close proximity of the neural tube. Neural crest cells are a temporary cell type and give rise to e.g., melanocytes, bone, craniofacial cartilage as well as smooth muscle tissue [8]. The mesoderm is responsible for

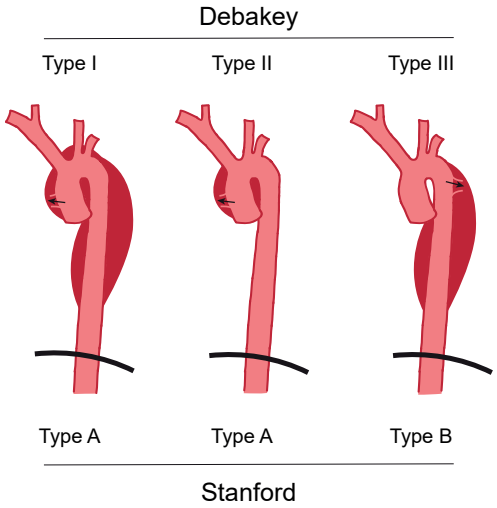

Figure 3. DeBakey and Stanford classification of aortic dissections

Aortic dissections can be classified according to the Debakey or the Stanford classification. The DeBakey system classifies into three types of dissections according to the first entry site of the dissection. Type I has an initial entry in the ascending aorta and continues into the descending aorta. Type II initially enters the ascending aorta and remains there. Type III has an initial entry in the descending aorta and propagates into the ascending aorta of further into the descending aorta. The Stanford system only classifies by the affected region of aorta, the ascending aorta (Type A) or the descending aorta (Type B).

the formation of cardiac and skeletal muscle tissue, connective tissue, adipose tissue and the circulatory system. The embryonic mesoderm can be subdivided into chordamesoderm or axial mesoderm (prechordal plate and notochord), initially unsegmented paraxial mesoderm that becomes segmented, intermediate and lateral plate mesoderm (with two leaflets, the splanchnic and the somatic leaflet). In amniotes (birds, mammals) the extra-embryonal mesoderm that is embryonic by origin forms the allantois and participates in formation of yolk sac and amnion [9, 10]. The vascular smooth muscle cells (VSMCs) of the ascending aorta and the aortic arch originate from the neural crest, while the VSMCs of the descending aorta arise from the somites. The VSMCs of the abdominal aorta as well as a small region around the diaphragm, derive from the splanchnic mesoderm (Fig. 4).

Apart from embryological origin, the regions of the aorta have different physical properties and compositions. One of these properties is the distensibility, or elasticity, of the aorta. The aorta needs to be able to stretch to resist the pressure of the blood flow from the heart, therefore the distensibility is of great importance. The distensibility of the thoracic aorta is far greater than of the abdominal aorta [11]. As previously explained, the aortic media contains VSMCs

surrounded by the extracellular matrix (ECM) they produce. The ECM is composed of elastin and collagen among others. Elastin, together with the microfibrils, forms the elastic laminae that are circumferentially oriented in the medial layer and are responsible for the elasticity of the aorta. Collagen provides the aorta with rigidity to withstand the pulses of the blood flow. The ratio of elastin to collagen is approximately 2:1 in the thoracic aorta, while it is 1:2 in the abdominal aorta. Analysis of the aorta has also revealed an increased presence of elastic laminae in the thoracic aorta compared to the abdominal aorta [11]. These differences in aortic composition can, in part, explain the difference in distensibility of the aortic regions. These differences in embryonic origin and aortic composition could explain the differences in susceptibility to aneurysm formation depending on the aortic region, since aneurysms occur more frequently in the abdominal aorta [11, 12].

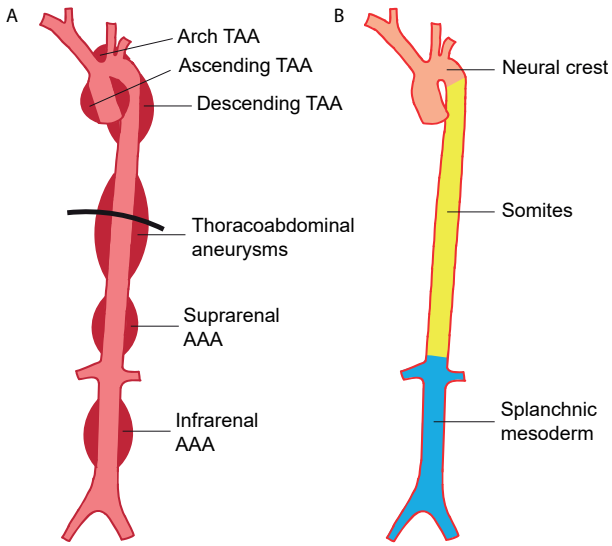

Figure 4. Locations of aorta aneurysms and embryological origins of aortic regions

A) Schematic overview of aorta aneurysms and their location. **B)** Representation of the difference in embryological origin of the thoracic and abdominal aorta.

The incidence of detected thoracic aortic aneurysms was estimated to be between 5.6 and 10.4 cases per 100,000 per year [13, 14]. However, studies likely underestimate the incidence of asymptomatic thoracic aortic aneurysms in the population since the diameter at risk is often defined as >5.0 cm, thereby excluding aneurysms with a diameter below this cut-off [15, 16]. For abdominal aortic aneurysms the incidence of newly detected AAA is between 3.5 and 6.5 per 1,000 per year [17-20].

The annual risk of rupture of a thoracic aortic aneurysm is less than 2% for aneurysms with a diameter between 4.0 and 4.9 cm, but almost 7% for aneurysms with a diameter of more than 6.0 cm [21]. The annual risk of rupture for abdominal aortic aneurysms is approximately 1% when the diameter is 4.0 to 4.9 cm. When the diameter exceeds 7 cm the annual risk of rupture ranges from 30 to 50% [22, 23].

Since aortic aneurysms are often asymptomatic and thereby discovered by coincidence, the mortality rate of aortic aneurysms is high. Results from a study performed from 1984 to 1993 that included unoperated aortic aneurysm patients revealed a 5-year survival of approximately 40% for TAA and 20% for AAA [24, 25]. Another study performed between 1985 and 1996 reports a 5-year survival of 64% for TAA patients [25, 26]. In this study half of the patients underwent surgery for their TAA, which could explain the higher survival rates. To lower this mortality, aortic aneurysms are traditionally treated with surgery to either replace the aneurysm by a surgical graft (open aneurysm repair) or to place a stent in the aorta that spans over the aneurysm (endovascular aneurysm repair, EVAR). During an open aneurysm repair the thorax or the abdomen has to be opened to place a graft in the healthy aorta and remove the excess tissue of the aneurysm. The first open abdominal aortic aneurysm repair was performed in France in 1951 [23, 27]. Since then the procedure has been optimized and elective open aortic aneurysm repairs are very effective in preventing deaths related to aortic dissections. The perioperative mortality, mortality related to surgery and recovery, of open elective repair varies in literature from 1% in centers of excellence to approximately 8% in population studies [23, 28]. The first EVAR procedure was performed in Buenos Aires in 1990 and was soon embraced as a less invasive alternative for open elective repair. Apart from being less invasive, the EVAR procedure is associated with a decreased perioperative mortality, approximately 0,5 to 1% compared to open elective repair [29-31]. The 4-year overall survival does not significantly differ between EVAR and open elective surgery [30, 32]. Although the EVAR procedure is often favorable compared to the open elective repair, not all abdominal aortic aneurysms are suitable for an EVAR procedure [23]. Therefore, the open elective repair remains an important procedure for the repair of aortic aneurysms.

GENETICS OF AORTIC ANEURYSMS

Thoracic aortic aneurysms

Thoracic aortic aneurysms (TAA) comprises hereditary TAA and sporadic aneurysms, e.g. without family history. In total, approximately 25% of the TAA is suspected to have a genetic component as an underlying cause. Of these 25%, approximately one fifth of TAAs are associated with a known genetic disorder, while the rest of patients with a TAA have a positive family history of aneurysmal disease but the causative gene is unknown [33-35]. A found genetic variant will be

referred as a mutation if the variant is known or predicted to be pathogenic, if the effects are unknown it will be referred to as a variant.

When TAA patients additionally present with syndromic features there is a higher chance of finding a genetic cause [36, 37]. Syndromic features can include, for instance, distinct facial features, tall stature or hypermobility of the joints. Well-known TAA syndromes are Marfan, Loeys-Dietz and Ehlers-Danlos syndrome. Marfan syndrome (MFS) was originally described in 1896 by Dr. Antoine Marfan, a French pediatrician. Characteristic features of Marfan patients are increased height, disproportionally long limbs and digits as well as other skeletal deformations. Other clinical features include aortic root aneurysms, ocular defects (in particular ectopia lentis and severe myopia) and hypermobility of the joints. In 1991 the *FBN1* gene, encoding for the ECM protein fibrillin-1, was identified via genetic linkage analysis as the causative gene for Marfan syndrome [38]. Loeys-Dietz syndrome (LDS) is a genetic disorder characterized by widespread vascular disease not limited to the aortic root. Other hallmarks of the disease include patent ductus arteriosus, skeletal malformations, craniofacial features such as bifide uvula, cutaneous findings and joint hypermobility. LDS is caused by a disease-causing mutation in one of six genes involved in the TGFβ pathway (*TGFBR1/2, SMAD2/3, TGFB2/3*), which is important for proper growth and development of the body's connective tissue [39-42]. Ehlers-Danlos syndrome (EDS) is a group of rare inherited disorders that affect connective tissues. Symptoms include joint hypermobility, skin hyperextensibility, atrophic scaring, bruisability and aortic aneurysms. To date 19 genes are identified to cause 13 subtypes of EDS, of which mutations in the collagen genes *COL5A1* and *COL5A2* cause classical EDS [43-45]. Mutations in *COL3A1* lead to vascular EDS [43, 46].

Cutis laxa encompasses a heterogeneous group of connective tissue disorders typified by loose and/or wrinkled skin. Although not all mutations that cause cutis laxa are associated with aortic aneurysms, mutations in *ELN* and *EFEMP2* do lead to aneurysm formation in cutis laxa patients. Zhang et al. identified heterozygous mutations in the *ELN* gene in patients with autosomal dominant cutis laxa [47]. In 2006 the first homozygous missense mutation in the *EFEMP2* gene (Fibulin-4) was identified in a patient with autosomal recessive cutis laxa [48].

Disease-causing mutations in the genes *ACTA2*, *MYH11*, *MYLK* and *PRKG1* lead to non-syndromic familial aortic aneurysms. These patients present with aortic aneurysms, but without other clinical features that are normally associated with syndromes such as Marfan and Loeys-Dietz. Via linkage analysis Guo et al. (2007) identified heterozygous missense mutations in the *ACTA2* gene in 15 families, five of which carried the same mutation although these families were unrelated [49]. Analysis of co-segregation and specific gene mutation screening by Zhu et al. revealed two different heterozygous mutations in *MYH11* [50]. In 2010 heterozygous disease-causing mutation in the *MYLK* gene were identified in families with TAAs and dissections by

segregation analysis [51]. Segregation analysis of four unrelated families with TAAs identified a heterozygous missense mutation in *PRKG1* by Guo et al. [52].

Abdominal aortic aneurysms

Abdominal aortic aneurysms (AAA) are often associated with common cardiovascular risks such as increased age, chronic inflammation, atherosclerosis and smoking [53]. It is therefore frequently thought that AAA is caused by an unhealthy lifestyle. Although this might be true for a part of AAA patients, there is also a genetic component in AAA. In the 1970s Clifton reported a case study of three brothers who all had a ruptured AAA [54]. There was no history of trauma, or signs of post-stenotic dilatation, sepsis or syphilis in any of the three brothers that could be responsible for the aneurysm formation [55-58]. The author therefore suggested a hereditary factor in these patients. The risk of AAA was increased in relatives of AAA patients compared to the general population [59]. In addition, the age onset of AAA formation in a relatives of AAA patients was also decreased [59]. Due to the association of AAA formation and atherosclerosis, a study was conducted to identify the atherosclerotic burden of patients with familial AAA and of patients with sporadic AAA [60]. Analysis of the carotid intima-media thickness (CIMT) revealed a lower atherosclerotic burden, reflected by a lower CIMT, in patients with familial AAA compared to patients with sporadic AAA. Familial AAA patients further presented less hypertension, diabetes mellitus and were less likely to smoke. This underlines the idea of a hereditary factor in AAA as opposed to common cardiovascular risk being the only cause for AAA.

Since the hereditary component in AAA is becoming more apparent, studies are conducted to identify possible causative genes for AAA. This identification is currently performed via different methods: family-based linkage, analysis of known TAA genes in the AAA population and genome-wide association studies (GWAS) [61, 62].

The most extensive family-based linkage analysis of familial AAA was performed by Shibamura et al. [63]. In this study 119 families were analyzed and two loci, 4q31 and 19q13, were shown to be in linkage with AAA, but only when sex and number of affected individuals were included as covariates. Due to the large size of the regions it was difficult to identify causative genes, however, they do harbor potential genes of interest. Endothelin receptor type A (*EDNRA*) in 4q31 and several kallikrein (*KLK*) genes in 19q13 were suggested as potential causative genes since their expression is altered in AAA tissue [64, 65].

Analysis of known TAA genes in 155 AAA patients revealed variants in some known TAA genes [62]. The found variants in AAA patients were classified according to (likely) benign, unknown significance (VUS) or (likely) pathogenic. VUS was defined as “Intronic, silent or missense variants that affect splicing, in-frame deletions/insertions, missense variants for which more than two *in silico* protein predictions are damaging”. The effect of these VUS is currently unknown

and a pathogenic effect cannot be excluded. In 99 familial AAA patients one pathogenic and segregating *COL3A1* mutation, one likely pathogenic and segregating *MYH11* mutation and 15 VUS were found. In 56 sporadic AAA cases one pathogenic *TGFBR2* mutation was found and seven VUS [62].

Currently the largest GWAS analysis of 4,972 cases and 99,858 controls was performed by a multinational consortium and is a meta-analysis of 6 GWAS studies from 5 countries (United States, United Kingdom, the Netherlands, Iceland and New Zealand). The outcome was further validated in eight independent cohorts [66]. Unfortunately, family history was not collected for these GWAS studies and therefore familial and sporadic AAA cannot be differentiated. The meta-analysis revealed ten genetic loci that were associated with AAA and of these nine loci remained below the genome-wide level of significance when validated in the independent cohorts. The loci and the nearest gene(s) mapped are summarized in Table 1 [61, 66].

Table 1. Genetic loci associated with AAA

Identification method	Locus	(Nearest associated) Gene(s)
Family-based linkage analysis	4q31	*EDNRA*
	19q13	Several *KLK* genes
Analysis of known TAA in AAA patients		*COL3A1*
		MYH11
		TGFBR2
GWAS (meta-) analysis	9p21	*CDKN2BAS1/ANRIL*
	9q33	*DAB2IP*
	12q13	*LRP1*
	1q21.3	*IL6R*
	1p13.3	*PSRC1/CELSR2/SORT1*
	19p13.2	*LDLR*
	1q32.3	*SET/MYND/SMYD2*
	13q12.11	*LINC00540*
	20q13.12	*PLTP/PCIF1/MMP9/ZNF335*
	21q22.2	*ERG*

Mouse models for aortic aneurysms

To study the progression and molecular mechanisms of aortic aneurysms, mouse models are used to mimic human aortic aneurysms. Mouse models can be generated by genetic modification or induced chemically.

I. Genetic mouse models

The effect of a genetic mutation can be difficult to analyze when the number of patients or the patient material is limited, therefore mouse models are often generated to investigate this. Inbred mice are genetically homogeneous and there is very little variation or heterogeneity within a pure inbred strain. This provides the opportunity to investigate the pathogenesis and outcome of specific gene associated diseases. The described genetic mouse models for aortic aneurysms are summarized in table 2.

For Marfan syndrome a number of mouse models with variable disease severities have been created. The *Fbn1*^{mgN} allele results in no *Fbn1* expression, *Fbn1*$^{mg\Delta}$ leads to severely decreased expression of *Fbn1* (approximately 10-fold) while *Fbn1*$^{GT\text{-}8}$ and *Fbn1*^{mgR} have a 4- to 5-fold reduced *Fbn1* expression. The *Fbn1*^{C1039G} allele results in a missense mutation with normal expression of *Fbn1* but leads to reduced fibrillin-1 fiber formation. Homozygous *Fbn1*$^{mg\Delta}$, *Fbn1*^{C1039G}, *Fbn1*^{mgN}, and *Fbn1*$^{GT\text{-}8}$ mice all die at an early postnatal age due to cardiovascular events, while homozygous *Fbn1*^{mgR} mice with reduced expression of normal fibrillin-1 have a milder phenotype and die around 4 months due to aortic dissection [67-71].

Tgfbr1 and *Tgfbr2* germline (conventional, total knock-out) and conditional (mostly cell-type specific) knock-out mice have been generated for LDS. The germline knock-out models show severe defects in the vascular development of the yolk sac and die during this phase of embryonic development [72, 73]. Conditional knock-outs in endothelial cells, VSMCs and neural crest cells, respectively, resulted in specific cardiovascular and craniofacial abnormalities. However, not all symptoms of human LDS are mimicked in these mice [74-76]. LDS type 3 conventional knock-out *Smad3*$^{-/-}$ mice present with aneurysm formation, fragmentation of the elastic laminae and immune infiltration in the aorta [77, 78].

Mutations in *ACTA2* and *MYH11* in humans result in familial TAA, however, *Acta2* null and *Myh11* null mice do not present with aneurysms. Nevertheless, *Acta2* null mice develop abnormal vascular contractility, tone and blood flow and *Myh11* null mice show delayed closure of the ductus arteriosus [79, 80].

Cutis laxa type 1b is characterized by aneurysm formation and non-elastic, loose skin and is caused by mutations in the *EFEMP2* gene. Several different *Fibulin-4* (mouse *EFEMP2*) mouse models have been made to resemble cutis laxa. Fibulin-4$^{-/-}$ mice often die during birth and only

10% of the mice survive until postnatal day 1 [81]. Arteries of *Fibulin-4*$^{-/-}$ mice show tortuosity, aneurysm formation and ruptures. Since complete absence of fibulin-4 is embryonically lethal, a VSMC specific knock-out model was generated [82-84]. Fibulin-4$^{f/-}$/SM22Cre^{+} mice only lack fibulin-4 in VSMCs of the aorta, resulting in aneurysm formation in the ascending aorta. Furthermore, Fibulin-4$^{f/-}$/SM22Cre^{+} aortas show severe fragmentation of the elastic laminae, however, the elastin layer adjacent to the endothelial cells appears to remain intact. In the hypomorphic Fibulin-4$^{R/R}$ mouse model the ^{R} stands for reduced fibulin-4 expression, as these mice have 25% of fibulin-4 expression compared to its wild-type littermate. Fibulin-4$^{R/R}$ mice show aneurysm formation along the entire aorta. Other characteristics of the aortic phenotype include fragmentation of the elastic laminae, increased TGFβ signaling and increase deposition of extracellular matrix [85, 86]. Fibulin-4$^{E57K/E57K}$ mice have a patient specific mutation that causes reduced ECM assembly and reduced binding to LTBP1s and LOX-propeptide [87, 88]. Like Fibulin-4$^{R/R}$ mice, Fibulin-4$^{E57K/E57K}$ show aneurysm formation and fragmentation of the elastic laminae. Disease-causing mutations in LOX result in cutis laxa and research shows that *Lox*$^{-/-}$ mice die soon after or just before birth due to large aortic aneurysms. This indicates the importance of LOX in proper ECM formation and elastic fiber assembly [89, 90].

Table 2. Genetic mouse models for aortic aneurysms

Disease	Gene	Mouse model	Effect on expression	Disease symptoms	References
Marfan syndrome	*Fbn1*	*Fbn1*^{mgN}	No *Fbn1* expression	Die at early postnatal age due to cardiovascular events	[71]
		Fbn1$^{mg\Delta}$	10-fold reduced *Fbn1* expression	Die at early postnatal age due to cardiovascular events	[67]
		Fbn1$^{GT\text{-}8}$	4- to 5-fold reduced *Fbn1* expression	Die at early postnatal age due to cardiovascular events	[70]
		Fbn1^{mgR}	4- to 5-fold reduced *Fbn1* expression	Die around 4 months due to aortic dissection	[68]
		Fbn1^{C1039G}	Missense mutation, normal expression	Die at early postnatal age due to cardiovascular events	[69]

Table 2. Continued

Loeys-Dietz syndrome	*Tgfbr1*	*Tgfbr1* knock-out	No *Tgfbr1* expression	Embryonic lethality due to severe defects in vascular development	[73]
		Tgfbr1 conditional knock-out (endothelium, VSMCs and neural crest)	No *Tgbr1* expression in specific cell types	Specific LDS craniofacial and cardiovascular abnormalities	[74]
	Tgfbr2	*Tgfbr2* knock-out	No *Tgfbr2* expression	Embryonic lethality due to severe defects in vascular development	[72]
		Tgfbr2 conditional knock-out (endothelium, VSMCs and neural crest)	No *Tgfbr2* expression in specific cell types	Specific LDS craniofacial and cardiovascular abnormalities	[74-76]
	Smad3	*Smad3*$^{-/-}$	No *Smad3* expression	Aneurysm formation, fragmentation of the elastic laminae and immune infiltration in the aorta	[77, 78]
Familial TAA	*Acta2*	*Acta2* null	No *Acta2* expression	Abnormal vascular contractility, tone and blood flow	[79]
	Myh11	*Myh11* null	No *Myh11* expression	Delayed closure of the ductus arteriosus	[80]
Cutis laxa type b	*Fibulin-4*	*Fibulin-4*$^{-/-}$	No *Fibulin-4* expression	Embryonic lethality due to tortuosity, aneurysm formation and ruptures	[81]
		Fibulin-4$^{fl/-}$/ *SM22Cre*$^{+}$	No *Fibulin-4* expression in VSMCs	Aneurysm formation and severe fragmentation of the elastic laminae	[82-84]
		Fibulin-4$^{R/R}$	4-fold reduced *Fibulin-4* expression	Aneurysm formation and severe fragmentation of the elastic laminae	[85, 86]
		Fibulin-4$^{E57K/E57K}$	Missense patient mutation, normal expression	Aneurysm formation, severe fragmentation of the elastic laminae and reduced binding of fibulin-4 to LTBP1 and LOX-propeptide	[87, 88]
	Lox	*Lox*$^{-/-}$	No *Lox* expression	Embryonic lethality due to large aneurysm formation	[89, 90]

II. Chemically induced mouse models

Since the knowledge on causative genes for AAA is still limited, there are no genetically generated AAA mouse models that develop abdominal aortic aneurysms without further (chemical, enzymatic) challenge (summary in table 3).

Chemical induction as such challenge can be performed in several ways, which often rely on the fragmentation of the elastic laminae. Exposure of the adventitial intraluminal space to elastase results in extensive destruction of the elastic laminae and infiltration of inflammatory cells in the adventitia [91]. Another methods relies on exposure to calcium chloride, which results in structural degradation of the medial layer and infiltration of the immune system. Both methods are known to cause typical AAA in mice [91].

Other chemical induction protocols can result in both TAA and AAA in mice. Administration of β-aminopropionitrile monofumarate (BAPN) could lead to the inhibition of LOX activity and can thereby induce medial degradation. In combination with induced hypertension, BAPN administration can cause TAA as well as AAA, but these aneurysms are often only observed by chance [92]. Treatment with angiotensin II in mice with an *ApoE*$^{-/-}$ or *LDLR*$^{-/-}$ background also result in TAA and AAA [93-95].

Table 3. Chemically induced mouse models.

Treatment	Outcome	TAA/AAA development
Elastase	Extensive destruction of the elastic laminae and infiltration of inflammatory cells	AAA
Calcium chloride	Structural degradation of the medial layer and infiltration of the immune system	AAA
β-aminopropionitrile monofumarate (BAPN)	Inhibition of LOX activity and can thereby induce medial degradation	TAA/AAA
Angiotensin II (in *ApoE*$^{-/-}$ or *LDLR*$^{-/-}$ background)	Medial disruption and results in luminal dilation	TAA/AAA

GENES, CELLULAR LOCATION AND MOLECULAR FUNCTION

Gene mutations that lead to aortic aneurysms result in alteration of the function of its associated protein or its abundance. These affected proteins are located in different cellular compartments and can be distinguished on the basis of their location or molecular function within the vascular smooth muscle cell. They can be divided into proteins for 1) proper functioning of the extracellular matrix (*FBN1*, *COL3A1*, *COL5A1/2*, *EFEMP2* and *ELN*), 2) functioning of the TGFβ signaling

pathway (*TGFBR1/2*, *SMAD2/3* and *TGFB2/3*) and 3) cytoskeleton organization (*ACTA2*, *MYH11*, *MYLK* and *PRKG1*). Although these proteins are located in different cellular compartments, they are all interconnected at the molecular level (Fig. 5). The ECM is connected to the cytoskeleton via integrins and focal adhesions. TGFβ that activates the TGFβ signaling pathway is stored in the ECM and activation of TGFβ signaling can result in upregulation of cytoskeleton proteins. Since the molecular processes are all connected, a disease-causing mutation in one molecular pathway can result in dysregulation at multiple molecular levels. The molecular function of the three categories in VSMC function will be discussed below for normal and diseased cells.

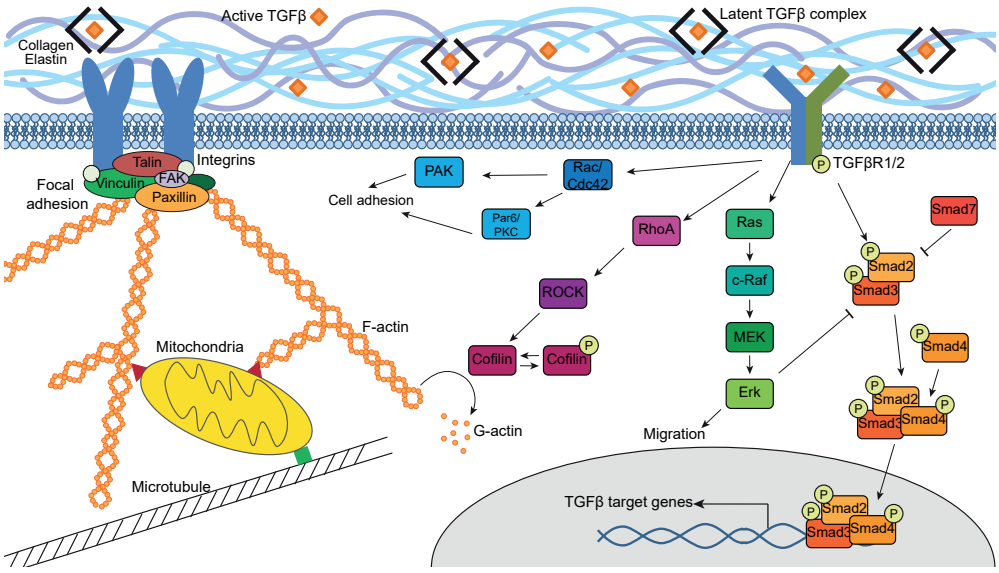

Figure 5. Cross talk between cellular components

The cellular components that are involved in aneurysm formation (ECM, TGFβ signaling and the cytoskeleton) all appear to be individually affected during aneurysm formation. However, these components are all interconnected with each other as is depicted in this figure. The ECM is build up out of collagen and elastin, among others, and serves as a base to which cells can adhere. A cell is bound to the ECM via its integrins and the cytoskeleton of the cell is connected to these integrins via the focal adhesions for stability. Focal adhesions are a cluster of linker proteins that include talin, vinculin, FAK and paxillin. The cytoskeleton is an important structural component of the cell and consists of multiple fibers with different functions and provides attachment of organelles, such as the mitochondria. The actin cytoskeleton is formed by F-actin fibers that consist of G-actin monomers and these fibers are continuously polymerized and depolymerized. Apart from providing attachment for cells, the ECM is needed for storage of cytokines, such as TGFβ. Inactive or latent TGFβ is stored in the ECM until activation of the TGFβ pathway is needed. When TGFβ is activated it can bind to the TGFβ receptors and thereby activate a number of processes. Transcription of TGFβ target genes is induced by the phosphorylation of Smad2/Smad3 and Smad4 after which they translocate to the nucleus and induce transcription. Cellular adhesion is influenced by TGFβ signaling via Rac/Cdc42, PAK and Par6/PKC. Cellular migration is affected by TGFβ via Ras, c-Raf, MEK and Erk. Additionally TGFβ influences the

actin (de)polymerization via RhoA, ROCK and by the phosphorylation status of cofilin. This illustrates that these different cellular components are all connected and that a mutation in one of the genes in this network can result in dysregulation at multiple levels.

Extracellular matrix aberrations in aortic aneurysms

The ECM is a non-cellular three-dimensional structure that is present between cells and organs. The ECM is important for the adhesion of cells to a basal membrane, but is ultimately responsible for cell signaling since growth factors are deposited and released from intrinsic components of the ECM. The ECM consists of a mixture of elastin, collagen, fibrillin, fibulin, laminin, fibronectin, microfibril-associated glycoproteins and proteoglycans [96, 97]. Although these proteins are all present in the ECM, their composition varies between different tissues and even within one tissue the composition can vary, as is shown in figure 6. For instance, the three aortic layers consist of different collagen types (collagen VIII, XV and XVIII in the intima vs collagen I, III and V in the media and adventitia) or the ratio between two collagen types is different (I>III in the media, while III>I in the adventitia).

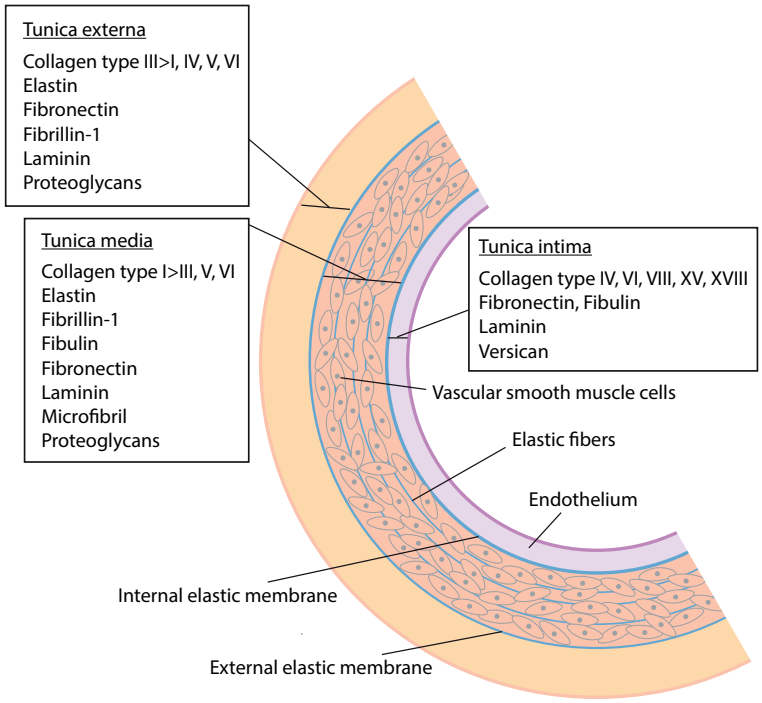

Figure 6. Representation of the aortic wall and the ECM components per layer

Overview of the ECM components that are present in each aortic wall layer.

ECM proteins are structurally dependent on each other and form structures together, such as fibrillin that covers the elastin core [98]. Mutations in major ECM components, such as elastin or fibrillin, lead to disorganization and weakening of the ECM, which can lead to aneurysm formation. Additionally, mutations in proteins that are essential for ECM assembly, such as LOX or fibulin-4, can lead to an unstructured ECM resulting in aneurysm formation.

III. Elastin

Elastin is a major component of the ECM in the medial layers of the aorta. Elastin layers are circumferentially oriented in the aortic media, providing elasticity and strength. Elastic fibers are formed out of microfibrils and the crosslinked elastin precursor protein, tropoelastin [99-101]. Tropoelastin contains lysine residues that serve to crosslink the precursor into a functional elastin polymer [97]. This crosslinking is mediated by the enzyme lysyl oxidase, which is recruited by fibulin-4 [99, 102]. If the elastin fibers are not properly formed, they will have a fragmented appearance and will not provide the elasticity and strength needed in the aorta [102]. Disease-causing mutations in the elastin assembly genes as well as mutations in the tropoelastin gene itself lead to weakening of the aorta and eventually causing aneurysm formation [102].

Fibulin-4 (*EFEMP2*) is part of the fibulin family that consists of seven members. Fibulins are ECM proteins that commonly contain multiple calcium binding EGF-like repeats and a motif in the C-terminus very similar to fibrillin proteins. Fibulin-4 strongly co-localizes with elastic fibers in the aortic wall. Alterations in the fibulin-4 protein lead to decreased secretion of fibulin-4 into the ECM or decreased binding to proteins such as lysyl oxidase, thereby preventing proper recruitment to the elastic fibers. These mutations in fibulin-4 lead to cutis laxa in patients [88, 96, 97].

Lysyl oxidase is essential for the crosslinking of tropoelastin, thereby maturing it to elastic fibers. The lysyl oxidase family consists of five members that are genetically very distinct from each other, but are all copper binding proteins. LOX, the first identified lysyl oxidase, is involved in crosslinking of elastic fibers. The function of the other lysyl oxidase family members is currently unknown. The amine oxidase activity of LOX catalyzes the formation of lysine-derived (and hydroxylysine-derived crosslinks in collagens) crosslinks in elastin [96].

I.V. Collagen

Apart from elasticity the aorta is also in need of rigidity to withstand the blood pressure after each heartbeat. Collagen deposition in the ECM can provide this strength to the aorta. Currently 28 types of collagen are identified of which type I, II, III, IV and V are the most prominent in the human body [103, 104]. Collagen is assembled from three alpha chains that are super-coiled and form a right-handed structure, also called procollagen. Procollagen peptidase then removes the N- and the C-terminal domains, leaving a helix structure called tropocollagen. Tropocollagen

is then assembled into a collagen fibril, which can be combined with other collagen fibrils to form a collagen fiber [103, 105, 106].

Improper formation of these collagen fibers by mutations in the collagen protein itself or the enzymes that are associated with its assembly, will lead to a disorganized ECM and can result in aneurysms by weakening of the aorta. Disease-causing mutations in collagen type I (*COL1A1*, *COL1A2*), III (*COL3A1*) and V (*COL5A1*, *COL5A2*) are known to cause Ehlers-Danlos syndrome. Collagen assembly enzymes that are known to cause aneurysms are: *ADAMTS2* and *PLOD1* [107, 108].

V. Fibrillin

Another major component of the elastic fiber is fibrillin. The glycoprotein fibrillin is secreted into the ECM by fibroblasts and forms a microfibril network with fibril diameters of 10 to 12 nm. Fibrillin is important for elastin assembly as the microfibrils cover the elastic core [109]. Furthermore, these microfibrils are important for the interaction with the latent TGFβ-binding proteins that retain inactive TGFβ in the ECM [109, 110]. Other proteins that are associated with microfibrils are microfibril-associated glycoproteins (MAGPs). These MAGPs interact with fibrillin to influence microfibril function. These MAGPS can further interact with TGFβ ligands and can induce TGFβ signaling by preventing the binding of latent TGFβ to fibrillin-1 as well as actively releasing latent TGFβ from fibrillin-1 [111]. Fibrillin monomers are assembled by a N- to C-terminal self-interaction leading to a beads-on-a-string appearance after assembly.

The presence of fibronectin is essential for the formation of fibrillin-1 into microfibrils [112]. Fibronectin is secreted from the cell as a soluble dimer, that is converted into larger insoluble fibrils in the ECM. Mutations in Fibrillin-1 affect elastin assembly, but also TGFβ activity. Disease-causing mutations in the *FBN1* gene (coding for the fibrillin-1 protein) clinically present as Marfan syndrome [113].

Cytoskeleton aberrations in aortic aneurysms

In a large group of patients with familial TAA, mutations have been identified in genes associated with contraction and the cytoskeleton. Cytoskeleton proteins are intracellular proteins that form the skeleton of the cell. These proteins are important for the shape of the cells, their ability to move, their contractile capacity, and they also facilitate intracellular transport along their fibers [114]. Components of the cytoskeleton can be subdivided into three types of filaments; microfilaments, microtubules and intermediate filaments. The combination of these three filament types makes up the cellular cytoskeleton [114, 115]. A subset of the cytoskeleton responsible for contraction is called the contractile apparatus. During contraction myosin can pull on the microfilaments (actin). Mutations in the cytoskeleton lead to problems with contractility and movement. Loss

of proper contractility can cause aneurysms, since the cell cannot properly react to forces from outside of the cell.

I. Actin

The microfilaments are the thinnest fibers present in the cytoskeleton, approximately 6 nm in diameter. Microfilaments are alternatively called actin fibers since they are built up of actin monomers. These actin monomers (globular actin or G-actin) are linked together to form the actin filament (filamentous actin or F-actin) upon hydrolysis of ATP. Each microfilament is made up out of two helical actin filaments and consists of a positive and a negative end. Polymerization of actin monomers happens at the positive side (barbed end) of the actin filament, while breakdown or depolymerization occurs at the negatively charged end (pointed end) [116-118].

Polymerization and depolymerization of actin fibers is tightly regulated by a number of proteins. Polymerization of actin monomers is facilitated by formins, profilin and the arp2/3 complex. Formins promote the elongation of actin fibers by removing capping proteins from the positive end, allowing attachment of new monomers. Profilin is an actin binding protein that catalyzes the exchange of ADP to ATP on the actin monomers, thereby making the monomers suitable for attachment to the actin filament at the positive end. The arp2/3 complex promotes side-branching by attaching itself to the main actin fiber as a new nucleation point [116, 119]. Depolymerization of actin fibers is performed by actin depolymerizing factor (ADF) and cofilin. By binding to the actin fiber, ADF and cofilin cause twisting of the fiber, resulting in structural weakening that leads to fiber decomposition. This process of polymerization/depolymerization is also known as actin filament treadmilling [116, 118-120].

During cellular contraction, actin filaments form the base network on which myosin filaments can pull to induce contraction. Organization of actin filaments into bundles makes a contraction more efficient. One of the main actin filament crosslinking proteins is α-actinin, an antiparallel homodimer that has actin binding sites at each end. Due to its structure α-actinin leaves space for interaction between actin and myosin [121, 122]. Typically, actin filaments are attached to a load near their barbed end, while during a contraction myosin moves towards the barbed end and can pull on the actin filament. In smooth muscle cells the barbed ends of actin filaments are embedded in dense bodies [122]. Mutations in the *ACTA2* gene are known to lead to familial TAA.

II. Myosin

Myosin is one of the proteins present in the contractile apparatus of VSMCs, that slides over the thin actin filament thereby creating contraction. Myosin consists of a head and a tail region; the head contains an actin binding site while the tail region can form a coil with another myosin tail. Myosin molecules can be formed by two myosin proteins and multiple myosin molecules will

form the thick myosin filament that is found in the contractile apparatus. The myosin molecule is also referred to as the heavy chain. The myosin light chain is located at the neck of the myosin molecule, and can be further subdivided into the essential and the regulatory light chain [118]. To start a cellular contraction a calcium influx is needed, which can either come from the extracellular space or from the sarcoplasmic reticulum. Calcium then binds to calmodulin, making it possible for calmodulin to phosphorylate the myosin light chain kinase (MYLK). After this activation, MYLK can phosphorylate the myosin light chain, thereby allowing cross-bridging of the myosin head and the actin fibers. Release from contraction can be induced by removal of the phosphate group from the myosin light chain by a myosin light chain phosphatase [123, 124]. Mutations in the myosin heavy chain (*MYH11*) are found in families with hereditary TAA. Myosin light chain kinase (*MYLK*) mutations also lead to hereditary TAA.

Deregulation of TGFβ signaling in aortic aneurysms

Mutations in components of the TGFβ pathway are associated with aortic aneurysm formation. Mutations in *TGFβ1*, *TGFβR1*, *TGFβR2* and *SMAD3* lead to the inability to activate the TGFβ signaling pathway or to transfer the signal to downstream effectors and are known to cause aneurysms [125-128].

TGFβ cytokines belong to the TGFβ family that in humans are encoded by 33 genes. These family members can be subdivided into two functional groups; 1) the TGF-like groups that, for instance, include TGFβs, Activins and Nodal, and 2) the BMP-like groups that include BMPs, growth and differentiation factors (GDFs). The TGFβ family is involved in a wide range of fundamental cell processes such as proliferation and differentiation, survival versus death as well as adhesion, migration and cytoskeleton dynamics [129].

TGFβ has three highly homologous isoforms, TGFβ1, TGFβ2 and TGFβ3, and these isoforms are synthesized as a precursor protein called pro-TGFβ (Fig. 7A). The precursor protein is cleaved by proprotein convertases (e.g. the Furin family) resulting in a mature homodimeric ligand and secreted from cells in a large complex that includes the cleaved proregion of the TGFβ precursor, also referred to as the latency associated peptide (LAP). This large complex is often called the small latent complex (SLC). The SLC is bound intracellularly, in the secretory pathway, by latent TGFβ binding proteins (LTBPs) to form the large latent complex (LLC) that is secreted and bound to the ECM via the N-terminal domain of LTBP [127, 129-133]. The C-terminal domain of LTBP is bound to the microfibrils via binding to the N-terminal domain of fibrillin-1. By storing TGFβ in the ECM, the activity of TGFβ can also be locally controlled [134]. Activation of TGFβ occurs via a multilevel process (Fig. 7B); first the LLC has to be removed from the matrix which can be done via proteolytic enzymes such as elastases. Second, the SLC has to be cleaved which is achieved by proteases like MMPs. Lastly LAP has to be removed from mature TGFβ by proteases such as plasmin or thrombospondin-1. However, this last activation step by proteases

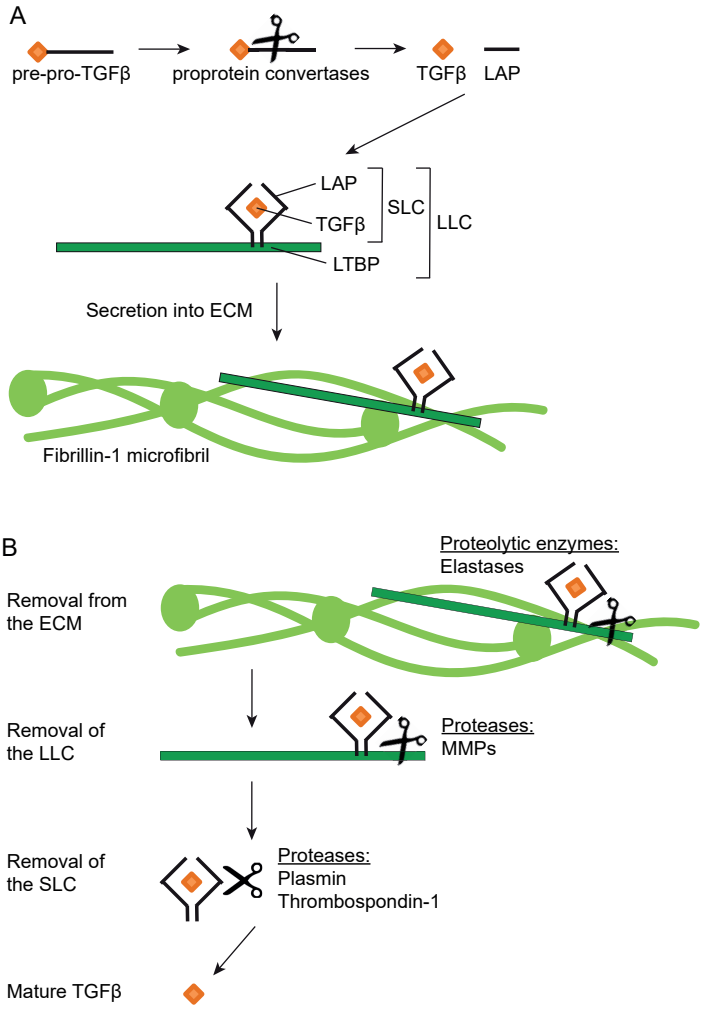

Figure 7. Storage and activation of TGFβ

A) Storage of TGFβ in the ECM. TGFβ is produced as a precursor protein (pre-pro-TGFβ) and is cleaved by proprotein convertases. The mature homodimeric ligand is then secreted from the cells in a large complex with the cleaved pro region of TGFβ also referred to as the latency associated protein (LAP), together they form the small latent complex (SLC). The SLC is bound to the latent TGFβ binding protein (LTBP) to form the large latent complex (LLC). The LLC is secreted and binds to the ECM via its N-terminal, while the C-terminal binds to the fibrillin-1 microfibrils. **B)** Activation of TGFβ in the ECM. Proteolytic enzymes remove the LLC from the ECM after which proteases remove the LTBP from the SLC. The LAP is then removed by proteases to expose active TGFβ that can activate the TGFBRs.

varies between cell types and the context of the activation [129, 135-138]. This intricate way of storing and activation of TGFβ regulates the bioavailability of TGFβ and thereby controls many essential processes.

When activated, the TGFβ signaling pathway can be divided into two parts; the canonical and the non-canonical pathway. The non-canonical pathway signals via ERK1/2, JNK/p38, RhoA and Akt, among others [139] (Fig. 5). The canonical pathway is often associated with aneurysm formation and makes use of TGFβ and receptor-activated phosphor-Smad2/3 for its signaling [127, 140]. The canonical TGFβ pathway is activated by binding of TGFβ to a TGFβ receptor 2 dimer (Fig. 8). A TGFβ receptor 1 dimer is then recruited to form a heterotetramer of TGFβ receptors. Binding of the TGFβR2 to the TGFβR1 enables TGFβR1 phosphorylation by TGFβR2, thereby activating the TGFβR1 in its juxtamembrane GS-rich segment (also named type 1 box). Smad2/3 proteins, which are auto-inhibited, are recruited to the TGFβR1 and are then phosphorylated. Phosphorylated Smad2/3 forms a complex with Smad4, which accumulates in the nucleus. Here the Smad2/3-Smad4 complex, via weak DNA binding, often with co-operation of Smad-interacting transcription factors, initiates transcription of downstream effector molecules such as matrix metalloproteases (MMPs), connective tissue growth factor (CTGF) and PAI-1 [126, 127, 140]. A negative feedback loop in the TGFβ signaling pathway is activated after transcriptional activation of the *SMAD7* gene. Smad7 inhibits TGFβ signaling by blocking Smad2 to Smad4 binding, and also by forming a stable complex with the TGFβR1 and preventing phosphorylation of Smad2 [127, 140, 141].

IMMUNE RESPONSE AND AORTIC ANEURYSMS

Next to genetic causes of aneurysm formation many non-genetic factors also contribute to aneurysm formation, an important one being the immune system. Influx of immune cells is thought to happen after an initial injury of the aorta, such as degradation of elastin fibers or loss of VSMCs. Animal studies in which aneurysms were induced with elastase showed that immune infiltration was present prior to aneurysm formation one week after elastase treatment [142, 143]. These studies further show that after the initial injury with elastase, reactive isotopes of the ECM were unmasked and immunoglobins with reactivity to microfibrils were identified. This increase in influx of immune cells and increased reactivity to the ECM leads to further attraction of the immune system and a snowball effect of aortic damage.

Most often AAA is thought to be associated with chronic inflammation and an increased immune response [53]. However, an increased immune response can also be found in TAA. *Smad3*$^{-/-}$ mice show an influx of CD3^{+} T cells and macrophages in their aorta [78]. Although less research was performed on the involvement of the immune system in human TAA, studies have shown that

half of the patients with a TAA or dissection under study have increased IFNγ expression [144]. This increase in IFNγ was associated with increased aortic diameter and reduced amounts of the ECM.

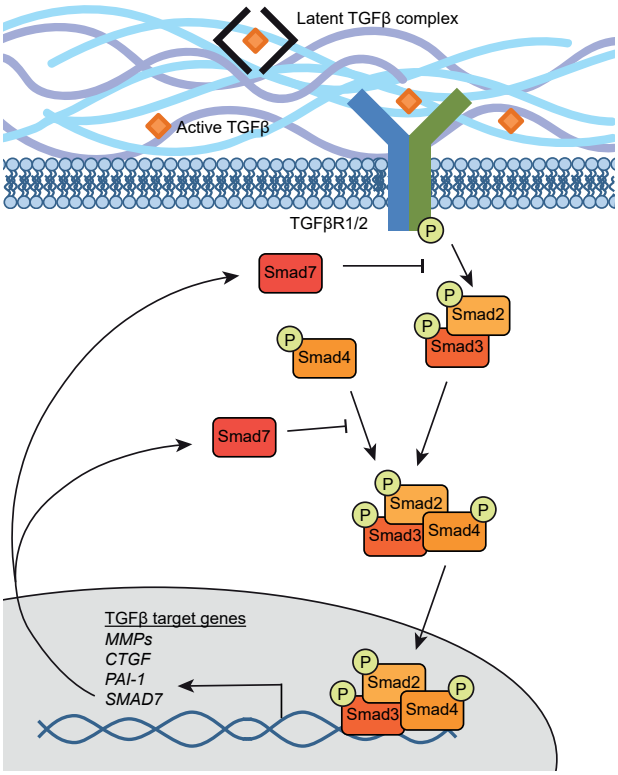

Figure 8. Activation of the TGFβ signaling pathway

Schematic overview of the TGF signaling pathway. TGFβ binds to a TGFβR2 dimer, a TGFβR1 dimer is then recruited to form a heterotetramer of TGFβ receptors. Binding of the TGFβR2 to the TGFβR1 enables TGFβR1 to be phosphorylated by the TGFβR2. Smad2/3 proteins are recruited to the TGFR1 and are phosphorylated. Phosphorylated Smad2/3 forms a complex with Smad4 to enter the nucleus, where they initiate transcription of TGFβ target genes, such as matrix metalloproteases (MMPs), connective tissue growth factor (CTGF) and PAI-1. The transcribed Smad7 serves as a negative feedback loop by preventing Smad2 to Smad4 binding and by preventing phosphorylation of Smad2.

Chronic infections of the aorta by microorganisms can also result in aneurysm formation by infiltration of the immune system. Inflammatory aneurysms were first mentioned in 1972 by Walker et al. and are caused by a viral or bacterial infection of the aorta. Inflammatory aneurysms are associated with thickening of the aortic wall and eventually dilation of the lumen, leading to aneurysm formation [145, 146]. Some human leukocyte antigen (HLA) classes are more predominant in AAA patients suggesting that AAA could also have an autoimmunity origin [147]. Furthermore, immunoglobins have been identified in AAA patients that showed reactivity to elastin and collagen [148].

MOLECULAR PHENOTYPING OF AORTIC ANEURYSM GENES

Although much research has been performed on potentially causative genes for aneurysm formation in relation to hereditability of aneurysms, nowadays many so-called variants of uncertain significance (VUS) are identified in the clinic. These VUS's are variants that are not directly identifiable as benign or pathogenic. VUS are defined as "intronic, silent or missense variants that affect splicing, in-frame deletions/insertions, or as missense variants for which more than two *in silico* protein predictions are damaging" [62]. The problem with these VUS's is that identification of potential pathogenicity cannot be based solely on the prediction models alone and would need additional testing and analysis to determine their effect. Furthermore, novel candidate genes for aneurysm formation are identified by new techniques such as whole exome and whole genome sequencing (WES/WGS). *In silico* analysis of these variants does not always lead to a conclusive result on the pathogenicity. One approach to analyze the consequence of a given variant would be an analysis using a cellular tests (functional test) that reports on a specific function of the gene of interest. Using this molecular phenotyping of aneurysm genes, VUS's can be compared to known 'aneurysm' genes to determine which molecular pathways they might be linked to. For example, in the past, identification of disease-causing mutations of *ACTA2* was performed by immunofluorescent staining of smooth muscle actin (SMA) in control VSMCs and VSMCs from TAA patients [49]. TAA patients with an *ACTA2* mutation showed less distinct SMA fibers in their cytoskeleton compared to control VSMCs.

As previously explained, disease-causing mutations in aortic aneurysm genes affect different cellular compartments: ECM, cytoskeleton and TGFβ signaling. Often aortic aneurysm genes are characterized by analysis of aortic material of patients. However, these results do not prove a causative link between a found mutation and aneurysm formation as the effects cannot be directly linked to the mutation. Inducing a patient mutation in a control cell line and analyzing the effects would be the ultimate proof for causality. However, specific functional assays on the function of aortic aneurysm genes in patient cells could also provide information on the

pathogenicity. To determine if specific functional analyses are more often used for one of these subgroups, we examined which assays are currently in use for which genes and subgroups.

Extracellular matrix

Fibrillin-1 (*FBN1*), fibulin-4 (*EFEMP2*) and tropoelastin (*ELN*) are important factors in the assembly and structural integrity of the ECM. Mutations in these genes lead to aneurysm formation and are often related to more complex clinical syndromes. *FBN1* mutations lead to Marfan syndrome, while *EFEMP2* and *ELN* mutations lead to cutis laxa. Aortas of Marfan and cutis laxa patients show improperly formed ECM. Aortas of patients with *EFEMP2* and *ELN* mutations often show fragmentation of the elastic laminae [149-151]. Loss of VSMCs was identified in the aortic wall of a population of Marfan patients which was accompanied by loss of SMA and SM22 protein [152]. *FBN1* mutations (p.P1225L, p.M1576T, p.G2003R) showed activation of the TGFβ pathway which was demonstrated using western blotting to detect increased phosphorylation of Smad2 [153]. Stability of mutated fibrillin-1 proteins was analyzed with a proteolytic assay by Kirschner et al., which showed increased susceptibility to degradation of mutated fibrillin-1 protein [154]. Studies were performed to determine the binding of fibulin-4 to LOX in the presence of different *EFEMP2* mutations [88]. Results showed that some *EFEMP2* (p.E57K, p.E126K, p.A397T) mutations resulted in reduced binding of fibulin-4 to LOX, while other mutated fibulin-4 proteins (p.C267Y, p.R279C) were not secreted, thereby preventing binding to LOX.

Cytoskeleton

Smooth muscle actin (*ACTA2*), myosin heavy chain 11 (*MYH11*) and myosin light chain kinase (*MYLK*) are important factors for the cytoskeleton and contractility of VSMCs. Disease-causing mutations in these proteins lead to aneurysm formation by dysregulation of VSMC contractility and are associated with hereditary aortic aneurysms. Mutations in *ACTA2* often lead to decreased SMA protein levels and this reduction was shown to reduce the force output of *ACTA2* mutated VSMCs via a one-bead laser trap experiment [52, 155, 156]. Analysis of aortic tissue of *ACTA2* and *MYLK* patients showed increased activation of the TGFβ signaling pathway via phosphorylation of Smad2 [157]. Similar to ECM mutations, fragmentation of the elastic laminae was found in aortic sections of *MYH11* and *MYLK* patients [50, 51].

Polymerization of mutant SMA molecules in yeast cells was performed by Malloy et al. to determine if *ACTA2* mutations affected the assembly of the cytoskeleton [158]. The most prevalent *ACTA2* mutation (R256H) showed a longer actin assembly time and less polymerization compared to control yeast cells, indicating that the polymerization is affected by *ACTA2* mutations. The cytoskeleton is also affected by *MYH11* mutations as MYH11$^{R247C/R247C}$, leading to decreased ATPase activity, VSMCs showed less polymerized actin and less actin in general [159]. These cytoskeleton aberrations also translated to decreased attachment of the MYH11$^{R247C/R247C}$ VSMCs by decreased focal adhesion size, which underlines the connectivity of all cellular compartments

[159]. Kinase activity of mutant MYLK was investigated by Wang et al. and lower maximum kinase activity was shown for the two tested *MYLK* mutations leading to lowered contraction [51].

TGFβ signaling pathway

Disease-causing mutations in the TGFβ signaling components *TGFβ2*, *TGFBR1*, *TGFBR2* and *SMAD3* lead to LDS, characterized by aneurysm formation, joint hypermobility and skeletal malformation amongst others. Fragmentation of the elastic laminae is found in aortic sections of *TGFβ2* and *TGFβR1* patients as well as in aortas of *Smad3*$^{-/-}$ mice [39, 77, 78, 160]. Electron microscopic analyses further revealed absence of elastic fiber association with VSMCs in *TGFβR1* patients [39]. Reduced presence of the cytoskeleton protein SMA was found in aortic sections of *TGFβ2* and *TGFβR2* patients compared to healthy controls [42, 161]. *Smad3*$^{-/-}$ mouse aortas also revealed alterations to the cytoskeleton by a decrease in α-actin protein levels [77, 78]. *TGFβ2*, *TGFβR1* and *SMAD3* patients were shown to have increased phosphorylation of Smad2, which suggest increased activation of the TGFβ pathway [40, 41, 160, 162]. Activation of the TGFβ signaling pathways was confirmed in TGFβ2$^{+/-}$ mice and CTGF and collagen, downstream targets of the TGFβ signaling pathway, are increased in *TGFβ2* patients [42, 160]. Boileau et al. further showed decreased protein levels of TGFβ2 in *TGFβ2* patients, while *TGFβ2* gene expression was increased. This suggests that the TGFβ2 protein is less stable upon mutation [160].

SCOPE OF THIS THESIS: MOLECULAR MECHANISMS OF AORTIC ANEURYSMS

Since characterization of aneurysm genes is mainly focused on analysis of the TGFβ signaling pathway and cytoskeleton proteins, it is important to identify the behavior of known aneurysm genes and controls in cellular functional assays that report on TGFβ signaling and cytoskeleton function. The read-outs of these functional assays can then be applied to identify the effects of VUS to determine their pathogenicity or to link newly discovered genes to molecular pathways that affect aneurysm formation. In **chapter 2** of this thesis we characterized fibroblast cell lines derived from control and aneurysm patients bearing *ACTA2*, *MYH11*, *SMAD3* and *FBN1* mutations. We analyzed the transdifferentiation of control and patient fibroblasts to VSMC-like cells. Subsequently we determined TGFβ responsiveness over time in these cells and analyzed functional parameters like cell migration and contractility. **Chapter 3** describes the characterization of a new mouse model for arterial tortuosity syndrome (ATS). Homozygous mutations in *SLC2A10* lead to ATS in humans and a knock-out model has been developed to better characterize the role of *SLC2A10*. Since *SLC2A10* (also referred to as GLUT10) has been suggested to work as a vitamin C transporter, the vitamin C transporter in mice, *GULO*, was also knocked-out. Aortas were analyzed on a macroscopic and microscopic level. Isolated aortic VSMCs were analyzed for mitochondrial function, ECM aberrations and TGFβ signaling.

To fully understand aneurysm formation and to identify possible therapeutic targets we must understand the molecular mechanisms that underlie aneurysm formation. Analyzing aneurysmal mouse models is an effective method to further identify processes that are involved in aneurysm formation. In this thesis we investigated *Fibulin-4* mouse models to detect affected processes at the cellular level. Since aneurysm patients often show increased TGFβ signaling it was long thought that this led to aneurysm formation. However, current research indicates that increased TGFβ signaling can be protective of aneurysmal disease in the initial stages but proved to be detrimental during later disease stages [163, 164]. This illustrates the need for research to elucidate the molecular mechanisms of aneurysm formation further.

Additionally, we want to identify other molecular mechanisms that are involved in aneurysm formation. In **chapter 4** of this thesis we show that total absence and reduced presence of fibulin-4 has different effects on cytoskeleton structure and dynamics as well as on TGFβ signaling. **Chapter 5** demonstrates that reduced levels of fibulin-4 in the *Fibulin-4*$^{R/R}$ mouse model lead to dysregulation of metabolism and altered mitochondrial respiration. Finally, **chapter 6** shows that mitochondrial dysfunction is also found in aortic tissue of Marfan syndrome patients and non-syndromic heritable thoracic aortic disease patients. This was identified by performing RNA sequencing on aortic aneurysm tissue that was retrieved after elective replacement of the aortic arch.

REFERENCES

1. Debakey, M.E., et al., *Surgical Management of Dissecting Aneurysms of the Aorta.* J Thorac Cardiovasc Surg, 1965. **49**: p. 130-49.
2. Fukui, T., *Management of acute aortic dissection and thoracic aortic rupture.* J Intensive Care, 2018. **6**: p. 15.
3. Daily, P.O., et al., *Management of acute aortic dissections.* Ann Thorac Surg, 1970. **10**(3): p. 237-47.
4. Chiles, C. and J.J. Carr, *Vascular diseases of the thorax: evaluation with multidetector CT.* Radiol Clin North Am, 2005. **43**(3): p. 543-69, viii.
5. Bertoli-Avella, A.M., et al., *Mutations in a TGF-beta ligand, TGFB3, cause syndromic aortic aneurysms and dissections.* J Am Coll Cardiol, 2015. **65**(13): p. 1324-1336.
6. Frederick, J.R. and Y.J. Woo, *Thoracoabdominal aortic aneurysm.* Ann Cardiothorac Surg, 2012. **1**(3): p. 277-85.
7. Hasham, S.N., D.C. Guo, and D.M. Milewicz, *Genetic basis of thoracic aortic aneurysms and dissections.* Curr Opin Cardiol, 2002. **17**(6): p. 677-83.
8. Huang, X. and J.P. Saint-Jeannet, *Induction of the neural crest and the opportunities of life on the edge.* Dev Biol, 2004. **275**(1): p. 1-11.
9. Tajbakhsh, S. and R. Sporle, *Somite development: constructing the vertebrate body.* Cell, 1998. **92**(1): p. 9-16.
10. Gilbert, S.F., *Developmental Biology, Lateral Plate Mesoderm*. 6th edition ed. 2000, Sunderland (MA): Sinauer Associates.
11. Ruddy, J.M., et al., *Regional heterogeneity within the aorta: relevance to aneurysm disease.* J Thorac Cardiovasc Surg, 2008. **136**(5): p. 1123-30.
12. Kuivaniemi, H., et al., *Understanding the pathogenesis of abdominal aortic aneurysms.* Expert Rev Cardiovasc Ther, 2015. **13**(9): p. 975-87.
13. Bickerstaff, L.K., et al., *Thoracic aortic aneurysms: a population-based study.* Surgery, 1982. **92**(6): p. 1103-8.
14. Clouse, W.D., et al., *Improved prognosis of thoracic aortic aneurysms: a population-based study.* JAMA, 1998. **280**(22): p. 1926-9.
15. Itani, Y., et al., *Measurement of aortic diameters and detection of asymptomatic aortic aneurysms in a mass screening program using a mobile helical computed tomography unit.* Heart Vessels, 2002. **16**(2): p. 42-5.
16. Kalsch, H., et al., *Body-surface adjusted aortic reference diameters for improved identification of patients with thoracic aortic aneurysms: results from the population-based Heinz Nixdorf Recall study.* Int J Cardiol, 2013. **163**(1): p. 72-8.
17. Forsdahl, S.H., et al., *Risk factors for abdominal aortic aneurysms: a 7-year prospective study: the Tromso Study, 1994-2001.* Circulation, 2009. **119**(16): p. 2202-8.
18. Vardulaki, K.A., et al., *Incidence among men of asymptomatic abdominal aortic aneurysms: estimates from 500 screen detected cases.* J Med Screen, 1999. **6**(1): p. 50-4.

19. Lederle, F.A., et al., *Yield of repeated screening for abdominal aortic aneurysm after a 4-year interval. Aneurysm Detection and Management Veterans Affairs Cooperative Study Investigators.* Arch Intern Med, 2000. **160**(8): p. 1117-21.
20. Wilmink, A.B., et al., *The incidence of small abdominal aortic aneurysms and the change in normal infrarenal aortic diameter: implications for screening.* Eur J Vasc Endovasc Surg, 2001. **21**(2): p. 165-70.
21. Davies, R.R., et al., *Yearly rupture or dissection rates for thoracic aortic aneurysms: simple prediction based on size.* Ann Thorac Surg, 2002. **73**(1): p. 17-27; discussion 27-8.
22. Lederle, F.A., et al., *Rupture rate of large abdominal aortic aneurysms in patients refusing or unfit for elective repair.* JAMA, 2002. **287**(22): p. 2968-72.
23. Robinson, D., et al., *Aortic aneurysms - screening, surveillance and referral.* Aust Fam Physician, 2013. **42**(6): p. 364-9.
24. Perko, M.J., et al., *Unoperated aortic aneurysm: a survey of 170 patients.* Ann Thorac Surg, 1995. **59**(5): p. 1204-9.
25. Bashir, M., et al., *A Perspective on Natural History and Survival in Nonoperated Thoracic Aortic Aneurysm Patients.* Aorta (Stamford), 2013. **1**(3): p. 182-9.
26. Coady, M.A., et al., *What is the appropriate size criterion for resection of thoracic aortic aneurysms?* J Thorac Cardiovasc Surg, 1997. **113**(3): p. 476-91; discussion 489-91.
27. Dubost, C., M. Allary, and N. Oeconomos, *Resection of an aneurysm of the abdominal aorta: reestablishment of the continuity by a preserved human arterial graft, with result after five months.* AMA Arch Surg, 1952. **64**(3): p. 405-8.
28. Moll, F.L., et al., *Management of abdominal aortic aneurysms clinical practice guidelines of the European society for vascular surgery.* Eur J Vasc Endovasc Surg, 2011. **41 Suppl 1**: p. S1-S58.
29. Prinssen, M., et al., *A randomized trial comparing conventional and endovascular repair of abdominal aortic aneurysms.* N Engl J Med, 2004. **351**(16): p. 1607-18.
30. participants, E.t., *Endovascular aneurysm repair versus open repair in patients with abdominal aortic aneurysm (EVAR trial 1): randomised controlled trial.* Lancet, 2005. **365**(9478): p. 2179-86.
31. Lederle, F.A., et al., *Outcomes following endovascular vs open repair of abdominal aortic aneurysm: a randomized trial.* JAMA, 2009. **302**(14): p. 1535-42.
32. Sicard, G.A., et al., *Endovascular abdominal aortic aneurysm repair: long-term outcome measures in patients at high-risk for open surgery.* J Vasc Surg, 2006. **44**(2): p. 229-36.
33. Milewicz, D.M. and E.S. Regalado, *Use of genetics for personalized management of heritable thoracic aortic disease: how do we get there?* J Thorac Cardiovasc Surg, 2015. **149**(2 Suppl): p. S3-5.
34. Albornoz, G., et al., *Familial thoracic aortic aneurysms and dissections--incidence, modes of inheritance, and phenotypic patterns.* Ann Thorac Surg, 2006. **82**(4): p. 1400-5.
35. Coady, M.A., et al., *Familial patterns of thoracic aortic aneurysms.* Arch Surg, 1999. **134**(4): p. 361-7.
36. Campens, L., et al., *Gene panel sequencing in heritable thoracic aortic disorders and related entities - results of comprehensive testing in a cohort of 264 patients.* Orphanet J Rare Dis, 2015. **10**: p. 9.

37. Verhagen, J.M.A., et al., *Expert consensus recommendations on the cardiogenetic care for patients with thoracic aortic disease and their first-degree relatives.* Int J Cardiol, 2018. **258**: p. 243-248.
38. Dietz, H.C., et al., *The Marfan syndrome locus: confirmation of assignment to chromosome 15 and identification of tightly linked markers at 15q15-q21.3.* Genomics, 1991. **9**(2): p. 355-61.
39. Loeys, B.L., et al., *A syndrome of altered cardiovascular, craniofacial, neurocognitive and skeletal development caused by mutations in TGFBR1 or TGFBR2.* Nat Genet, 2005. **37**(3): p. 275-81.
40. Loeys, B.L., et al., *Aneurysm syndromes caused by mutations in the TGF-beta receptor.* N Engl J Med, 2006. **355**(8): p. 788-98.
41. van de Laar, I.M., et al., *Mutations in SMAD3 cause a syndromic form of aortic aneurysms and dissections with early-onset osteoarthritis.* Nat Genet, 2011. **43**(2): p. 121-6.
42. Lindsay, M.E., et al., *Loss-of-function mutations in TGFB2 cause a syndromic presentation of thoracic aortic aneurysm.* Nat Genet, 2012. **44**(8): p. 922-7.
43. Cortini, F., et al., *Understanding the basis of Ehlers-Danlos syndrome in the era of the next-generation sequencing.* Arch Dermatol Res, 2019. **311**(4): p. 265-275.
44. Nicholls, A.C., et al., *An exon skipping mutation of a type V collagen gene (COL5A1) in Ehlers-Danlos syndrome.* J Med Genet, 1996. **33**(11): p. 940-6.
45. Michalickova, K., et al., *Mutations of the alpha2(V) chain of type V collagen impair matrix assembly and produce ehlers-danlos syndrome type I.* Hum Mol Genet, 1998. **7**(2): p. 249-55.
46. Pepin, M., et al., *Clinical and genetic features of Ehlers-Danlos syndrome type IV, the vascular type.* N Engl J Med, 2000. **342**(10): p. 673-80.
47. Zhang, M.C., et al., *Cutis laxa arising from frameshift mutations in exon 30 of the elastin gene (ELN).* J Biol Chem, 1999. **274**(2): p. 981-6.
48. Hucthagowder, V., et al., *Fibulin-4: a novel gene for an autosomal recessive cutis laxa syndrome.* Am J Hum Genet, 2006. **78**(6): p. 1075-80.
49. Guo, D.C., et al., *Mutations in smooth muscle alpha-actin (ACTA2) lead to thoracic aortic aneurysms and dissections.* Nat Genet, 2007. **39**(12): p. 1488-93.
50. Zhu, L., et al., *Mutations in myosin heavy chain 11 cause a syndrome associating thoracic aortic aneurysm/aortic dissection and patent ductus arteriosus.* Nat Genet, 2006. **38**(3): p. 343-9.
51. Wang, L., et al., *Mutations in myosin light chain kinase cause familial aortic dissections.* Am J Hum Genet, 2010. **87**(5): p. 701-7.
52. Guo, D.C., et al., *Recurrent gain-of-function mutation in PRKG1 causes thoracic aortic aneurysms and acute aortic dissections.* Am J Hum Genet, 2013. **93**(2): p. 398-404.
53. Guo, D.C., et al., *Pathogenesis of thoracic and abdominal aortic aneurysms.* Ann N Y Acad Sci, 2006. **1085**: p. 339-52.
54. Clifton, M.A., *Familial abdominal aortic aneurysms.* Br J Surg, 1977. **64**(11): p. 765-6.
55. Tasoglu, I., et al., *Thoracic aortic aneurysms after blunt trauma.* Ulus Travma Acil Cerrahi Derg, 2013. **19**(4): p. 343-7.
56. Kline, J.L., J.L. Gimenez, and R.J. Maloney, *Post-stenotic vascular dilatation: confirmation of an old hypothesis by a new method.* J Thorac Cardiovasc Surg, 1962. **44**: p. 738-48.

57. Sorelius, K. and P.G. di Summa, *On the Diagnosis of Mycotic Aortic Aneurysms.* Clin Med Insights Cardiol, 2018. **12**: p. 1179546818759678.
58. Yuan, S.M., *Syphilitic aortic aneurysm Syphilitisches Aortenaneurysma.* Z Rheumatol, 2018. **77**(8): p. 741-748.
59. Baird, P.A., et al., *Sibling risks of abdominal aortic aneurysm.* Lancet, 1995. **346**(8975): p. 601-4.
60. van de Luijtgaarden, K.M., et al., *Lower atherosclerotic burden in familial abdominal aortic aneurysm.* J Vasc Surg, 2014. **59**(3): p. 589-93.
61. Pinard, A., G.T. Jones, and D.M. Milewicz, *Genetics of Thoracic and Abdominal Aortic Diseases.* Circ Res, 2019. **124**(4): p. 588-606.
62. van de Luijtgaarden, K.M., et al., *First genetic analysis of aneurysm genes in familial and sporadic abdominal aortic aneurysm.* Hum Genet, 2015. **134**(8): p. 881-93.
63. Shibamura, H., et al., *Genome scan for familial abdominal aortic aneurysm using sex and family history as covariates suggests genetic heterogeneity and identifies linkage to chromosome 19q13.* Circulation, 2004. **109**(17): p. 2103-8.
64. Nikpay, M., et al., *A comprehensive 1,000 Genomes-based genome-wide association meta-analysis of coronary artery disease.* Nat Genet, 2015. **47**(10): p. 1121-1130.
65. Biros, E., et al., *A single nucleotide polymorphism in exon 3 of the kallikrein 1 gene is associated with large but not small abdominal aortic aneurysm.* Atherosclerosis, 2011. **217**(2): p. 452-7.
66. Jones, G.T., et al., *Meta-Analysis of Genome-Wide Association Studies for Abdominal Aortic Aneurysm Identifies Four New Disease-Specific Risk Loci.* Circ Res, 2017. **120**(2): p. 341-353.
67. Pereira, L., et al., *Targetting of the gene encoding fibrillin-1 recapitulates the vascular aspect of Marfan syndrome.* Nat Genet, 1997. **17**(2): p. 218-22.
68. Pereira, L., et al., *Pathogenetic sequence for aneurysm revealed in mice underexpressing fibrillin-1.* Proc Natl Acad Sci U S A, 1999. **96**(7): p. 3819-23.
69. Judge, D.P., et al., *Evidence for a critical contribution of haploinsufficiency in the complex pathogenesis of Marfan syndrome.* J Clin Invest, 2004. **114**(2): p. 172-81.
70. Charbonneau, N.L., et al., *In vivo studies of mutant fibrillin-1 microfibrils.* J Biol Chem, 2010. **285**(32): p. 24943-55.
71. Carta, L., et al., *Fibrillins 1 and 2 perform partially overlapping functions during aortic development.* J Biol Chem, 2006. **281**(12): p. 8016-23.
72. Oshima, M., H. Oshima, and M.M. Taketo, *TGF-beta receptor type II deficiency results in defects of yolk sac hematopoiesis and vasculogenesis.* Dev Biol, 1996. **179**(1): p. 297-302.
73. Larsson, J., et al., *Abnormal angiogenesis but intact hematopoietic potential in TGF-beta type I receptor-deficient mice.* EMBO J, 2001. **20**(7): p. 1663-73.
74. Carvalho, R.L., et al., *Compensatory signalling induced in the yolk sac vasculature by deletion of TGFbeta receptors in mice.* J Cell Sci, 2007. **120**(Pt 24): p. 4269-77.
75. Choudhary, B., et al., *Cardiovascular malformations with normal smooth muscle differentiation in neural crest-specific type II TGFbeta receptor (Tgfbr2) mutant mice.* Dev Biol, 2006. **289**(2): p. 420-9.

76. Choudhary, B., et al., *Absence of TGFbeta signaling in embryonic vascular smooth muscle leads to reduced lysyl oxidase expression, impaired elastogenesis, and aneurysm.* Genesis, 2009. **47**(2): p. 115-21.
77. Ye, P., et al., *GM-CSF contributes to aortic aneurysms resulting from SMAD3 deficiency.* J Clin Invest, 2013. **123**(5): p. 2317-31.
78. van der Pluijm, I., et al., *Defective Connective Tissue Remodeling in Smad3 Mice Leads to Accelerated Aneurysmal Growth Through Disturbed Downstream TGF-beta Signaling.* EBioMedicine, 2016. **12**: p. 280-294.
79. Schildmeyer, L.A., et al., *Impaired vascular contractility and blood pressure homeostasis in the smooth muscle alpha-actin null mouse.* FASEB J, 2000. **14**(14): p. 2213-20.
80. Morano, I., et al., *Smooth-muscle contraction without smooth-muscle myosin.* Nat Cell Biol, 2000. **2**(6): p. 371-5.
81. McLaughlin, P.J., et al., *Targeted disruption of fibulin-4 abolishes elastogenesis and causes perinatal lethality in mice.* Mol Cell Biol, 2006. **26**(5): p. 1700-9.
82. Huang, J., et al., *Fibulin-4 deficiency results in ascending aortic aneurysms: a potential link between abnormal smooth muscle cell phenotype and aneurysm progression.* Circ Res, 2010. **106**(3): p. 583-92.
83. Huang, J., et al., *Angiotensin-converting enzyme-induced activation of local angiotensin signaling is required for ascending aortic aneurysms in fibulin-4-deficient mice.* Sci Transl Med, 2013. **5**(183): p. 183ra58, 1-11.
84. Yamashiro, Y., et al., *Abnormal mechanosensing and cofilin activation promote the progression of ascending aortic aneurysms in mice.* Sci Signal, 2015. **8**(399): p. ra105.
85. Hanada, K., et al., *Perturbations of vascular homeostasis and aortic valve abnormalities in fibulin-4 deficient mice.* Circ Res, 2007. **100**(5): p. 738-46.
86. Ramnath, N.W., et al., *Fibulin-4 deficiency increases TGF-beta signalling in aortic smooth muscle cells due to elevated TGF-beta2 levels.* Sci Rep, 2015. **5**: p. 16872.
87. Igoucheva, O., et al., *Fibulin-4 E57K Knock-in Mice Recapitulate Cutaneous, Vascular and Skeletal Defects of Recessive Cutis Laxa 1B with both Elastic Fiber and Collagen Fibril Abnormalities.* J Biol Chem, 2015. **290**(35): p. 21443-59.
88. Sasaki, T., et al., *Functional consequence of fibulin-4 missense mutations associated with vascular and skeletal abnormalities and cutis laxa.* Matrix Biol, 2016. **56**: p. 132-149.
89. Hornstra, I.K., et al., *Lysyl oxidase is required for vascular and diaphragmatic development in mice.* J Biol Chem, 2003. **278**(16): p. 14387-93.
90. Maki, J.M., et al., *Inactivation of the lysyl oxidase gene Lox leads to aortic aneurysms, cardiovascular dysfunction, and perinatal death in mice.* Circulation, 2002. **106**(19): p. 2503-9.
91. Daugherty, A. and L.A. Cassis, *Mouse models of abdominal aortic aneurysms.* Arterioscler Thromb Vasc Biol, 2004. **24**(3): p. 429-34.
92. Kanematsu, Y., et al., *Pharmacologically induced thoracic and abdominal aortic aneurysms in mice.* Hypertension, 2010. **55**(5): p. 1267-74.

93. Daugherty, A. and L. Cassis, *Chronic angiotensin II infusion promotes atherogenesis in low density lipoprotein receptor -/- mice.* Ann N Y Acad Sci, 1999. **892**: p. 108-18.
94. Daugherty, A., M.W. Manning, and L.A. Cassis, *Angiotensin II promotes atherosclerotic lesions and aneurysms in apolipoprotein E-deficient mice.* J Clin Invest, 2000. **105**(11): p. 1605-12.
95. Daugherty, A., et al., *Angiotensin II infusion promotes ascending aortic aneurysms: attenuation by CCR2 deficiency in apoE-/- mice.* Clin Sci (Lond), 2010. **118**(11): p. 681-9.
96. Wagenseil, J.E. and R.P. Mecham, *Vascular extracellular matrix and arterial mechanics.* Physiol Rev, 2009. **89**(3): p. 957-89.
97. Kelleher, C.M., S.E. McLean, and R.P. Mecham, *Vascular extracellular matrix and aortic development.* Curr Top Dev Biol, 2004. **62**: p. 153-88.
98. Frantz, C., K.M. Stewart, and V.M. Weaver, *The extracellular matrix at a glance.* J Cell Sci, 2010. **123**(Pt 24): p. 4195-200.
99. Mithieux, S.M. and A.S. Weiss, *Elastin.* Adv Protein Chem, 2005. **70**: p. 437-61.
100. Mecham, R.P., *Elastin synthesis and fiber assembly.* Ann N Y Acad Sci, 1991. **624**: p. 137-46.
101. Wagenseil, J.E. and R.P. Mecham, *New insights into elastic fiber assembly.* Birth Defects Res C Embryo Today, 2007. **81**(4): p. 229-40.
102. Papke, C.L. and H. Yanagisawa, *Fibulin-4 and fibulin-5 in elastogenesis and beyond: Insights from mouse and human studies.* Matrix Biol, 2014. **37**: p. 142-9.
103. Muiznieks, L.D. and F.W. Keeley, *Molecular assembly and mechanical properties of the extracellular matrix: A fibrous protein perspective.* Biochim Biophys Acta, 2013. **1832**(7): p. 866-75.
104. Myllyharju, J. and K.I. Kivirikko, *Collagens, modifying enzymes and their mutations in humans, flies and worms.* Trends Genet, 2004. **20**(1): p. 33-43.
105. Shoulders, M.D. and R.T. Raines, *Collagen structure and stability.* Annu Rev Biochem, 2009. **78**: p. 929-58.
106. Riso E.M, K.P., Seene T, *Remodelling of skeletal muscle extracellular matrix: effect of unloading and reloading.*, in *Composition and function of the extracellular matrix in the human body.* . 2016, InTech, Reijka. p. 45–68.
107. De Paepe, A. and F. Malfait, *The Ehlers-Danlos syndrome, a disorder with many faces.* Clin Genet, 2012. **82**(1): p. 1-11.
108. Colige, A., et al., *Novel types of mutation responsible for the dermatosparactic type of Ehlers-Danlos syndrome (Type VIIC) and common polymorphisms in the ADAMTS2 gene.* J Invest Dermatol, 2004. **123**(4): p. 656-63.
109. Kielty, C.M., et al., *Fibrillin: from microfibril assembly to biomechanical function.* Philos Trans R Soc Lond B Biol Sci, 2002. **357**(1418): p. 207-17.
110. Robertson, I.B., et al., *The N-Terminal Region of Fibrillin-1 Mediates a Bipartite Interaction with LTBP1.* Structure, 2017. **25**(8): p. 1208-1221 e5.
111. Mecham, R.P. and M.A. Gibson, *The microfibril-associated glycoproteins (MAGPs) and the microfibrillar niche.* Matrix Biol, 2015. **47**: p. 13-33.
112. Sabatier, L., et al., *Fibrillin assembly requires fibronectin.* Mol Biol Cell, 2009. **20**(3): p. 846-58.

113. Milewicz, D.M., *Identification of defects in the fibrillin gene and protein in individuals with the Marfan syndrome and related disorders.* Tex Heart Inst J, 1994. **21**(1): p. 22-9.
114. Tang, D.D. and B.D. Gerlach, *The roles and regulation of the actin cytoskeleton, intermediate filaments and microtubules in smooth muscle cell migration.* Respir Res, 2017. **18**(1): p. 54.
115. Small, J.V. and M. Gimona, *The cytoskeleton of the vertebrate smooth muscle cell.* Acta Physiol Scand, 1998. **164**(4): p. 341-8.
116. Blanchoin, L., et al., *Actin dynamics, architecture, and mechanics in cell motility.* Physiol Rev, 2014. **94**(1): p. 235-63.
117. Reisler, E., *Actin molecular structure and function.* Curr Opin Cell Biol, 1993. **5**(1): p. 41-7.
118. Cooper, G.M., *Structure and Organization of Actin Filaments*, in *The Cell: A Molecular Approach* 2000, Sinauer Associates, Inc.: Sunderland (MA).
119. Wear, M.A., D.A. Schafer, and J.A. Cooper, *Actin dynamics: assembly and disassembly of actin networks.* Curr Biol, 2000. **10**(24): p. R891-5.
120. Neuhaus, J.M., et al., *Treadmilling of actin.* J Muscle Res Cell Motil, 1983. **4**(5): p. 507-27.
121. Sjoblom, B., A. Salmazo, and K. Djinovic-Carugo, *Alpha-actinin structure and regulation.* Cell Mol Life Sci, 2008. **65**(17): p. 2688-701.
122. Svitkina, T., *The Actin Cytoskeleton and Actin-Based Motility.* Cold Spring Harb Perspect Biol, 2018. **10**(1).
123. Kamm, K.E. and J.T. Stull, *The function of myosin and myosin light chain kinase phosphorylation in smooth muscle.* Annu Rev Pharmacol Toxicol, 1985. **25**: p. 593-620.
124. Webb, R.C., *Smooth muscle contraction and relaxation.* Adv Physiol Educ, 2003. **27**(1-4): p. 201-6.
125. Gillis, E., L. Van Laer, and B.L. Loeys, *Genetics of thoracic aortic aneurysm: at the crossroad of transforming growth factor-beta signaling and vascular smooth muscle cell contractility.* Circ Res, 2013. **113**(3): p. 327-40.
126. Cannaerts, E., et al., *TGF-beta signalopathies as a paradigm for translational medicine.* Eur J Med Genet, 2015. **58**(12): p. 695-703.
127. MacFarlane, E.G., et al., *TGF-beta Family Signaling in Connective Tissue and Skeletal Diseases.* Cold Spring Harb Perspect Biol, 2017. **9**(11).
128. Renard, M., et al., *Clinical Validity of Genes for Heritable Thoracic Aortic Aneurysm and Dissection.* J Am Coll Cardiol, 2018. **72**(6): p. 605-615.
129. Weiss, A. and L. Attisano, *The TGFbeta superfamily signaling pathway.* Wiley Interdiscip Rev Dev Biol, 2013. **2**(1): p. 47-63.
130. Robertson, I.B. and D.B. Rifkin, *Regulation of the Bioavailability of TGF-beta and TGF-beta-Related Proteins.* Cold Spring Harb Perspect Biol, 2016. **8**(6).
131. Robertson, I.B., et al., *Latent TGF-beta-binding proteins.* Matrix Biol, 2015. **47**: p. 44-53.
132. Dubois, C.M., et al., *Processing of transforming growth factor beta 1 precursor by human furin convertase.* J Biol Chem, 1995. **270**(18): p. 10618-24.
133. Saharinen, J., J. Taipale, and J. Keski-Oja, *Association of the small latent transforming growth factor-beta with an eight cysteine repeat of its binding protein LTBP-1.* EMBO J, 1996. **15**(2): p. 245-53.

134. Neptune, E.R., et al., *Dysregulation of TGF-beta activation contributes to pathogenesis in Marfan syndrome.* Nat Genet, 2003. **33**(3): p. 407-11.
135. Kaartinen, V. and D. Warburton, *Fibrillin controls TGF-beta activation.* Nat Genet, 2003. **33**(3): p. 331-2.
136. Sato, Y. and D.B. Rifkin, *Inhibition of endothelial cell movement by pericytes and smooth muscle cells: activation of a latent transforming growth factor-beta 1-like molecule by plasmin during co-culture.* J Cell Biol, 1989. **109**(1): p. 309-15.
137. Yu, Q. and I. Stamenkovic, *Cell surface-localized matrix metalloproteinase-9 proteolytically activates TGF-beta and promotes tumor invasion and angiogenesis.* Genes Dev, 2000. **14**(2): p. 163-76.
138. Annes, J.P., J.S. Munger, and D.B. Rifkin, *Making sense of latent TGFbeta activation.* J Cell Sci, 2003. **116**(Pt 2): p. 217-24.
139. Zhang, Y.E., *Non-Smad pathways in TGF-beta signaling.* Cell Res, 2009. **19**(1): p. 128-39.
140. Jones, J.A., F.G. Spinale, and J.S. Ikonomidis, *Transforming growth factor-beta signaling in thoracic aortic aneurysm development: a paradox in pathogenesis.* J Vasc Res, 2009. **46**(2): p. 119-37.
141. Hayashi, H., et al., *The MAD-related protein Smad7 associates with the TGFbeta receptor and functions as an antagonist of TGFbeta signaling.* Cell, 1997. **89**(7): p. 1165-73.
142. Anidjar, S., et al., *Experimental study of determinants of aneurysmal expansion of the abdominal aorta.* Ann Vasc Surg, 1994. **8**(2): p. 127-36.
143. Halpern, V.J., et al., *The elastase infusion model of experimental aortic aneurysms: synchrony of induction of endogenous proteinases with matrix destruction and inflammatory cell response.* J Vasc Surg, 1994. **20**(1): p. 51-60.
144. Tang, P.C., et al., *Transmural inflammation by interferon-gamma-producing T cells correlates with outward vascular remodeling and intimal expansion of ascending thoracic aortic aneurysms.* FASEB J, 2005. **19**(11): p. 1528-30.
145. Walker, D.I., et al., *Inflammatory aneurysms of the abdominal aorta.* Br J Surg, 1972. **59**(8): p. 609-14.
146. Shimizu, K., R.N. Mitchell, and P. Libby, *Inflammation and cellular immune responses in abdominal aortic aneurysms.* Arterioscler Thromb Vasc Biol, 2006. **26**(5): p. 987-94.
147. Rasmussen, T.E., et al., *Human leukocyte antigen class II immune response genes, female gender, and cigarette smoking as risk and modulating factors in abdominal aortic aneurysms.* J Vasc Surg, 2002. **35**(5): p. 988-93.
148. Gregory, A.K., et al., *Features of autoimmunity in the abdominal aortic aneurysm.* Arch Surg, 1996. **131**(1): p. 85-8.
149. Al-Hassnan, Z.N., et al., *Recessively inherited severe aortic aneurysm caused by mutated EFEMP2.* Am J Cardiol, 2012. **109**(11): p. 1677-80.
150. Kappanayil, M., et al., *Characterization of a distinct lethal arteriopathy syndrome in twenty-two infants associated with an identical, novel mutation in FBLN4 gene, confirms fibulin-4 as a critical determinant of human vascular elastogenesis.* Orphanet J Rare Dis, 2012. **7**: p. 61.
151. Callewaert, B., et al., *New insights into the pathogenesis of autosomal-dominant cutis laxa with report of five ELN mutations.* Hum Mutat, 2011. **32**(4): p. 445-55.

152. Grewal, N. and A.C. Gittenberger-de Groot, *Pathogenesis of aortic wall complications in Marfan syndrome.* Cardiovasc Pathol, 2018. **33**: p. 62-69.

153. Buchan, J.G., et al., *Rare variants in FBN1 and FBN2 are associated with severe adolescent idiopathic scoliosis.* Hum Mol Genet, 2014. **23**(19): p. 5271-82.

154. Kirschner, R., et al., *Classical and neonatal Marfan syndrome mutations in fibrillin-1 cause differential protease susceptibilities and protein function.* J Biol Chem, 2011. **286**(37): p. 32810-23.

155. Lu, H., et al., *Vascular disease-causing mutation R258C in ACTA2 disrupts actin dynamics and interaction with myosin.* Proc Natl Acad Sci U S A, 2015. **112**(31): p. E4168-77.

156. Lu, H., et al., *Severe Molecular Defects Exhibited by the R179H Mutation in Human Vascular Smooth Muscle alpha-Actin.* J Biol Chem, 2016. **291**(41): p. 21729-21739.

157. Renard, M., et al., *Novel MYH11 and ACTA2 mutations reveal a role for enhanced TGFbeta signaling in FTAAD.* Int J Cardiol, 2013. **165**(2): p. 314-21.

158. Malloy, L.E., et al., *Thoracic aortic aneurysm (TAAD)-causing mutation in actin affects formin regulation of polymerization.* J Biol Chem, 2012. **287**(34): p. 28398-408.

159. Kuang, S.Q., et al., *Rare, nonsynonymous variant in the smooth muscle-specific isoform of myosin heavy chain, MYH11, R247C, alters force generation in the aorta and phenotype of smooth muscle cells.* Circ Res, 2012. **110**(11): p. 1411-22.

160. Boileau, C., et al., *TGFB2 mutations cause familial thoracic aortic aneurysms and dissections associated with mild systemic features of Marfan syndrome.* Nat Genet, 2012. **44**(8): p. 916-21.

161. Inamoto, S., et al., *TGFBR2 mutations alter smooth muscle cell phenotype and predispose to thoracic aortic aneurysms and dissections.* Cardiovasc Res, 2010. **88**(3): p. 520-9.

162. Regalado, E.S., et al., *Exome sequencing identifies SMAD3 mutations as a cause of familial thoracic aortic aneurysm and dissection with intracranial and other arterial aneurysms.* Circ Res, 2011. **109**(6): p. 680-6.

163. Cook, J.R., et al., *Dimorphic effects of transforming growth factor-beta signaling during aortic aneurysm progression in mice suggest a combinatorial therapy for Marfan syndrome.* Arterioscler Thromb Vasc Biol, 2015. **35**(4): p. 911-7.

164. Li, W., et al., *Tgfbr2 disruption in postnatal smooth muscle impairs aortic wall homeostasis.* J Clin Invest, 2014. **124**(2): p. 755-67.

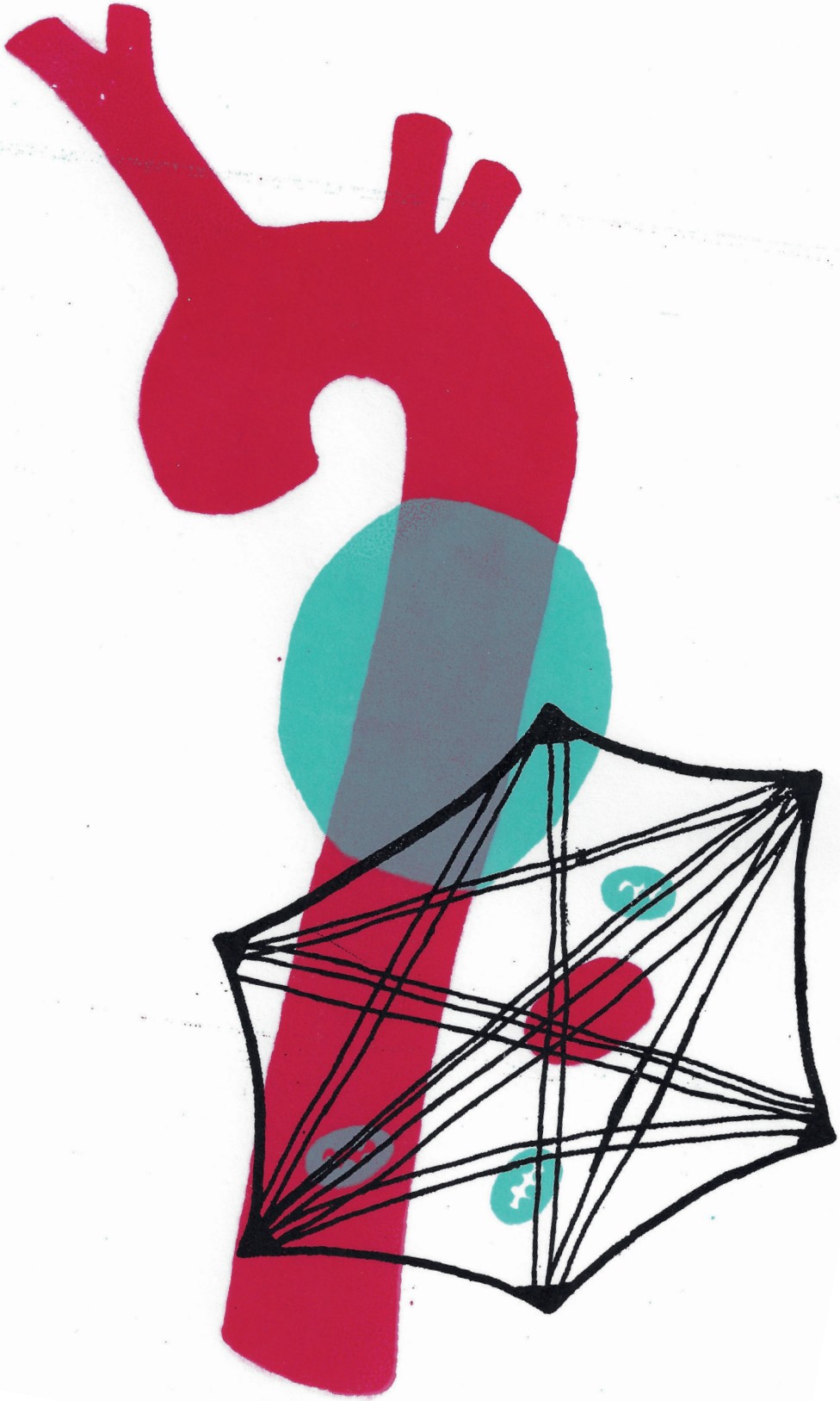

CHAPTER 2

MOLECULAR PHENOTYPING AND QUANTITATIVE FUNCTIONAL ASSESSMENT OF PATHOGENIC VARIANTS IN ANEURYSM GENES *ACTA2*, *MYH11*, *SMAD3* AND *FBN1*

Joyce Burger[1,2*], Natalija Bogunovic[3,4*], Hui Liu[5], Arne IJpma[2,6], Alessandra Maugeri[7], Dimitra Micha[7], Timo L.M. ten Hagen[5], Danielle Majoor-Krakauer[2], Ingrid van der Pluijm[1,5], Jeroen Essers[1,8,9,#], Kak K. Yeung[3,4 #]

[1]Department of Molecular Genetics, Oncode Institute, Erasmus University Medical Center, Rotterdam, The Netherlands, [2]Department of Clinical Genetics, Erasmus University Medical Center, Rotterdam, The Netherlands, [3]Department of Surgery, Institute for Cardiovascular Research, Amsterdam University Medical Centers, location VU University Medical Center, Amsterdam, The Netherlands, [4]Department of Physiology, Institute for Cardiovascular Research, Amsterdam University Medical Centers, location VU University Medical Center, Amsterdam, The Netherlands, [5]Department of Pathology, Erasmus University Medical Center, Rotterdam, The Netherlands, [6]Department of Bioinformatics, Erasmus University Medical Center, Rotterdam, The Netherlands, [7]Department of Clinical Genetics, Institute for Cardiovascular Research, Amsterdam University Medical Centers, location VU University Medical Center, Amsterdam, The Netherlands, [8]Department of Vascular Surgery, Erasmus University Medical Center, Rotterdam, The Netherlands, [9]Department of Radiation Oncology, Erasmus University Medical Center, Rotterdam, The Netherlands.

**These authors contributed equally.*

Manuscript in preparation.

ABSTRACT

Aortic aneurysm (AA) is a pathological dilatation of the aortic wall. The natural course of the disease is to grow and rupture; ruptured AA are associated with a mortality of 80% due to life threatening internal bleeding. Certain patients develop an aneurysm due to genetic mutations that can be associated with malfunctioning of vascular smooth muscle cells (VSMC). A number of genes associated with AA development has been identified, primarily encoding proteins that are involved in TGFβ signaling, contractile machinery and proper organization of the extracellular matrix (ECM). However, only a small portion of variants in these genes lead to a pathogenic effect which results in AA formation.

Our goal was to identify functional assays to investigate the effects of (pathogenic) variants in aneurysm genes associated with thoracic and abdominal AA. Since VSMC can only be obtained during invasive surgery, we used a TGFβ induced transdifferentiation protocol previously developed by our group. We performed growth factor-induced transdifferentiation of skin fibroblasts of controls and patients with a mutation in genes encoding for components of cytoskeleton contractility (*ACTA2*, *MYH11*), TGFβ signaling (*SMAD3*) and a dominant negative (DN) and missense variants (HI) in the extracellular matrix (*FBN1*). We analyzed the transdifferentiation potential, structural integrity of the cytoskeleton, TGFβ signaling profile as well as migration velocity and maximum contraction.

TGFβ-induced transdifferentiation was strongly reduced in the *SMAD3* and *FBN1* DN cells. Both *ACTA2* and *FBN1* DN patient cells showed a decrease in Smad2 phosphorylation. Migration velocity was impaired for *ACTA2* and *MYH11* patient cells. Furthermore, *ACTA2* cells showed reduced contractility.

In conclusion, we find that transdifferentiation potential measured as the amount of SMA production is a distinctive readout as cells with a pathogenic *SMAD3* of *FBN1* DN variant can be identified by their inability to express SMA after TGFβ stimulation. Assays based on functionality, e.g. migration or contractility, could distinguish cells with pathogenic variants in *ACTA2* and *MYH11* from controls. Therefore, we conclude that functional assays are a valuable tool for classifying VUS in aneurysm related genes

INTRODUCTION

Aortic aneurysms are pathological dilatations of the aorta that are life-threatening in case of rupture. Aortic aneurysms can occur in the thoracic as well as abdominal aorta and both show a clear genetic predisposition [1, 2]. Aortic aneurysms may arise from a variety of pathogenic gene variants encoding structural components of ECM, cytoskeletal/smooth muscle contraction proteins, and proteins associated with the TGFβ pathway. Pathogenic variants in the cytoskeleton/contractile genes may lead to altered contractility of vascular smooth muscle cells (VSMCs), caused by structural defects or imbalance of regulatory proteins. Known affected proteins in this group are α-smooth muscle actin (ACTA2), myosin heavy chain 11 (MYH11), myosin light chain kinase (MYLK) and cGMP-dependent protein kinase 1 alpha isozyme (PRKG1) [3-6]. The TGFβ signaling system consists of extrinsic ligands and cell-intrinsic effector proteins, including Smads and Smad-interacting proteins, that determine the outcome of TGFβ signaling. Pathogenic variations in these proteins will lead to hampered signaling of this pathway. Mutations in TGFβ pathway genes known to cause aneurysms are TGFβ receptor 1 (TGFBR1), TGFBR2, TGFB2, TGFB3, SMAD2 and SMAD3 [7-16]. Pathogenic variants in genes encoding for components of the extracellular matrix (ECM) lead to improper assembly of the ECM. This results in aneurysm formation due to loss of cell attachment, loss of vessel elasticity and strength, and altered ability to retain latent TGFβ. Proteins in this group include fibrillin-1 (FBN1), collagen type 3 α1 (COL3A1), elastin (ELN), fibulin-4 (EFEMP2) and lysyl oxidase (LOX) [17-28].

VSMCs are embedded between elastic laminae in the medial layer of the aorta. Both the VSMCs and elastic laminae are important components in maintaining the elasticity and contractility of the aorta. During aneurysm formation of the aortic medial layer is often disintegrated which leads to reduced elasticity and contractility [29]. To study cell biological and molecular consequences of aneurysm formation, VSMCs can be isolated from aortic tissue retrieved from open surgery. Alternatively, dermal fibroblasts grown on a scaffold containing collagen and elastin or coverslips, can be transdifferentiated into VSMC-like cells within 2-weeks using 5 ng TGFβ1/ml. The induced VSMC-like cells are comparable to primary human aortic SMC with regard to mRNA expression of SMC markers *ACTA2*, *SM22* and *CNN1* [30].

The potential pathogenicity of a number of variants in aneurysm-causing genes cannot be classified based on existing classification systems [31-34] and remain variants of unknown clinical significance (VUS). To assess VUS, a set of functional assays is needed to identify the (pathogenic) effect of suspected causative gene variants for aortic aneurysms. The aim of this study is to develop these novel functional assays with robust read outs for the investigation of the effects of pathogenic variants in four aneurysm genes (*ACTA2*, *MYH11*, *SMAD3*, *FBN1* haploinsufficient and dominant negative) based on TGFβ induced transdifferentiation of skin fibroblasts of aneurysm patients. These functional assays could help to reclassify VUS into either

nonpathogenic or pathogenic variants. This could be a potential diagnostic tool to predict the effect of these variants on aneurysm formation.

MATERIALS AND METHODS

Patient cells and characteristics

Primary dermal fibroblasts of aneurysm patients from the biobanks of the departments of Clinical Genetics (Amsterdam University Medical Center - location VU and Erasmus University Medical Center) were used for all experiments. Fibroblasts were cultured in Dulbecco's Modified Eagle's Medium (DMEM, Lonza BioWhittaker) supplemented with 10% fetal calf serum (FCS) and 1% penicillin/streptomycin (PS) at 37°C with 5% CO_2. Human fibroblasts of healthy controls and aneurysm patients with heterozygous mutations in *ACTA2* (cytoskeleton), *MYH11* (cytoskeleton), *SMAD3* (TGFβ signaling) and *FBN1* (extracellular matrix) were used for all experiments (see Table 1 for patient mutations). These mutations were evaluated by the Alamut Visual, a decision-support software for genome variant diagnostics, and predicted to be a class 5 pathogenic.

Transdifferentiation

Fibroblasts were seeded at a density of 2,5 million cells/ml, as previously described [30]. Fibroblasts were seeded in DMEM with 10% FCS and 1% penicillin/streptomycin at a density of 2,5 million cells/ml on the corners of a 1cm^2 piece of matriderm (MedSkin Solutions). Two days after seeding, the medium was changed to DMEM supplemented with 2% heat-inactivated fetal calf serum, 1% PS and 5ng/ml human recombinant TGFβ1 (4342-5, Biovision). Heat-inactivation was performed by placing the FCS in a 56°C water bath for 30 minutes and mixing regularly. Medium supplemented with TGFβ1 was changed every 4 days. After 14 days, the cells were enzymatically extracted from the matriderm with the use of a collagenase solution in complete medium (2000IU/ml, Worthington) at 37°C on a shaker for 3 hours. Centrifugation was performed to remove collagenase and cells were transferred to new flasks and cultured for further experiments. Passage number of 'VSMC-like' cells after transdifferentiation was kept below 5 to prevent loss of transdifferentiation markers.

RNA isolation and real-time PCR

Fibroblasts were seeded in triplicate per condition in 12-well plates at a density of 100.000 cells/well. After two days day 0 samples were taken and medium was changed to DMEM supplemented with 2% heat-inactivated fetal calf serum, 1% PS and 5ng/ml human recombinant TGFβ1 (4342-5, Biovision) for the transdifferentiation samples. TGFβ1 supplemented medium was changed every 4 days and after 14 days RNA was isolated.

RNA was isolated with the RNeasy mini kit (Qiagen). cDNA was made with iScript cDNA synthesis kit (Biorad) according to manufacturing protocol. q-PCR was performed with 200 nM forward and reverse primers and iQ™ SYBR® Green Supermix (Biorad) on the CFX96 system (Biorad); denaturation at 95°C for 3min, 40 cycles denaturation at 95°C for 15 s, annealing/extension at 55°C for 30 s. *TBP* was used as reference gene. Relative gene expression levels were determined with the comparative Ct (also referred to as ΔΔCt) method according to the MIQE guidelines. See Table 2 for primers used to detect gene of interest expression.

Table 1. Gene, cell line, pathogenic variant and additional information on the affected protein.

Gene	Cell line	Pathogenic variant	Expected effect on protein	Cellular process
ACTA2 (NM_001613.3)	ACTA2 #1	c.445C>T, p.R149C	Missense mutation, presumably affecting the fiber formation due to the disappearance of a positive amino acid load	Cytoskeleton contractility
MYH11 (NM_002474.2)	MYH11 #1	c.3879+2dup, p. ?	Frameshift, premature stop codon. Effects on the protein are currently unknown but could include reduced protein levels	Cytoskeleton contractility
SMAD3 (NM_005902.3)	SMAD3 #1	c.859C>T, p.R287W	Missense mutation, potential loss of H-bridges at interacting site that leads to reduced SMAD3/SMAD4 complex stability	TGFβ signaling
FBN1 (NM_000138.4)	FBN1 #1	c.2369insC, p. ?	Frameshift, premature stop codon resulting in haploinsufficiency	Extracellular matrix organization
	FBN1 #2	c.2851insG, p. ?	Frameshift, premature stop codon resulting in haploinsufficiency	Extracellular matrix organization
	FBN1 #3	c.2132G>A, p.C711Y	Missense mutation in the TGFβ binding protein-like domain that could affect binding to fibrillin-1 and results in a dominant negative effect on the protein	Extracellular matrix organization

Table 2. Primer sequences for qPCR.

Gene name	Protein name	RefSeq	Fw and rev primer seq
TBP	TATA-box binding protein	NM_003194	AGTTCTGGGATTGTACCGCA
			TCCTCATGATTACCGCAGCA
ACTA2	SMA	NM_001141945	ACTGGGACGACATGGAAAAG
			CATACATGGCTGGGACATTG
CNN1	Calponin	NM_001308341	GCCCAGAAGTATGACCACCA
			TGATGAAGTTGCCGATGTTC
TAGLN/SM22	SM22	NM_001001522	AAGAATGATGGGCACTACCG
			AGCCCTCTCCGCTCTAACTG

Immunofluorescent staining and image quantification

Dermal fibroblasts were seeded on 18mm coverslips in 12-well plates with a density of 100,000 cells/well in DMEM with 10% FCS and 1%PS. Two days after seeding the medium was changed to DMEM supplemented with 2% heat-inactivated fetal calf serum, 1% PS and 5ng/ml human recombinant TGFβ1 (4342-5, Biovision). TGFβ supplemented medium was changed every 4 days and after 14 days cells were fixed with 2% paraformaldehyde in PBS for 15 minutes. After fixation cells were washed with PBS supplemented with 0,1% Triton X-100 and blocked with PBS+ (0,5% BSA and 0,15% glycine in PBS) for 30 minutes. Primary antibodies were incubated overnight at 4°C in PBS+; mouse monoclonal anti-smooth muscle actin (SMA) (1:1.000, ab7817, Abcam) and rabbit polyclonal anti-SM22 (1:400 ab14106, Abcam). Cells were washed with PBS supplemented with Triton-X100 and incubated shortly with PBS+ prior to incubation with the secondary antibody in PBS+ (1:1.000, anti-mouse Alexa Fluor 488 and anti-rabbit Alexa Fluor 594, Molecular Probes) for 1 hour at room temperature. Simultaneously, actin filaments were stained with SiR-Actin (1:1.000, Cytoskeleton). After incubation coverslips were mounted on glass slides with Vectashield supplemented with DAPI (H-1200, Vector laboratories) and sealed with nail polish. Images were recorded on a wide field epifluorescent microscope (Axio Imager D2, Zeiss).

Quantification of the immunofluorescent signal was performed by calculating the corrected total cell fluorescence (CTCF) of SMA and actin. The CTCF of actin and SMA was determined by setting a color threshold to select the fibers in the image with Fiji image analyzing software [35] and determining the integrated density of this area (intensity of the fluorescence). This measurement was corrected for the background fluorescence and the total area of the fibers and results in the CTCF. The percentage of fluorescence is then calculated by dividing the SMA CTCF and actin CTCF to determine what percentage of the actin cytoskeleton is positive for SMA compared to the total actin cytoskeleton.

Cytoskeletal fiber organization was assessed by measuring anisotropy on microscopic images using FibrilTool plug-in in Fiji [36]. The anisotropy coefficient ranges from zero to one; parallel

lines result in an anisotropy coefficient of one, whereas nonparallel structures have an anisotropy coefficient close to zero. The alignment of F-actin and SMA fibers was assessed in confocal images of transdifferentiated cells of controls and patients with a mutation. According to the published protocol, X-Y fields of view were marked as regions of interest (ROI), and anisotropy was quantified within those regions.

Western blotting

VSMC-like cells were seeded at 100.000 cells/6-well and allowed to attach for 48 hours. Cells were scraped in PBS supplemented with protease inhibitor cocktail (1:100, 11836145001, Roche applied science) and phosphatase inhibitor cocktail (1:100, P0044, Sigma) and lysed in equal volumes of 2x Laemmli buffer (4% SDS, 20% glycerol, 120mM Tris pH 6,8) supplemented with protease inhibitor cocktail and phosphatase inhibitor. Lysates were cleared of large DNA by passing through a 25G needle and then heated to 65°C for 10 minutes. Protein concentrations were measured with the Lowry protein assay [37]. Equal amounts of protein were size separated by SDS-PAGE and separated proteins were then transferred to a PVDF membrane (1hour, 100V, Immobilon). Membranes were blocked for 1 hour at room temperature by either 5% BSA or 3% milk in PBS supplemented with 0,1% Tween-20. Membranes were incubated 45 minutes at room temperature with primary antibody (see Table 3 for primary antibodies). Membranes were washed 5 times with 0,1% Tween-20 in PBS and then incubated with horseradish peroxidase-conjugated secondary antibodies (1:2.000, Jackson ImmunoResearch) for 1 hour at room temperature. Bound secondary antibodies were detected with an Amersham Imager 600 (GE Healthcare Life Sciences) using chemiluminescence. Band intensity was quantified using Fiji image analyzing software [35].

Table 3. Primary antibodies.

Primary antibody	Predicted kDa	Dilution	Manufacturer	Catalog number
Rabbit α-SM22 IgG	23	1:2000	Abcam	Ab14106
Mouse α-SMA IgG2a	40	1:10.000	Abcam	Ab7817
Rabbit α-pSmad2 IgG	55-60	1:400	Merck Millipore	04-953
Rabbit α-Smad2 IgG	60	1:1000	Cell signaling	5339S
Mouse α-β catenin IgG1	92	1:2000	BD Bioscience	610153

Stimulation with TGFβ

Stimulation with TGFβ was performed to determine the sensitivity of control and patient fibroblasts to TGFβ. Fibroblasts were seeded in DMEM supplemented with 10% FCS and 1% PS in 6-well plates to reach confluence and were allowed to attach for 24 hours. The following day, medium was changed to DMEM supplemented with 1% PS and fibroblasts were serum deprived for 24 hours prior to stimulation with human recombinant TGFβ. Protein samples were

collected after 0 minutes, 15 minutes, 30 minutes, 1 hour and 4 hours of stimulation with TGFβ1 (4342-5, Biovision). Lysis of cells and western blotting was performed as previously described. Membranes were incubated overnight at 4°C with primary antibody (see Table 3 for primary antibodies).

Ring barrier migration assay

To measure the migration length and efficiency, a ring barrier migration assay was performed [38]. In this assay a barrier is placed in a cell culture chamber that prevents cells from entering the cell-free area. VSMC-like cells are seeded outside of this barrier and form a monolayer prior to the removal of the barrier. Upon removal of the barrier VSMC-like cells can migrate into the cell-free area and migration can be monitored. Migration parameters such as total and effective migration can be monitored. Migration velocity can be calculated based on total migration and the duration of the experiment. 50,000 VSMC-like cells were seeded in the outer ring of the set-up and were allowed to attach for 24 hours. After removing the ring barrier, cells were washed twice with DMEM supplemented with 1% PS (serum free) and were left in this medium during migration to prevent cell division. Multiple locations at the migration front were selected to monitor movement. Every 10 minutes pictures were taken at the selected locations for 24 hours. Data was analyzed with the axiovision software (version 4.5.0.0) by measuring the total migration length of multiple cells and calculating the migration velocity.

Measuring cell contractility

Cell contractility was measured and calculated according to previously published protocol [39]. VSMC-like cells were seeded in duplicate in the array at a density of 30,000 cells/well in a sterile 96 well plate array well (96w10; Ibidi, Planegg, Germany). Cells were cultured for 48 hours prior to stimulation. The impedance was recorded at a frequency of 4,000 Hz.

VSMC-like cells were stimulated with 10μg ionomycin/ml (Sigma Aldrich, Darmstadt, Germany). Contractile responses were measured in duplicate in each experiment. Contraction (C) of each well equals one minus the ratio between the resistance post- and pre-stimulation post empty well value subtraction, as depicted in equation 1:

$$C = \left(1 - \frac{(PoS[\Omega] - 290\ [\Omega])}{(PrS[\Omega] - 290\ [\Omega])}\right) \bullet 100$$

Equation 1: contractile response

The change in contraction was recorded and expressed as maximum contraction. To characterize the contractile output of the patients, the mean response of the control group was used as a reference. Contraction of the patient VSMC-like cells was compared to a range between 2xSD above and below the mean contractile response of the control group.

Statistics

Number of experiment replicates and independent samples are stated in the figure legends. Data were corrected for outliers with the Grubbs' test for outliers. Statistical analysis was performed with a non-parametric Mann-Whitney test. Significance was tested 2-tailed against the mean of the controls. Significance in gene expression analysis of stimulated controls was tested 2-tailed against unstimulated controls. A p-value <0.05 was considered to indicate a significant difference between groups. In the figures $p<0.05$ is show with *, $p<0.01$ with **, $p<0.001$ with $^{\#}$. Results are expressed as mean ± SD, real-time PCR results are expressed as geometric mean ± geometric SD. All analyses were performed using Graphpad, version 7.03.

RESULTS

Assessment of baseline measurements for control VSMC-like cells

A schematic overview of the transdifferentiation protocol is given in figure 1A. Transdifferentiation was initiated by replacing the culture medium from DMEM supplemented with 10% FCS and 1% PS with DMEM supplemented with 2% heat-inactivated serum, 1% PS and 5ng/ml TGFβ1. According to previous protocols [30], medium was refreshed every 4 days and TGFβ stimulation was terminated after 14 days. Efficiency of transdifferentiation was determined by analyzing the RNA expression level of genes specifically expressed in vascular smooth muscle cells (VSMCs, Table 2). A 4.5-fold increased expression of *ACTA2* was measured within 5 days after addition of TGFβ1 and steady-state mRNA expression levels continued to rise until the end of the experiment (14 days) (Fig. 1B).

We determined the induction of *ACTA2* gene expression in three healthy control fibroblast cell lines to analyze the variability in fold change expression and determine a baseline for comparison with the patients. On average, a consistent 5.5-fold induction of *ACTA2* gene expression was measured in all controls after 14 days of TGFβ stimulation (Fig 1C). *CNN1* gene expression was 2.5-3.5 fold and *SM22* 1.8-2.2 fold increased after 14 days of TGFβ stimulation. The expression of both genes showed considerably more variation compared to *ACTA2* upregulation (Fig. 1D and E).

Subsequently we determined the transdifferentiation potential by analyzing the protein expression level of SMA and SM22 by immunofluorescence and western blot analysis. Supplementary figure 1 shows a comparison of fibroblasts prior to stimulation and VSMC-like cells after stimulation with TGFβ for 14 days. Immunofluorescence staining after 14 days of transdifferentiation showed that all control fibroblast cell lines are positive for SMA which is organized in elongated cytoplasmic SMA fibers stretched throughout the cell. Induction of SMA shows variability between the control cell lines (Fig. 1F). Positive staining for SM22 and actin was observed in all control cell lines. To

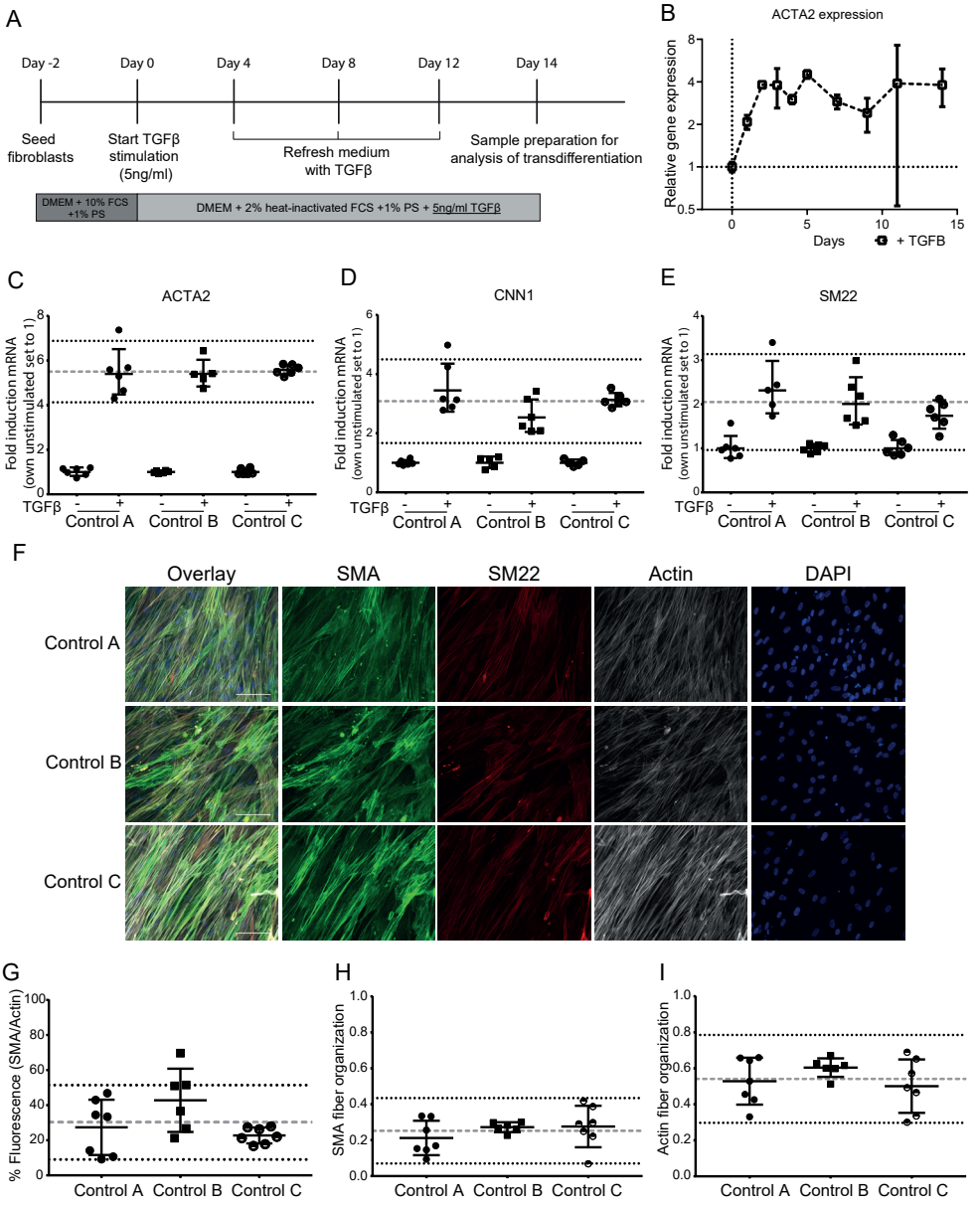

Figure 1. Continous on the next page

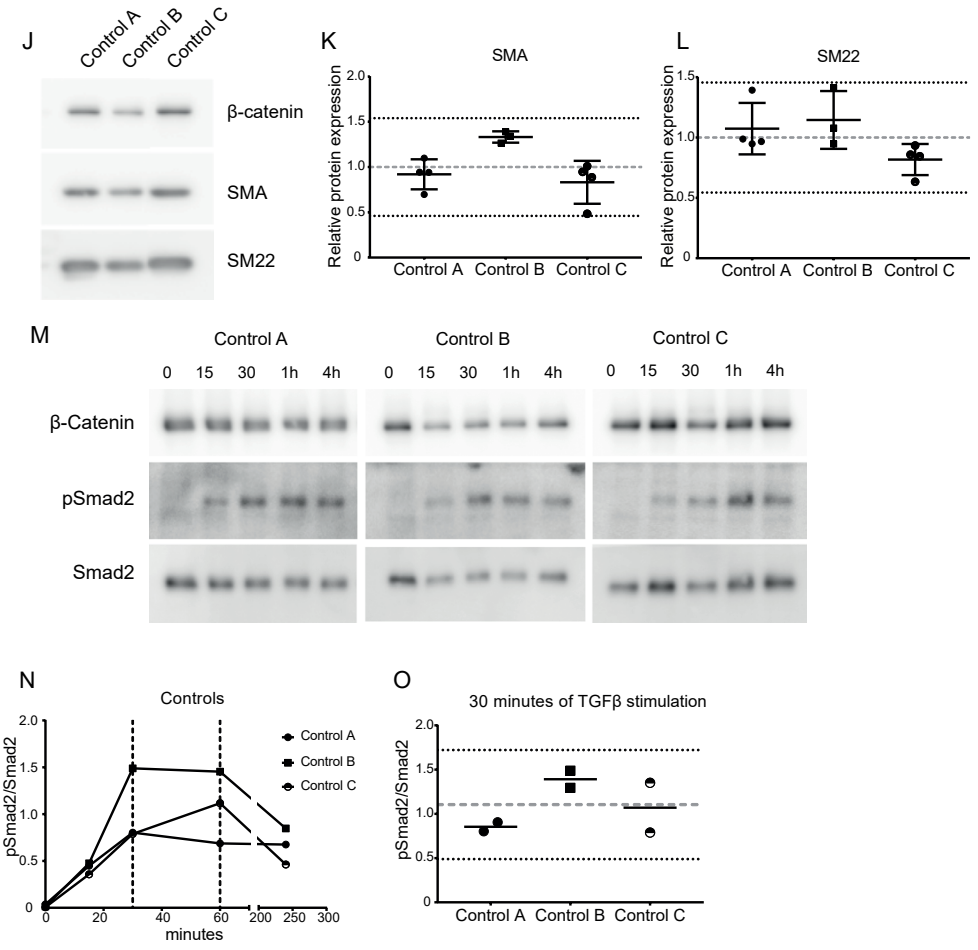

Figure 1. Assessment of baseline measurements for control VSMC-like cells

A) Time line of TGFβ induced transdifferentiation of 3 healthy control cell lines. **B)** Gene expression of *ACTA2* during 14 days of TGFβ stimulation. **C)** *ACTA2* gene expression in controls after 14 days of stimulation with TGFβ. **D)** *CNN1* gene expression in controls after 14 days of stimulation with TGFβ. **E)** *SM22* gene expression in controls after 14 days of stimulation with TGFβ. Unstimulated samples are set to one to compare the fold induction and determine the variability in controls. Results are presented as geometric mean ± geometric SD, figures also include the geometric mean of the controls (dashed grey line) and the 2x geometric SD range of the controls (dotted black line). 3 samples, n=2. **F)** Immunofluorescent staining of SMA (green), SM22 (red), actin (gray) and DAPI (blue) after 14 days of transdifferentiation. Scale bar represents 100 μm. **G)** Quantification of the fluorescent signal of SMA set out against the fluorescent signal of actin. Quantified 7 representative images per cell line. **H)** Quantification of SMA fiber organization in control VSMC-like cells. Alignment of SMA fibers was analyzed for 7 representative images per cell line. **I)** Quantification of actin fiber organization in control VSMC-like cells. Alignment of actin fibers was analyzed for 7 representative images per cell line. **J)** Western blots detecting SMA and SM22 in VSMC-like cells. β-catenin levels serve as a loading control. **K)** Quantification of SMA levels as shown in panel J. **L)** Quantification of SM22 levels as shown in

panel J. 2 independent samples, n=3. **M)** Western blots detecting pSmad2 and Smad2 in control fibroblasts upon stimulation with TGFβ (15 min, 30 min, 1 hour and 4 hours) after serum deprivation. β-catenin levels serve as a loading control. **N)** pSmad2/Smad2 ratio visualized over time in controls. **O)** Quantification of pSmad2/Smad2 ratio at 30 minutes of stimulation, n=2. Results are presented as mean ± SD. Grey dashed line represents mean of the controls and the black dotted line represents 2xSD range of controls.

quantify the amount of SMA fiber fluorescence intensity, we determined the ratio between SMA fibers to the total actin content in the cytoplasm. The transdifferentiated controls showed an overlay of approximately 30% of SMA fiber fluorescence with total F-actin, with the 2xSD range running from 9% to 51% (Fig. 1G). Anisotropy, and thereby organization, of the SMA fibers was quantified in control VSMC-like cells. The anisotropy coefficient ranges from zero to one; parallel lines result in an anisotropy coefficient of one, whereas nonparallel structures have an anisotropy coefficient close to zero. Control VSMC-like cells showed a mean anisotropy coefficient of 0.25, with a range from 0.07 to 0.43 (Fig. 1H). Analysis of actin organization showed a mean a of 0.54 in control VSMC-like cells with a range from 0.29 to 0.79 (Fig. 1I).

Western blot analysis of SMA and SM22 expression showed the presence of both proteins in all controls after transdifferentiation (Fig. 1J). Quantification of SMA and SM22 protein levels revealed variability between the controls. The variability in relative protein expression of SMA in the controls ranged from 0.46 to 1.54. For SM22 the variability in relative protein expression ranged between 0.54 to 1.45 in the controls (Fig. 1K and L).

To determine TGFβ signaling activity the c-terminal phosphorylation of Smad2 was analyzed over time. The response of non-transdifferentiated control fibroblasts to TGFβ in time was determined as the ratio of receptor-activated (phosphorylated) Smad2 compared to total Smad2 protein after TGFβ stimulation (Fig. 1M and N). Overall, phosphorylated Smad2 was already detected 15 minutes after stimulation with TGFβ. The amount of phosphorylated Smad2 reached a maximum level between 30 and 60 minutes, after which it decreased. As the controls almost reached their measured maximum at 30 minutes after TGFβ stimulation we used the expression level at this time point as a reference for TGFβ activation. At the 30-minute time point the mean pSmad2/Smad2 ratio is approximately 1.1 and ranged from 0.49 to 1.72 (Fig. 1O).

Taken together, these data show that all controls can be transdifferentiated to VSMC-like cells upon stimulation with TGFβ, assessed by the RNA and protein expression of SMA, SM22 and CNN1 as well as SMA fiber organization and pSmad2 mediated TGFβ signaling upon TGFβ stimulation.

Transdifferentiation efficiency of fibroblasts of aneurysm patients

The goal of our study is to use these parameters to determine aberrant phenotypes in aneurysmal patient cells. We used the mean and 2xSD range of the control cell lines to determine of patient cells were outside of this range they were considered significantly aberrant from controls.

The differentiation potential of fibroblasts of aneurysmal patients was assessed by quantitative analysis of SMA fibers after transdifferentiation. ACTA2 #1 and MYH11 #1 VSMC-like-cells both showed SMA and SM22 fibers after transdifferentiation. However, MYH11 #1 VSMC-like cells visually showed elongated SMA fibers that stretched throughout the cell whereas ACTA2 #1 VSMC-like cells showed disorganization of SMA fibers (Fig. 2A). Quantification of SMA fiber fluorescence, normalized for total F-actin, showed that both ACTA2 #1 and MYH11 #1 VSMC-like cells have a similar SMA fluorescence as the controls, 30% and 29% respectively (Fig. 2B). Analysis of anisotropy confirmed decreased organization of SMA (0.099) and actin (0.32) in ACTA2 #1 VSMC-like cells compared to controls (Fig. 2C and D, $p<0.001$). MYH11 #1 VSMC-like cells showed a similar anisotropy for SMA (0.23) and actin (0.46) as controls (Fig. 2C and D).

SMAD3 #1 fibroblasts did not appear to form SMA fibers after TGFβ stimulation, while SM22 was present (Fig. 2A). Quantification of SMA fluorescence levels revealed that SMA fluorescence levels (6.5%) were significantly reduced in SMAD3 #1 VSMC-like cells (Fig. 2B, $p<0.001$). SMA fibers that were present in SMAD3 #1 VSMC-like cells after TGFβ stimulation furthermore showed a significantly decreased SMA anisotropy (0.12) compared to controls (Fig. 2C, $p<0.01$). Actin fiber organization (0.51) was similar to controls (Fig. 2D).

Analysis of haploinsufficient FBN1 #1 and FBN1 #2 VSMC-like cells revealed elongated SMA and SM22 fibers after stimulation with TGFβ (Fig. 2A). Both FBN1 #1 and FBN1 #2 VSMC-like cells showed similar SMA fluorescence, 22% and 26% respectively, compared to controls (Fig. 2B). Quantification of anisotropy for SMA (0.22 and 0.30) and actin (0.52 and 0.46) in FBN1 #1 and FBN1 #2 VSMC-like cells revealed no aberrations in the fiber organization compared to controls (Fig. 2C and D). In contrast, after stimulation with TGFβ dominant negative FBN1 #3 VSMC-like cells showed a very low presence of SMA positive cells compared to controls. Quantification of SMA fluorescence showed a significant decrease in intensity (8.9%) compared to controls, suggesting reduced transdifferentiation potential (Fig. 2A and B, $p<0.001$). The SMA fibers that were present in FBN1 #3 VSMC-like cells showed no aberrations in SMA anisotropy (0.20) compared to controls (Fig. 2C). Actin fiber anisotropy of FBN1 #3 VSMC-like cells showed similar organization (0.58) as controls (Fig. 2D).

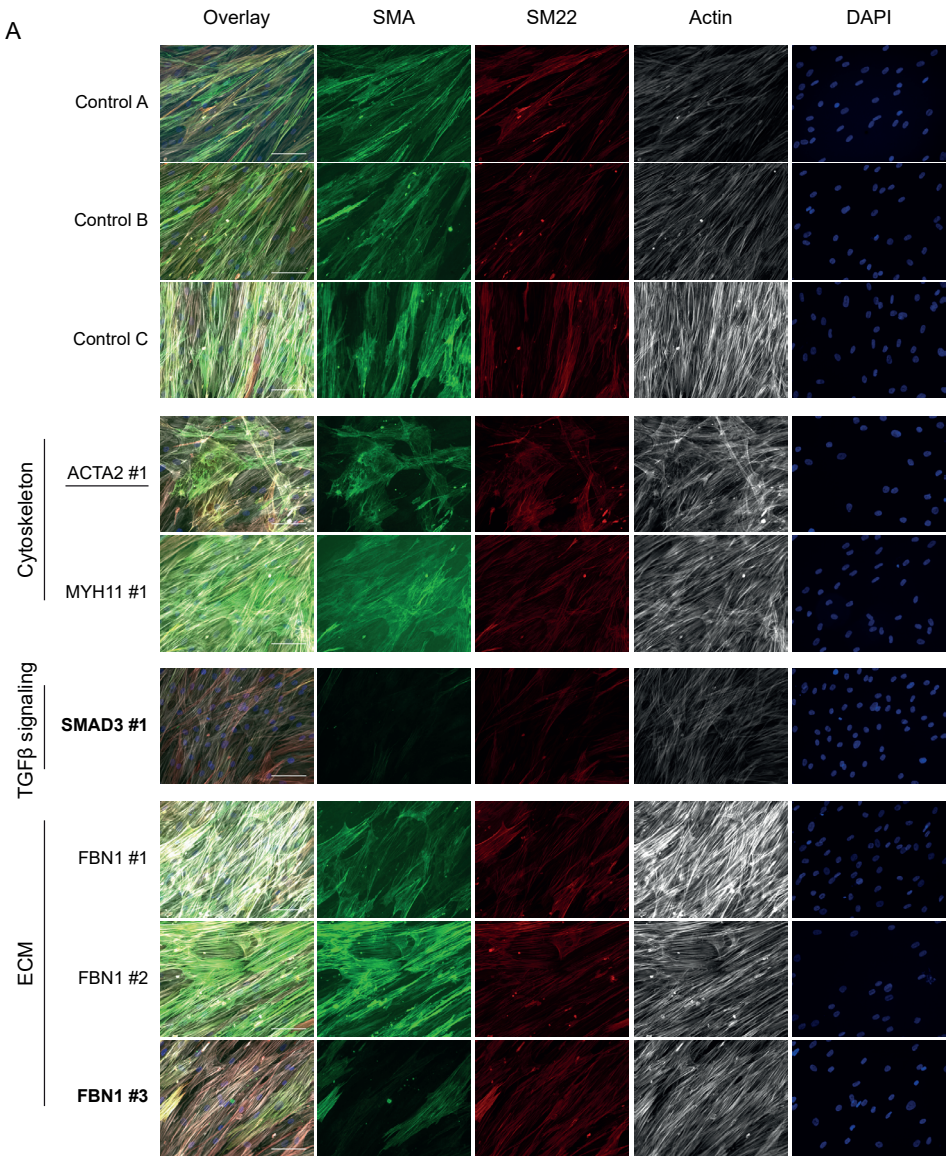

Figure 2. Continuous on the next page

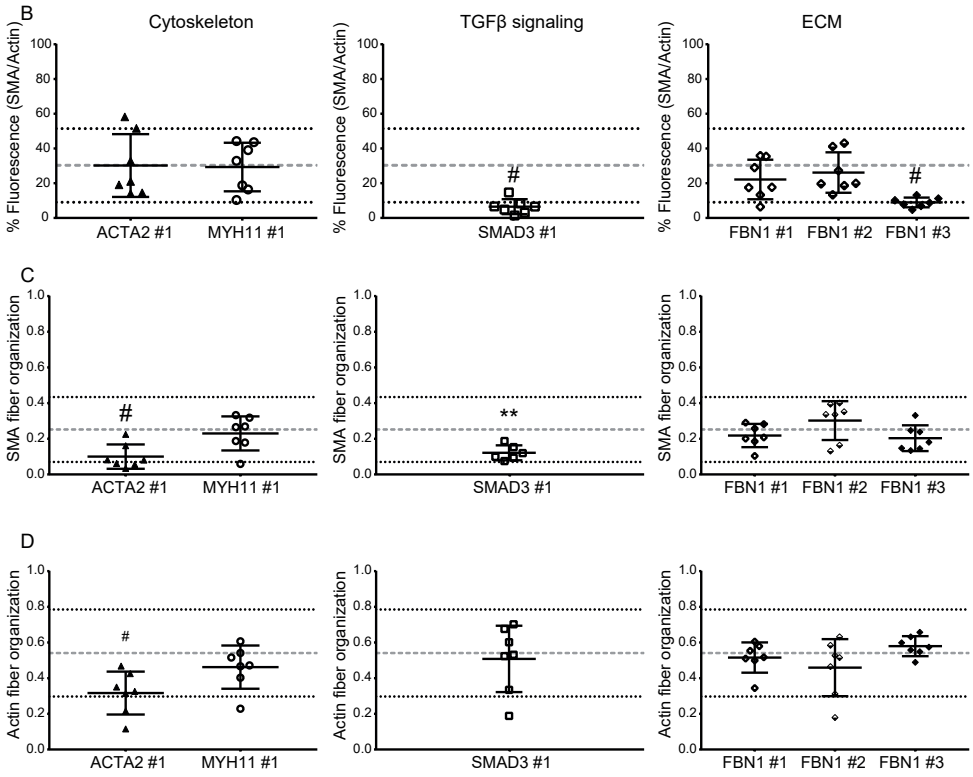

Figure 2. Continuous on the next page

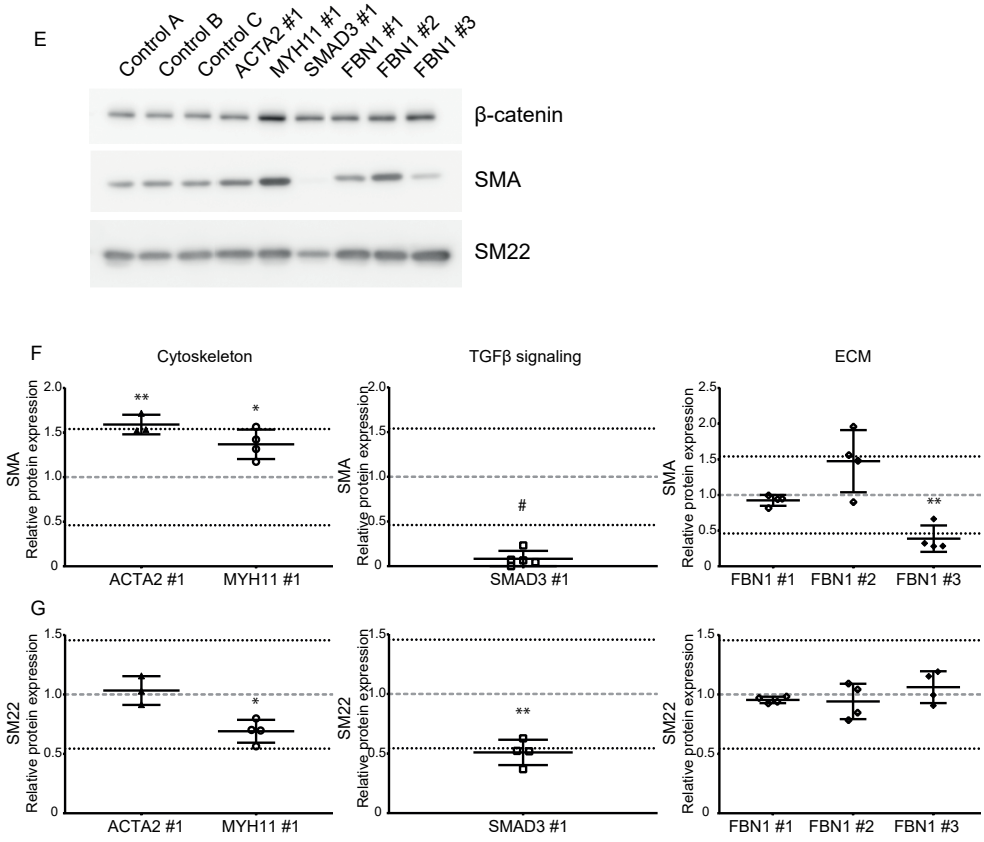

Figure 2. Transdifferentiation of fibroblasts of aneurysm patients

A) Immunofluorescent staining of SMA (green), SM22 (red), F-actin (gray) and DAPI (blue) after 14 days of transdifferentiation. Scale bar represent 100 μm. Underlined cell lines visually showed disorganization of the cytoskeleton. **Bold** cell lines visually showed decreased presence of SMA fibers. **B)** Quantification of the fluorescent signal of SMA set out against the fluorescent signal of actin. Quantified 7 representative images per cell line. **C)** Quantification of SMA fiber organization in pathogenic variant VSMC-like cells. Alignment of SMA fibers was analyzed for 7 representative images per cell line. **D)** Quantification of actin fiber organization in pathogenic variant VSMC-like cells. Alignment of actin fibers was analyzed for 7 representative images per cell line. **E)** Western blots detecting SMA and SM22 in pathogenic variant VSMC-like cells. β-catenin levels serve as a loading control. **F)** Quantification of SMA levels as shown in panels E. **G)** Quantification of SM22 levels as shown in panels E. 2 independent samples, n=3. Grey dashed line represents mean of the controls and black dotted line represents 2xSD range of controls. * p=< 0,05, ** p=<0,01, # p=<0,001.

Besides by immunofluorescence, differentiation potential was further determined by quantitative western blot analysis of SMA and SM22 protein levels after stimulation with TGFβ. SMA and SM22 was present after transdifferentiation in both ACTA2 #1 and MYH11 #1 VSMC-like cells (Fig. 2E). Quantification revealed increased SMA protein levels (1.59) in ACTA2 #1 VSMC-like cells (Fig. 2F, $p<0.01$), whereas SM22 protein levels (1.03) were comparable to controls (Fig. 2G). MYH11 #1 VSMC-like cells showed increased SMA protein levels (1.37) compared to controls, suggesting increased transdifferentiation potential (Fig. 2F, $p<0.05$). SM22 was significantly decreased (0.69) in MYH11 #1 VSMC-like cells compared to controls, but was also remained in the control range (Fig. 2G, $p<0.05$).

After stimulation with TGFβ SMA remained almost absent (0.08) in SMAD3 #1 VSMC-like cells compared to controls and SM22 protein levels (0.51) were decreased (Fig. 2E, F and G, $p<0.001$). FBN1 #1 and FBN1 #2 VSMC-like cells showed similar SMA (0.92 and 1.47 respectively) and SM22 (0.94 and 0.95 respectively) protein levels to controls after transdifferentiation (Fig. 2E, F and G). FBN1 #3 VSMC-like cells showed decreased SMA protein levels (0.39) compared to controls (Fig. 2E and F, $p<0.01$), while having comparable SM22 protein levels (1.06) (Fig. 2E and G).

In conclusion, SMA and SM22 immunostaining and western blot indicate that SMAD3 #1 and FBN1 #3 cells have decreased transdifferentiation potential. While SMAD3 #1 and FBN1 #3 VSMC-like cells did not show SMA fibers, ACTA2 #1 VSMC-like cells showed disorganized SMA fibers. This suggests that SMAD3 #1 and FBN1 #3 VSMC-like cells show reduced transdifferentiation after TGFβ stimulation. A summary of the data in the results section can be found in figure 6.

Kinetics of pSmad2 activation of fibroblasts of aneurysm patients

TGFβ signaling activity was analyzed by examining the ratio of phosphorylated Smad2 to total Smad2 over time as a measure of TGFβ responsiveness. ACTA2 #1 fibroblasts showed reduced induction of Smad2 phosphorylation after TGFβ stimulation. When quantified, ACTA2 #1 fibroblasts showed a pSmad2/Smad2 ratio of 0.44 after 30 minutes of TGFβ stimulation which was below the 2xSD range of the controls (Fig. 3A and B). MYH11 #1 fibroblasts showed comparable phosphorylation of Smad2 to control fibroblasts (Fig. 3A). Quantification also indicated a normal pSmad2/Smad2 ratio of 0.98 for MYH11 #1 fibroblasts compared to controls (Fig. 3B).

Phosphorylation of Smad2 was comparable to controls for SMAD3 #1 fibroblasts, the pSmad2/Smad2 ratio at 30 minutes of 1.35 and was therefore similar to the controls (Fig. 3A and C).

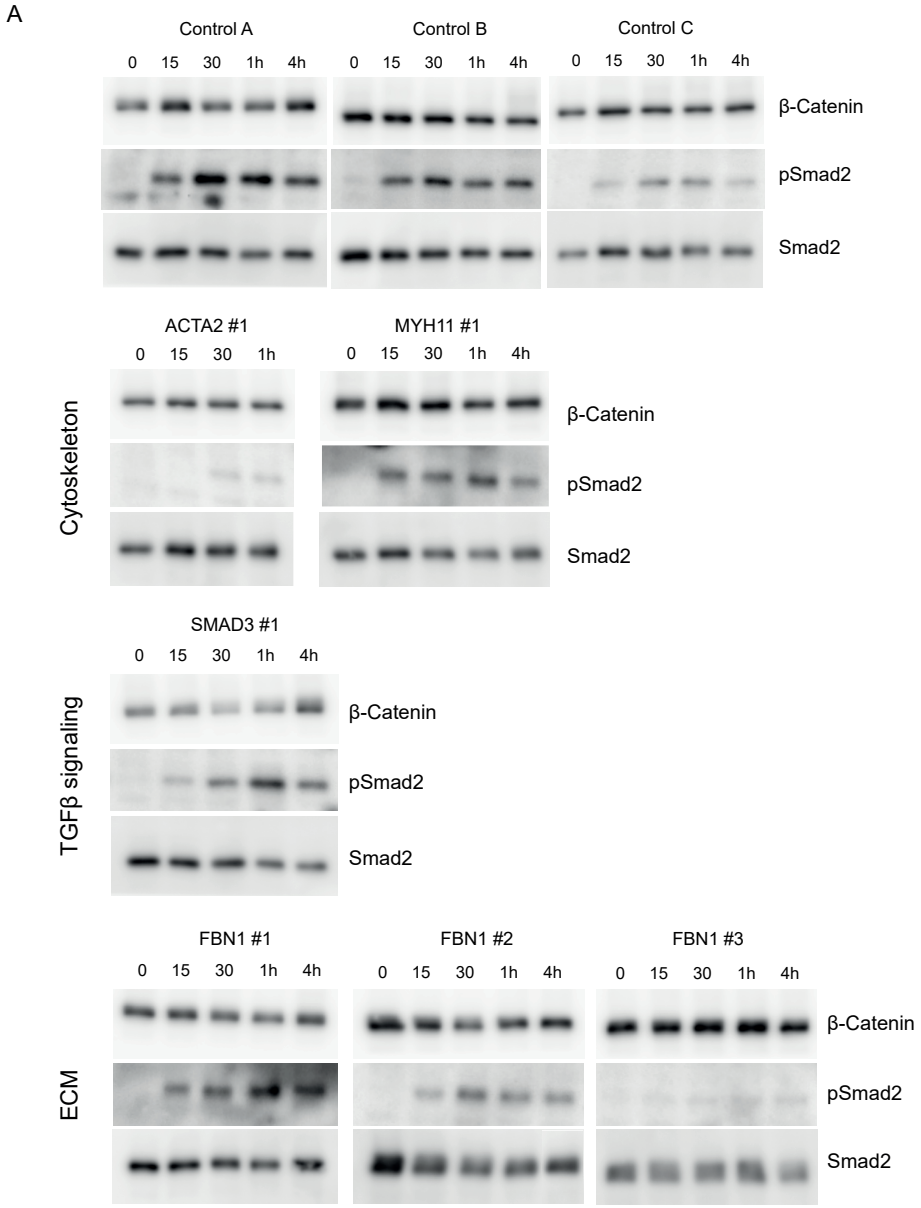

Figure 3. Continous on the next page

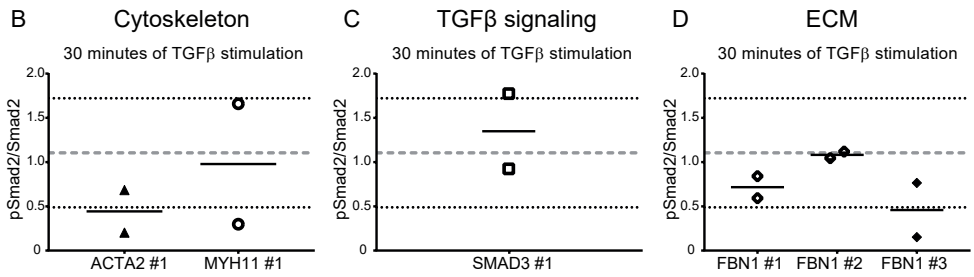

Figure 3. TGFβ responsiveness over time of fibroblasts of aneurysm patients

A) Western blots detecting pSmad2 and Smad2 in TAA mutant fibroblasts upon stimulation with TGFβ (15 min, 30 min, 1 hour and 4 hours) after serum deprivation. β-catenin levels serve as a loading control. **B)** Quantification of pSmad2/Smad2 ratio at 30 minutes of stimulation in ACTA2 and MYH11 variant fibroblasts. **C)** Quantification of pSmad2/Smad2 ratio at 30 of minutes stimulation in SMAD3 variant fibroblasts. **D)** Quantification of pSmad2/Smad2 ratio at 30 minutes of stimulation in FBN1 variant fibroblasts. 2 independent samples, n=2. Grey dashed line represents mean of the controls and black dotted line represents 2xSD range of controls.

Smad2 phosphorylation in FBN1 #1 and FBN1 #2 fibroblasts showed similar pSmad2/Smad2 ratios, 0.72 and 1.08 respectively, compared to controls after 30 minutes of TGFβ stimulation (Fig. 3A and D). FBN1 #3 fibroblasts showed reduced phosphorylation of Smad2 after TGFβ stimulation (Fig. 3A). The pSmad2/Smad2 ratio of 0.46 for FBN1 #3 fibroblasts after 30 minutes of TGFβ stimulation remained below the 2xSD range of the controls (Fig. 3D).

Taken together, these data show that pSmad2 activation is highly dynamic. In non-transdifferentiated cells we detected differences in ACTA2#1 and FBN1 #3 cells compared to controls although there is a large range for the readouts. A summary of the data in this results section can also be found in figure 6.

Migration capacity of pathogenic variant and control VSMC-like cells

The migration capacity of the induced VSMC-like cells was analyzed by performing a ring barrier migration assay.

Migration velocity of ACTA2 #1 VSMC-like cells (5.0 μm/hr) was decreased compared to the migration velocity of controls (9.0 μm/hr) ($p<0.001$, Fig. 4A). Interestingly, MYH11 #1 VSMC-like cells also showed decreased migration velocity (3.5 μm/hr) compared to controls (9.4 μm/hr) ($p<0.001$, Fig. 4B). SMAD3 #1 VSMC-like cells displayed a comparable velocity to the control migration velocity (Fig. 4C). FBN1 #1, #2 and #3 VSMC-like cells all did not differ in migration velocity from controls (Fig. 4D and E).

These data indicate that both cytoskeleton mutations, ACTA2 #1 and MYH11 #1 VSMC-like cells, display reduced migration after transdifferentiation compared to controls. A summary of the data in this results section can also be found in figure 6.

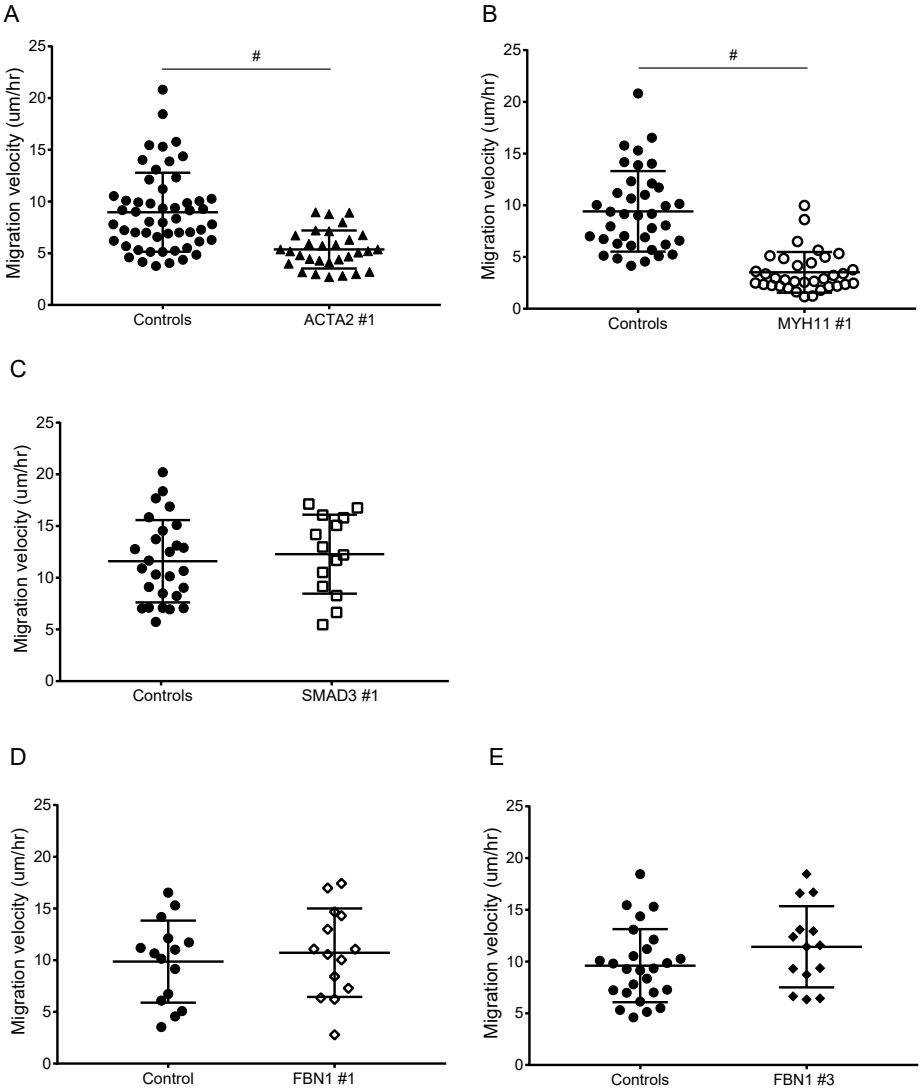

Figure 4. Migration potential of pathogenic variant and control VSMC-like cells

Migration velocity of pathogenic variant VSMC-like cells compared to controls. **A)** ACTA2, B) MYH11, **C)** SMAD3, **D)** FBN1 #1, and **E)** FBN1 #3 VSMC-like cells. n=2, # p=<0,001

Contractility of pathogenic variant and control VSMC-like cells

Contractility was determined to analyze the effects that pathogenic variants. The maximum contraction of control VSMC-like cells was on average 49.7% with a 2xSD ranging from 23.3 to 76.1% (Fig. 5A). The maximum contraction of ACTA2 #1 VSMC-like cells was 16.3% and thereby below the 2xSD range of the controls. MYH11 #1 VSMC-like cells showed a maximum contraction of 42.1% and did not differ from controls (Fig. 5B). SMAD3 #1 VSMC-like cells displayed a maximum contraction of 70.4% and showed a relatively high contractility, however, the maximum contraction did not differ from the controls (Fig. 5C). FBN1 #1 and FBN1 #2 VSMC-like cells presented with a maximum contractility of 47.8 and 47.2% respectively and were thereby comparable to the controls. FBN1 #3 VSMC-like cells also did not differ from the controls with a maximum contraction of 46.5%. (Fig. 5D).

From these data we can conclude that ACTA2 #1 VSMC-like cells show reduced contractility compared to controls. A summary of the data in this results section can also be found in figure 6.

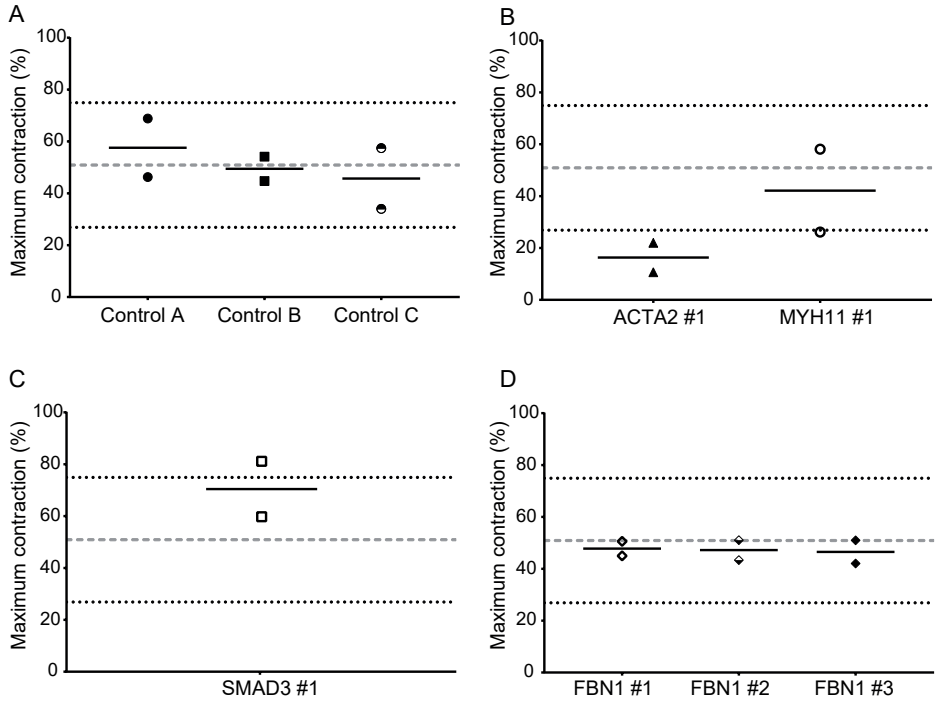

Figure 5. Contractility of patient and control VSMC-like cells

Maximum contraction of pathogenic variant VSMC-like cells compared to controls. **A)** Maximum contraction of controls VSMC-like cells. **B)** Maximum contraction of ACTA2 and MYH11 variant VSMC-like cells. **C)** Maximum contraction of SMAD3 variant VSMC-like cells. **D)** Maximum contraction of FBN1 variant VSMC-like cells. Grey dashed line represents mean of the controls and black dotted line represents 2xSD range of controls. n=2.

	Transdifferentiation potential						TGFβ responsiveness	Cytoskeleton functionality	
	Immunofluorescence				Western blotting		pSmad2/Smad2 ratio (30 min)	Migration	Contractility
	SMA fibers visually	% SMA	SMA organization quantification	Actin organization quantification	SMA	SM22			
Pathogenic variant		Compared to controls	Compared to controls	Compared to controls	Compared to controls	Compared to controls	Compared to controls	Compared to controls	Compared to controls
ACTA2 #1	Disorganized	~	↓*	↓*	↑	~	↓	↓	↓
MYH11 #1	Normal	~	~	~	↑*	↓*	~	↓	~
SMAD3 #1	Almost absent	↓	↓*	~	↓	↓	~	~	~
FBN1 #1	Normal	~	~	~	~	~	~	~	~
FBN1 #2	Normal	~	~	~	~	~	~	-	~
FBN1 #3	Almost absent	↓	~	~	↓	~	↓	~	~

Figure 6. Summary of functional assay results of transdifferentiated fibroblasts of aneurysm patients with a pathogenic variant in aneurysm genes

Overview of results per pathogenic variant and experiment. Significant differences compared to the mean of the controls are noted as decreased (↓) or increased (↑) in the "compared to controls" column. If the mean of the samples of the patient cell line was within the 2xSD control range the arrow is marked with an *. No difference compared to the controls is visualized as ~.

DISCUSSION

Variants in aneurysm-related genes are often associated with aneurysm formation. However, the significance of the effect of these mutations on the protein is not always clear, and thus, the clinical relevance is hard to assess. In this study, we used cells of aneurysm patients with six different pathogenic variants to evaluate the clinical relevance of novel functional assays to determine the pathogenic effects of variants. Such assays are certainly an unmet need in the diagnostic setting; since the wide implementation of next generation sequencing a growing number of VUS are being identified but can currently not be assessed for their potential pathogenicity. We measured a strong decrease in SMA staining and thereby reduced transdifferentiation potential in *SMAD3* and *FBN1* dominant negative (FBN1 #3) patients cells. *ACTA2* and *FBN1* dominant negative patients also showed a decrease in pSmad2 activation. Migration velocity was impaired for *ACTA2* and *MYH11*, while only *ACTA2* showed reduced contractility. Our data suggests that TGFβ-induced transdifferentiation of fibroblasts allowed distinguishing clear effects from pathogenic variants in cytoskeleton, TGFβ pathway and ECM aneurysm genes for *ACTA2*, *MYH11*, *SMAD3*, *FBN1* dominant negative, but not for *FBN1* haploinsufficient variants. A limitation of our study is that only one cell line was used per mutation as proof of concept. In order to draw more significant conclusions on the role of mutations of these genes in AA formation, replication in a larger number of these and other aneurysm genes are needed. Below, we will discuss these results per aneurysm-causing gene analyzed. A summary of the data can also be found in figure 6.

ACTA2

ACTA2 #1 VSMC-like cells produced SMA protein after TGFβ stimulation and showed similar transdifferentiation potential as controls. However, the SMA fibers appeared fragmented and disorganized. Guo et al. previously showed lack of SMA fibers in VSMCs of patient with *ACTA2* variants (p.R118Q and p.T353N) [3]. Our data shows that the p.R149C variant of ACTA2 #1 resembles other known *ACTA2* pathogenic variants with its disorganized SMA fibers after transdifferentiation. Clinical data on *ACTA2* p.R149C, p.R256H and p.T353N aortic sections confirmed that SMA protein is produced, but that VSMCs appear to be disorganized and lack structure [40]. Complications with the assembly of mutant SMA (p.R256H) is further confirmed by analysis of mutant *ACTA2* in yeast [40]. Analysis of SMA fiber assembly by Malloy et al. showed decreased SMA polymerization and elongated assembly times in *ACTA2* p.R256H mutant yeast compared to wild-type yeast. Studies on *ACTA2* mutations (p.R118Q, p.R256H and p.T353N) show overall disorganization of SMA fibers that is caused by dysfunctional assembly of SMA. Our results confirmed the overall disorganization of SMA for an additional *ACTA2* pathogenic variant (p.R149C) in VSMC-like cells.

Additionally, ACTA2 #1 VSMC-like cells showed decreased migration and contractility. During migration the cytoskeleton is polymerized in the direction of movement, while depolymerization occurs at the rear-end of cells. Variants in proteins that constitute the cytoskeleton, such as *ACTA2* and *MYH11*, can be explanatory for the observed defective migration. Literature revealed that *ACTA2* is induced during migration as well as during metastasis, suggesting that *ACTA2* is essential for migration [41, 42]. Decreased contractility of multiple *ACTA2* pathogenic variant VSMCs was previously found by Lu et al. (2015) by performing a one-bead laser trap experiment to analyze force-output. Our data on the reduced contractility of ACTA2 #1 VSMC-like cells is in line with this finding and indicates the importance of *ACTA2* for the contractility of VSMCs.

MYH11

MYH11 #1 VSMC-like cells showed decreased SM22 protein levels on western blot. Overexpression of *MYH11* has been reported to induce degradation and turnover of thick filament associated proteins and cytoskeleton proteins like SM22 but not SMA [43]. Since *MYH11* c.3879+2dup (MYH11 #1) is a relatively unknown variant, it is unclear whether this variant could lead to a gain-of-function of *MYH11* and thereby inducing the degradation of specific cytoskeleton proteins or that this pathogenic variant leads to reduced levels or function of *MYH11*. Our finding that SMA is not degraded is in line with the results of Kwartler et al. and suggests that this *MYH11* pathogenic variant could indeed induce the described unfolded protein response that induces degradation of specific cytoskeleton proteins.

Although the MYH11 #1 VSMC-like cells were able to transdifferentiate, migration velocity was decreased in *MYH11* variant VSMC-like cells, similar to the ACTA2 #1 VSMC-like cells. *MYH11* pathogenic variants have been predicted to decrease SMC contractility as well as compromising migration, which is in line with our results [44, 45].

SMAD3

SMAD3 #1 VSMC-like cells lacked induction of SMA fibers upon TGFβ stimulation, which suggests reduced induction of transdifferentiation. This lack of SMA can be explained by disturbance in the TGFβ signaling pathway caused by the *SMAD3* pathogenic variant. Induction of SMA by TGFβ was shown to occur via *SMAD3* [46, 47], suggesting that induction will not occur when *SMAD3* is mutated. Like SMA, SM22 is induced via activation of the TGFβ pathway, specifically via *SMAD3* [48]. This also explains the reduced SM22 protein levels of *SMAD3* pathogenic variant VSMC-like cells.

The TGFβ signaling pathway is often considered physiologically active when Smad2 is phosphorylated upon TGFβ stimulation, yet, for *SMAD3* variants resulting in absent or defective Smad3 proteins, this is not necessarily true [49]. Although, the initial response to TGFβ stimulation is intact in *SMAD3* knock-out cells, downstream signaling is impaired due to absence of Smad3

protein. This hampers induction of target genes, thereby leading to impaired induction of SMA and SM22 and thus diminished transdifferentiation.

FBN1

VSMC-like cells with a *FBN1* dominant negative pathogenic variant (FBN1 #3) express less SMA protein as wells as SMA fibers after transdifferentiation. This could be caused by defective ECM build-up resulting from the *FBN1* variant, resulting in reduced binding sites for the cytoskeleton via integrins. The rigidity of the ECM is also important for the development of the cytoskeleton as, for example, a soft matrix results in a less well-defined cytoskeleton [50-52]. The effect of a defective matrix on the cytoskeleton has recently also been shown in the *Fibulin-4* VSMC specific knock-out mouse model in which absence of fibulin-4 led to absence of SMA protein and fibers [53].

Transdifferentiation of *FBN1* dominant negative and haploinsufficient patient fibroblasts reveals differential results between two (predicted) types of *FBN1* pathogenic variants. While the dominant negative FBN1 #3 VSMC-like cells show decreased induction of SMA and SM22, results from FBN1 #1 and #2 haploinsufficient fibroblasts appear quite similar to controls. Clinical data have previously also suggested differences between the *FBN1* dominant negative and haploinsufficient variant in their responsiveness to treatment with losartan [54, 55]. Patients with an *FBN1* haploinsufficient pathogenic variant that received treatment with losartan were responsive to the inhibition of aortic root dilation by losartan, whereas *FBN1* dominant negative patients did not respond to treatment [54]. Furthermore, patients with an *FBN1* haploinsufficient variant showed improvement in biventricular end diastolic volume and stroke volume upon losartan treatment. This effect was not found in *FBN1* dominant negative patients that received losartan [55]. This indicates that mutations in one gene can lead to different outcomes and could result in different clinical consequences for patients. The nature of the *FBN1* variants and their effects are in line with this as haploinsufficient variants result in half of the normal protein levels while dominant negative variants interfere with the normal protein and can result in nonfunctional protein levels. Our functional assays proved to be able to identify characteristics potentially distinguishing between *FBN1* haploinsufficient and dominant negative mutations and could potentially simplify the identification of haploinsufficient and dominant negative patients. Especially the presence or absence of SMA and potentially the pSmad2/Smad2 ratio after TGFβ stimulation can distinguish *FBN1* dominant negative VSMC-like cells from *FBN1* haploinsufficient VSMC-like cells.

Conclusion

The assays we have chosen are suitable to determine the effect of the mutation on the functionality of the protein. We detected reduced transdifferentiation potential in SMAD3 #1 and FBN1 #3, defective migration in MYH11 #1 and ACTA2 #1 and defective contractility ACTA2

#1. Our results suggest a potential application for these novel functional assays in assessing the functionality of a larger number of proteins encoded by the same genes. Hopefully, this will result in the ability to analyze the potential pathogenic effect of VUS in aneurysm genes and thereby promote more accurate genetic diagnosis and family screening for aneurysms.

Acknowledgements

We would like to thank Stichting Lijf en Leven (Genexpressie analyse ter detective van de moleculaire mechanismen van aneurysmavorming – GAMMA) and Amsterdam Cardiovascular Sciences Institute (ICaR AiO 2015 PhD grant) for supporting this research.

REFERENCES

1. Ziganshin, B.A., et al., *Routine Genetic Testing for Thoracic Aortic Aneurysm and Dissection in a Clinical Setting.* Ann Thorac Surg, 2015. **100**(5): p. 1604-11.
2. van de Luijtgaarden, K.M., et al., *First genetic analysis of aneurysm genes in familial and sporadic abdominal aortic aneurysm.* Hum Genet, 2015. **134**(8): p. 881-93.
3. Guo, D.C., et al., *Mutations in smooth muscle alpha-actin (ACTA2) lead to thoracic aortic aneurysms and dissections.* Nat Genet, 2007. **39**(12): p. 1488-93.
4. Zhu, L., et al., *Mutations in myosin heavy chain 11 cause a syndrome associating thoracic aortic aneurysm/aortic dissection and patent ductus arteriosus.* Nat Genet, 2006. **38**(3): p. 343-9.
5. Wang, L., et al., *Mutations in myosin light chain kinase cause familial aortic dissections.* Am J Hum Genet, 2010. **87**(5): p. 701-7.
6. Guo, D.C., et al., *Recurrent gain-of-function mutation in PRKG1 causes thoracic aortic aneurysms and acute aortic dissections.* Am J Hum Genet, 2013. **93**(2): p. 398-404.
7. Loeys, B.L., et al., *A syndrome of altered cardiovascular, craniofacial, neurocognitive and skeletal development caused by mutations in TGFBR1 or TGFBR2.* Nat Genet, 2005. **37**(3): p. 275-81.
8. Loeys, B.L., et al., *Aneurysm syndromes caused by mutations in the TGF-beta receptor.* N Engl J Med, 2006. **355**(8): p. 788-98.
9. Mizuguchi, T., et al., *Heterozygous TGFBR2 mutations in Marfan syndrome.* Nat Genet, 2004. **36**(8): p. 855-60.
10. Lindsay, M.E., et al., *Loss-of-function mutations in TGFB2 cause a syndromic presentation of thoracic aortic aneurysm.* Nat Genet, 2012. **44**(8): p. 922-7.
11. Boileau, C., et al., *TGFB2 mutations cause familial thoracic aortic aneurysms and dissections associated with mild systemic features of Marfan syndrome.* Nat Genet, 2012. **44**(8): p. 916-21.
12. Rienhoff, H.Y., Jr., et al., *A mutation in TGFB3 associated with a syndrome of low muscle mass, growth retardation, distal arthrogryposis and clinical features overlapping with Marfan and Loeys-Dietz syndrome.* Am J Med Genet A, 2013. **161A**(8): p. 2040-6.
13. Matyas, G., et al., *De novo mutation of the latency-associated peptide domain of TGFB3 in a patient with overgrowth and Loeys-Dietz syndrome features.* Am J Med Genet A, 2014. **164A**(8): p. 2141-3.
14. Bertoli-Avella, A.M., et al., *Mutations in a TGF-beta ligand, TGFB3, cause syndromic aortic aneurysms and dissections.* J Am Coll Cardiol, 2015. **65**(13): p. 1324-1336.
15. van de Laar, I.M., et al., *Mutations in SMAD3 cause a syndromic form of aortic aneurysms and dissections with early-onset osteoarthritis.* Nat Genet, 2011. **43**(2): p. 121-6.
16. van de Laar, I.M., et al., *Phenotypic spectrum of the SMAD3-related aneurysms-osteoarthritis syndrome.* J Med Genet, 2012. **49**(1): p. 47-57.
17. Dietz, H.C., et al., *The Marfan syndrome locus: confirmation of assignment to chromosome 15 and identification of tightly linked markers at 15q15-q21.3.* Genomics, 1991. **9**(2): p. 355-61.
18. Milewicz, D.M., *Identification of defects in the fibrillin gene and protein in individuals with the Marfan syndrome and related disorders.* Tex Heart Inst J, 1994. **21**(1): p. 22-9.

19. Pepin, M., et al., *Clinical and genetic features of Ehlers-Danlos syndrome type IV, the vascular type.* N Engl J Med, 2000. **342**(10): p. 673-80.
20. Schwarze, U., et al., *Haploinsufficiency for one COL3A1 allele of type III procollagen results in a phenotype similar to the vascular form of Ehlers-Danlos syndrome, Ehlers-Danlos syndrome type IV.* Am J Hum Genet, 2001. **69**(5): p. 989-1001.
21. Plancke, A., et al., *Homozygosity for a null allele of COL3A1 results in recessive Ehlers-Danlos syndrome.* Eur J Hum Genet, 2009. **17**(11): p. 1411-6.
22. Zhang, M.C., et al., *Cutis laxa arising from frameshift mutations in exon 30 of the elastin gene (ELN).* J Biol Chem, 1999. **274**(2): p. 981-6.
23. Tassabehji, M., et al., *An elastin gene mutation producing abnormal tropoelastin and abnormal elastic fibres in a patient with autosomal dominant cutis laxa.* Hum Mol Genet, 1998. **7**(6): p. 1021-8.
24. Szabo, Z., et al., *Aortic aneurysmal disease and cutis laxa caused by defects in the elastin gene.* J Med Genet, 2006. **43**(3): p. 255-8.
25. Hucthagowder, V., et al., *Fibulin-4: a novel gene for an autosomal recessive cutis laxa syndrome.* Am J Hum Genet, 2006. **78**(6): p. 1075-80.
26. Dasouki, M., et al., *Compound heterozygous mutations in fibulin-4 causing neonatal lethal pulmonary artery occlusion, aortic aneurysm, arachnodactyly, and mild cutis laxa.* Am J Med Genet A, 2007. **143A**(22): p. 2635-41.
27. Lee, V.S., et al., *Loss of function mutation in LOX causes thoracic aortic aneurysm and dissection in humans.* Proc Natl Acad Sci U S A, 2016. **113**(31): p. 8759-64.
28. Guo, D.C., et al., *LOX Mutations Predispose to Thoracic Aortic Aneurysms and Dissections.* Circ Res, 2016. **118**(6): p. 928-34.
29. Thompson, R.W., S. Liao, and J.A. Curci, *Vascular smooth muscle cell apoptosis in abdominal aortic aneurysms.* Coron Artery Dis, 1997. **8**(10): p. 623-31.
30. Yeung, K.K., et al., *Transdifferentiation of Human Dermal Fibroblasts to Smooth Muscle-Like Cells to Study the Effect of MYH11 and ACTA2 Mutations in Aortic Aneurysms.* Hum Mutat, 2017. **38**(4): p. 439-450.
31. Plon, S.E., et al., *Sequence variant classification and reporting: recommendations for improving the interpretation of cancer susceptibility genetic test results.* Hum Mutat, 2008. **29**(11): p. 1282-91.
32. Li, M.M., et al., *Standards and Guidelines for the Interpretation and Reporting of Sequence Variants in Cancer: A Joint Consensus Recommendation of the Association for Molecular Pathology, American Society of Clinical Oncology, and College of American Pathologists.* J Mol Diagn, 2017. **19**(1): p. 4-23.
33. Richards, S., et al., *Standards and guidelines for the interpretation of sequence variants: a joint consensus recommendation of the American College of Medical Genetics and Genomics and the Association for Molecular Pathology.* Genet Med, 2015. **17**(5): p. 405-24.
34. den Dunnen, J.T., et al., *HGVS Recommendations for the Description of Sequence Variants: 2016 Update.* Hum Mutat, 2016. **37**(6): p. 564-9.
35. Schindelin, J., et al., *Fiji: an open-source platform for biological-image analysis.* Nat Methods, 2012. **9**(7): p. 676-82.

36. Boudaoud, A., et al., *FibrilTool, an ImageJ plug-in to quantify fibrillar structures in raw microscopy images.* Nat Protoc, 2014. **9**(2): p. 457-63.
37. Lowry, O.H., et al., *Protein measurement with the Folin phenol reagent.* J Biol Chem, 1951. **193**(1): p. 265-75.
38. Das, A.M., A.M. Eggermont, and T.L. ten Hagen, *A ring barrier-based migration assay to assess cell migration in vitro.* Nat Protoc, 2015. **10**(6): p. 904-15.
39. Bogunovic, N., et al., *Impaired smooth muscle cell contractility as a novel concept of abdominal aortic aneurysm pathophysiology.* Sci Rep, 2019. **9**(1): p. 6837.
40. Malloy, L.E., et al., *Thoracic aortic aneurysm (TAAD)-causing mutation in actin affects formin regulation of polymerization.* J Biol Chem, 2012. **287**(34): p. 28398-408.
41. Rockey, D.C., N. Weymouth, and Z. Shi, *Smooth muscle alpha actin (Acta2) and myofibroblast function during hepatic wound healing.* PLoS One, 2013. **8**(10): p. e77166.
42. Lee, H.W., et al., *Alpha-smooth muscle actin (ACTA2) is required for metastatic potential of human lung adenocarcinoma.* Clin Cancer Res, 2013. **19**(21): p. 5879-89.
43. Kwartler, C.S., et al., *Overexpression of smooth muscle myosin heavy chain leads to activation of the unfolded protein response and autophagic turnover of thick filament-associated proteins in vascular smooth muscle cells.* J Biol Chem, 2014. **289**(20): p. 14075-88.
44. Kuang, S.Q., et al., *Rare, nonsynonymous variant in the smooth muscle-specific isoform of myosin heavy chain, MYH11, R247C, alters force generation in the aorta and phenotype of smooth muscle cells.* Circ Res, 2012. **110**(11): p. 1411-22.
45. Pannu, H., et al., *MYH11 mutations result in a distinct vascular pathology driven by insulin-like growth factor 1 and angiotensin II.* Hum Mol Genet, 2007. **16**(20): p. 2453-62.
46. Hu, B., Z. Wu, and S.H. Phan, *Smad3 mediates transforming growth factor-beta-induced alpha-smooth muscle actin expression.* Am J Respir Cell Mol Biol, 2003. **29**(3 Pt 1): p. 397-404.
47. Vardouli, L., et al., *A novel mechanism of TGFbeta-induced actin reorganization mediated by Smad proteins and Rho GTPases.* FEBS J, 2008. **275**(16): p. 4074-87.
48. Qiu, P., X.H. Feng, and L. Li, *Interaction of Smad3 and SRF-associated complex mediates TGF-beta1 signals to regulate SM22 transcription during myofibroblast differentiation.* J Mol Cell Cardiol, 2003. **35**(12): p. 1407-20.
49. van der Pluijm, I., et al., *Defective Connective Tissue Remodeling in Smad3 Mice Leads to Accelerated Aneurysmal Growth Through Disturbed Downstream TGF-beta Signaling.* EBioMedicine, 2016. **12**: p. 280-294.
50. Choquet, D., D.P. Felsenfeld, and M.P. Sheetz, *Extracellular matrix rigidity causes strengthening of integrin-cytoskeleton linkages.* Cell, 1997. **88**(1): p. 39-48.
51. Lo, C.M., et al., *Cell movement is guided by the rigidity of the substrate.* Biophys J, 2000. **79**(1): p. 144-52.
52. Saez, A., et al., *Is the mechanical activity of epithelial cells controlled by deformations or forces?* Biophys J, 2005. **89**(6): p. L52-4.

53. Burger, J., et al., *Fibulin-4 deficiency differentially affects cytoskeleton structure and dynamics as well as TGFbeta signaling.* Cell Signal, 2019. **58**: p. 65-78.
54. Franken, R., et al., *Beneficial Outcome of Losartan Therapy Depends on Type of FBN1 Mutation in Marfan Syndrome.* Circ Cardiovasc Genet, 2015. **8**(2): p. 383-8.
55. den Hartog, A.W., et al., *The effect of losartan therapy on ventricular function in Marfan patients with haploinsufficient or dominant negative FBN1 mutations.* Neth Heart J, 2016. **24**(11): p. 675-681.

SUPPLEMENTAL DATA

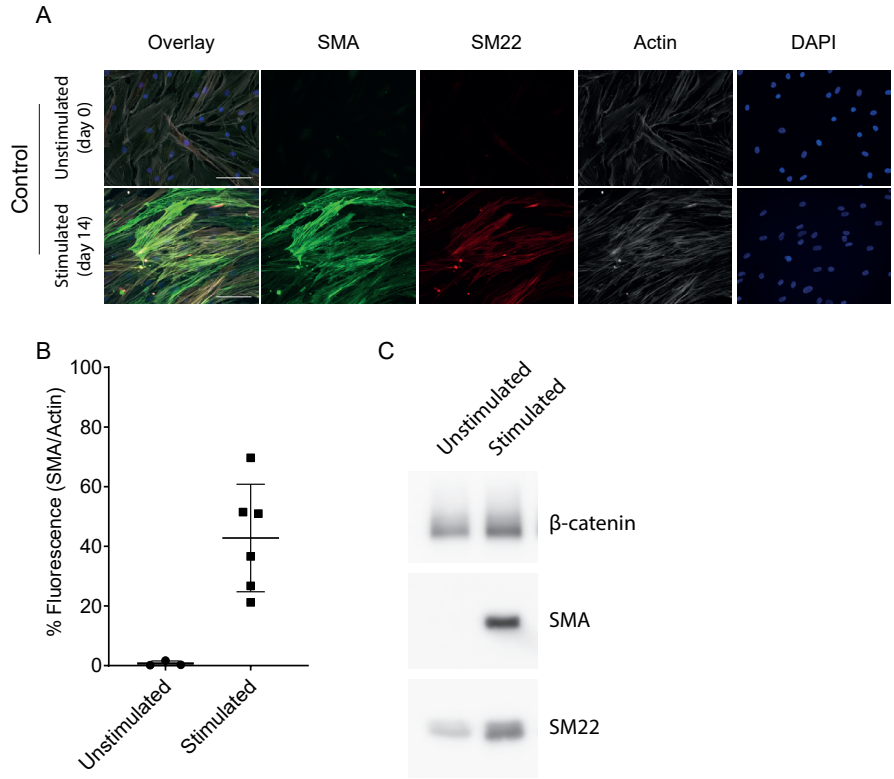

Supplemental figure 1. Comparison control fibroblasts unstimulated and stimulated for 14 days with TGFβ

A) Immunofluorescent staining of SMA (green), SM22 (red), actin (gray) and DAPI (blue) of a healthy control prior to stimulation (unstimulated) and after 14 days of TGFβ stimulation (Stimulated). Scale bar represent 100 μm. **B)** Quantification of the fluorescent signal of SMA set out against the fluorescent signal of actin. **C)** Western blots detecting SMA and SM22 in a healthy control prior to stimulation (unstimulated) and after 14 days of TGFβ stimulation (Stimulated).

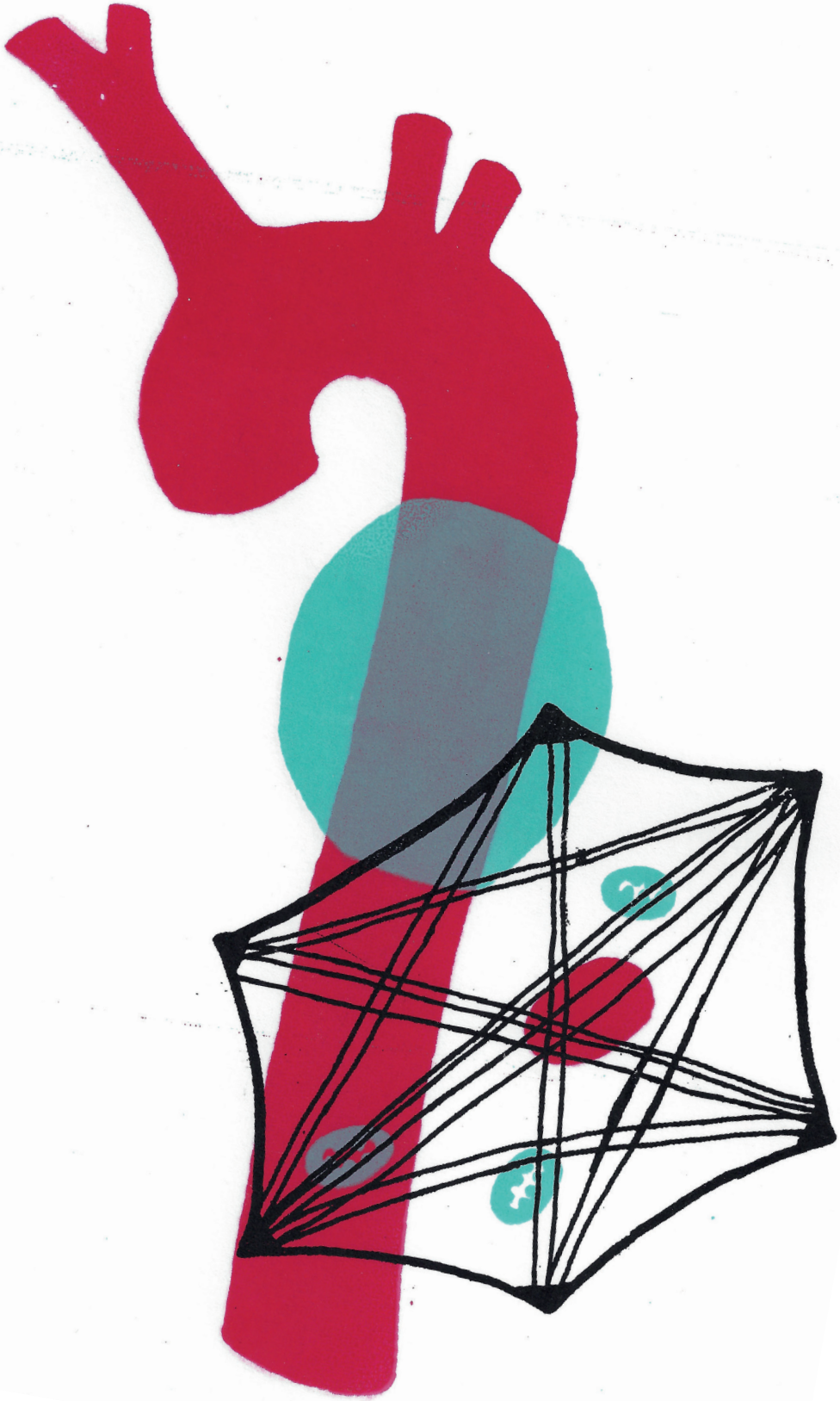

CHAPTER 3

SLC2A10 KNOCK-OUT MICE DEFICIENT IN ASCORBIC ACID SYNTHESIS RECAPITULATE ASPECTS OF ARTERIAL TORTUOSITY SYNDROME AND DISPLAY MITOCHONDRIAL RESPIRATION DEFECTS

Annekatrien Boel [1,2], Joyce Burger [3], Marine Vanhomwegen [1], Aude Beyens [1,4], Marjolijn Renard [1], Sander Barnhoorn [3], Christophe Casteleyn [5], Dieter P. Reinhardt [6], Benedicte Descamps [7], Christian Vanhove [7], Ingrid van der Pluijm [3,8], Paul Coucke [1], Andy Willaert [1], Jeroen Essers [3,8,9], Bert Callewaert [1]

[1] Center For Medical Genetics Ghent, Department of Biomolecular Medicine, Ghent University, Ghent, Belgium [2] Ghent-Fertility and Stem cell Team, Department for Reproductive Medicine, Ghent University Hospital, Ghent, Belgium [3] Department of Molecular Genetics, Erasmus University Medical Center, Rotterdam, the Netherlands; Department of Clinical Genetics, Erasmus University Medical Center, Rotterdam, the Netherlands [4] Department of Dermatology, Ghent University Hospital, Ghent, Belgium [5] Department of Morphology, Faculty of Veterinary Medicine, Ghent University, Merelbeke, Belgium [6] McGill University, Faculty of Medicine, Department of Anatomy and Cell Biology and Faculty of Dentistry, Montreal, Quebec, Canada [7] Infinity (IBiTech-MEDISIP), Department of Electronics and Information Systems, Ghent University, Ghent, Belgium [8] Department of Vascular Surgery, Erasmus University Medical Center, Rotterdam, the Netherlands [9] Department of Radiation Oncology, Erasmus University Medical Center, Rotterdam, the Netherlands

Accepted Human Molecular Genetics 2020 Apr

ABSTRACT

Arterial tortuosity syndrome (ATS) is a recessively inherited connective tissue disorder, mainly characterized by tortuosity and aneurysm formation of the major arteries. ATS is caused by loss-of-function mutations in *SLC2A10*, encoding the facilitative glucose transporter GLUT10. Former studies implicated GLUT10 in the transport of dehydroascorbic acid, the oxidized form of ascorbic acid (AA). Mouse models carrying homozygous *Slc2a10* missense mutations did not recapitulate the human phenotype. Since mice, in contrast to humans, are able to intracellularly synthesize AA, we generated a novel ATS mouse model, deficient for *Slc2a10* as well as *Gulo,* which encodes for L-gulonolactone oxidase, an enzyme catalyzing the final step in AA biosynthesis in mouse. *Gulo;Slc2a10* double knock-out mice showed mild phenotypic anomalies, which were absent in single knock-out controls. While *Gulo;Slc2a10* double knock-out mice did not fully phenocopy human ATS, histological and immunocytochemical analysis revealed compromised extracellular matrix formation. Transforming growth factor beta signaling remained unaltered, while mitochondrial function was compromised in smooth muscle cells derived from *Gulo;Slc2a10* double knock-out mice. Altogether, our data add evidence that ATS is an ascorbate compartmentalization disorder, but additional factors underlying the observed phenotype in humans remain to be determined.

INTRODUCTION

Arterial Tortuosity Syndrome (ATS, MIM#208050) is a rare autosomal recessive connective tissue disorder, characterized by severe patterning defects in blood vessel development. Main features of the disease include elongation, tortuosity, and stenosis of the large and middle-sized arteries, with an increased risk for aneurysm formation and ischemic events [1-3]. Patients may present with additional connective tissue-related features, such as *cutis laxa*, diaphragmatic hernias, joint laxity, distinctive craniofacial malformations and a marfanoid habitus. Finally, corneal thinning causing pellucid corneas and keratoconus were recently described [2, 4]. The disease has shown to be variable in terms of severity, ranging from early mortality to mild manifestations in adulthood [1, 2, 5, 6]. Arterial histopathology shows disorganization and fragmentation of the elastic fibers [1, 7-10]. Cultured fibroblasts of ATS patients showed disorganization of the actin cytoskeleton and multiple extracellular matrix (ECM) components, including fibronectin, fibrillin, type 3 and type 5 collagen, and decorin [11, 12].

ATS is caused by loss-of-function mutations in the *SLC2A10* gene, encoding the GLUT10 protein [3]. GLUT10 belongs to the GLUT family of facilitative transporters, consisting of 14 transmembrane proteins, enabling the transport of monosaccharides, polyols, and other small carbon compounds across the membranes of eukaryotic cells [13]. GLUT members show specific functionalities, but some functional redundancy has been observed. Recent evidence identified GLUT10 as a transporter of dehydroascorbic acid (DHA), the oxidized form of ascorbic acid (AA), but its subcellular localization remains enigmatic and may change upon physiological states. GLUT10 has been shown to reside in mitochondria [14], the nuclear envelope [3], and/or the endoplasmic reticulum (ER) [15-17].

It remains to be solved how defective DHA transport results in a vasculopathy related to Loeys-Dietz [18] or Marfan Syndrome [19, 20], respectively caused by perturbed transforming growth factor beta (TGFβ) pathway signaling or altered ECM proteins. In the absence of relevant vascular patient material, several ATS disease models have been developed. *Slc2a10* knockdown in a morpholino-based zebrafish model showed abnormal vascular patterning and mitochondrial respiration [21]. Two knock-in mouse models, either carrying a homozygous likely pathogenic G128E or S150F missense substitution in *Slc2a10* [22, 23], were previously phenotyped by two different research groups. While no ATS-related abnormalities could be discerned in either mutant by one of both groups at 3 months of age [23], the other group found elastic fiber proliferation in older homozygous G128E mutant mice only [22]. It is unclear whether this is related to the elastic fiber fragmentation seen in the vascular wall of ATS patients. Recent follow-up studies in this mouse model indicated altered redox homeostasis and mitochondrial dysfunction as pathogenic mechanisms underlying ATS [24], similar to observations in the morpholino zebrafish

knockdown model [21], and in ATS knockdown cell lines (rat A10, mouse 3T3-L1) [14]. Altered redox homeostasis contributes to the pathogenesis in other aneurysm-related diseases [25].

Growing evidence that GLUT10 functions as an AA transporter has led to the hypothesis that the innate AA synthesizing capacity of mice could rescue the phenotype. Therefore, we characterized a novel mouse model for ATS, with gene disruptions of both *Slc2a10*, the causal gene for ATS, and *Gulo*, which encodes L-gulonolactone, the enzyme catalyzing the last step in AA biosynthesis in mouse.

RESULTS

Generation of the *Slc2a10*;*Gulo* double knock-out mouse model

We developed a novel mouse model for ATS in a mixed 129/SvEv-C57BL/6 genetic background by crossing constitutive knock-out lines for *Gulo* and *Slc2a10*, both harboring a selection cassette replacing multiple exons (Supplementary Figure 1A). To take into account any possible effect of a variable genetic background on the acquired data, all studies were performed on littermates from the F2 generation (Supplementary Figure 1B). RT-qPCR-based expression analysis, using primers targeting the sequence replaced by the selection cassette, confirmed the absence of wild type *Slc2a10* RNA in skin and aorta obtained from *Slc2a10* $^{-/-}$ animals (DKO and *Slc2a10* KO) (Figure 1).

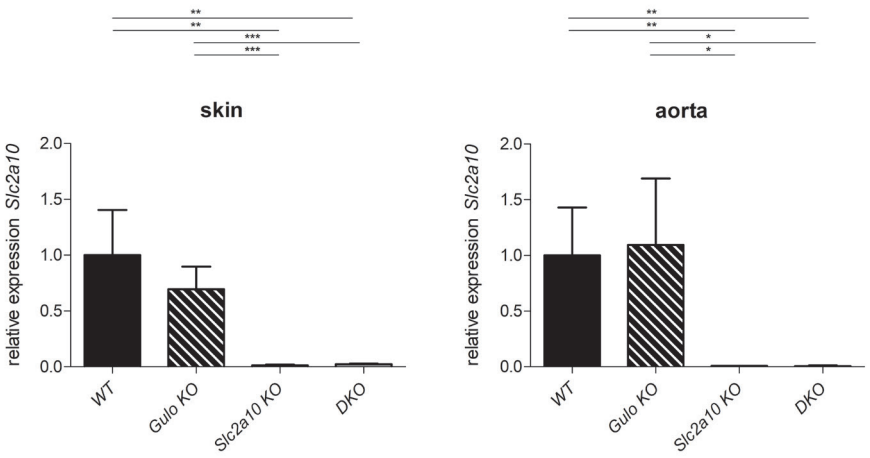

Figure 1. *Slc2a10* expression levels in skin and aortic tissue.

RT-qPCR analysis identifies a near absence of *Slc2a10* WT mRNA in mice homozygous for *Slc2a10* mutations (*Slc2a10* KO and DKO), compared to mice harboring the *Slc2a10* wild type allele (*Gulo* KO and WT). Displayed average values represent the relative expression data in skin or aorta for 3 male and 3 female mice. Error bars represent the SD, *: $p \leq 0.05$; **: $p \leq 0.01$; ***: $p \leq 0.001$.

Double knock-out mice (DKO – *Gulo* $^{tm1mae/\ tm1mae}$;*Slc2a10* $^{-/-}$) were born with expected Mendelian frequency and had a normal lifespan to at least 9 months of age, similar to their control littermates (*Gulo* KO – *Gulo* $^{tm1mae/\ tm1mae}$;*Slc2a10* $^{+/+}$, *Slc2a10* KO – *Gulo* $^{+/+}$;*Slc2a10* $^{-/-}$ and WT – *Gulo* $^{+/+}$;*Slc2a10* $^{+/+}$). Double knock-out mice developed normally, and showed no obvious gross anomalies, skeletal dysmorphisms or skin abnormalities. However, the weight of female DKO mice was slightly reduced, at each measurement time point (Supplementary Figure 2).

S*lc2a10*;*Gulo* double knock-out mice do not completely copy the human ATS phenotype

We carried out serial ultrasound measurements at multiple locations in the cardiovascular system of 10 male and 10 female mice of each selected genotype (DKO, *Slc2a10* KO, *Gulo* KO, WT) at 6 weeks, 3, 6, and 9 months of age. Diameters of the ascending aorta, distal ascending aorta, aortic arch and descending aorta showed a subtle but statistically significant decrease in DKO mice compared to their wild type littermates, for a given age and sex (Figure 2). More distal measurements (carotid arteries) did not reveal any significant diameter alterations (Supplementary Figure 3). Fractional shortening and ejection fraction were comparable between the selected genotypes at 6 weeks and 3 months of age (Supplementary Figure 4). We did not detect aortic or mitral valve insufficiency using pulsed Doppler. Detailed microscopic analysis of the aortic tree, eye arterioles and the circle of Willis, obtained from polymer replicas of the cardiovascular system at 9 months of age, did not indicate any omnipresent structural anomalies such as tortuosity, abnormal implantation of the aortic side-branches or aneurysms. However, one out of three analyzed female DKO mice had a local stenosis in the vertebral artery (Figure 3, Supplementary Figure 5). At 9 months, elastic fiber staining of aortic tissue showed mild age-related changes, such as sporadic elastic fiber fragmentation or accumulation, in the *tunica media* of the aortic wall across all selected genotypes.

Picrosirius red polarization staining on skin tissue showed no major alterations in collagen deposition, but patches of increased collagen deposition could be discerned in female DKO mice (Figure 4, Supplementary Figure 6).

Transmission electron microscopy (TEM) analysis of female skin samples showed a normal elastic fiber architecture (Supplementary Figure 7). Collagen fibril diameters were significantly reduced in DKO compared to WT mice (Figure 5).

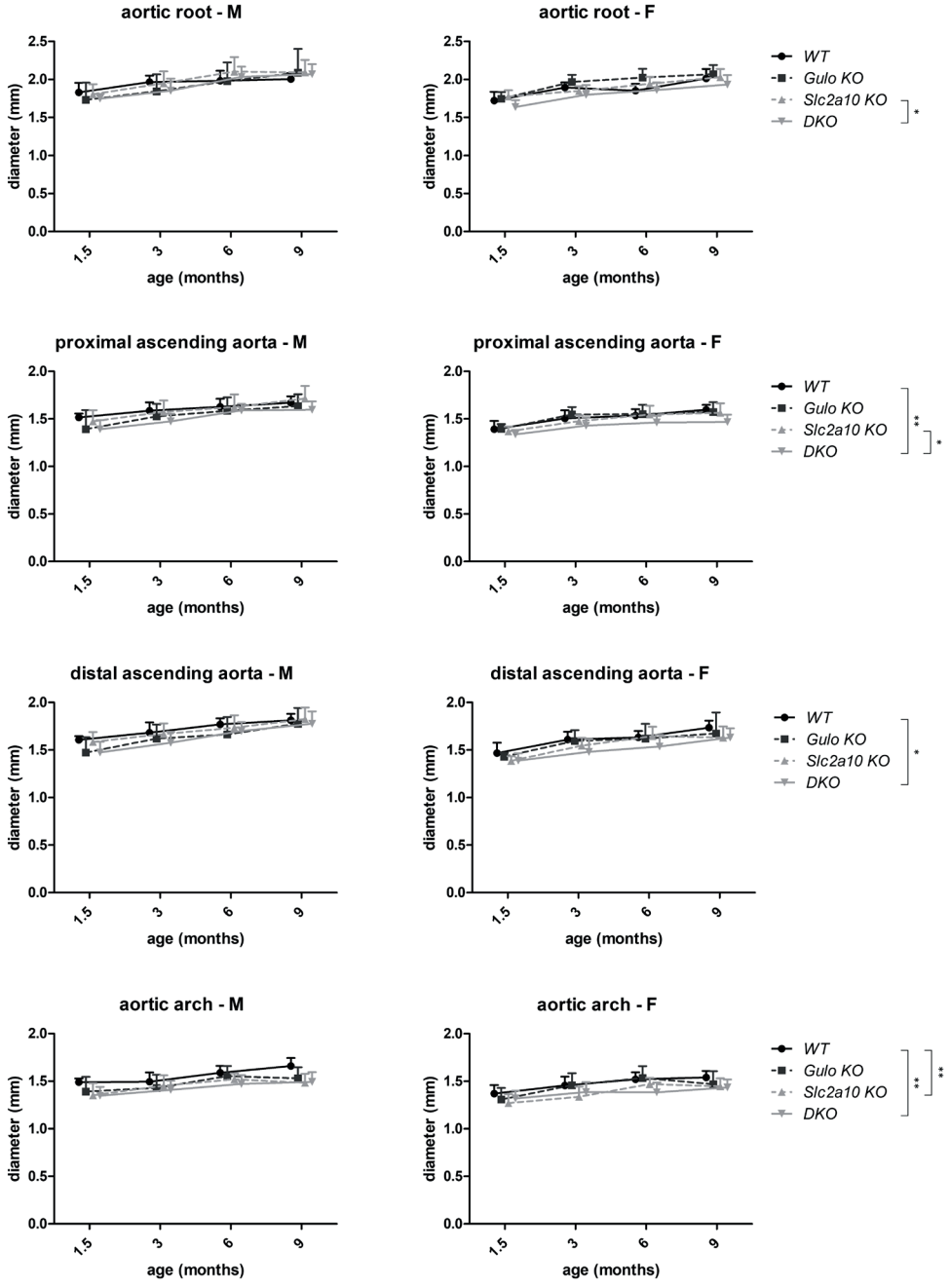

Figure 2. Serial ultrasound measurements obtained in WT, Gulo KO , Slc2a10 KO and DKO mice at 6 weeks, 3, 6 and 9 months of age.

Shown data were acquired at the level of the aortic root, proximal ascending aorta, distal ascending aorta and aortic arch. Left and right column images represent data obtained in male (M) and female (F) animals, respectively. Shown p-values were obtained using a linear mixed model with covariance pattern modeling, without interactions. As a result, p-values should be interpreted when making the comparison for a given age and sex. Error bars represent 95% confidence intervals. *: $p \leq 0.05$; **: $p \leq 0.01$.

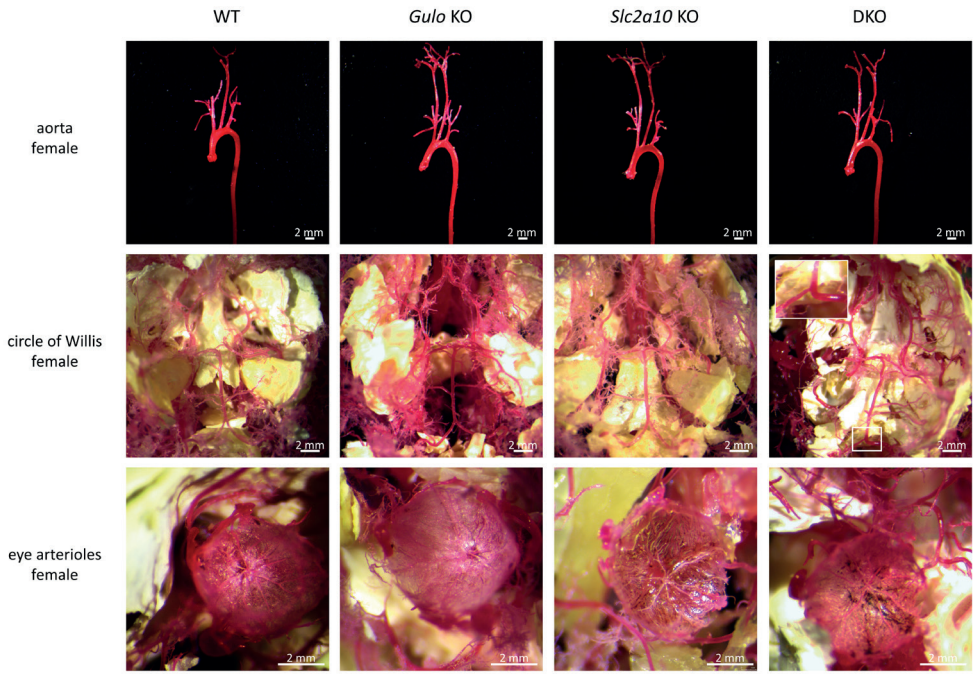

Figure 3. Vascular corrosion casts of WT, Gulo KO , Slc2a10 KO and DKO female mice.

Representative images of the aortic arch and its side branches, the circle of Willis and the eye arterioles are shown. A local narrowing in the vertebral artery in the circle of Willis could be observed in one DKO mouse (white-framed enlargement). Scale bars: 2 mm.

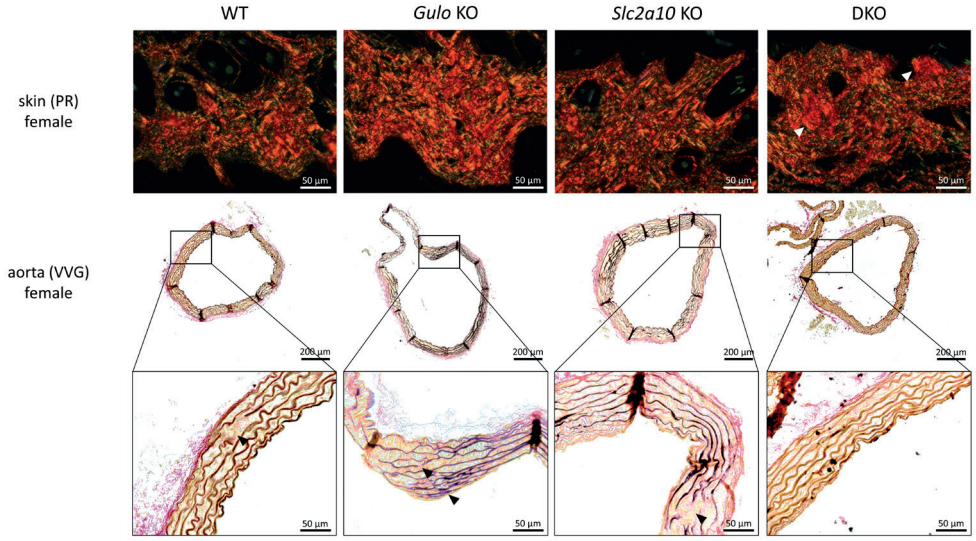

Figure 4. Histological analysis of WT, Gulo KO , Slc2a10 KO and DKO female mice.

Picrosirius red (PR) polarization staining (upper row) for collagen reveals the presence of patches with accumulated collagen deposition (white arrows) in the skin of DKO mice. Verhoeff-Van Gieson (VVG) elastic fiber staining (middle row) shows mild elastic fiber anomalies in the aortic wall of all studied mice (black arrows).

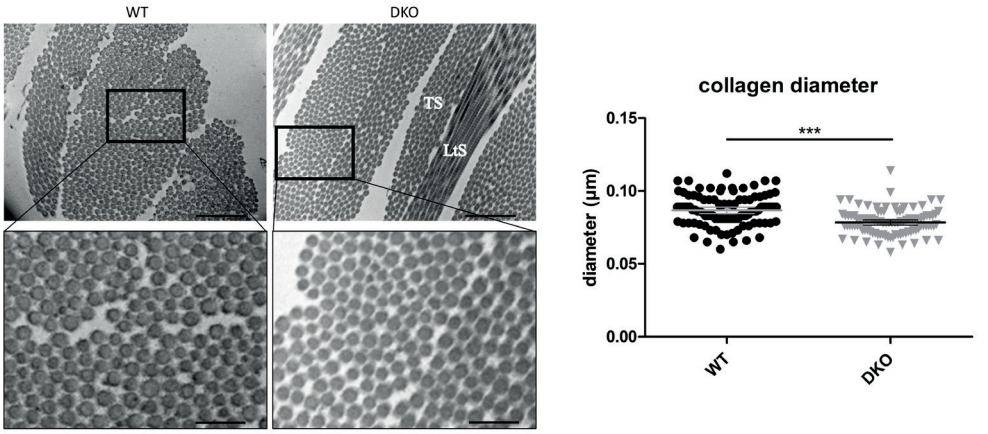

Figure 5. Electron microscopic quantification of collagen diameters in WT and DKO skin samples.

DKO mice show decreased collagen fiber diameters, compared to WT mice (measurements on EM micrographs of two animals per genotype). TS: transverse section, LtS: longitudinal section. Scale bar upper row: 1.0 μm, lower row: 0.3 μm. Error bars represent 95% confidence intervals. ***: $p \leq 0.001$.

In vitro analysis of *Slc2a10;Gulo* double knock-out vascular smooth muscle cells shows decreased ECM deposition

We examined the ECM deposition in vascular smooth muscle cells (VSMCs) of the DKO and WT genotypes (Figure 6). In contrast to WT VSMCs, DKO VSMCs did not show a base network of recognizable and organized fibronectin fibers stretching between the cells, but presented with a reduced intensity of fibronectin staining with a more fuzzy appearance (Figure 6A, Supplementary Figure 8). A similar observation was made for fibrillin-1 where stained fibers appeared thinner in DKO VSMCs (Figure 6B, Supplementary Figure 8). WT VSMCs showed clear staining of tropoelastin that appeared in a fibrillar structure (Figure 6C), next to the presence of a strong fiber network of both fibulin-4 (Figure 6D) and fibulin-5 (Figure 6E). In DKO VSMCs, a reduced staining of fibulin-4 and fibulin-5 (Figure 6D and E, Supplementary Figure 8) and an overlapping network of tropoelastin and fibulins (Figure 6C, Supplementary Figure 8) could be observed. We further assessed LTBP-4, which was present in clear fibrillar structures (Figure 6F) in both WT and DKO VSMCs, but appeared less intense in DKO VSMCs, organized in a more densely packed fibril network (Figure 6F, Supplementary Figure 8). Taken together, these data show that DKO VSMCs displayed decreased deposition of the various components of the ECM compared to WT VSMCs.

Slc2a10;Gulo double knock-out VSMCs do not show altered activation of canonical TGFβ signaling

We investigated canonical TGFβ signaling activation in VSMCs derived from WT and DKO mouse aortas. Under an unstimulated serum deprived condition, DKO VSMCs showed similar levels of Smad2 phosphorylation compared to WT VSMCs (Figure 7A and B). Following TGFβ stimulation, both WT and DKO VSMCs demonstrated a strong and comparable increase in phosphorylation of Smad2 after 15 minutes (Figure 7A). Quantification of phosphorylated Smad2 to total Smad2 ratio revealed a further increase to its maximum at 60 minutes of stimulation after which it decreased (Figure 7A and B). In conclusion, our data do not support aberrations in the activation of the canonical TGFβ signaling pathway in DKO VSMCs compared to control VSMCs.

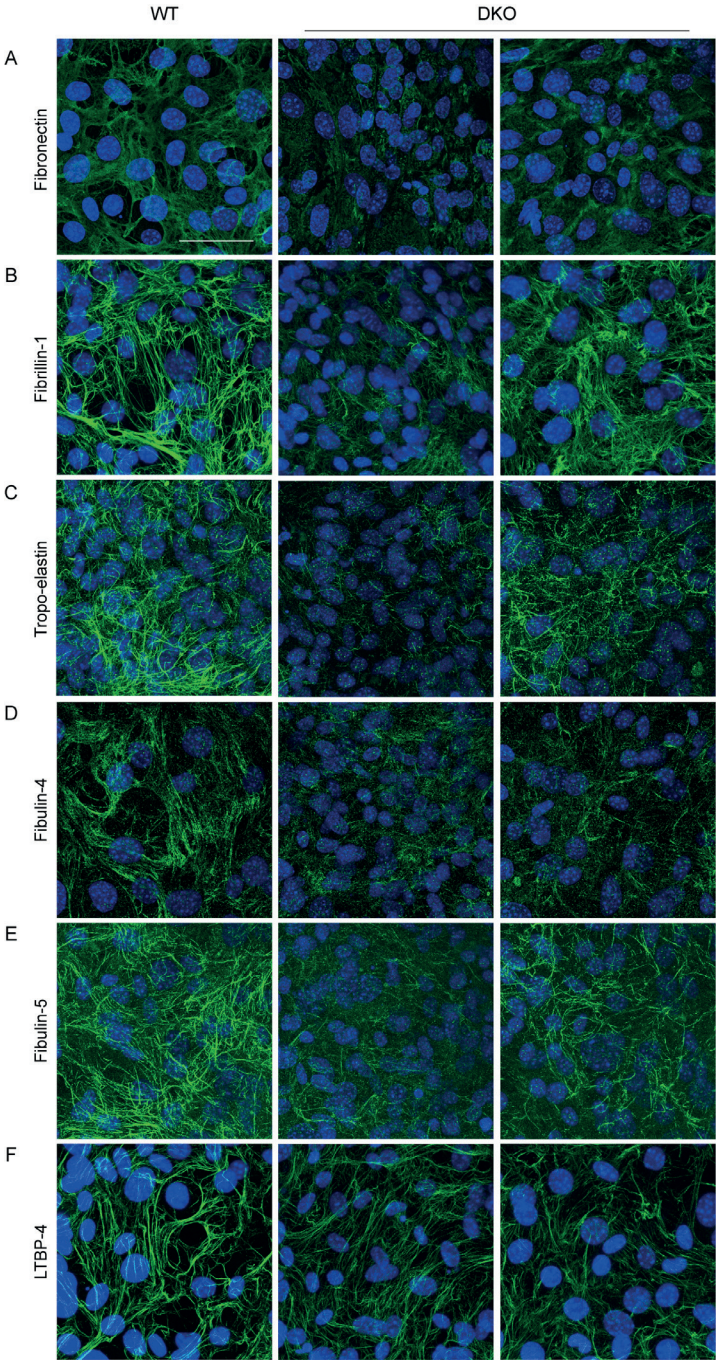

Figure 6. DKO VSMCs show decreased ECM deposition.

Immunofluorescent images show deposition of multiple ECM components after 7 days of culture. DKO VSMCs show less distinct ECM structures compared to WT VSMCs. Scale bars represent 100 μm.

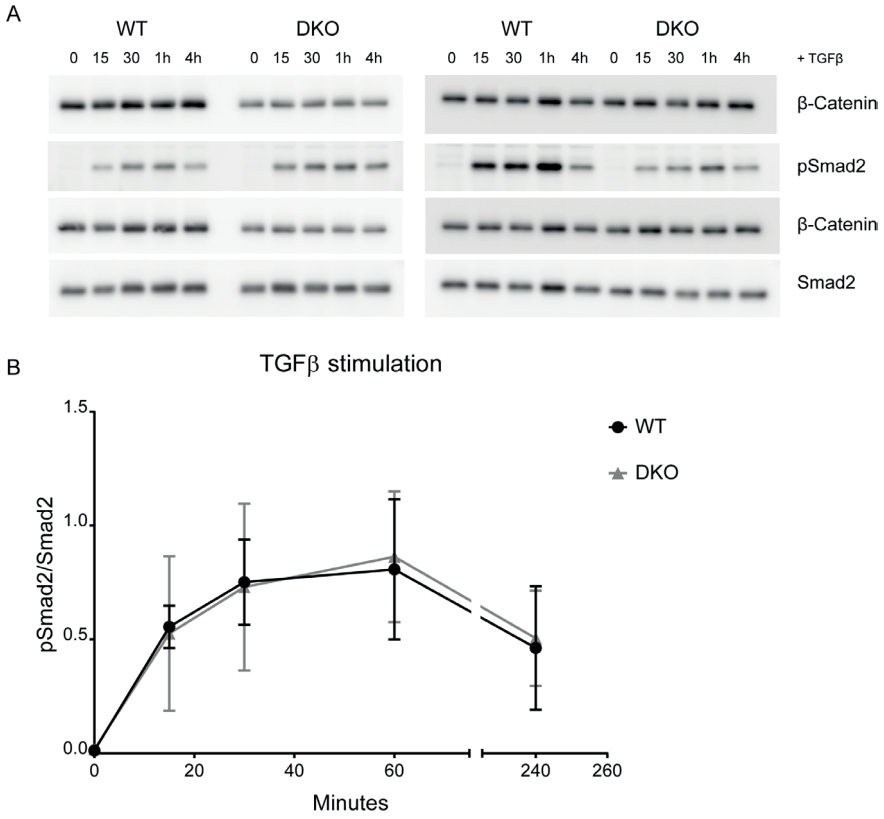

Figure 7. DKO VSMCs do not show altered activation of the canonical TGFβ signaling pathway.

DKO VSMCs do not show increased phosphorylation of Smad2 without TGFβ stimulation and do not differ from WT VSMCs in basal conditions. Stimulation with TGFβ led to increased phosphorylation of Smad2 in both WT and DKO VSMCs. There was no difference in pSmad2/Smad2 ratio between the two genotypes. The data show 2 independent cell lines from 2 experiments. The data points represent average values of an independent cell line per experiment. Results are depicted as mean ± SD.

Slc2a10;Gulo double knock-out VSMCs show a reduced maximum oxygen consumption rate

Since GLUT10 impairment has previously been associated with mitochondrial dysfunction in a Glut10 mouse model with missense mutations [24] and a s*lc2a10* zebrafish knockdown model [21], we analyzed the oxygen consumption rate (OCR) of DKO compared to WT VSMCs as a marker for mitochondrial function (Figure 8A). Phase I represents the basal and unstimulated OCR. Addition of oligomycin in phase II inhibits the ATP synthase and reduces the OCR. In Phase III, treatment with fluoro-carbonyl cyanide phenylhydrazone (FCCP) uncouples oxygen consumption from ATP production and raises OCR to its maximum. Addition of antimycin A in

phase IV inhibits complex III of the mitochondria and blocks mitochondrial respiration. Figure 8B and C contain the quantification of the mean value of phase I and III per genotype. Basal OCR did not differ between both genotypes (Figure 8A and B). However, when VSMCs were treated with FCCP to reach maximum respiration, DKO VSMCs displayed decreased maximum respiration rates compared to WT VSMCs (Figure 8A and C).

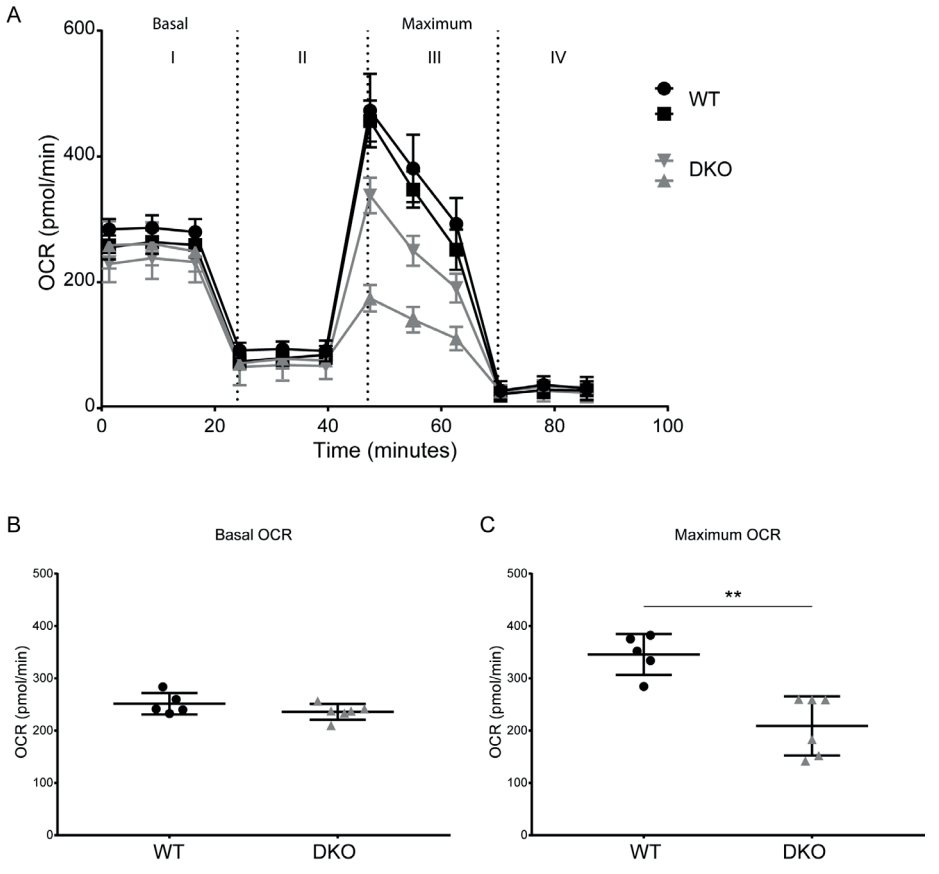

Figure 8. DKO VSMCs show a reduced maximum OCR.

In basal conditions, DKO and WT VSMCs do not differ in OCR, while treatment with FCCP results in a decreased maximum OCR of DKO VSMCs. Data represents 2 independent cell lines per genotype measured in 3 technical replicates. The data points represent average values of an independent cell line per experiment. Results are depicted as mean ± SD. ** $p \leq 0.01$.

DISCUSSION

Arterial tortuosity may occur in both innate and acquired vasculopathies, such as persistent hypertension and neoangiogenesis, and may associate with an increased vascular risk, including aneurysm formation and blood vessel rupture. Monogenic conditions may be helpful in delineating the underlying pathophysiology of altered vascular patterning. In this study, we developed and characterized a novel mouse model for ATS, since the previously reported mouse models for ATS failed to recapitulate the major hallmarks of the human disease [22, 23]. Our model addressed two concerns regarding the previous models. Firstly, we developed an *Slc2a10* knock-out, which abolishes GLUT10 function while the previously reported missense mutations were only predicted to be pathogenic [22, 23]. Secondly, we impaired AA synthesis in our model by disrupting the *Gulo* gene, aiming to mimic the physiological conditions in human more reliably. Indeed, *Gulo* encodes L-gulonolactone oxidase, an endoplasmic reticulum membrane-bound enzyme that catalyzes the last step in the vitamin C biosynthesis pathway [26]. It became mutated in many species, such as teleost fishes, guinea pigs and anthropoid primates, including humans, making these species unable to synthesize vitamin C and rely on its dietary uptake [27]. Vitamin C plays an essential role as an anti-oxidant and in collagen synthesis. Since recent evidence indicates that GLUT10 function may include transport of DHA into subcellular compartments [14, 17, 24], it could be hypothesized that murine developmental processes do not suffer from *Slc2a10* mutations and localized vitamin C hypovitaminosis, which would explain the absence of a relevant phenotype in *Slc2a10* mutant mice [16, 23].

Nevertheless, in this study, we only observed mild cardiovascular manifestations in the double knock-out ATS mouse model. Ultrasound-guided characterization revealed a subtle stenosis from the proximal ascending aorta to the descending aorta in DKO mice, but only statistically significant when compared with their wild type littermates. Moreover, the reduced weight in the double knock-out mice further questions the biological relevance of these results.

Histopathology of ATS patient vascular tissue invariably shows substantial fragmentation of the elastic laminae in the *tunica media* [1] while conversely the previously described Glut10^{G128E} mouse model mainly presented with increased arterial wall thickness, most prominent at the age of 15 months [22, 24]. Our model only reveals mild elastic fiber anomalies in all genotypes, that are likely age-related changes. Nevertheless, dermal collagen histology revealed patches of increased collagen deposition in female DKO mice, which has also been observed in skin tissue of ATS patients [1], and might contribute to their 'doughy' skin characteristics. Ultrastructural analysis of skin tissue of double knock-out mice additionally revealed collagen fiber diameter alterations in DKO mice, but did not reveal major defective elastin deposition, which contrasts with TEM observations in ATS patients [1].

The observed mild phenotypic abnormalities seem to be more pronounced in female mice, suggesting a sex discrepancy, even for nulliparous mice. Influences of sex in connective tissue homeostasis and disease have been previously recognized. However, most studies indicate that male mouse models for connective tissue disorders show more severe phenotypes than female mice [28-31], which contrasts with our study.

Despite the absence of a major clinical or histological phenotype, we did identify defective ECM deposition in cultured VSMCs of DKO mice. Ascorbic acid is a cofactor for cross-linking enzymes such as lysyl oxidase and lysyl oxidase-like enzymes. Hence, it is not surprising that elastin and collagen assembly are primarily affected. Nevertheless, our observations also indicate reduced deposition of the early stage fibril forming networks including the fibronectin and fibrillin-1 microfibrillar scaffolds. This reflects an earlier observation that in the absence of ascorbic acid, not only deposition of collagen, but also of fibronectin is greatly reduced [32]. Indeed, collagen I fibers interact preferentially with relaxed (but in a lesser extent to stretched) fibronectin fibers [32] and collagen 1 increases fibronectin deposition [33]. Therefore, ECM assembly cannot be seen as a consequential process but rather as an interactive and growing mechano-sensing network of components. Similarly, fibulin-4, -5 deposition was clearly reduced, while LTBP4 deposition was only slightly affected. Though further experimentation is necessary, we hypothesize that latent TGFβ-binding proteins (LTBPs) might be upregulated due their primary role in elastogenesis [34]. Our results are in line with findings by Zoppi *et al.,* who previously showed ECM disarray in skin fibroblasts of ATS patients [12]. In addition, a recent study revealed an abnormal microfibrillar scaffold and incomplete elastic core assembly in skin samples of ATS patients [1], that likely reflect defective ECM assembly at multiple levels, as shown in our model. Since defective ECM assembly is often associated with vascular phenotypes [35, 36], this might indicate that mice may rely on other mechanisms that overcome the deleterious defects of abnormal ECM assembly.

In several aneurysm syndromes, dysregulation of the canonical TGFβ signaling pathway is at play in aneurysm formation [37, 38]. However, while we observed ECM abnormalities, DKO VSMCs do not show altered phosphorylation of Smad2 upon TGFβ stimulation over time as well as under basal, unstimulated, conditions. An initial report indicated a prolonged signal increase for downstream readouts of TGFβ signalling in arterial tissue of (one) ATS patient [3]. This finding remained unconfirmed on both fibroblast cultures [12], skin or artery tissue [1] in an extended number of patients. A role for non-canonical αvβ3 integrin-mediated TGFβ signalling in the ATS pathomechanisms has been suggested [12]. Our results add to the uncertainty regarding the role of TGFβ signalling in the pathomechanisms underlying many elastic fiber diseases, but cannot account for a possible contribution of spatiotemporal regulation of TGFβ signalling.

A number of studies have pointed towards a key role for oxidative stress in ATS pathogenesis. For instance, GLUT10 has been identified as a mitochondrial DHA transporter, and it was shown that increased mitochondrial targeting of GLUT10 and associated increased mitochondrial DHA uptake was triggered by stress and aging conditions [14, 24]. In a morpholino *slc2a10* knockdown zebrafish model, altered OCR and differential gene expression analysis showed involvement in oxidative signalling [21]. In the Glut10^{G128E} mouse model, Syu and coworkers similarly identified a decreased maximum OCR in early passage Glut10^{G128E} VSMCs [24]. In this study, we compared basal and maximal OCR in VSMCs of double knock-out and control mice and identified a normal basal OCR in DKO VSMCs. However, following treatment with FCCP, a decreased maximum OCR could be observed in DKO VSMCs, compared to WT. Since basal OCR was comparable in DKO and WT VSMCs, the need for a stressor to dysregulate mitochondrial function in DKO VSMCs could explain the reduced maximum OCR after FCCP treatment. However, it has been suggested that an aberrant maximal OCR only corresponds to the initial symptoms of mitochondrial dysfunction caused by *SLC2A10* mutations, due to reactive oxygen species (ROS) that trigger arterial wall remodeling. In its turn, this leads to additional ROS production, and disease progression promotes further decline in mitochondrial function. It is also plausible that mitochondrial dysfunction is a more ubiquitous phenomenon associated with aneurysmal disease. Van der Pluijm *et al.* investigated mitochondrial function in Fibulin-4$^{R/R}$ and Tgfbr-1$^{M318R/+}$ mouse VSMCs and found decreased mitochondrial respiration in these mouse models. In addition, skin fibroblasts of aneurysmal patients with *FBN1, TGFBR2* or *SMAD3* mutations revealed mitochondrial dysfunction as well [25].

Finally, due to the mild nature and low abundance of relevant phenotypic alterations, it could be argued that this novel ATS double knock-out mouse model does not appear to be a suitable disease model to study the pathomechanisms underlying ATS [22, 23]. While the lack of a severe phenotype could be attributed to the genetic background of the used mouse strains, possibly hindering phenotypic penetrance [39], the underlying cause could also be biological robustness. This is a phenomenon by which the functionality of the mutated gene is maintained by increased expression of related genes [40, 41], as was demonstrated earlier in a number of other mouse disease models [42, 43]. One mechanism of biological robustness is transcriptional adaptation [44, 45]. This mechanism is triggered by mRNA degradation products and is believed to act via sequence similarity [46, 47]. Since *Slc2a10* is a member of a large family of facilitative glucose transporter proteins harboring a high sequence similarity, this mechanism is plausible [48]. It could also be argued that an extensive dose (60 mg/kg body weight) of ascorbic may have masked the development of a relevant phenotype, since this dose exceeds the daily recommended dose in human (1 mg/kg body weight) extensively. However, species differences might complicate the direct comparison or extrapolation of the optimal daily dose between mouse and human. A daily ascorbic acid dose of 1mg/kg body weight corresponds in human to plasma ascorbic acid

levels of 25 μM respectively. To reach comparable levels in mouse plasma, a significantly higher dose (80 mg/kg body weight) needs to be administered [49].

Nevertheless, the current double knock-out mouse model could be of importance in revealing redundant gene networks, alternative pathways or modifier genes, possibly providing clues for future therapies. Moreover, since isolated VSMCs of double knock-out mice mimicked cellular disturbances found in cell cultures of ATS patients, these VSMCs could potentially be used for further identification of the molecular mechanisms that underlie ATS, while analyses at the histological level may reveal adaptive mechanisms that contribute to the phenotypic rescue.

In conclusion, we developed a novel mouse model for ATS, double knock-out for *Gulo* and *Slc2a10*. While our model does not phenocopy human ATS, it did reveal alterations at the cellular level including disturbed ECM assembly and altered cellular respiration. Our model confirms a role for ascorbate synthesis and compartmentalization in the disease mechanisms leading to ATS and may be helpful to identify the mechanisms underlying the phenotypic rescue in mice.

MATERIALS & METHODS

Animals

Heterozygous knock-out mice for *Slc2a10,* in which a selection cassette replaces a sequence ranging from exon 2 to the beginning of exon 5, were purchased from Taconic Biosciences (cat. nr. TF2438), (Supplementary Figure 1A). The mutation resides in a mixed 129/SvEv-C57BL/6 genetic background. Heterozygous knock-out mice for *Gulo,* in which a selection cassette replaces exons 3 and 4, were purchased from MMRRC (RRID MMRRC_000015-UCD) (Supplementary Figure 1A). This mouse line, residing in a mixed 129/SvEv-C57BL/6 genetic background as well, was previously described by Maeda and colleagues [49]. The two lines were crossed according to a breeding scheme depicted in Supplementary Figure 1B. To allow for valid data generation and to take into account any potential influence of genetic background, all comparisons were made between littermates from the F2 generation. Male and female mice of the following genotypes were studied: double knock-out (DKO – *Gulo* $^{tm1mae/\ tm1mae}$;*Slc2a10* $^{-/-}$), single knock-out (*Gulo* KO – *Gulo* $^{tm1mae/\ tm1mae}$;*Slc2a10* $^{+/+}$ and *Slc2a10* KO – *Gulo* $^{+/+}$;*Slc2a10* $^{-/-}$) and wild type (WT – *Gulo* $^{+/+}$;*Slc2a10* $^{+/+}$). All procedures were conducted in compliance with the European Parliament Directive 2010/63/EU, and with the approval of the Ghent University ethical committee on animal experiments (Permit Number: ECD 13/17). All animals were fed ad libitum with a standard mouse breeding feed, supplemented with 300 mg/kg ascorbic acid (Ssniff® Spezialdiäten). The administered ascorbic acid dose is based on an average food intake of 4 g/day, for a mouse with an average weight of 20 g. This dose translates to a daily dose of 60 mg/kg body weight, which is comparable to the average administered ascorbic acid dose of the first

report on this model (110 mg/kg), by Maeda *et al.* [49]. Mice were maintained in a fully controlled animal facility (12:12 h light:dark cycle at ± 22 °C).

Genotyping

Seven-day-old mice were toe-clipped, after which genomic DNA was prepared from the tissue using the KAPA Express Extract DNA Extraction Kit (Kapa Biosystems, cat. nr. KK7103). For both *Gulo* and *Slc2a10* the DNA was PCR-amplified using specific primers detecting the wild type and mutant alleles. The genotype was determined based on PCR product presence and band size (Supplementary Table 1).

Quantitative real-time PCR

Skin and aortic tissue from 3 male and 3 female mice of each selected genotype were harvested at the age of 9 months and submerged in RNAlater™ Stabilization Solution (Thermo Fisher Scientific, cat. nr. AM7020) prior to the RNA extraction procedure, carried out with the RNeasy® Mini kit (Qiagen, cat. nr. 74106). Next, cDNA synthesis was performed using the iScript cDNA synthesis kit (Bio-Rad, cat. nr. 1708891). RT-qPCR reactions were carried out in quadruple on an LC480 machine (Roche). The reaction mix consisted of cDNA, LightCycler® 1536 DNA Probes Master (Roche, cat. nr. 05502381001), LightCycler® 480 High Resolution Melting Dye (Roche, cat. nr. 04909640001) and specific primers amplifying the *Slc2a10* transcript or Expressed Repeat Elements (EREs) (Supplementary Table 2) [50], to which all reactions were normalized. Data analysis was carried out with qBase+ (Biogazelle). Values plotted correspond to the means of 3 male and 3 female biological replicates. Error bars shown represent 95% confidence intervals. Data were analyzed using Welch's ANOVA, followed by a Games-Howell post-hoc test.

***In vivo* imaging**

Serial ultrasound imaging was performed using a dedicated ultrasound apparatus (Vevo 2100, VisualSonics), equipped with a high-frequency linear array transducer (MS 550D, frequency 22–55 MHz). Imaging was carried out on mice of 6 weeks, 3, 6 and 9 months old. Ten male and 10 female mice of the selected genotypes were studied. The mice were anesthetized with 1.5% isoflurane mixed with 0.5 L/min 100% O_2. Body temperature was maintained at 37°C, by placing the mice on a heating pad. Artery and cardiac measurements were carried out in concordance with previously established guidelines [51]. In short, the diameter measurements of the aorta at the level of the aortic root, proximal ascending aorta, distal ascending aorta, aortic arch and descending aorta were performed, next to diameter measurements of the carotid arteries and cardiac assessment. Three cardiac cycles for each animal were analyzed (VevoLAB 1.7.0, VisualSonics). For each measurement location, a linear mixed model with covariance pattern modelling was fitted to account for correlated responses (diameters) within the same subject. Genotype, age and sex were considered as categorical explanatory variables. Starting from a saturated mean model with unstructured covariance matrix and using residual

maximum likelihood (REML), the covariance model was simplified by comparison with simpler structures through Akaike's Information Criterion. The following covariance matrices that were as parsimonious as possible, were selected: unstructured (aortic root), autoregressive (proximal ascending aorta), Toeplitz (distal ascending aorta), compound symmetry (all other measurement locations). Afterwards, the fixed part of the model was simplified by testing simpler models using maximum likelihood. All final models included the main effects of genotype, age, and sex without interaction terms and were refitted with REML. Values plotted correspond to the means of ±10 biological replicates. Error bars shown represent 95% confidence intervals.

Vascular corrosion casting

The vascular corrosion casting technique, based on the injection of a polymer to capture the 3D structure of the vasculature, was performed on 3 male and 3 female mice of each selected genotype at the age of 9 months as previously described [23]. Briefly, 2 to 3 ml Batson's solution (Polysciences, Batson's #17 corrosion kit) was retrogradely injected in the abdominal aorta through a 26G catheter. After completion of the polymerization reaction, mouse bodies were macerated overnight in a 25% KOH solution. The resulting casts were cleaned, evaluated and photographed using a dissecting microscope, equipped with a 5-megapixel camera (Leica).

Histology

From 3 male and 3 female mice of each selected genotype, skin and aorta (9-month-old animals) and ocular tissue (3-week-old mice) were collected for histological analysis. Samples were formalin-fixed and paraffin-embedded, after which 5 μm-thick paraffin sections were made. Sections were subjected to the standard Verhoeff-Van Gieson (VVG) and picrosirius red (PR) histological staining procedures, prior to visualization on a Zeiss Axio Observer Z1 microscope.

Transmission Electron Microscopy

Sample fixation was carried out in a 4% formaldehyde (EM grade), 2.5% glutaraldehyde (EM grade), 0.1M cacodylate buffer solution. Samples were placed in a vacuum oven for 30 min and left rotating for 3 hours at room temperature. This solution was later replaced with fresh fixative and samples were left rotating over night at 4 °C. After washing, samples were post-fixed in 1% OsO_4 with $K_3Fe(CN)6$ in 0.1 M NaCacodylate buffer, pH 7.2. After washing in double-distilled H_2O, samples were subsequently dehydrated through a graded ethanol series, including bulk staining with 2% uranyl acetate at the 50% ethanol step, followed by embedding in Spurr's resin. To select the area of interest on the block and in order to have an overview of the phenotype, semi-thin sections were first cut at 0.5 μm and stained with toluidine blue. Ultrathin sections of a gold interference color were cut using an ultramicrotome (Leica EM UC6, Wetzlar, Germany), followed by post-staining in a Leica EM AC20 for 40 min in uranyl acetate at 20 °C and for 10 min in lead stain at 20 °C. Sections were collected on formvar-coated copper slot grids. Grids were viewed with a JEM 1400plus transmission electron microscope (JEOL, Tokyo, Japan) operating

at 80 kV. Collagen diameter measurements were carried out with Fiji [52]. Error bars shown represent 95% confidence intervals. Data were analyzed with a two-tailed t-test. Error bars shown represent 95% confidence intervals.

Vascular smooth muscle cell isolation and cell culture

Mice (at an age of 25 days) were euthanized (CO_2) and autopsied according to standard protocols. Primary VSMCs from the thoracic aorta were isolated according to the collagenase digestion method of Proudfoot and Shanahan [53]. Each cell line was derived from a single aorta. Primary VSMCs were cultured on gelatinized dishes in SmBM medium supplemented with the SmGM-2 kit (Lonza, cat. nr. CC-3182). Unless otherwise specified, two cell lines per genotype were assessed.

Immunofluorescence of extracellular matrix

ECM protein production by VSMCs was determined by immunofluorescence. VSMCs were seeded at 50,000 cells/well in 8-well removable chamber slides and grown for 7 days to allow ECM deposition. VSMCs were fixed with an ice-cold 70:30 methanol:acetone mixture for 5 minutes and washed with PBS. Coverslips were blocked for 1 hour with PBS supplemented with 10% normal goat serum (Agilent, cat. nr. X0907). Primary antibodies (Supplementary Table 3) were incubated overnight at 4°C in PBS. Coverslips were washed three times with PBS for 5 minutes each prior to incubation with the secondary antibody for 1.5 hours at room temperature (Molecular Probes, anti-rabbit Alexa Fluor 594, 1:1,000). Coverslips were washed and mounted to glass slides with Vectashield supplemented with DAPI (Vector laboratories, cat. nr. H-1200) and sealed with nail polish. Images were recorded on a wide field epifluorescent microscope (Axio Imager D2, Zeiss). Quantification of the immunofluorescent signal was performed by calculating the corrected total cell fluorescence (CTCF) of the ECM components corrected for the number of nuclei. The CTCF was determined by setting a color threshold to select the fibers in the image with Fiji image analyzing software [52] and determining the integrated density of this area (intensity of the fluorescence). This measurement was corrected for the background fluorescence and the total area of the fibers and results in the CTCF. The CTCF was then divided by the number of nuclei that were present in the measured image. Data were corrected for outliers with the Grubbs' test for outliers [54]. Statistical analysis was performed with a non-parametric Mann-Whitney test. Significance was tested 2-tailed. Results are expressed as mean $\pm$ SD.

TGFβ stimulation

VSMCs were seeded in 6-well plates to reach confluence and were allowed to attach for 24 hours. The following day, medium was changed to SmGM-2 medium without fetal calf serum and VSMCs were serum deprived for 24 hours prior to TGFβ stimulation. Protein samples were collected after 0 minutes, 15 minutes, 30 minutes, 1 hour and 4 hours of stimulation with TGFβ1

(Biovision, cat. nr. 4342-5). Cells were scraped in PBS supplemented with protease inhibitor cocktail (Roche applied science, cat. nr. 11836145001, 1:100) and phosphatase inhibitor cocktail (Sigma, cat. nr. P0044, 1:100) and lysed in an equal volume of 2x Laemmli buffer (4% SDS, 20% glycerol, 120mM Tris pH 6,8) supplemented with protease inhibitor cocktail and phosphatase inhibitor. Lysates were first cleared from large DNA by passing through a 25G needle and then heated to 65°C for 10 minutes. Protein concentrations were measured with the Lowry protein assay as previously described [55]. Equal amounts of protein were separated for size by SDS-PAGE and then transferred to a PVDF membrane (1 hour, 100V, Immobilon) and blocked with 3% milk in PBS supplemented with 0.1% Tween-20 (1 hour, room temperature). The primary antibody was incubated for 45 minutes at room temperature or overnight at 4°C for phosphorylated Smad2 (see Supplementary Table 3 for primary antibodies). The membranes were washed 5 times with 0.1% Tween-20 in PBS and then incubated with horseradish peroxidase-conjugated secondary antibodies (Jackson ImmunoResearch, 1:2,000) for 1 hour at room temperature. Bound secondary antibodies were detected with an Amersham Imager 600 (GE Healthcare Life Sciences) using chemiluminescence. Band intensity was quantified using Fiji image analyzing software [52]. Data were corrected for outliers with the Grubbs' test for outliers [54]. Statistical analysis was performed with a non-parametric Mann-Whitney test. Significance was tested 2-tailed. Results are expressed as mean ± SD.

Mitochondrial respiration

Oxygen consumption rate was measured using an XF-24 Extracellular Flux Analyzer (Seahorse Bioscience). Respiration was measured in XF assay media (non-buffered DMEM), in basal conditions and in response to 1 μM oligomycin (ATP synthase inhibitor), 1 μM fluoro-carbonyl cyanide phenylhydrazone (FCCP, uncoupler), 1 μM antimycin A (complex III inhibitor). Smooth muscle cells were seeded at a density of 30,000 cells/well and analyzed after 24 hours. Optimal cell densities were determined experimentally to ensure a proportional response to FCCP with cell number. For these experiments 6-8 wells were measured per time point [56, 57]. Data were corrected for outliers with the Grubbs' test for outliers [54]. Statistical analysis was performed with a non-parametric Mann-Whitney test. Significance was tested 2-tailed. Results are expressed as mean ± SD.

Acknowledgements

This work was supported by Ghent University [Methusalem BOFMET2015000401 to A.D.P.]; Research Foundation – Flanders (FWO) [FWOOPR2013025301]; and the 'Lijf and Leven' grant [2014, "GAMMA" (Genexpressie analyse ter detectie van de moleculaire mechanismen van aneurysmavorming)]. B.C. is a Senior Clinical Investigator of the Research Foundation – Flanders (FWO). M.R. was supported by the Research Foundation - Flanders (FWO) as a postdoctoral fellow. Ghent University Hospital is a member of the European Reference Networks for vascular and skin disorders (VASCERN and ERN-Skin).

Conflicts of interest statement

None declared.

REFERENCES

1. Beyens, A., et al., *Arterial tortuosity syndrome: 40 new families and literature review.* Genet. Med., 2018. **20**(10): p. 1236-1245.
2. Callewaert, B.L., et al., *Arterial tortuosity syndrome: clinical and molecular findings in 12 newly identified families.* Hum. Mutat., 2008. **29**(1): p. 150-8.
3. Coucke, P.J., et al., *Mutations in the facilitative glucose transporter GLUT10 alter angiogenesis and cause arterial tortuosity syndrome.* Nat. Genet., 2006. **38**(4): p. 452-7.
4. Hasler, S., J. Sturmer, and C. Kaufmann, *Keratoglobus and deep stromal corneal opacification in a case of arterial tortuosity syndrome.* Klin. Monatsbl. Augenh. , 2011. **228**(4): p. 345-6.
5. Wessels, M.W., et al., *Three new families with arterial tortuosity syndrome.* Am. J. Med. Genet., 2004. **131**(2): p. 134-43.
6. Castori, M., et al., *Adult presentation of arterial tortuosity syndrome in a 51-year-old woman with a novel homozygous c.1411+1G>A mutation in the SLC2A10 gene.* Am. J. Med. Genet., 2012. **158A**(5): p. 1164-9.
7. Ades, L.C., et al., *Clinicopathologic findings in congenital aneurysms of the great vessels.* Am. J. Med. Genet., 1996. **66**(3): p. 289-99.
8. Beuren, A.J., et al., *Dysplasia of the systemic and pulmonary arterial system with tortuosity and lengthening of the arteries. A new entity, diagnosed during life, and leading to coronary death in early childhood.* Circulation, 1969. **39**(1): p. 109-15.
9. Ertugrul, A., *Diffuse tortuosity and lengthening of the arteries.* Circulation, 1967. **36**(3): p. 400-7.
10. Pletcher, B.A., et al., *Four sibs with arterial tortuosity: description and review of the literature.* Am. J. Med. Genet., 1996. **66**(2): p. 121-8.
11. Gardella, R., et al., *Exclusion of candidate genes in a family with arterial tortuosity syndrome.* Am. J. Med. Genet., 2004. **126A**(3): p. 221-8.
12. Zoppi, N., et al., *GLUT10 deficiency leads to oxidative stress and non-canonical alphavbeta3 integrin-mediated TGFbeta signalling associated with extracellular matrix disarray in arterial tortuosity syndrome skin fibroblasts.* Hum. Mol. Genet., 2015. **24**(23): p. 6769-87.
13. Mueckler, M. and B. Thorens, *The SLC2 (GLUT) family of membrane transporters.* Mol. Aspects Med., 2013. **34**(2-3): p. 121-38.
14. Lee, Y.C., et al., *Mitochondrial GLUT10 facilitates dehydroascorbic acid import and protects cells against oxidative stress: mechanistic insight into arterial tortuosity syndrome.* Hum. Mol. Genet., 2010. **19**(19): p. 3721-33.
15. Gamberucci, A., et al., *GLUT10-Lacking in Arterial Tortuosity Syndrome-Is Localized to the Endoplasmic Reticulum of Human Fibroblasts.* Int. J. Mol., 2017. **18**(8).
16. Segade, F., *Glucose transporter 10 and arterial tortuosity syndrome: the vitamin C connection.* FEBS Lett., 2010. **584**(14): p. 2990-4.
17. Nemeth, C.E., et al., *Glucose transporter type 10-lacking in arterial tortuosity syndrome-facilitates dehydroascorbic acid transport.* FEBS Lett., 2016. **590**(11): p. 1630-40.

18. Loeys, B.L., et al., *Aneurysm syndromes caused by mutations in the TGF-beta receptor.* N. Engl. J. Med., 2006. **355**(8): p. 788-98.
19. Judge, D.P. and H.C. Dietz, *Marfan's syndrome.* Lancet, 2005. **366**(9501): p. 1965-76.
20. Neptune, E.R., et al., *Dysregulation of TGF-beta activation contributes to pathogenesis in Marfan syndrome.* Nat. Genet., 2003. **33**(3): p. 407-11.
21. Willaert, A., et al., *GLUT10 is required for the development of the cardiovascular system and the notochord and connects mitochondrial function to TGFbeta signaling.* Hum. Mol. Genet., 2012. **21**(6): p. 1248-59.
22. Cheng, C.H., et al., *Mutations in the SLC2A10 gene cause arterial abnormalities in mice.* Cardiovasc. Res., 2009. **81**(2): p. 381-8.
23. Callewaert, B.L., et al., *Absence of arterial phenotype in mice with homozygous slc2A10 missense substitutions.* Genesis, 2008. **46**(8): p. 385-9.
24. Syu, Y.W., et al., *GLUT10 maintains the integrity of major arteries through regulation of redox homeostasis and mitochondrial function.* Hum. Mol. Genet., 2018. **27**(2): p. 307-321.
25. van der Pluijm, I., et al., *Decreased mitochondrial respiration in aneurysmal aortas of Fibulin-4 mutant mice is linked to PGC1A regulation.* Cardiovasc. Res., 2018. **114**(13): p. 1776-1793.
26. Linster, C.L. and E. Van Schaftingen, *Vitamin C. Biosynthesis, recycling and degradation in mammals.* FEBS J., 2007. **274**(1): p. 1-22.
27. Drouin, G., J.R. Godin, and B. Page, *The genetics of vitamin C loss in vertebrates.* Curr. Genom., 2011. **12**(5): p. 371-8.
28. van der Pluijm, I., et al., *Defective Connective Tissue Remodeling in Smad3 Mice Leads to Accelerated Aneurysmal Growth Through Disturbed Downstream TGF-beta Signaling.* EBioMedicine, 2016. **12**: p. 280-294.
29. Smith, L.B., et al., *Haploinsufficiency of the murine Col3a1 locus causes aortic dissection: a novel model of the vascular type of Ehlers-Danlos syndrome.* Cardiovasc. Res., 2011. **90**(1): p. 182-90.
30. Cooper, T.K., et al., *The haploinsufficient Col3a1 mouse as a model for vascular Ehlers-Danlos syndrome.* Vet. Pathol., 2010. **47**(6): p. 1028-39.
31. D'Hondt, S., et al., *Type III collagen affects dermal and vascular collagen fibrillogenesis and tissue integrity in a mutant Col3a1 transgenic mouse model.* Matrix Biol., 2018. **70**: p. 72-83.
32. Kubow, K.E., et al., *Mechanical forces regulate the interactions of fibronectin and collagen I in extracellular matrix.* Nat. Commun., 2015. **6**: p. 8026.
33. Dzamba, B.J., et al., *Fibronectin binding site in type I collagen regulates fibronectin fibril formation.* J. Cell Biol., 1993. **121**(5): p. 1165-72.
34. Dabovic, B., et al., *Function of latent TGFbeta binding protein 4 and fibulin 5 in elastogenesis and lung development.* J. Cell. Physiol., 2015. **230**(1): p. 226-36.
35. Dietz, H.C., et al., *Marfan syndrome caused by a recurrent de novo missense mutation in the fibrillin gene.* Nature, 1991. **352**(6333): p. 337-9.
36. Hucthagowder, V., et al., *Fibulin-4: a novel gene for an autosomal recessive cutis laxa syndrome.* Am. J. Hum. Genet., 2006. **78**(6): p. 1075-80.

37. Dietz, H., *Marfan Syndrome*, in *GeneReviews((R))*, M.P. Adam, et al., Editors. 1993: Seattle (WA).
38. Loeys, B.L. and H.C. Dietz, *Loeys-Dietz Syndrome*, in *GeneReviews((R))*, M.P. Adam, et al., Editors. 1993: Seattle (WA).
39. Montagutelli, X., *Effect of the genetic background on the phenotype of mouse mutations.* J. Am. Soc. Nephrol., 2000. **11 Suppl 16**: p. S101-5.
40. Barbaric, I., G. Miller, and T.N. Dear, *Appearances can be deceiving: phenotypes of knockout mice.* Brief. Funct. Genomic. Proteomic., 2007. **6**(2): p. 91-103.
41. Whitacre, J.M., *Biological robustness: paradigms, mechanisms, and systems principles.* Front. Genet., 2012. **3**: p. 67.
42. Nedvetzki, S., et al., *RHAMM, a receptor for hyaluronan-mediated motility, compensates for CD44 in inflamed CD44-knockout mice: a different interpretation of redundancy.* Proc. Natl. Acad. Sci. U. S. A., 2004. **101**(52): p. 18081-6.
43. von Koch, C.S., et al., *Generation of APLP2 KO mice and early postnatal lethality in APLP2/APP double KO mice.* Neurobiol. Aging, 1997. **18**(6): p. 661-9.
44. El-Brolosy, M.A., et al., *Genetic compensation triggered by mutant mRNA degradation.* Nature, 2019. **568**(7751): p. 193-197.
45. El-Brolosy, M.A. and D.Y.R. Stainier, *Genetic compensation: A phenomenon in search of mechanisms.* PLoS Genet., 2017. **13**(7): p. e1006780.
46. Sztal, T.E., et al., *Genetic compensation triggered by actin mutation prevents the muscle damage caused by loss of actin protein.* PLoS Genet., 2018. **14**(2): p. e1007212.
47. Rossi, A., et al., *Genetic compensation induced by deleterious mutations but not gene knockdowns.* Nature, 2015. **524**(7564): p. 230-3.
48. Scheepers, A., H.G. Joost, and A. Schurmann, *The glucose transporter families SGLT and GLUT: molecular basis of normal and aberrant function.* J. Parenter. Enter. Nutr., 2004. **28**(5): p. 364-71.
49. Maeda, N., et al., *Aortic wall damage in mice unable to synthesize ascorbic acid.* Proc. Natl. Acad. Sci. U. S. A., 2000. **97**(2): p. 841-6.
50. Renard, M., et al., *Expressed repetitive elements are broadly applicable reference targets for normalization of reverse transcription-qPCR data in mice.* Sci. Rep., 2018. **8**(1): p. 7642.
51. Renard, M., et al., *Absence of cardiovascular manifestations in a haploinsufficient Tgfbr1 mouse model.* PloS one, 2014. **9**(2): p. e89749.
52. Schindelin, J., et al., *Fiji: an open-source platform for biological-image analysis.* Nat. Methods, 2012. **9**(7): p. 676-82.
53. Proudfoot, D. and C. Shanahan, *Human vascular smooth muscle cell culture.* Methods Mol. Biol., 2012. **806**: p. 251-63.
54. Barnett, V., and Lewis T., *Outliers in Statistical Data*. 3rd ed. 1994: J. Wiley & Sons.
55. Lowry, O.H., et al., *Protein measurement with the Folin phenol reagent.* J. Biol. Chem., 1951. **193**(1): p. 265-75.
56. Plitzko, B., E.N. Kaweesa, and S. Loesgen, *The natural product mensacarcin induces mitochondrial toxicity and apoptosis in melanoma cells.* J Biol Chem, 2017. **292**(51): p. 21102-21116.

57. Plitzko, B. and S. Loesgen, *Measurement of Oxygen Consumption Rate (OCR) and Extracellular Acidification Rate (ECAR) in Culture Cells for Assessment of the Energy Metabolism*. Bio-protocol, 2018. **8**(10): p. e2850.

SUPPLEMENTARY DATA

Supplementary figures

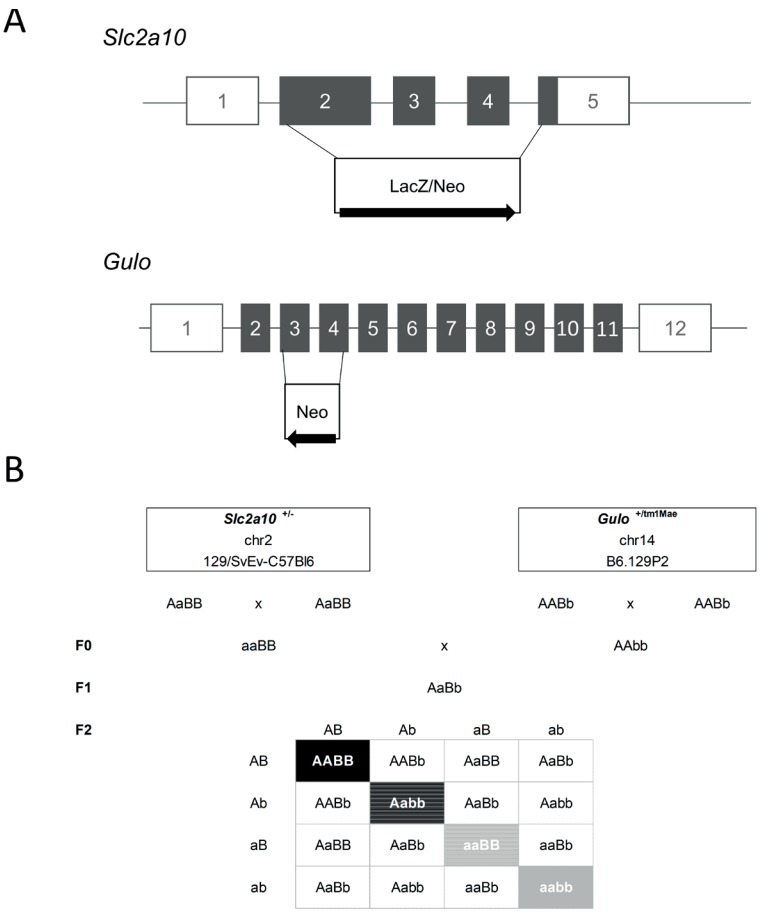

Supplementary figure 1. Genetics of the novel ATS mouse model, deficient for both GLUT10 and GULO.

A) Mutation image of the mouse models employed in this study. The *Slc2a10* constitutive knock-out model harbors a LacZ/Neo selection cassette replacing a sequence ranging from exon 2 to beginning of exon 5, oriented in the same transcriptional orientation than the *Slc2a10* gene (indicated by a black arrow). The *Gulo* constitutive knock-out model harbors a Neo selection cassette replacing a sequence comprising exon 3 and 4, oriented in the opposite transcriptional orientation than the *Gulo* gene (indicated by a black arrow). **B)** Breeding scheme executed in this study. Mice, mutant for either *Slc2a10* (F0: aaBB) or *Gulo* (F0: AAbb) were crossed with each other to obtain mice heterozygous for both genes (F1). Crossing in these mice can result in pups with 9 different genotypes. Four genotypes were selected for further study: WT (*Gulo* $^{+/+}$;*Slc2a10* $^{+/+}$ - black), *Gulo* KO (*Gulo* $^{tm1mae/\ tm1mae}$;*Slc2a10* $^{+/+}$ - black dashed), *Slc2a10* KO (*Gulo* $^{+/+}$;*Slc2a10* $^{-/-}$ - grey dashed) and DKO (*Gulo* $^{tm1mae/\ tm1mae}$;*Slc2a10* $^{-/-}$ - grey).

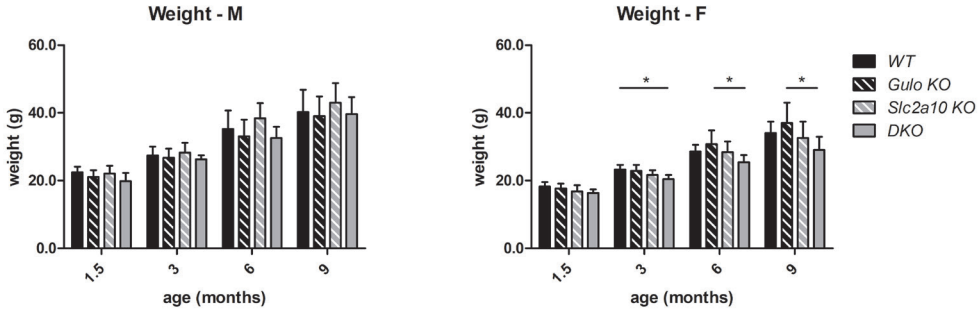

Supplementary Figure 2: Mouse body weight.

Values plotted correspond to the means of 10 biological replicates. Error bars shown represent 95% confidence intervals. Data were analyzed using one-way ANOVA, followed by a Tukey post-hoc test. *: $p \leq 0.05$, M: male, F: female

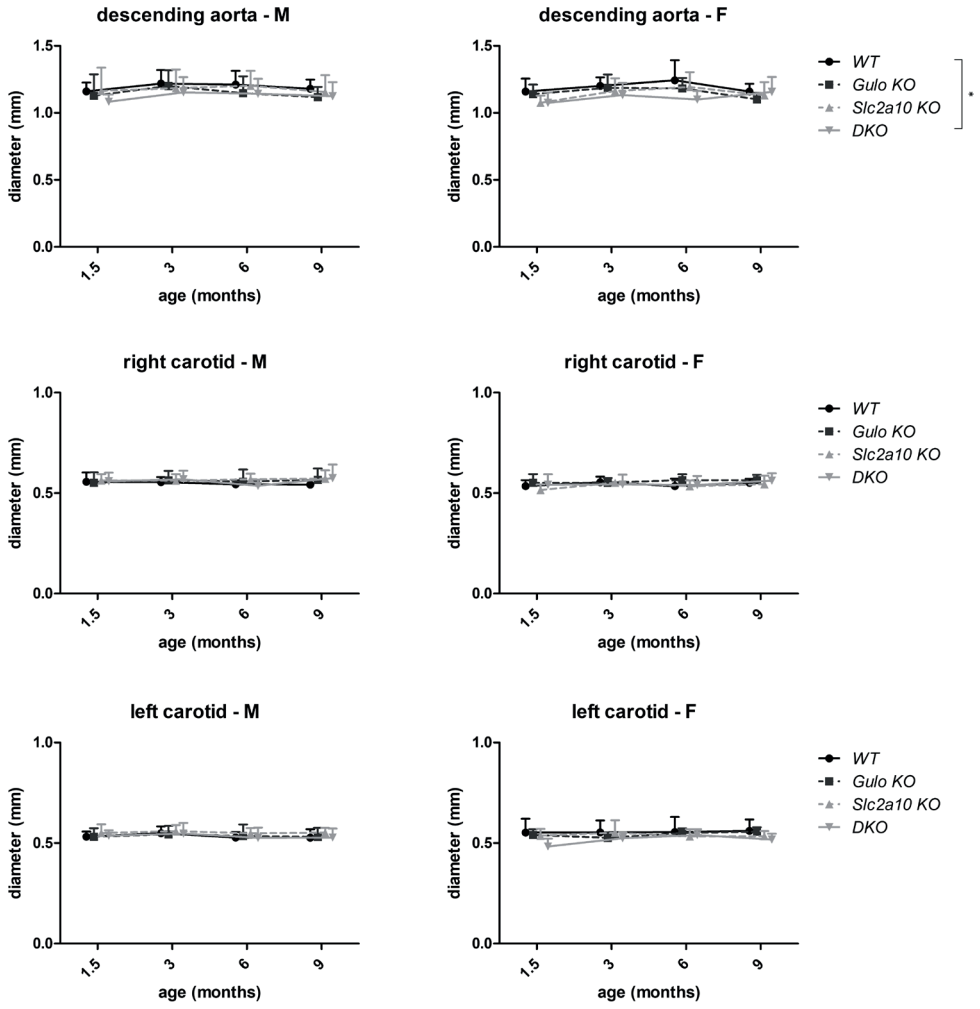

Supplementary Figure 3. Serial ultrasound measurements obtained at 6 weeks, 3, 6 and 9 months of age at the descending aorta and carotids.

Left and right column images represent data obtained in male and female animals respectively. Shown p-values were obtained using a linear mixed model with covariance pattern modeling, without interactions. As a result, p-values should be interpreted when making the comparison for a given age and sex. Error bars shown represent 95% confidence intervals. *: $p \leq 0.05$, M: male, F: female

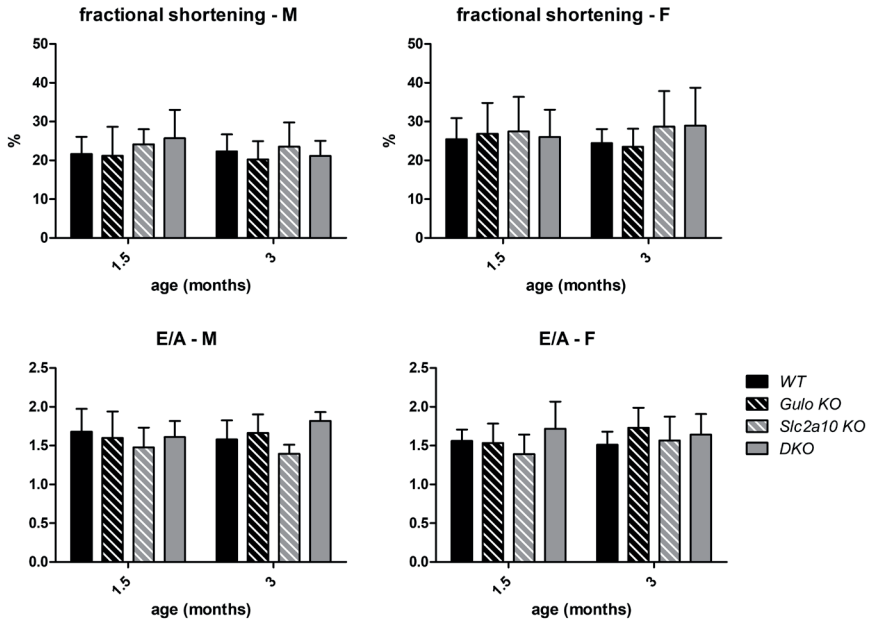

Supplementary Figure 4. Cardiac parameters indicative for left ventricular function at 6 weeks and 3 months of age.

Error bars shown represent 95% confidence intervals. FS: fractional shortening. E/A: ratio of the early (E) to late (A) ventricular filling velocities. M: male, F: female

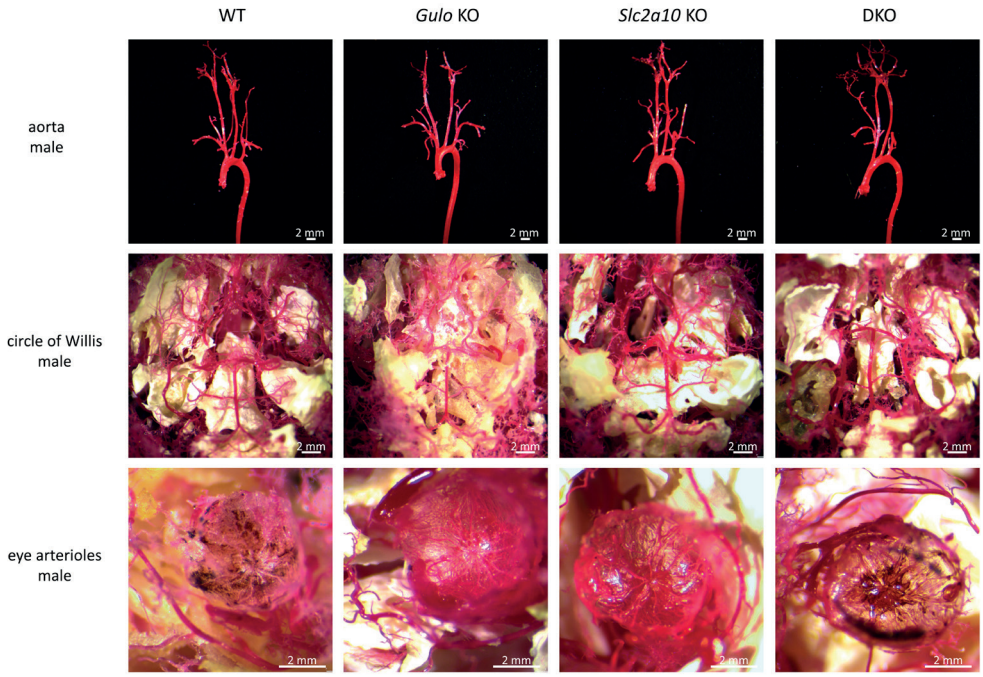

Supplementary Figure 5. Vascular corrosion casts of WT, Gulo KO, Slc2a10 KO and DKO male mice.

Representative images of the aortic arch and its side branches, the circle of Willis and the eye arterioles are shown.

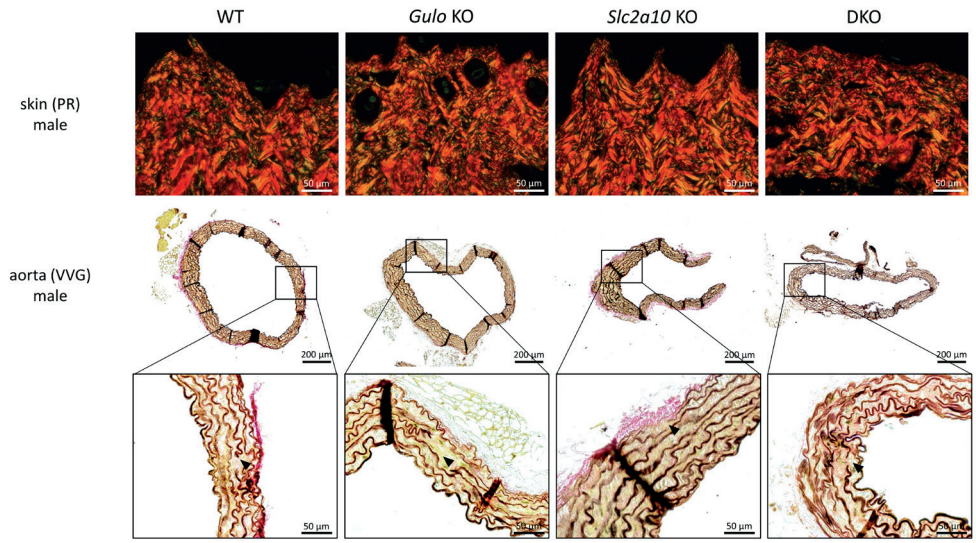

Supplementary Figure 6. Histological analysis of WT, Gulo KO, Slc2a10 KO and DKO male mice.

Picrosirius red (PR) polarization staining (upper row) for collagen does not reveal abnormal collagen deposition in the skin of *Gulo* $^{tm1mae/\ tm1mae}$;*Slc2a10* $^{-/-}$ mice. Verhoeff-Van Gieson (VVG) elastic fiber staining (middle row) shows mild elastic fiber anomalies in the aortic wall of all studied mice (black arrows).

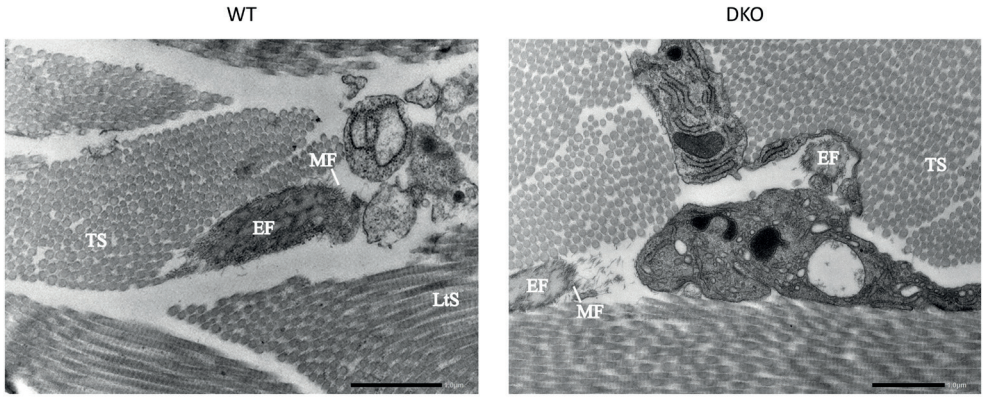

Supplementary Figure 7. Transmission electron microscopy of elastic fibers in a skin biopsy.

DKO mice do not show an altered elastic fiber assembly, compared to WT mice. TS: collagen transverse section, LtS: collagen longitudinal section, EF: elastic core, MF: microfibrils. Scale bar: 1.0 μm.

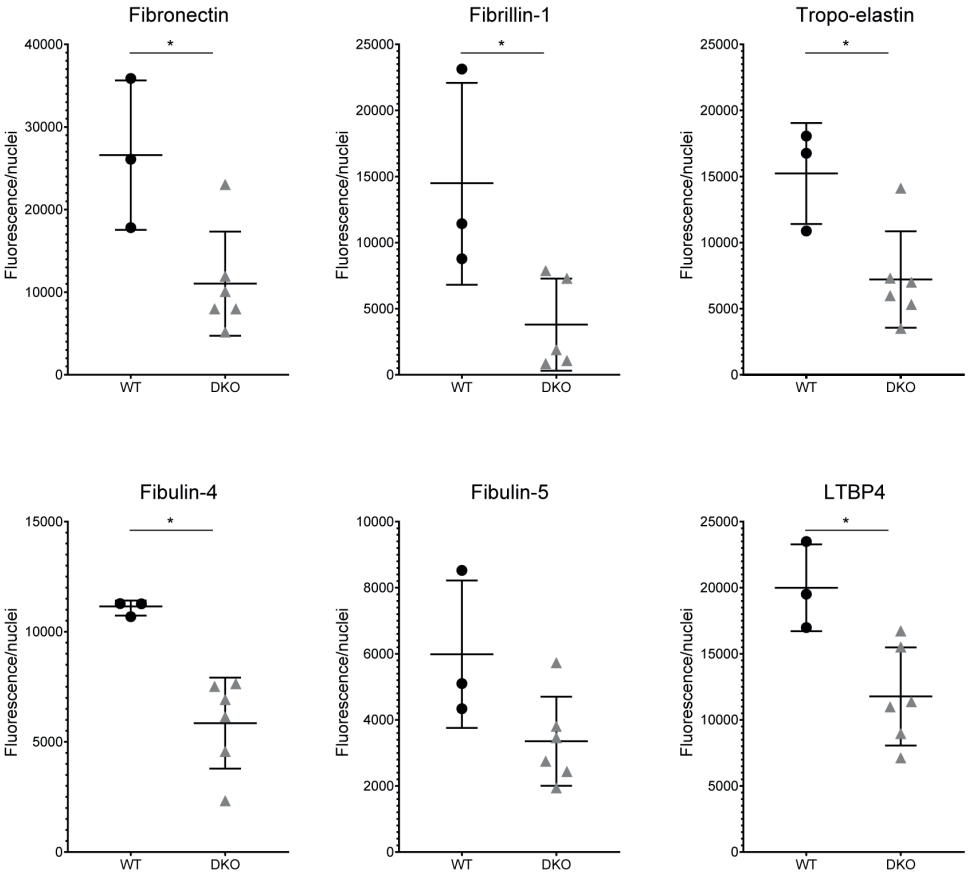

Supplementary Figure 8. Quantification of total cell fluorescence of the ECM components corrected for the number of nuclei for the graphs, displayed in Figure 6.

Results are expressed as mean ± SD. *: $p \leq 0.05$.

Supplementary tables

Supplementary Table 1: PCR genotyping primers and products

Slc2a10			
Wild type-specific product		**Mutation-specific product**	
Forward (5'-3')	CCTTGTCGGGGGCTTCCTCATTG	Forward (5'-3')	GCAGCGCATCGCCTTCTATC
Reverse (5'-3')	CACCAGCCCCAGCCCCACTACAG	Reverse (5'-3')	CCTCAGAGTCTCACACTCAA
Wild-type Band	532 bp	Wild-type Band	none
Mutant band	none	Mutant band	325 bp
Gulo			
PCR with 3 primers			
Primer 1 (5'-3')	CGCGCCTTAATTAAGGATCC		
Primer 2 (5'-3')	GTCGTGACAGAATGTCTTGC		
Primer 3 (5'-3')	CCCAGTGACTAAGGATAAGC		
Wild-type Band	343 bp		
Mutant band	230 bp		

Supplementary Table 2: RT-qPCR primers

Slc2a10	
Forward (5'-3')	TTGGCCTGGCTTTCATCTAC
Reverse (5'-3')	GCTTGTCTGAAACTGCTGCTC
ERE 1 – Rltr10b2	
Forward (5'-3')	CCAATCCGGGTGTGAGACA
Reverse (5'-3')	CTGACTCGCCAGCAAGAAC
ERE 2 – Rltr2aiap	
Forward (5'-3')	CATGTGCCAAGGGTAGTTCTC
Reverse (5'-3')	GCAAGAGAGAGAATGGCGAAAC

Supplementary Table 3: Antibodies

Primary antibody	Predicted kDa	Dilution	Manufacturer	Cat. nr.
Rabbit α-Fibronectin IgG	-	1:80	Millipore	AB2033
Rabbit α-mouse Fibrillin-1	-	1:1,000	Generated in Reinhardt Lab	-
Rabbit α-mouse Tropo-elastin	-	1:500	Generated in Reinhardt Lab	-
Rabbit α-mouse Fibulin-4	-	1:500	Generated in Reinhardt Lab	-
Rabbit α-mouse Fibulin-5	-	1:500	Generated in Reinhardt Lab	-
Rabbit α-mouse LTBP-4	-	1:500	Generated in Reinhardt Lab	-
Rabbit α-SMAD2 IgG	60	1:1000	Cell signaling	5339S
Rabbit α-pSMAD2 IgG	55-60	1:400	Merck Millipore	04-953
Mouse α-β catenin IgG1	92	1:2000	BD Bioscience	610153

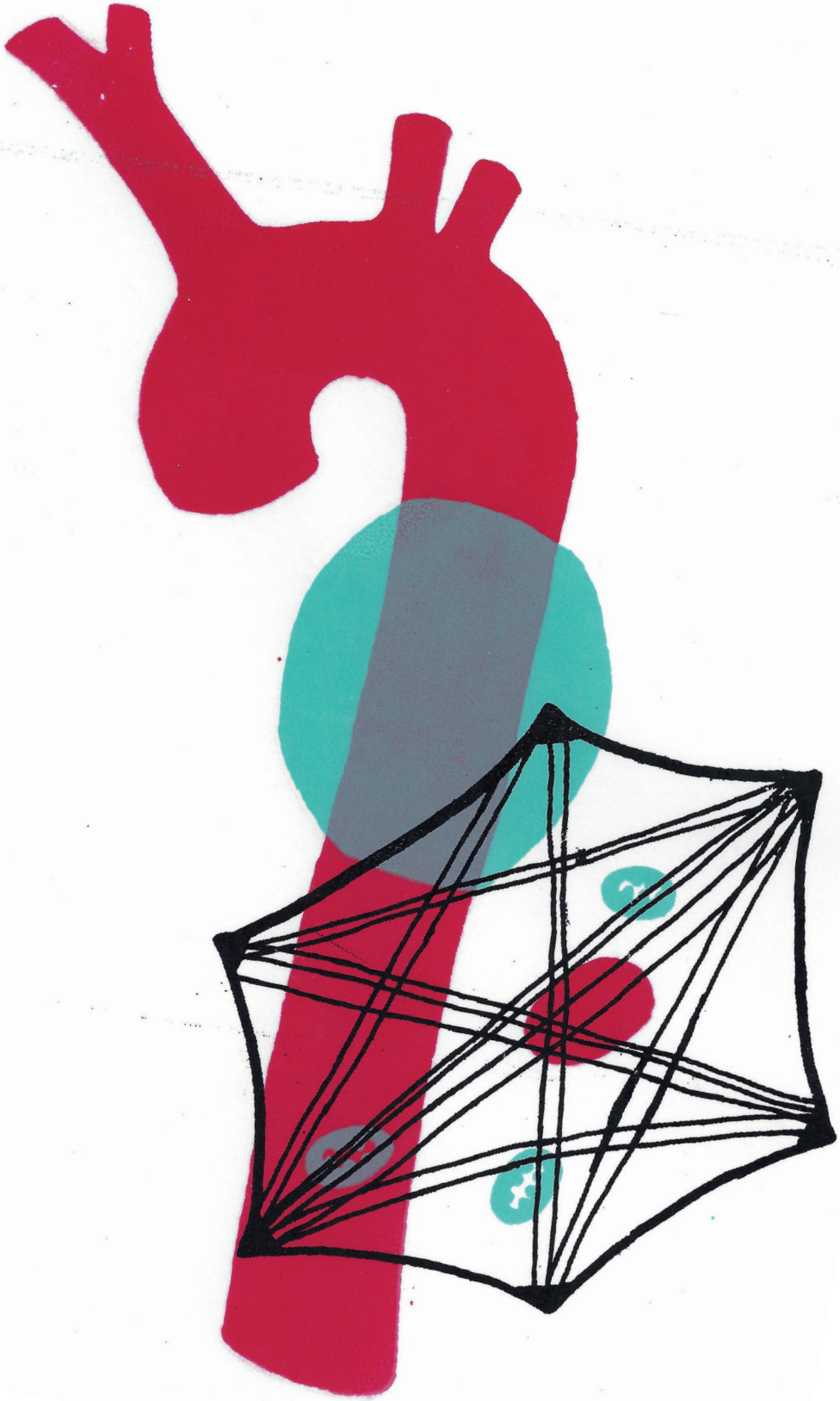

CHAPTER 4

FIBULIN-4 DEFICIENCY DIFFERENTIALLY AFFECTS CYTOSKELETON STRUCTURE AND DYNAMICS AS WELL AS TGFβ SIGNALING

Joyce Burger[1,2], Nicole van Vliet[1], Paula van Heijningen[1], Heena Kumra[3], Gert-Jan Kremers[5], Maria Alves[2], Gert van Cappellen[5], Hiromi Yanagisawa[6], Dieter P. Reinhardt[3,4], Roland Kanaar[1,7], Ingrid van der Pluijm[1,8], Jeroen Essers[1,8,9,#]

[1]Department of Molecular Genetics, Erasmus University Medical Center, Rotterdam, The Netherlands, [2]Department of Clinical Genetics, Erasmus University Medical Center, Rotterdam, The Netherlands, [3]Faculty of Medicine, Department of Anatomy and Cell Biology and [4]Faculty of Dentistry, McGill University, Montreal, Quebec, Canada, [5]Erasmus Optical Imaging Centre, Department of Pathology, Erasmus University Medical Center, Rotterdam, The Netherlands, [6]Life Science Center for Survival Dynamics, Tsukuba Advanced Research Alliance (TARA), University of Tsukuba, Tsukuba, Japan, [7]Oncode Institute, Erasmus University Medical Center, Rotterdam, The Netherlands, [8]Department of Vascular Surgery, Erasmus University Medical Center, Rotterdam, The Netherlands, [9]Department of Radiation Oncology, Erasmus University Medical Center, Rotterdam, The Netherlands

Cell Signal. 2019 Jun;58:65-78.

ABSTRACT

Fibulin-4 is an extracellular matrix (ECM) protein essential for elastogenesis and mutations in this protein lead to aneurysm formation. In this study, we isolated vascular smooth muscle cells (VSMCs) from mice with reduced Fibulin-4 protein expression (Fibulin-$4^{R/R}$) and from mice with a smooth muscle cell specific deletion of the Fibulin-4 gene (Fibulin-$4^{f/-}$/SM22Cre^{+}). We subsequently analyzed and compared the molecular consequences of reduced Fibulin-4 expression versus total ablation of Fibulin-4 expression with regard to effects on the SMC specific contractile machinery, cellular migration and TGFβ signaling.

Analysis of the cytoskeleton showed that while Fibulin-$4^{f/-}$/SM22Cre^{+} VSMCs lack smooth muscle actin (SMA) fibers, Fibulin-$4^{R/R}$ VSMCs were able to form SMA fibers. Furthermore, Fibulin-$4^{f/-}$/SM22Cre^{+} VSMCs showed a decreased pCofilin to Cofilin ratio, suggesting increased actin depolymerization, while Fibulin-$4^{R/R}$ VSMCs did not display this decrease. Yet, both Fibulin-4 mutant VSMCs showed decreased migration. We found increased activation of TGFβ signaling in Fibulin-$4^{R/R}$ VSMCs. However, TGFβ signaling was not increased in Fibulin-$4^{f/-}$/SM22Cre^{+} VSMCs.

From these results we conclude that both reduction and absence of Fibulin-4 leads to structural and functional impairment of the SMA cytoskeleton. However, while reduced levels of Fibulin-4 result in increased TGFβ activation, complete absence of Fibulin-4 does not result in increased TGFβ activation. Since both mouse models show thoracic aortic aneurysm formation, we conclude that not only hampered TGFβ signaling, but also SMA cytoskeleton dynamics play an important role in aortic aneurysmal disease.

INTRODUCTION

Aortic aneurysms are dilations of the aorta caused by a general weakening of the aortic wall. Patients affected by such dilations have a high risk of mortality upon rupture. Approximately 1-2% of all deaths in the western world are caused by aortic aneurysms and dissections [1]. The aortic wall consists of three layers, the intima, the media and the adventitia. The medial layer of the aortic wall contains the elastic laminae interspaced by vascular smooth muscle cells (VSMCs) and is important for the elasticity and contractility of the ascending aorta. During aneurysm formation the medial layer of the aorta is characterized by elastin layer fragmentation, loss of VSMCs and deposition of excess of extracellular matrix (ECM) material. These processes weaken the aortic wall and increase the risk of rupture [1, 2].

Multiple genes have been identified to cause aneurysm formation when mutated. Mutations in the extracellular matrix protein fibrillin-1 (FBN1) lead to Marfan syndrome [3]. Mutations in proteins implicated in TGFβ signaling, such as TGFβ receptor 1 and 2 (TGFβR1 and TGFβR2) as well as SMAD3, lead to Loeys-Dietz syndrome characterized by aneurysm formation [4-8]. In addition, contractile or cytoskeletal protein mutations, such as α-smooth muscle actin (ACTA2) and myosin heavy chain 11 (MYH11) have been identified as causal genes for aneurysm formation [9-12]. Although these proteins are localized in different topological compartments, they most likely cooperate at a mechanistic molecular level and collectively play a role in aneurysm formation. We hypothesize that reduced presence or complete absence of the extracellular matrix protein Fibulin-4 could influence cytoskeleton structure and dynamics since cell-ECM contact is mediated by transmembrane cell adhesion receptors, such as integrins, that interact with extracellular matrix proteins as well as a number of cytoplasmic adaptor proteins that interact with the actin cytoskeleton or function in signal transduction.

Fibulin-4 is an ECM protein that is essential for elastogenesis and is responsible for the recruitment of lysyl oxidase [13]. Lysyl oxidase is required for proper crosslinking of the elastin precursor tropoelastin to form mature elastic laminae [14]. These elastic laminae are of importance for the elasticity of the aorta and for deposition of latent TGFβ complexes [15]. When Fibulin-4 is absent or unable to recruit lysyl oxidase, tropoelastin is not properly crosslinked. This leads to irregular elastic laminae that have a fragmented appearance [16]. *EFEMP2* (*Fibulin-4*) mutations in patients lead to cutis laxa, an autosomal recessive disease that is characterized by non-elastic and loose skin, aneurysms and tortuosity of the large arteries [17-19]. Cutis laxa patients have either reduced Fibulin-4 protein levels in tissues, or reduced binding of Fibulin-4 to its targets. Furthermore, increased TGFβ signaling is detected in these patients [17, 20].

Different mouse models have been generated to investigate the role of Fibulin-4 in aneurysm formation. While complete absence of Fibulin-4 is perinatal lethal, hypomorphic mice with 4-fold

reduced expression levels (Fibulin-$4^{R/R}$, in which 'R' indicates the reduced expression allele) are viable [21, 22]. Like cutis laxa patients, Fibulin-$4^{R/R}$ mice show aortic aneurysm formation, elastic laminae fragmentation and increased TGFβ signaling [22, 23]. In addition, VSMC-specific knock-out mice for Fibulin-4 (Fibulin-$4^{f/-}$/SM22Cre^{+}) also develop aneurysms exclusively in the ascending aorta [24]. This mouse model has previously been used to determine the role of Fibulin-4 in aortic development, and is instrumental to determine the role of Fibulin-4 in aneurysm formation and VSMC function.

In this study we compared VSMCs isolated from aortas of Fibulin-$4^{R/R}$ and Fibulin-$4^{f/-}$/SM22Cre^{+} mice to analyze the consequences of diminished and completely ablated Fibulin-4 expression on cytoskeleton dynamics, cell movement and TGFβ signaling.

MATERIALS AND METHODS

Mice

Fibulin-$4^{R/R}$ and Fibulin-$4^{f/-}$/SM22Cre^{+} were generated and described previously [22, 24]. Animals were housed at the Animal Resource Centre (Erasmus University Medical Centre), which operates in compliance with the "Animal Welfare Act" of the Dutch government, using the "Guide for the Care and Use of Laboratory Animals" as its standard. As required by Dutch law, formal permission to generate and use genetically modified animals was obtained from the responsible local and national authorities. An independent Animal Ethics Committee consulted by Erasmus Medical Center (Stichting DEC Consult) approved these studies (permit number 140-12-05), in accordance with national and international guidelines. Animals were sacrificed by CO_2 inhalation, unless stated otherwise. This study conforms to the guidelines from Directive 2010/63/EU of the European Parliament on the protection of animals used for scientific purposes or the NIH guidelines.

VSMC isolation and cell culture

Mice (at an age of 100 days) were euthanized and autopsied according to standard protocols. Primary VSMCs from the thoracic aorta were isolated according to the collagenase digestion method of Proudfoot and Shanahan [25]. Each cell line was derived from a single aorta. Fibulin-$4^{+/+}$ and Fibulin-$4^{f/+}$/SM22Cre^{+} VSMCs were used as controls, in which Fibulin-$4^{f/+}$/SM22Cre^{+} VSMCs also served as controls for the potential toxic effects of Cre recombinase. Due to differences in the genetic background of the mice (Fibulin-$4^{+/+}$ and Fibulin-$4^{R/R}$: C57Bl/6, Fibulin-$4^{f/+}$/SM22Cre^{+} and Fibulin-$4^{f/-}$/SM22Cre^{+}: C57Bl/6 and SJL), Fibulin-$4^{f/+}$/SM22Cre^{+} VSMCs will be used as a primary control for Fibulin-$4^{f/-}$/SM22Cre^{+} VSMCs. Fibulin-$4^{f/+}$/SM22Cre^{+} VSMCs show a decrease in Fibulin-4 expression compared to Fibulin-$4^{+/+}$ VSMCs (Fig 1A), due to the deletion of one floxed allele by Cre recombinase. When experiments were performed

simultaneously, we depicted all four genotypes (Fibulin-$4^{+/+}$, Fibulin-$4^{R/R}$, Fibulin-$4^{f/+}$/SM22Cre^{+} and Fibulin-$4^{f/-}$/SM22Cre^{+}) together. In the figures, Fibulin-$4^{f/+}$/SM22Cre^{+} and Fibulin-$4^{f/-}$/SM22Cre^{+} VSMCs are referred to as Fibulin-$4^{f/+}$ and Fibulin-$4^{f/-}$, respectively. Unless otherwise specified two cell lines were used per genotype. Primary VSMCs were cultured on gelatinized dishes in Dulbecco's Modified Eagle's Medium (DMEM) (Lonza BioWhittaker) supplemented with 1% penicillin-streptomycin (PS) and 10% fetal calf serum (FCS).

RNA isolation and real-time PCR

RNA from VSMCs was isolated with the RNeasy mini kit (Qiagen). cDNA was made with iScript cDNA synthesis kit (Biorad) according to manufacturing protocol. Q-PCR was performed with 200 nM forward and reverse primers and iQ™ SYBR® Green Supermix (Biorad) on the CFX96 system (Biorad); denaturation at 95°C for 3min, 40 cycles denaturation at 95°C for 15 s, annealing/extension at 55°C for 30 s. *B2M* and *β-actin* were used as reference genes and gave similar expression. Data is shown with *B2M* as a reference gene. Relative gene expression levels were determined with the comparative Ct (also referred to as ΔΔCt) method according to the MIQE guidelines. See Table 1 for primers used. Number of replicates is specified in the figure legends.

Table 1. Primer sequences used for real-time PCR

Gene	Fw sequence	Rev sequence
Fibulin-4	GGGTTATTTGTGTCTGCCTCG	TGGTAGGAGCCAGGAAGGTT
B2M	CTCACACTGAATTCACCCCCA	GTCTCGATCCCAGTAGACGGT
β-actin	AGATCAAGATCATTGCTCCTCCTG	GGGTGTAAAACGCAGCTCAG

Western blotting

Western blot analysis was performed to determine protein amounts in extracts of Fibulin-$4^{f/-}$/SM22Cre^{+} and Fibulin-$4^{R/R}$ VSMCs compared to their controls. Cultured VSMCs were scraped in PBS supplemented with protease inhibitor cocktail (1:100, 11836145001, Roche applied science) and phosphatase inhibitor cocktail (1:100, P0044, Sigma) and lysed in an equal volume of 2x Laemmli buffer (4% SDS, 20% glycerol, 120mM Tris pH 6,8) supplemented with protease inhibitor cocktail and phosphatase inhibitor. Lysates were first cleared from large DNA by passing through a 25G needle and then heated to 65°C for 10 minutes. Protein concentrations were measured with the Lowry protein assay as described [26]. Equal amounts of protein (10ug per sample) were separated for size by SDS-PAGE and then transferred to a PVDF membrane (1 hour, 100V, Immobilon) and blocked with either 3% milk or 5% BSA in PBS supplemented with 0.1% Tween-20 (1 hour, room temperature). The primary antibody was incubated overnight at 4°C (see Table 2 for primary antibodies). The membranes were washed 5 times with 0.1% Tween-20 in PBS and then incubated with horseradish peroxidase-conjugated secondary antibodies (1:2,000, Jackson ImmunoResearch) for 1 hour at room temperature.

Bound secondary antibodies were detected with an Amersham Imager 600 (GE Healthcare Life Sciences) using chemiluminescence. Band intensity was quantified using Fiji image analyzing software [27]. Number of replicates is specified in the figure legends.

Table 2. Antibodies used for Western blot analysis.

Primary antibody	Predicted kDa	Dilution	Manufacturer	Catalog number
Mouse α-β actin IgG2b	43	1:500.000	Merck Millipore	MAB1501
Mouse α-SMA IgG2a	40	1:10.000	Abcam	Ab7817
Rabbit α-SM22 IgG	23	1:2000	Abcam	Ab14106
Rabbit α-Cofilin IgG	19	1:2000	Abcam	Ab11062-50
Rabbit α-pCofilin (Ser3) IgG	19	1:1000	Cell signaling	3313S
Rabbit α-SMAD2 IgG	60	1:1000	Cell signaling	5339S
Rabbit α-pSMAD2 IgG	55-60	1:400	Merck Millipore	04-953
Mouse α-β catenin IgG1	92	1:2000	BD Bioscience	610153

Immunofluorescence

For *in situ* visualization of actin fibers, α-SMA and paxillin, VSMCs were seeded on 0.01% collagen coated coverslips and allowed to attach for 48 hours. VSMCs were fixed with 2% paraformaldehyde in PBS for 15 minutes. After fixation coverslips were washed with PBS with 0.1% Trition-X100 and blocked with PBS+ (PBS supplemented with 0.15% glycine and 0.5% bovine serum albumin) for 30 minutes. Primary antibodies were incubated overnight at 4°C in PBS+, α-SMA (1:750, ab7871, Abcam) and Paxillin (1:400, ab32115, Abcam). Coverslips were washed with PBS with 0.1% trition-X100 and incubated shortly with PBS+ prior to incubation with the secondary antibody in PBS+ (1:1,000, anti-mouse Alexa Fluor 488 and anti-rabbit Alexa Fluor 594, Molecular Probes) at RT for 1 hour. After incubation the coverslips were mounted on glass slides with Vectashield supplemented with DAPI (H-1200, Vector laboratories) and sealed with nail polish. Images were recorded on a wide field epifluorescent microscope (Axio Imager D2, Zeiss).

Live cell imaging

VSMCs were seeded at a density of 10,000 cells/cm^2 on a 0.01% collagen coated coverslip. VSMCs were allowed to attach for 48 hours prior to transfection with a Paxillin-EGFP construct (2 μg/6-well) using Lipofectamin 3000 (L3000-015, Thermo Fisher). Plasmid pPaxillin-EGFP encodes an Paxillin-EGFP fusion protein, consisting of the chicken (Gallus gallus) paxillin protein fused to EGFP through a 22 amino acid linker. Plasmid pPaxillin-EGFP was made by substituting the mTurquoise cDNA in plasmid pmTurquoise-Paxillin-22 (Addgene plasmid # 55573) for the EGFP cDNA from plasmid pEGFP-N1 (Clontech) as a BamH1/NotI DNA fragment. After 6 hours, the transfection medium was replaced with regular medium and VSMCs were allowed to recover

overnight. The medium was replaced with medium supplemented with 150 nM SiR-Actin (SC001, Cytoskeleton, Inc.) to label actin filaments. After 6 hours the VSMCs were imaged overnight with a confocal laser scanning microscope, Leica SP5 microscope (Leica, Mannheim). Images were recorded every 10 minutes at three levels of the cell (base, middle and top, 1 μm separated from each other). Movement of the VSMCs was quantified by Fiji image analysis software. After delineating the maximum projection, VSMCs were manually tracked with MTrackJ [28]. Total length of the path was used for comparing the mean total migration of Fibulin-$4^{f/+}$, Fibulin-$4^{f/-}$, Fibulin-$4^{+/+}$ and Fibulin-$4^{R/R}$ VSMCs.

G-actin/F-actin in vivo assay

The ratio between filamentous actin and monomeric actin was determined with a G-actin/F-actin in vivo assay kit (BK037, Cytoskeleton, Inc.). Two days prior to the experiment, VSMCs were seeded on 0.01% collagen coated wells to reach an almost confluent density at the time of lysis. Manufacturer protocol was followed for the lysis and fractionation of the F- and G-actin, ultracentrifugation of the samples was performed at room temperature. Equal volumes of supernatant (G-actin) and pellet (F-actin) lysates (10 μl per sample) were run on 12% gels according to the above described Western blotting protocol. Analysis of the fractions was performed with Fiji image analysis software. Number of replicates is specified in the figure legends.

Immunofluorescence of extracellular matrix

ECM protein production by VSMCs was determined by immunofluorescence. VSMCs were seeded at 25,000 cells/well, except for Fibulin-4 staining that required a higher seeding density of 75,000 cells/well, in 8-well removable chamber slides and grown in DMEM supplemented with 10% heat-inactivated FCS and 1% PS for 7 days to allow ECM deposition. VSMCs were fixed with an ice-cold 70:30 methanol:acetone mixture for 5 minutes and washed with PBS. Coverslips were blocked for 1 hour with PBS supplemented with 10% normal goat serum (X0907, Agilent). Primary antibodies (Table 3) were incubated overnight at 4°C in PBS. Coverslips were washed three times with PBS for 5 minutes each prior to incubation with the secondary antibody for 1.5 hours at room temperature (1:1,000, anti-rabbit Alexa Fluor 594, Molecular Probes). Coverslips were washed and mounted to glass slides with Vectashield supplemented with DAPI (H-1200, Vector laboratories) and sealed with nail polish. Images were recorded on a wide field epifluorescent microscope (Axio Imager D2, Zeiss). Fibulin-4 images were recorded on a Axio Imager M2 epifluorescent microscope, Zeiss.

Table 3. Antibodies used for immunofluorescent staining of the ECM.

Primary antibody	Dilution	Manufacturer	Catalog number
Rabbit α-Fibronectin IgG	1:80	Millipore	AB2033
Rabbit α-mouse Fibrillin-1	1:1,000	Generated in Reinhardt Lab	-
Rabbit α-mouse LTBP4	1:1,000	Generated in Reinhardt Lab	-

TGFβ reporter assay

Downstream activation of the TGFβ pathway was determined via a CAGA-MLP-luciferase promoter reporter construct [29]. This construct contains palindromic repeats of the SMAD3/SMAD4 binding site of the PAI-1 promoter and was shown to be sensitive to TGFβ [29]. VSMCs were seeded the day prior to transfection in gelatinized 24 well plates. Subconfluent cells were transfected with Lipofectamin 3000 according to the manufacturer protocol. A SV40-renilla construct (Addgene plasmid # 27163, [30]) was co-transfected to correct for transfection efficiency. After 6 hours, the transfection medium was replaced with DMEM supplemented with 10% FCS and 1% PS. On the following day the VSMCs were serum starved for 2 hours by DMEM supplemented with 0.2% FCS and 1% PS. The VSMCs were then treated overnight with serum starvation medium supplemented with 5 ng/ml TGFβ1 (4342-5, Biovision) or 10 μM SB43542 hydrate (S4317-5mg, Sigma) or without stimulation. VSMCs were washed with PBS, lysed and luciferase activity was measured with the dual-luciferase kit (E1910, Promega) with the GloMax-multi detection system (Promega). Number of replicates is specified in the figure legends.

Statistical analysis

All experiments were performed in triplicate using three independent samples. Data were corrected for outliers with the Grubbs' test for outliers. Statistical analysis was performed with a non-parametric Mann-Whitney test. Significance was tested 2-tailed. A p-value <0.05 was considered to indicate a significant difference between groups. In the figures $p<0.05$ is show with *, $p<0.01$ with $, $p<0.001$ with ‡, and $p<0.0001$ with #. Results are expressed as mean ± SD, real-time PCR results are expressed as geometric mean ± geometric SD. All analyses were performed using Graphpad, version 7.03.

RESULTS

Fibulin-4 mutations affect the SMA cytoskeleton

To compare the consequences of complete Fibulin-4 deletion versus decreased expression of Fibulin-4, we isolated VSMCs from aortas of Fibulin-$4^{f/-}$/SM22Cre^{+} (VSMC-specific deletion of the Fibulin-4 gene) and Fibulin-$4^{R/R}$ (reduced expression of the Fibulin-4 gene) animals and their respective control littermates. First, *Fibulin-4* gene expression was determined in Fibulin-$4^{R/R}$, Fibulin-$4^{f/-}$/SM22Cre^{+}, Fibulin-$4^{+/+}$ and Fibulin-$4^{f/+}$/SM22Cre^{+} VSMCs. *Fibulin-4* expression in Fibulin-$4^{R/R}$ VSMCs is approximately 20% of the Fibulin-$4^{+/+}$ VSMCs (Fig. 1A). No *Fibulin-4* expression was detected in Fibulin-$4^{f/-}$/SM22Cre^{+} VSMCs while *Fibulin-4* gene expression was present in the control Fibulin-$4^{f/+}$/SM22Cre^{+} VSMCs, but significantly reduced to about 50% compared to Fibulin-$4^{+/+}$ (Fig. 1A).

Previously Huang et al. have shown that VSMC-specific deletion of *Fibulin-4* leads to decreased expression of ACTA2 in Fibulin-$4^{f/-}$/SM22Cre^{+} aortas, indicating that absence of Fibulin-4 impairs differentiation and proper SMA cytoskeleton formation [24]. To further analyze these isolated VSMCs, cells were stained for SMA and paxillin. SMA is a marker for the contractile, non-proliferative phenotype of adult VSMCs and paxillin is a multidomain adaptor localized at the interface between the plasma membrane and the actin cytoskeleton. The control VSMCs, Fibulin-$4^{f/+}$/SM22Cre^{+} and Fibulin-$4^{+/+}$ showed numerous SMA stress fibers spanning their cytoplasm (Fig. 1B). The well spread controls adhered to the surface with elongated focal contacts positive for paxillin, positioned at the end of the individual SMA fibers (Fig. 1C, top and bottom image). The arrows indicate the overlay between SMA fibers and the focal adhesions in yellow. In Fibulin-$4^{f/-}$/SM22Cre^{+} VSMCs SMA stress fibers were not present and paxillin staining identified small rounded podosome-like structures instead of the elongated structures observed in control VSMCs. This was further confirmed in higher magnification images (Fig. 1C and D). The Fibulin-$4^{R/R}$ VSMC did show SMA stress fibers, however, these fibers were not as distinct as in control VSMCs. Yet, paxillin did localize to the ends of SMA fibers and also formed elongated structures as was seen in the control VSMCs. Western blotting on whole cell lysates showed presence of SMA in both the Fibulin-$4^{f/+}$/SM22Cre^{+} and the Fibulin-$4^{+/+}$ control VSMCs. Compared to the Fibulin-$4^{f/+}$/SM22Cre^{+} and Fibulin-$4^{+/+}$ VSMCs SMA expression was significantly decreased in Fibulin-$4^{f/-}$/SM22Cre^{+} (Fig. 1E and F, $p<0.0001$). In contrast, Fibulin-$4^{R/R}$ VSMCs whole cell lysates showed an increase in SMA protein levels compared to Fibulin-$4^{+/+}$ whole cell lysates (Fig. 1E and F, $p<0.0001$). Similarly, Fibulin-$4^{f/+}$/SM22Cre^{+} VSMCs with 50% Fibulin-4 gene expression showed a significant increase in SMA protein compared to Fibulin-$4^{+/+}$ VSMCs (Fig. 1E and F, $p<0.0001$).

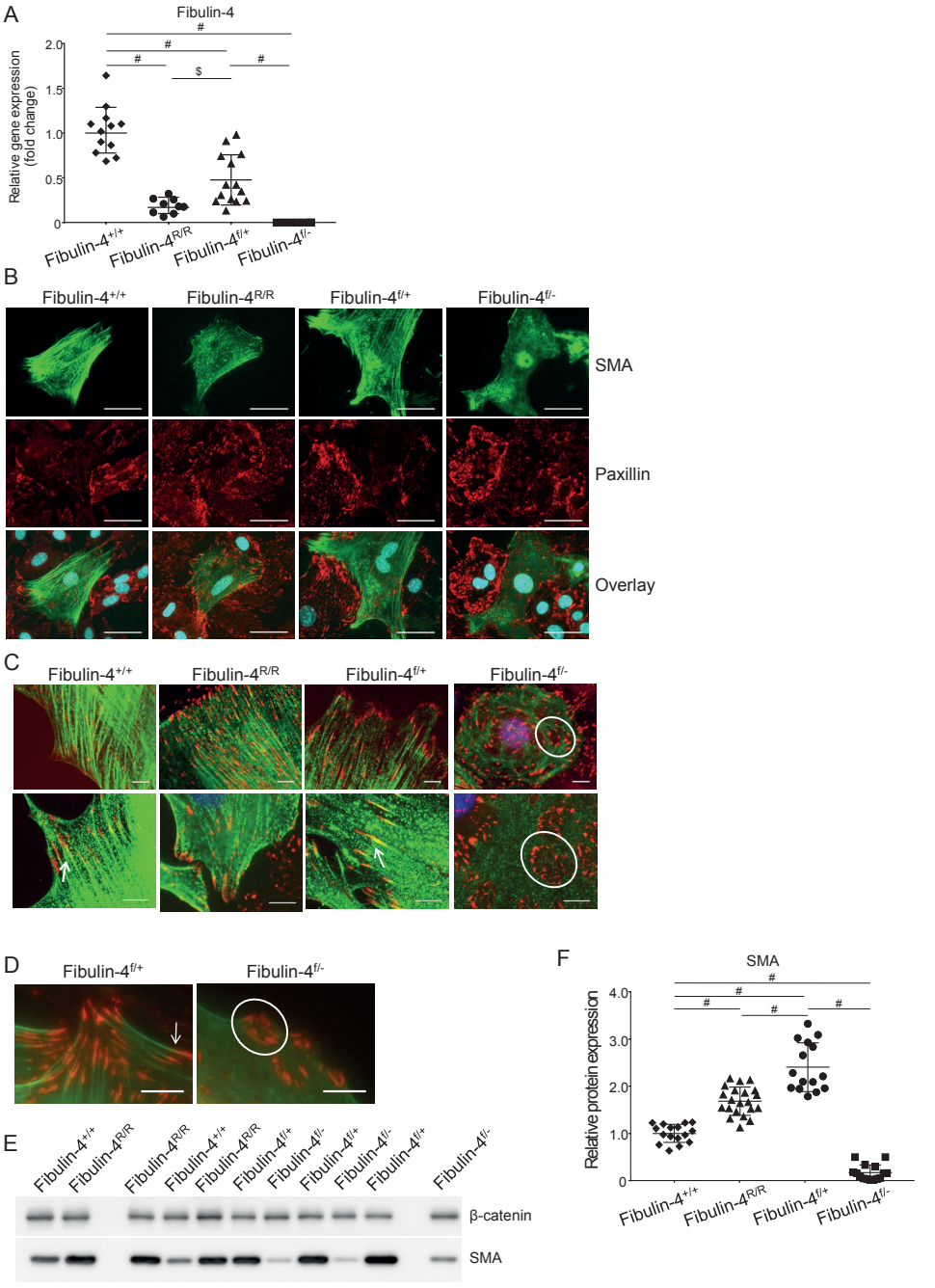

Figure 1. Fibulin-4 is needed for SMA fiber formation.

A) Relative gene expression of Fibulin-4 in Fibulin-4$^{+/+}$, Fibulin-4$^{f/+}$, Fibulin-4$^{R/R}$ and Fibulin-4$^{f/-}$ VSMCs. Data is shown for n=3-7 lysates in 2 independent experiments. **B)** Immunofluorescent staining of SMA in green and

paxillin in red. Scale bar represents 50 μm. **C)** Close up of paxillin and SMA staining. Paxillin forms elongated structures that localize to the tips of SMA fibers in Fibulin-$4^{+/+}$ and Fibulin-$4^{f/+}$ VSMCs (arrow indicates an example of overlap between SMA and paxillin). In Fibulin-$4^{f/-}$ VSMCs paxillin did not localize to SMA fibers and formed small rounded podosome-like structures (one example shown in circle). Scale bar represents 10 μm. **D)** further close-up of actin fibers and paxillin overlay in Fibulin-$4^{f/+}$ and podosome-like structures of paxillin in Fibulin-$4^{f/-}$ VSMC. Scale bar represent 10 μm. **E)** Western blots detecting SMA in Fibulin-$4^{+/+}$, Fibulin-$4^{f/+}$, Fibulin-$4^{R/R}$ and Fibulin-$4^{f/-}$ VSMC protein extracts. β-catenin levels serve as a loading control. **F)** Quantification of SMA levels as shown in panel E, respectively. Data is shown for n=7-8 lysates in 3 independent experiments. Bars represent mean ± SD. Mann-Whitney test. \$ $p<0.01$, # $p<0.0001$.

These results show that complete absence of Fibulin-4 leads to loss of SMA stress fibers, while reduced levels of Fibulin-4 can support SMA fiber formation. However, this fiber formation appears affected, even though the total amount of SMA protein is increased in Fibulin-$4^{R/R}$ VSMCs. Furthermore, absence of Fibulin-4 in the Fibulin-$4^{f/-}$/SM22Cre^{+} VSMCs also leads to an aberrant, podosome-like, appearance of the focal adhesion structures.

Actin dynamics are differentially affected by Fibulin-4 mutations

The actin cytoskeleton is a dynamic structure in which actin monomers are continuously polymerized and depolymerized. The lack of SMA fibers in Fibulin-$4^{f/-}$/SM22Cre^{+} VSMCs suggests less polymerization of actin monomers into actin fibers or, alternatively, increased depolymerization in Fibulin-$4^{f/-}$/SM22Cre^{+} VSMCs. Previously, alteration in actin depolymerization in Fibulin-$4^{f/-}$/SM22Cre^{+} aortic tissue lysates has been linked to decrease in phosphorylated cofilin to total cofilin ratio and the restoration of cofilin phosphorylation prevented aneurysm formation [31]. This shift increases activity of cofilin leading to increased depolymerization of the actin fibers. In addition, SM22, an actin crosslinking protein and VSMC differentiation marker, is decreased in Fibulin-$4^{f/-}$/SM22Cre^{+} aortic tissue lysates, suggesting that the VSMCs are not fully differentiated into mature VSMCs when Fibulin-4 is completely absent [31-33].

To determine if actin is still polymerized in mature actin filaments in Fibulin-$4^{f/-}$/SM22Cre^{+} VSMCs and Fibulin-$4^{R/R}$ VSMCs, we performed an F-/G-actin fractionation by which the ratio of polymerized versus free actin monomers can be determined (Fig. 2A and B). This fractionation revealed a decrease in F-actin levels over G-actin levels in Fibulin-$4^{f/-}$/SM22Cre^{+} VSMCs compared to control Fibulin-$4^{f/+}$/SM22Cre^{+} VSMCs (Fig. 2B, $p<0.01$). No significant difference in F-actin/G-actin fraction was found in Fibulin-$4^{R/R}$ VSMCs compared to Fibulin-$4^{+/+}$ VSMCs (Fig. 2B). The F-actin/G-actin fraction of Fibulin-$4^{f/-}$/SM22Cre^{+} VSMCs was also significantly decreased compared to both Fibulin-$4^{+/+}$ and Fibulin-$4^{R/R}$ VSMCs (Fig. 2B, $p<0.05$).

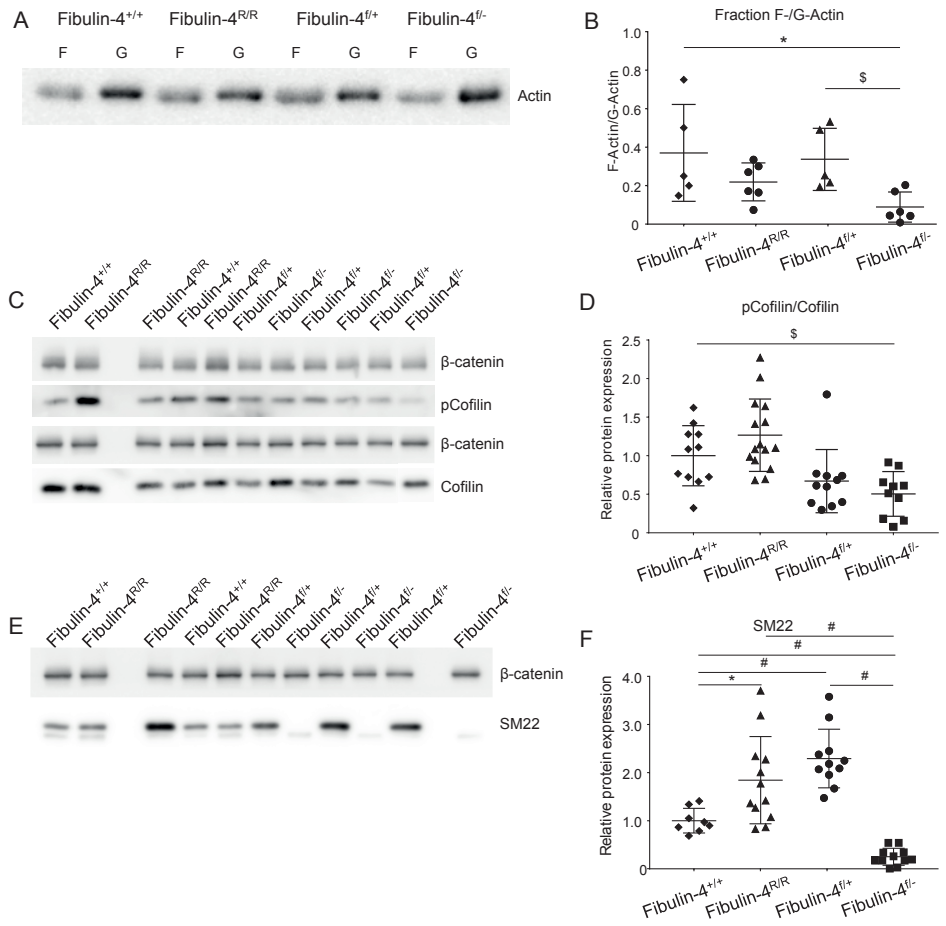

Figure 2. Altered cytoskeleton dynamics in Fibulin-4$^{f/+,}$ Fibulin-4$^{R/R}$ and Fibulin-4^{f-} VSMCs.

A) Western blot of F-/G-actin containing fractions in Fibulin-4$^{+/+}$, Fibulin-4$^{f/+,}$ Fibulin-4$^{R/R}$, and Fibulin-4^{f-} VSMC protein extracts. **B)** Quantification of F-actin to G-actin ratio. Data is shown for n=2 samples in 3 independent experiments. **C)** Western blot detecting pCofilin, Cofilin and loading control β-catenin in Fibulin-4$^{+/+}$, Fibulin-4$^{f/+}$, Fibulin-4$^{R/R}$ and Fibulin-4$^{f/-}$ VSMC protein extracts. **D)** Quantification of pCofilin/Cofilin ratio. Data is shown for n=4-6 samples in 3 independent experiments. **E)** Western blot for SM22 and loading control β-catenin for Fibulin-4$^{+/+}$, Fibulin-4$^{f/+}$, Fibulin-4$^{R/R}$ and Fibulin-4$^{f/-}$ VSMC protein extracts. **F)** Quantification of SM22 shown in E). Data is shown for n=4 lysates in 3 independent experiments. Bars represent mean ± SD. Mann-Whitney test. * $p<0.05$, \$ $p<0.01$, # $p<0.0001$.

The ratio of phosphorylated cofilin to cofilin was determined by western blot analysis to analyze the amount of inactive to active cofilin, respectively. We observed a decrease in the phosphorylated cofilin to cofilin ratio in Fibulin-4$^{f/-}$/SM22Cre^{+} VSMCs compared to Fibulin-4$^{+/+}$ VSMCs (Fig. 2C and D, $p<0,01$). This shift in ratio towards more active cofilin leads to increased depolymerization

of actin fibers in Fibulin-$4^{f/-}$/SM22Cre^{+} VSMCs. In Fibulin-$4^{R/R}$ VSMCs the ratio of phosphorylated cofilin to cofilin was comparable to Fibulin-$4^{+/+}$ VSMCs (Fig. 2C and D). When comparing the ratio of phosphorylated cofilin to cofilin in Fibulin-$4^{f/+}$/SM22Cre^{+} VSMCs no difference was found compared to Fibulin-$4^{+/+}$ VSMCs (Fig. 2C and D).

Western blot analysis for SM22 protein levels was performed to assess the differentiation status of the VSMCs and the actin crosslinking potential in Fibulin-$4^{f/-}$/SM22Cre^{+} and Fibulin-$4^{R/R}$ VSMCs. SM22 protein levels were significantly lower in Fibulin-$4^{f/-}$/SM22Cre^{+} VSMCs compared to Fibulin-$4^{f/+}$/SM22Cre^{+} VSMCs (Fig. 2F and G, $p<0.0001$). In Fibulin-$4^{R/R}$ VSMCs, SM22 protein levels were increased compared to Fibulin-$4^{+/+}$ VSMCs (Fig. 2F and G, $p<0.05$). Similarly, when comparing Fibulin-$4^{f/+}$/SM22Cre^{+} VSMCs to Fibulin-$4^{+/+}$, SM22 protein levels were increased in Fibulin-$4^{f/+}$/SM22Cre^{+} VSMCs (Fig. 2F and G, $p<0.0001$). Hence, reduction of Fibulin-4 leads to increased SM22 levels, whereas complete absence of Fibulin-4 leads to reduced SM22.

These results show that the actin dynamics are altered in both Fibulin-$4^{f/-}$/SM22Cre^{+} VSMCs as well as Fibulin-$4^{R/R}$ VSMCs. While Fibulin-$4^{f/-}$/SM22Cre^{+} VSMCs showed a decreased F-actin fraction, increased depolymerization and decreased SM22 levels, Fibulin-$4^{R/R}$ VSMCs showed no decrease in F-actin fraction and, opposite to Fibulin-$4^{f/-}$/SM22Cre^{+} VSMCs increased SM22 protein levels.

Migration is disturbed by Fibulin-4 mutations

We subsequently investigated whether the changes in cytoskeletal composition and actin (de) polymerization have implications for spontaneous cellular migration. We stained the overall actin cytoskeleton present in all cells (in contrast to the VSMC specific actin protein, SMA), by addition of the SiR-Actin probe, which is incorporated into the actin cytoskeleton and allows monitoring of cellular migration and measuring migration velocity by live cell imaging.

During cellular migration, new actin fibers and focal adhesions are formed in the direction of migration, while actin fibers are depolymerizing and focal adhesions are detaching at the back of the cell. Live cell imaging of VSMCs labeled with SiR-Actin and overexpression of the focal adhesion protein paxillin-eGFP displays this directional migration (online, Movie_1). Fig. 3A displays a limited set of frames from these live cell movies with the arrows indicating migration direction. A close up of a Fibulin-$4^{f/+}$/SM22Cre^{+} VSMC shows the formation of new focal adhesions in the direction of movement and disappearance of focal adhesions at the detaching side of the cells. Interestingly, Fibulin-$4^{f/-}$/SM22Cre^{+} VSMCs showed formation of new focal adhesions evenly distributed around the entire cell membrane and migration of individual cells occurs in all directions. Since this direction of migration occurred simultaneously in opposite directions, this resulted in reduced effective migrations and expansion of individual cells (Fig. 3A and online, Movie_2).

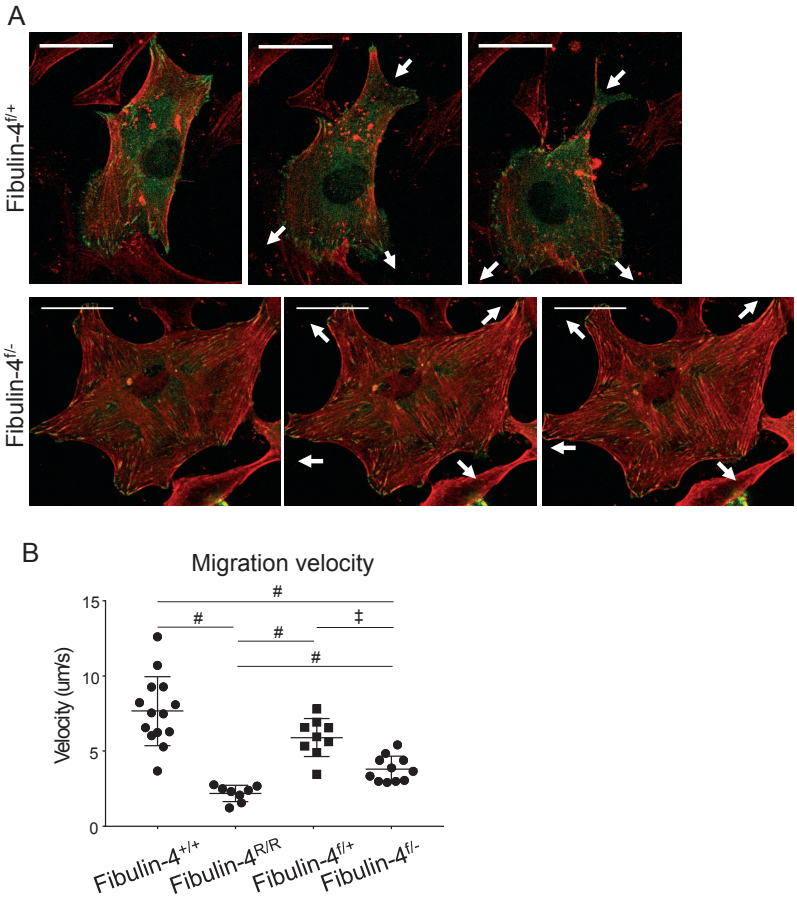

Figure 3. Fibulin-4$^{f/-}$ and Fibulin-4$^{R/R}$ VSMCs show less migration.

A) Selected frames of live cell imaging (online movie_1 and movie_2) showing the migration of Fibulin-4$^{f/+}$ and Fibulin-4$^{f/-}$ VSMCs. Paxillin overexpression is depicted in green and actin (SiR-Actin) is depicted in red. Direction of movement is indicated by the arrows. Scale bars equals 50 μm. **B)** Quantification of migration velocity of Fibulin-4$^{+/+}$, Fibulin-4$^{f/+,}$ Fibulin-4$^{R/R}$ and Fibulin-4$^{f/-}$ VSMCs (online movie_3, movie_4, movie_5 and movie_6). Bars represent mean ± SD. Mann-Whitney test, ‡ $p<0.01$ # $p<0.0001$.

To obtain an overview of migration and to quantify migration velocity cells were imaged at lower magnification. Fibulin-$4^{f/-}$/SM22Cre^{+} VSMCs showed a shorter path length compared to Fibulin-$4^{f/+}$/SM22Cre^{+} VSMCs and thus less migration. When total migration was corrected for time, migration velocity was obtained. Fibulin-$4^{f/-}$/SM22Cre^{+} VSMCs showed a decreased migration velocity compared to control VSMCs (Fig. 3B, $p<0.001$). Fibulin-$4^{R/R}$ VSMCs also showed decreased migration velocity compared to Fibulin-$4^{+/+}$ VSMCs (Fig. 3B, $p<0.0001$). Unlike Fibulin-$4^{f/-}$/SM22Cre^{+} VSMCs, directionality of movement was seen in Fibulin-$4^{R/R}$ VSMCs. Migration velocity did not differ between Fibulin-$4^{f/+}$/SM22Cre^{+} and Fibulin-$4^{+/+}$ VSMCs. Example movies can be found online (Movie_3 to Movie_6).

Taken together these data show that when Fibulin-4 is absent or reduced, VSMCs exhibit decreased migration and have a lower migration velocity compared to control cells.

Analysis of ECM production and TGFβ signaling pathway in Fibulin-$4^{f/-}$/SM22Cre^{+} and Fibulin-$4^{R/R}$ VSMCs

Since Fibulin-4 plays an important role in ECM integrity and both Fibulin-$4^{R/R}$ and Fibulin-$4^{f/-}$/SM22Cre^{+} mutant VSMCs show decreased migration, we investigated whether this similarity in aberrant movement was caused by similar changes in ECM composition. Immunofluorescent staining of the ECM components, fibulin-4, fibronectin-1, fibrillin-1 and latent TGFβ binding protein 4 (LBTP4), was performed after 7 days of culture to asses ECM production in both types of Fibulin-4 mutant VSMCs.

Fibulin-4 is essential for elastogenesis and recruitment of lysyl oxidase. Lysyl oxidase is needed for crosslinking of the elastin precursor tropoelastin and the formation of mature elastic laminae. In contrast to Fibulin-$4^{+/+}$ VSMCs, Fibulin-$4^{R/R}$ VSMCs do not show a clear network of fibulin-4 fibers (Fig. 4A). Fibulin-$4^{f/+}$/SM22Cre^{+} VSMCs do show fibulin-4 fibers, however, with less intensity than Fibulin-$4^{+/+}$ VSMCs (Fig. 4A). In Fibulin-$4^{f/-}$/SM22Cre^{+} VSMCs fibulin-4 fibers and protein are not detectable (Fig. 4A). Fibronectin serves as a base network on which other ECM proteins are deposited. Therefore, production of fibronectin is essential for proper ECM formation. A more extensive network of fibronectin fibers were apparent in Fibulin-$4^{R/R}$ VSMCs compared to Fibulin-$4^{+/+}$ VSMCs, (Fig. 4B). In contrast, Fibulin-$4^{f/-}$/SM22Cre^{+} VSMCs produced a minimal amount of fibronectin fibers compared to Fibulin-$4^{f/+}$/SM22Cre^{+} and Fibulin-$4^{+/+}$ VSMCs. Fibulin-$4^{f/+}$/SM22Cre^{+} VSMCs show a slight increase in fibronectin fibers compared to Fibulin-$4^{+/+}$ VSMCs. Fibrillin-1 is the central component of microfibrils and is important for structural support in tissues and elastic fiber formation. Similarly to the fibronectin network, the fibrillin-1 fiber network of Fibulin-$4^{R/R}$ VSMCs is more extensive than of Fibulin-$4^{+/+}$ VSMCs (Fig. 4C). However, Fibulin-$4^{f/-}$/SM22Cre^{+} VSMCs show a less extensive fibrillin-1 fiber network compared to Fibulin-$4^{f/+}$/SM22Cre^{+} and Fibulin-$4^{+/+}$ VSMCs. Like the fibronectin fibers, Fibulin-$4^{f/+}$/SM22Cre^{+} VSMCs show a slight increase in fibrillin-1 fibers compared to Fibulin-$4^{+/+}$ VSMCs (Fig. 4C). LTBP4 binds inactive TGFβ to the ECM where it is stored until activation occurs. LTBP4 is of importance for the bioavailability of TGFβ and, therefore, activation of the TGFβ signaling pathway. While LTBP4 is

detected in Fibulin-4$^{f/-}$/SM22Cre^{+} VSMCs and fibers are formed, the number of LTBP4 fibers is far less compared to Fibulin-4$^{f/+}$/SM22Cre^{+} VSMCs. Fibulin-4$^{R/R}$ VSMCs showed increased staining of LTBP4 present in an extensive ECM network compared to Fibulin-4$^{+/+}$ VSMCs. Again, Fibulin-4$^{f/+}$/SM22Cre^{+} VSMCs show a slight increase in LTBP4 compared to Fibulin-4$^{+/+}$ VSMCs (Fig. 4D). The slight increase in ECM production by Fibulin-4$^{f/+}$/SM22Cre^{+} VSMCs could explained by the reduced expression of fibulin-4. In conclusion, this suggests that a reduction in fibulin-4 results in upregulation of ECM deposition but a complete absence of fibulin-4 abolishes the deposition/assembly of various ECM proteins.

The difference in ECM deposition found between Fibulin-4$^{R/R}$ and Fibulin-4$^{f/-}$/SM22Cre^{+} VSMCs could indicate differential activities of the TGFβ pathway signaling in both mutants. Hence, we next performed analysis of TGFβ signaling components as well as TGFβ pathway activation. To determine if Fibulin-4$^{f/-}$/SM22Cre^{+} VSMCs show increased TGFβ signaling, we performed western blotting to determine the phosphorylation status of SMAD2 (pSMAD2) (Fig. 4E and F). While SMAD2 protein levels were comparable, Fibulin-4$^{f/-}$/SM22Cre^{+} cell lysates showed lower pSMAD2 protein levels compared to Fibulin-4$^{f/+}$/SM22Cre^{+} lysates. (Fig. 4E). Fibulin-4$^{R/R}$ VSMC whole cell lysates showed higher pSMAD2 protein levels compared to Fibulin-4$^{+/+}$ lysates as also previously observed (Fig. 4E) [23]. Quantification of the pSMAD2 and SMAD2 levels showed a significant decrease in pSMAD2/SMAD2 ratio in Fibulin-4$^{f/-}$/SM22Cre^{+} VSMCs compared to Fibulin-4$^{f/+}$/SM22Cre^{+} lysates (Fig. 4F, $p<0.05$), while Fibulin-4$^{R/R}$ VSMCs showed an increased pSMAD2/SMAD2 ratio compared to its control (Fig. 4F, $p<0.05$).

To examine downstream activation of the TGFβ pathway, a TGFβ reporter assay was performed. In this assay PAI-1 promoter activation, represented by luciferase activity, is measured. PAI-1 can be activated by binding of the phosphorylated SMAD2/SMAD3 complex. Fibulin-4$^{R/R}$ VSMCs showed spontaneous increased TGFβ signaling pathway activation compared to Fibulin-4$^{+/+}$ VSMCs (Fig. 4G, $p<0.001$). Our previous research on Fibulin-4$^{R/R}$ VSMCs showed that increased TGFβ signaling could be reduced by treatment of the cells with SB431542 hydrate, a TGFβ receptor blocker [23]. As visualized in Figure 4H, the intrinsic, cell autonomous TGFβ signaling pathway activation in Fibulin-4$^{f/-}$/SM22Cre^{+} VSMCs was decreased compared to Fibulin-4$^{f/+}$/SM22Cre^{+} VSMCs ($p<0.05$). When TGFβ signaling was inhibited by SB431542 hydrate in Fibulin-4$^{f/-}$/SM22Cre^{+} VSMCs there was no significant decrease in PAI-1 promoter, while Fibulin-4$^{R/R}$ VSMCs did show such a decrease in PAI-1 promoter activation after treatment with SB431542 hydrate (Fig. 4 I and J).

When stimulated with TGFβ, the TGFβ pathway can be activated in Fibulin-$4^{f/-}$/SM22Cre^{+} VSMCs as well as in Fibulin-$4^{R/R}$ VSMCs (Fig. 4K and L, $p<0.0001$). Western blot analysis of protein lysates of VSMCs stimulated with and without TGFβ further showed increased pSMAD2 levels after TGFβ stimulation. Interestingly, stimulation with TGFβ increased SMA protein levels in Fibulin-$4^{f/-}$/SM22Cre^{+} VSMCs compared to non-stimulated Fibulin-$4^{f/-}$/SM22Cre^{+} VSMCs. However, it did not increase SM22 protein levels. Fibulin-$4^{R/R}$ VSMCs also showed increased pSMAD2 protein levels upon TGFβ stimulation. A further increase of TGFβ signaling in Fibulin-$4^{R/R}$ VSMCs did not result in a large increase in SMA and SM22 protein levels.

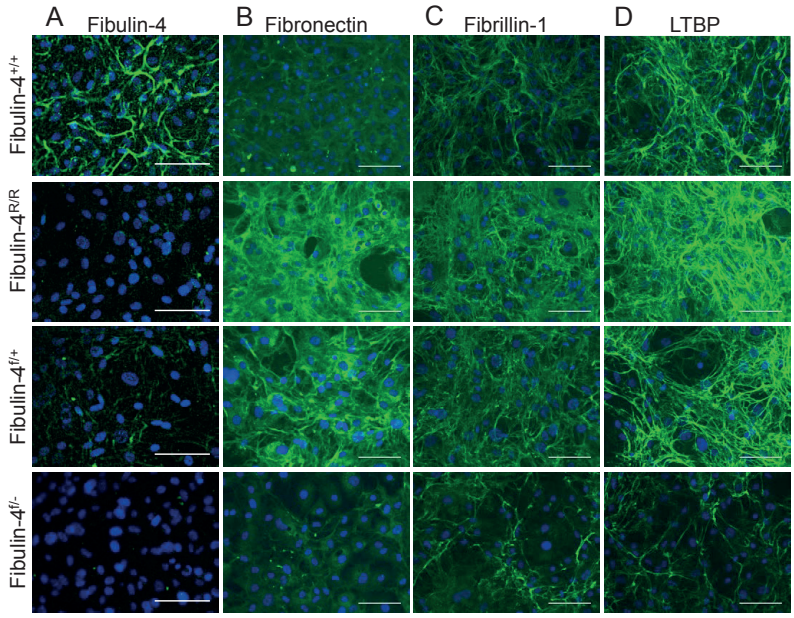

Figure 4. Continuous on the next page

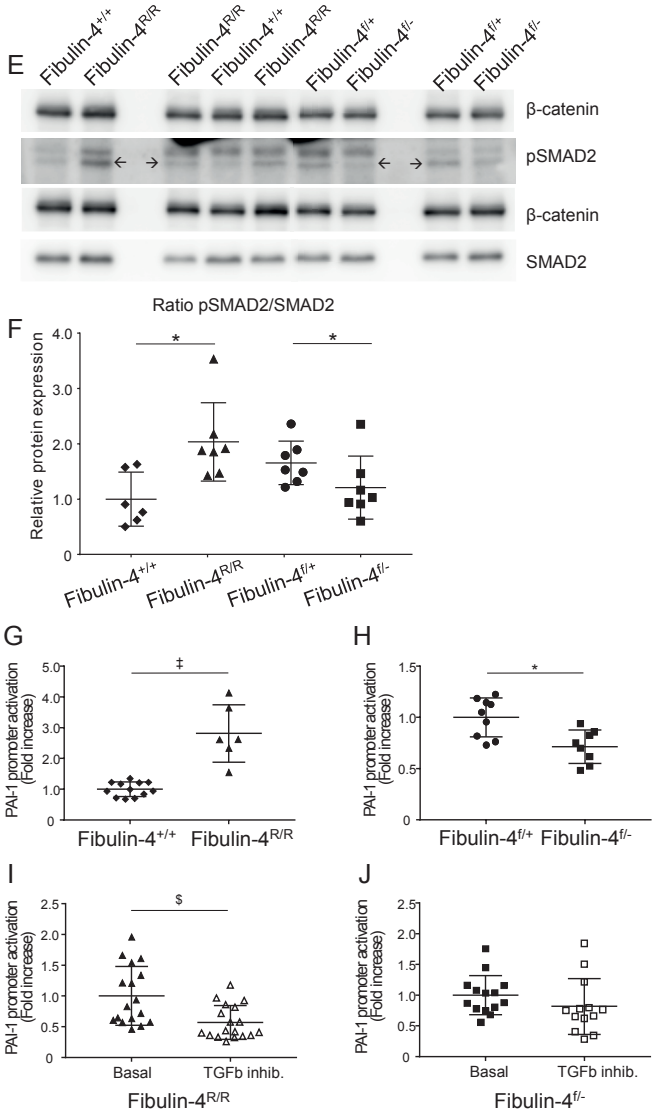

Figure 4. Continuous on the next page

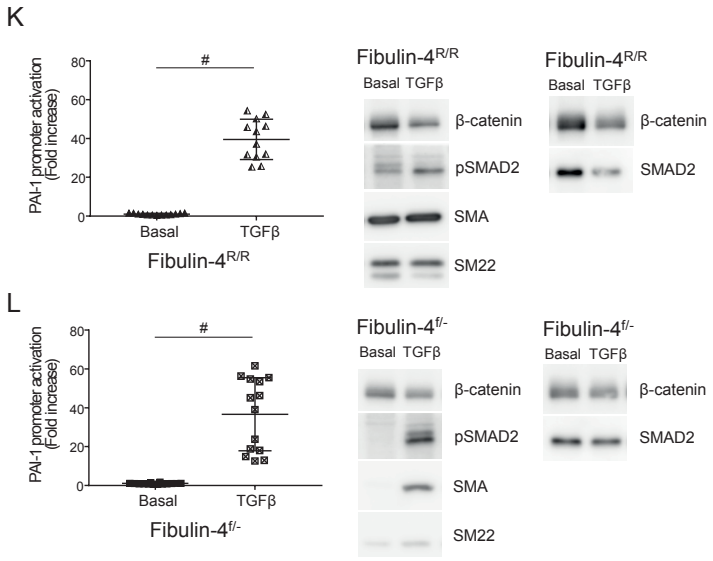

Figure 4. Analysis of ECM production and TGFβ signaling in Fibulin-4$^{f/+,}$ Fibulin-4$^{R/R}$ and Fibulin-4$^{f/-}$ VSMCs.

Immunofluorescent staining of production of ECM proteins by VSMCs after 7 days in culture. Representative images are shown, scale bar is 100 μm. **A)** Immunofluorescent staining of Fibulin-4. **B)** Immunofluorescent staining of fibronectin. **C)** Immunofluorescent staining of fibrillin-1. **D)** Immunofluorescent staining of latent TGFβ binding protein (LTBP4). **E)** Western blots for pSMAD2, SMAD2 and loading control β-catenin for Fibulin-4$^{+/+}$, Fibulin-4$^{f/+}$, Fibulin-4$^{R/R}$ and Fibulin-4$^{f/-}$ VSMC protein extracts. **F)** Quantification of pSMAD2/SMAD2 ratio. Data is shown for n=2-3 lysates in 3 independent experiments. **G)** Luciferase TGFβ transcriptional based assay showing increased activation of the PAI-1 promoter in Fibulin-4$^{R/R}$ VSMCs compared to Fibulin-4$^{+/+}$ VSMCs. n=3 independent experiments in triplicate. **H)** Luciferase TGFβ transcriptional based assay showing a decrease in pathway activation in Fibulin-4$^{f/-}$ VSMCs compared to Fibulin-4$^{f/+}$ VSMCs. n=3 independent experiments in triplicate. **I)** and **J)** Luciferase TGFβ transcriptional based assay showing no decrease in pathway activation after TGFβ inhibition in Fibulin-4$^{f/-}$, while Fibulin-4$^{R/R}$ VSMCs do show decreased TGFβ pathway after inhibition. Data is shown for 3 independent experiments with n=3-4 samples. **K)** Luciferase TGFβ transcriptional based assay showing increased pathway activation after TGFβ stimulation in Fibulin-4$^{R/R}$ VSMCs. Data is shown for 3 independent experiments with n=4 samples. Western blots for pSMAD2, SMAD2, SMA, SM22 and loading control β-catenin for Fibulin-4$^{R/R}$ VSMC protein extracts, with and without TGFβ stimulation. **L)** Luciferase TGFβ transcriptional based assay showing increased pathway activation after TGFβ stimulation in Fibulin-4$^{f/-}$ VSMCs. Data is shown for 3 independent experiments with n=4-5 samples. Western blots for pSMAD2, SMAD2, SMA, SM22 and loading control β-catenin for Fibulin-4$^{f/-}$ VSMC protein extracts, with and without TGFβ stimulation. Bars represent mean ± SD. Mann-Whitney test. * $p<0.05$, $ $p<0,01$ ‡ $p<0.001$, # $p<0.0001$.

DISCUSSION

Our current data reveal that actin cytoskeleton structure and dynamics are affected in both Fibulin-4$^{f/-}$/SM22Cre^{+} as well as Fibulin-4$^{R/R}$ VSMCs. Strikingly, we show that while TGFβ activation is increased in VSMCs when Fibulin-4 levels are reduced (Fibulin-4$^{R/R}$), no changes in the activation of TGFβ signaling are observed in the absence of Fibulin-4 (Fibulin-4$^{f/-}$/SM22Cre^{+}). Thus, a complete absence versus reduced levels of Fibulin-4 differentially affects TGFβ signaling, intracellular cytoskeleton structures and consequently cell movement.

Both the Fibulin-4$^{R/R}$ and Fibulin-4$^{f/-}$/SM22Cre^{+} mouse model show aortic aneurysm formation. Histological analysis of the aortas shows fragmentation of the elastic laminae and thickening of the aortic wall in both models. However, there are striking differences in the fragmentation of the elastic laminae differs between the two models. Although Fibulin-4$^{f/-}$/SM22Cre^{+} aortas show severe fragmentation, it appears that the first elastic laminae adjacent to the endothelial layer remain intact [22, 24]. In Fibulin-4$^{R/R}$ aortas elastic laminae throughout the entire media are fragmented. In this respect, the affected cell populations in each model might explain this difference; in Fibulin-4$^{R/R}$ mice all cells have reduced Fibulin-4 expression, while in Fibulin-4$^{f/-}$/SM22Cre^{+} mice Fibulin-4 is specifically deleted in VSMCs, surrounded by wild-type endothelial cells and fibroblasts. Which is the reason why in this study we compared VSMCs from both models.

Our data showed that both Fibulin-4 models display changes in their cytoskeleton composition. Previous research by Huang et al. has shown that aortas of Fibulin-4 germline knock-out embryos (Fibulin-4^{GKO}) contain less SMA [24]. Fibulin-4^{GKO} VSMCs also displayed less distinct actin fibers upon detection with phalloidin. Gene expression of *ACTA2* and *SM22* is decreased in Fibulin-4$^{f/-}$/SM22Cre^{+} aortas [24, 31], which is in accordance with our results of decreased SMA and SM22 protein levels in Fibulin-4$^{f/-}$/SM22Cre^{+} VSMCs. Although we find decreased SM22 protein levels in Fibulin-4$^{f/-}$/SM22Cre^{+} VSMCs, the SM22 promoter must have been active during development, as the Cre expression in the VSMC specific Fibulin-4 knock out is regulated by the *SM22* promotor. Decreased presence of SMA has previously also been found by Arnold et al. in a neural crest cell specific knock-out of integrin linked kinase (ILK) [34]. Wnt1cre; Ilk$^{flox/flox}$ embryos present with a severe aneurysmal arterial trunk, which leads to embryonic lethality during late gestation. Decreased differentiation of smooth muscle tissue has been observed as well as disorganization of F-actin stress fibers. In addition, these embryos have decreased pSmad3 staining. The similarities in the Fibulin-4$^{f/-}$/SM22Cre^{+} model and the Wnt1cre; Ilk$^{flox/flox}$ model highlights a fundamental basis for the mechanistic link between the TGFβ signaling and proper cytoskeleton formation in aneurysmal disease. In contrast to Fibulin-4$^{f/-}$/SM22Cre^{+} VSMCs, Fibulin-4$^{R/R}$ VSMCs show increased SMA protein levels. Research by Ramnath et al. has shown increased *SMA* mRNA in Fibulin-4$^{R/R}$ VSMCs [23]. Our current data now indicate that

this increased SMA expression is also translated into increased protein levels. From literature it is known that TGFβ signaling is involved in VSMC differentiation and induces expression of SMA and SM22 [35, 36]. The increased TGFβ signaling in Fibulin-$4^{R/R}$ VSMCs and aortas could therefore be responsible for the increased expression of SMA and SM22.

As previously mentioned, less distinct actin fibers have been found in Fibulin-4^{GKO} VSMCs by Huang et al. [24]. Yamashiro et al. investigated the actin fibers further in Fibulin-$4^{f/-}$/SM22Cre^{+} aortas and have shown that the ratio of F-actin to G-actin is significantly decreased in the ascending aorta of Fibulin-$4^{f/-}$/SM22Cre^{+} mice compared to their controls [31]. This decrease in F-actin to G-actin is in line with our results in VSMCs derived from Fibulin-$4^{f/-}$/SM22Cre^{+} aortas, however, there is no significant decrease detected in Fibulin-$4^{R/R}$ VSMCs. The decreased phosphorylated cofilin to cofilin ratio we observe in the Fibulin-$4^{f/-}$/SM22Cre^{+} VSMCs, which could result in increased depolymerization of actin, can explain the decrease in F-actin. The interaction between actin dynamics and ECM composition, as we find for Fibulin-$4^{f/-}$/SM22Cre^{+} and Fibulin-$4^{R/R}$ VSMCs, has also been observed for different biological systems and in different experimental set-ups [37-39].

Increased activation of the TGFβ signaling pathway is often thought to be causative in aneurysm formation. Yet, our results do not show increased activation of the TGFβ pathway in Fibulin-$4^{f/-}$/SM22Cre^{+} VSMCs. Recent data suggests a dual role for TGFβ signaling in aneurysm formation; while increased signaling can be protective in early stages of the disease, it can be detrimental in later disease stages [40, 41]. This implies that disturbed TGFβ signaling is not the single culprit in aneurysm formation. Our data also underlines the importance of the cytoskeleton in aneurysm formation, since we show that Fibulin-4 defects lead to cytoskeleton alterations. While Fibulin-$4^{R/R}$ VSMCs show overproduction of the ECM, increased TGFβ signaling and increased production of SMA, Fibulin-$4^{f/-}$/SM22Cre^{+} VSMCs show less ECM production, no increased TGFβ signaling and a lack of SMA production and SMA fiber formation. This suggests that a defect in the ECM protein fibulin-4 can lead to alterations of the cytoskeleton. Recent research has shown the importance of the VSMC cytoskeleton in combination with the ECM to contractility of the VSMCs and aneurysm formation. Without proper connections of the cytoskeleton to the ECM, a VSMC cannot generate force for its contractions. This shows that the ECM and the cytoskeleton are of great importance for the contractility of the aorta and may be primary drivers of thoracic aortic aneurysms when these are defective [42].

Our data show that activation of the TGFβ pathway by TGFβ stimulation is possible in Fibulin-$4^{f/-}$/SM22Cre^{+} VSMCs and thus receptor expression and signal transduction is still intact. We show that addition of exogenous TGFβ to Fibulin-$4^{f/-}$/SM22Cre^{+} VSMCs results in increased SMA protein levels. This result shows the direct interconnection between TGFβ pathway signaling and SMA protein levels. From literature it is known that TGFβ is involved in VSMC differentiation [43-

45]. This differentiation is directly induced by TGFβ via binding of SMAD3 to the SM22 promoter and induction of SMA production via RhoA [46, 47].

The difference in TGFβ pathway activation between the Fibulin-4$^{f/-}$/SM22Cre^{+} and Fibulin-4$^{R/R}$ mouse model could be the result of the difference in ECM composition. The increased TGFβ levels in the Fibulin-4$^{R/R}$ models is thought to be due to less stable binding of the large latent complex (LLC) to fibrillin-1 [23]. Our data show increased ECM deposition by Fibulin-4$^{R/R}$ VSMCs and increased amounts of LTBP4, implicating higher bioavailability of TGFβ, together explaining the augmented TGFβ activation. Furthermore, Bultmann-Mellin et al. showed that LTBP4-L is needed for the deposition of Fibulin-4 in the ECM and thereby proper elastogenesis, and they showed a physical interaction between LTBP4 and Fibulin-4 [48, 49]. Increased TGFβ activation in the Fibulin-4$^{R/R}$ model has previously been discovered by RNA expression analysis of Fibulin-4$^{R/R}$ aortas and TGFβ cytokine analysis in aortic extracts and blood of Fibulin-4$^{R/R}$ mice [23, 50]. In contrast, the less extensive ECM deposition we find in Fibulin-4$^{f/-}$/SM22Cre^{+} VSMCs could lead to decreased TGFβ signaling activity since there is no properly formed ECM to bind the latent TGFβ. Massam-Wu et al. have shown that Fibulin-4 binds with high affinity to LTBP1, a key mediator in binding of latent TGFβ in the ECM by binding to LTBP4 as well as fibrillin-1 [51]. This suggests that Fibulin-4$^{f/-}$/SM22Cre^{+} VSMCs are unable to confine latent TGFβ in their matrix due to the absence of Fibulin-4. Reduced storage of TGFβ could, in part, explain the decreased TGFβ signaling seen in Fibulin-4$^{f/-}$/SM22Cre^{+} VSMCs. Especially since we show that exogenous addition of TGFβ is able to activate the TGFβ pathway. Further research would be needed to determine if the decrease in TGFβ signaling in Fibulin-4$^{f/-}$/SM22Cre^{+} VSMCs is caused by reduced production or secretion of TGFβ.

Since depolymerization of actin fibers is needed for retraction of the cells during migration [52, 53], increased deposition of ECM proteins by Fibulin-4$^{R/R}$ VSMCs in combination with increased production of SMA and decreased depolymerization of the cytoskeleton could explain why Fibulin-4$^{R/R}$ VSMCs show less migration compared to control VSMCs. Furthermore, the more elaborate ECM of Fibulin-4$^{R/R}$ VSMCs could lead to a stronger attachment to the culture plate, leading to less effective migration. The increased SMA protein levels also implicates a more contractile phenotype in Fibulin-4$^{R/R}$ VSMCs, as literature suggests less migration for this contractile VSMC phenotype compared to the synthetic VSMC phenotype [54]. Although Fibulin-4$^{f/-}$/SM22Cre^{+} VSMCs show less deposition of ECM proteins, their migration is still less effective compared to Fibulin-4$^{f/+}$/SM22Cre^{+} VSMCs. In this case, the reduced effective movement could be caused by the absence of SMA fibers, less differentiation of the VSMCs and decreased attachment due to the low ECM content. However, it remains to be determined if the absence of Fibulin-4 and lack of ECM production by Fibulin-4$^{f/-}$/SM22Cre^{+} VSMCs is causative for the cytoskeleton alterations.

Our results show that while reduction or absence of Fibulin-4 shows opposite effects in cytoskeleton dynamics and TGFβ signaling, both result in aneurysm formation in the mouse. Our data underlines the need for new possible treatments of aneurysmal disease. Currently most therapies are based on increased TGFβ signaling, while we show that the Fibulin-$4^{f/-}$/SM22Cre^{+} lack increased TGFβ signaling. Yet, Fibulin-$4^{f/-}$/SM22Cre^{+} mice do show aneurysm formation. Since both Fibulin-$4^{R/R}$ and Fibulin-$4^{f/-}$/SM22Cre^{+} mouse models show alterations in the cytoskeleton, we propose that this is an additional underlying cause of aneurysm formation, which would be a potential target for the development of novel therapies.

CONCLUSION

From these results we conclude that Fibulin-4 mutations lead to SMA cytoskeleton instabilities as well as dysregulation of the TGFβ pathway. However, reduced levels of Fibulin-4 have a strikingly different effect compared to the complete absence of Fibulin-4. When Fibulin-4 is absent the production of ECM is reduced, the TGFβ pathway is not activated and SMA is not produced. In contrast, reduced levels of Fibulin-4 lead to excessive ECM deposition, over-activation of the TGFβ pathway and cytoskeleton fibers aberrations. Although these models show opposite effects, both mutations lead to aneurysm formation. Moreover, we conclude that not only TGFβ signaling, but also cytoskeleton dynamics could be causative for aortic aneurysmal disease.

ACKNOWLEDGEMENTS

We would like to thank Dr. ir. Jacob Hoogenboom from the department of Imaging Physics at Delft University of Technology for helping us with the microscopy for the close-ups of the focal adhesions, Dr. Yoshito Yamashiro from the Life Science Center for Survival Dynamics, Tsukuba Advanced Research Alliance (TARA) from the University of Tsukuba for sending the Fibulin-$4^{f/-}$/SM22Cre^{+} VSMCs, Lleroy Weerwind for performing initial western blotting analysis of cytoskeleton proteins in the Fibulin-$4^{f/-}$/SM22Cre^{+} and Fibulin-$4^{R/R}$ VSMCs, Karin Legerstee for providing us with the paxillin-eGFP plasmid.

This work was supported by the 'Lijf and Leven' grant (2014) "GAMMA" (Genexpressie analyse ter detectie van de moleculaire mechanismen van aneurysmavorming).

DECLARATION OF INTEREST

Declarations of interest: none.

REFERENCES

1. Lindsay, M.E. and H.C. Dietz, *Lessons on the pathogenesis of aneurysm from heritable conditions.* Nature, 2011. **473**(7347): p. 308-16.
2. Isselbacher, E.M., *Thoracic and abdominal aortic aneurysms.* Circulation, 2005. **111**(6): p. 816-28.
3. Dietz, H.C., et al., *The Marfan syndrome locus: confirmation of assignment to chromosome 15 and identification of tightly linked markers at 15q15-q21.3.* Genomics, 1991. **9**(2): p. 355-61.
4. Loeys, B.L., et al., *A syndrome of altered cardiovascular, craniofacial, neurocognitive and skeletal development caused by mutations in TGFBR1 or TGFBR2.* Nat Genet, 2005. **37**(3): p. 275-81.
5. Loeys, B.L., et al., *Aneurysm syndromes caused by mutations in the TGF-beta receptor.* N Engl J Med, 2006. **355**(8): p. 788-98.
6. Mizuguchi, T., et al., *Heterozygous TGFBR2 mutations in Marfan syndrome.* Nat Genet, 2004. **36**(8): p. 855-60.
7. van de Laar, I.M., et al., *Mutations in SMAD3 cause a syndromic form of aortic aneurysms and dissections with early-onset osteoarthritis.* Nat Genet, 2011. **43**(2): p. 121-6.
8. Regalado, E.S., et al., *Exome sequencing identifies SMAD3 mutations as a cause of familial thoracic aortic aneurysm and dissection with intracranial and other arterial aneurysms.* Circ Res, 2011. **109**(6): p. 680-6.
9. Guo, D.C., et al., *Mutations in smooth muscle alpha-actin (ACTA2) lead to thoracic aortic aneurysms and dissections.* Nat Genet, 2007. **39**(12): p. 1488-93.
10. Milewicz, D.M., et al., *De novo ACTA2 mutation causes a novel syndrome of multisystemic smooth muscle dysfunction.* Am J Med Genet A, 2010. **152A**(10): p. 2437-43.
11. Zhu, L., et al., *Mutations in myosin heavy chain 11 cause a syndrome associating thoracic aortic aneurysm/aortic dissection and patent ductus arteriosus.* Nat Genet, 2006. **38**(3): p. 343-9.
12. Pannu, H., et al., *MYH11 mutations result in a distinct vascular pathology driven by insulin-like growth factor 1 and angiotensin II.* Hum Mol Genet, 2007. **16**(20): p. 2453-62.
13. Papke, C.L. and H. Yanagisawa, *Fibulin-4 and fibulin-5 in elastogenesis and beyond: Insights from mouse and human studies.* Matrix Biol, 2014. **37**: p. 142-9.
14. Mithieux, S.M. and A.S. Weiss, *Elastin.* Adv Protein Chem, 2005. **70**: p. 437-61.
15. Robertson, I.B., et al., *Latent TGF-beta-binding proteins.* Matrix Biol, 2015. **47**: p. 44-53.
16. Horiguchi, M., et al., *Fibulin-4 conducts proper elastogenesis via interaction with cross-linking enzyme lysyl oxidase.* Proc Natl Acad Sci U S A, 2009. **106**(45): p. 19029-34.
17. Hucthagowder, V., et al., *Fibulin-4: a novel gene for an autosomal recessive cutis laxa syndrome.* Am J Hum Genet, 2006. **78**(6): p. 1075-80.
18. Dasouki, M., et al., *Compound heterozygous mutations in fibulin-4 causing neonatal lethal pulmonary artery occlusion, aortic aneurysm, arachnodactyly, and mild cutis laxa.* Am J Med Genet A, 2007. **143A**(22): p. 2635-41.
19. Hoyer, J., et al., *Lethal cutis laxa with contractural arachnodactyly, overgrowth and soft tissue bleeding due to a novel homozygous fibulin-4 gene mutation.* Clin Genet, 2009. **76**(3): p. 276-81.

20. Renard, M., et al., *Altered TGFbeta signaling and cardiovascular manifestations in patients with autosomal recessive cutis laxa type I caused by fibulin-4 deficiency.* Eur J Hum Genet, 2010. **18**(8): p. 895-901.
21. McLaughlin, P.J., et al., *Targeted disruption of fibulin-4 abolishes elastogenesis and causes perinatal lethality in mice.* Mol Cell Biol, 2006. **26**(5): p. 1700-9.
22. Hanada, K., et al., *Perturbations of vascular homeostasis and aortic valve abnormalities in fibulin-4 deficient mice.* Circ Res, 2007. **100**(5): p. 738-46.
23. Ramnath, N.W., et al., *Fibulin-4 deficiency increases TGF-beta signalling in aortic smooth muscle cells due to elevated TGF-beta2 levels.* Sci Rep, 2015. **5**: p. 16872.
24. Huang, J., et al., *Fibulin-4 deficiency results in ascending aortic aneurysms: a potential link between abnormal smooth muscle cell phenotype and aneurysm progression.* Circ Res, 2010. **106**(3): p. 583-92.
25. Proudfoot, D. and C. Shanahan, *Human vascular smooth muscle cell culture.* Methods Mol Biol, 2012. **806**: p. 251-63.
26. Lowry, O.H., et al., *Protein measurement with the Folin phenol reagent.* J Biol Chem, 1951. **193**(1): p. 265-75.
27. Schindelin, J., et al., *Fiji: an open-source platform for biological-image analysis.* Nat Methods, 2012. **9**(7): p. 676-82.
28. Meijering, E., O. Dzyubachyk, and I. Smal, *Methods for cell and particle tracking.* Methods Enzymol, 2012. **504**: p. 183-200.
29. Dennler, S., et al., *Direct binding of Smad3 and Smad4 to critical TGF beta-inducible elements in the promoter of human plasminogen activator inhibitor-type 1 gene.* EMBO J, 1998. **17**(11): p. 3091-100.
30. Chen, X. and R. Prywes, *Serum-induced expression of the cdc25A gene by relief of E2F-mediated repression.* Mol Cell Biol, 1999. **19**(7): p. 4695-702.
31. Yamashiro, Y., et al., *Abnormal mechanosensing and cofilin activation promote the progression of ascending aortic aneurysms in mice.* Sci Signal, 2015. **8**(399): p. ra105.
32. Prinjha, R.K., et al., *Cloning and sequencing of cDNAs encoding the actin cross-linking protein transgelin defines a new family of actin-associated proteins.* Cell Motil Cytoskeleton, 1994. **28**(3): p. 243-55.
33. Adam, P.J., et al., *Positive- and negative-acting Kruppel-like transcription factors bind a transforming growth factor beta control element required for expression of the smooth muscle cell differentiation marker SM22alpha in vivo.* J Biol Chem, 2000. **275**(48): p. 37798-806.
34. Arnold, T.D., K. Zang, and A. Vallejo-Illarramendi, *Deletion of integrin-linked kinase from neural crest cells in mice results in aortic aneurysms and embryonic lethality.* Dis Model Mech, 2013. **6**(5): p. 1205-12.
35. Hautmann, M.B., C.S. Madsen, and G.K. Owens, *A transforming growth factor beta (TGFbeta) control element drives TGFbeta-induced stimulation of smooth muscle alpha-actin gene expression in concert with two CArG elements.* J Biol Chem, 1997. **272**(16): p. 10948-56.

36. Liu, Y., S. Sinha, and G. Owens, *A transforming growth factor-beta control element required for SM alpha-actin expression in vivo also partially mediates GKLF-dependent transcriptional repression.* J Biol Chem, 2003. **278**(48): p. 48004-11.
37. Pelham, R.J., Jr. and Y. Wang, *Cell locomotion and focal adhesions are regulated by substrate flexibility.* Proc Natl Acad Sci U S A, 1997. **94**(25): p. 13661-5.
38. Byfield, F.J., et al., *Endothelial actin and cell stiffness is modulated by substrate stiffness in 2D and 3D.* J Biomech, 2009. **42**(8): p. 1114-9.
39. Halliday, N.L. and J.J. Tomasek, *Mechanical properties of the extracellular matrix influence fibronectin fibril assembly in vitro.* Exp Cell Res, 1995. **217**(1): p. 109-17.
40. Cook, J.R., et al., *Dimorphic effects of transforming growth factor-beta signaling during aortic aneurysm progression in mice suggest a combinatorial therapy for Marfan syndrome.* Arterioscler Thromb Vasc Biol, 2015. **35**(4): p. 911-7.
41. Li, W., et al., *Tgfbr2 disruption in postnatal smooth muscle impairs aortic wall homeostasis.* J Clin Invest, 2014. **124**(2): p. 755-67.
42. Milewicz, D.M., et al., *Altered Smooth Muscle Cell Force Generation as a Driver of Thoracic Aortic Aneurysms and Dissections.* Arterioscler Thromb Vasc Biol, 2017. **37**(1): p. 26-34.
43. Chen, S. and R.J. Lechleider, *Transforming growth factor-beta-induced differentiation of smooth muscle from a neural crest stem cell line.* Circ Res, 2004. **94**(9): p. 1195-202.
44. Morishita, R., et al., *Expression of smooth muscle cell-specific proteins in neural progenitor cells induced by agonists of G protein-coupled receptors and transforming growth factor-beta.* J Neurochem, 2007. **101**(4): p. 1031-40.
45. Shah, N.M., A.K. Groves, and D.J. Anderson, *Alternative neural crest cell fates are instructively promoted by TGFbeta superfamily members.* Cell, 1996. **85**(3): p. 331-43.
46. Chen, S., M. Kulik, and R.J. Lechleider, *Smad proteins regulate transcriptional induction of the SM22alpha gene by TGF-beta.* Nucleic Acids Res, 2003. **31**(4): p. 1302-10.
47. Chen, S., et al., *RhoA modulates Smad signaling during transforming growth factor-beta-induced smooth muscle differentiation.* J Biol Chem, 2006. **281**(3): p. 1765-70.
48. Bultmann-Mellin, I., et al., *Modeling autosomal recessive cutis laxa type 1C in mice reveals distinct functions for Ltbp-4 isoforms.* Dis Model Mech, 2015. **8**(4): p. 403-15.
49. Bultmann-Mellin, I., et al., *Function of Ltbp-4L and fibulin-4 in survival and elastogenesis in mice.* Dis Model Mech, 2016. **9**(11): p. 1367-1374.
50. van der Pluijm, I., et al., *Decreased mitochondrial respiration in aneurysmal aortas of Fibulin-4 mutant mice is linked to PGC1A regulation.* Cardiovasc Res, 2018.
51. Massam-Wu, T., et al., *Assembly of fibrillin microfibrils governs extracellular deposition of latent TGF beta.* J Cell Sci, 2010. **123**(Pt 17): p. 3006-18.
52. Gallo, G., *Myosin II activity is required for severing-induced axon retraction in vitro.* Exp Neurol, 2004. **189**(1): p. 112-21.
53. Mseka, T. and L.P. Cramer, *Actin depolymerization-based force retracts the cell rear in polarizing and migrating cells.* Curr Biol, 2011. **21**(24): p. 2085-91.

54. Rensen, S.S., P.A. Doevendans, and G.J. van Eys, *Regulation and characteristics of vascular smooth muscle cell phenotypic diversity.* Neth Heart J, 2007. **15**(3): p. 100-8.

EXAMPLE MOVIES

Movie_1 Migration of Fibulin-4$^{f/+}$ VSMC. Paxillin-EGFP overexpression is depicted in green and actin (SiR-Actin) is depicted in red. Scale bar represents 50 μm.

Movie_2 Migration of Fibulin-4$^{f/-}$ VSMC. Paxillin-EGFP overexpression is depicted in green and actin (SiR-Actin) is depicted in red. Scale bar represents 50 μm.

Movie_3 Migration of Fibulin-4$^{f/+}$ VSMCs. Actin (SiR-Actin) is depicted in red. Scale bar represents 50 μm. Individual VSMCs were tracked to measure migration velocity by path length over time.

Movie_4 Migration of Fibulin-4$^{f/-}$ VSMCs. Actin (SiR-Actin) is depicted in red. Scale bar represents 50 μm. Individual VSMCs were tracked to measure migration velocity by path length over time.

Movie_5 Migration of Fibulin-4$^{+/+}$ VSMCs. Actin (SiR-Actin) is depicted in red. Scale bar represents 50 μm. Individual VSMCs were tracked to measure migration velocity by path length over time.

Movie_6 Migration of Fibulin-4$^{R/R}$ VSMCs. Actin (SiR-Actin) is depicted in red. Scale bar represents 50 μm. Individual VSMCs were tracked to measure migration velocity by path length over time.

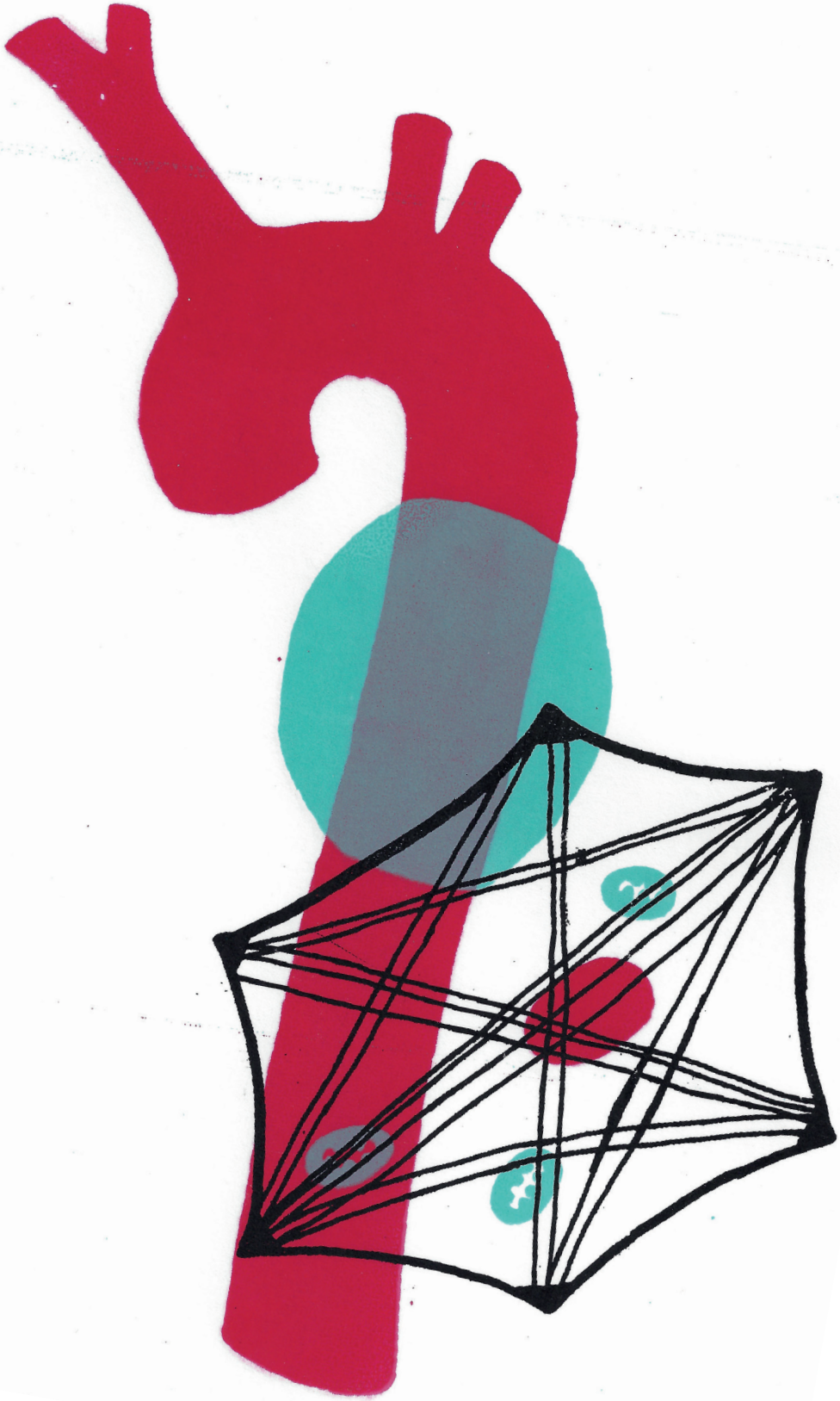

CHAPTER 5

DECREASED MITOCHONDRIAL RESPIRATION IN ANEURYSMAL AORTAS OF FIBULIN-4 MUTANT MICE IS LINKED TO PGC1A REGULATION

I. van der Pluijm[1,2], J. Burger[2,3*], P.M. van Heijningen[2*], A. IJpma[3,4], N. van Vliet[2], C. Milanese[2,5], K. Schoonderwoerd[3], W. Sluiter[2], L.J. Ringuette[6], D.H.W. Dekkers[7], I. Que[8], E.L. Kaijzel[8], L. te Riet[1,9], E. MacFarlane[10], D. Das[2,11], R. van der Linden[12], M. Vermeij[13], J.A. Demmers[7], P.G. Mastroberardino[2], E.C. Davis[6], H. Yanagisawa[14,15], H. Dietz[10], R. Kanaar[2,16], J. Essers[1,2,16]

* These authors contributed equal

[1]Department of Vascular Surgery, Erasmus MC, Rotterdam, The Netherlands; [2]Department of Molecular Genetics, Erasmus MC, Rotterdam, The Netherlands; [3]Department of Clinical Genetics, Erasmus MC, Rotterdam, The Netherlands; [4]Clinical Bioinformatics Unit, Department of Pathology, Erasmus MC, Rotterdam, The Netherlands; Department of Anatomy and Cell Biology, McGill University, Montreal, Canada; [6]Proteomics Center, Erasmus MC, Rotterdam, The Netherlands; [7]Department of Radiology, Leiden University Medical Center, Leiden, The Netherlands; [8]Department of Pharmacology, Erasmus MC, Rotterdam, The Netherlands; [9]Department of Surgery, McKusick-Nathans Institute of Genetic Medicine, Johns Hopkins University School of Medicine, Baltimore, USA; [10]Stem cell Institute, Erasmus MC, Rotterdam, The Netherlands; [11]Department of Pathology, Erasmus MC, Rotterdam, The Netherlands; [12]Life Science Center, Tsukuba Advanced Research Alliance, University of Tsukuba, Tsukuba, Japan; [13]Institute of Genetic Medicine, Johns Hopkins University School of Medicine, Baltimore, USA; [14]Division of Pediatric Cardiology, Department of Pediatrics, and Department of Medicine, Johns Hopkins University School of Medicine, Baltimore, USA; [15]Department of Radiation Oncology, Erasmus MC, Rotterdam, The Netherlands; and [16]Department of Molecular Genetics, Oncode Institute, Erasmus MC, Rotterdam, The Netherlands

Cardiovasc Res. 2018 Nov 1;114(13):1776-1793.

ABSTRACT

Aim

Thoracic aortic aneurysms are a life-threatening condition often diagnosed too late. To discover novel robust biomarkers, we aimed to better understand the molecular mechanisms underlying aneurysm formation.

Methods and Results

In Fibulin-4$^{R/R}$ mice, the extracellular matrix protein Fibulin-4 is 4-fold reduced, resulting in progressive ascending aneurysm formation and early death around 3 months of age. We performed proteomics and genomics studies on Fibulin-4$^{R/R}$ mouse aortas.

Intriguingly, we observed alterations in mitochondrial protein composition in Fibulin-4$^{R/R}$ aortas. Consistently, functional studies in Fibulin-4$^{R/R}$ vascular smooth muscle cells (VSMCs) revealed lower oxygen consumption rates, but increased acidification rates. Yet, mitochondria in Fibulin-4$^{R/R}$ VSMCs showed no aberrant cytoplasmic localization. We found similar reduced mitochondrial respiration in Tgfbr-1$^{M318R/+}$ VSMCs, a mouse model for Loeys-Dietz syndrome. Interestingly, also human fibroblasts from Marfan (FBN1) and Loeys-Dietz syndrome (TGFBR2 and SMAD3) patients showed lower oxygen consumption. While individual mitochondrial complex I-V activities were unaltered in Fibulin-4$^{R/R}$ heart and muscle, these tissues showed similar decreased oxygen consumption. Furthermore, aortas of aneurysmal Fibulin-4$^{R/R}$ mice displayed increased ROS levels. Consistent with these findings, gene expression analyses revealed dysregulation of metabolic pathways. Accordingly, blood ketone levels of Fibulin-4$^{R/R}$ mice were reduced and liver fatty acids were decreased, while liver glycogen was increased, indicating dysregulated metabolism at the organismal level. As predicted by gene expression analysis, the activity of PGC1α, a key regulator between mitochondrial function and organismal metabolism, was downregulated in Fibulin-4$^{R/R}$ VSMCs. Increased TGFβ reduced PGC1α levels, indicating involvement of TGFβ signalling in PGC1α regulation. Activation of PGC1α restored the decreased oxygen consumption in Fibulin-4$^{R/R}$ VSMCs and improved their reduced growth potential, emphasizing the importance of this key regulator.

Conclusion

Our data indicate altered mitochondrial function and metabolic dysregulation, leading to increased ROS levels and altered energy production, as a novel mechanism, which may contribute to thoracic aortic aneurysm formation.

INTRODUCTION

Disorders of the heart and blood vessels, together known as cardiovascular disease (CVD), are a leading cause of death. Most often patients present with symptoms at a late and irreversible stage. A striking example is aneurysmal disease, of which the incidence increases with age. Aneurysms are large dilatations of the aorta that, when not detected in time, will result in aortic rupture associated with high mortality. This dilation of the aorta frequently occurs unnoticed up to a point where surgery is the only optional treatment left. Although most risk factors, such as lifestyle and age are known, the molecular mechanisms involved are often not yet fully understood. Without this knowledge, proper diagnosis and intervention treatments are difficult to implement.

The most important factors known to be involved to date are extracellular matrix (ECM) degeneration and alterations in the renin-angiotensin system (RAS) and transforming growth factor β (TGFβ) signalling pathways[1-12]. In fact, intervention strategies based on these targets are being explored[13]. Although some mitigating effects on degeneration and dilatation of the aorta have been observed, none of these treatments rescue the disease or reverse symptoms[14-16]. This must mean that still many processes and molecules involved need to be identified to complete the picture of how aneurysms are formed and progress.

To study the molecular mechanisms that underlie aneurysm formation we developed a Fibulin-4 mouse model[17-19]. Fibulin-4 is a secreted glycoprotein, which is expressed in medial layers of blood vessels and is a critical component for the structural integrity and elasticity of the aortic wall[20-22]. Fibulin-4 protein levels in the aorta are essential for vascular maturation. The protein is located in microfibril bundles which tether elastic fibres to smooth muscle cells via integrin-mediated binding to regions of the cell membrane that are occupied by intracellular membrane-associated anchoring sites for actin filaments[23]. Insufficient levels of fibulin-4 compromise the structural integrity of the aortic wall, which can lead to aneurysm formation. In agreement, patients with mutations in Fibulin-4 suffer from cardiovascular complications including aortic aneurysms, arterial tortuosity and elastin abnormalities[24-27].

Fibulin-4 is an essential gene and complete deletion of this gene in the mouse leads to perinatal lethality[28, 29]. However, in our Fibulin-$4^{R/R}$ mouse model, Fibulin-4 is 4-fold reduced[17], resulting in severe aortic aneurysms with associated aortic valve disease, thereby closely mimicking aneurysm formation of genetically affected patients. Notably, genome-wide aorta transcriptome and histological analyses of young Fibulin-$4^{R/R}$ animals revealed TGFβ signalling as one of the critical events in the pathogenesis of the observed aneurysm formation[17].

In this study, in order to identify additional underlying molecular mechanisms that may contribute to aneurysm formation, we performed proteomics, genomics and functional experiments on aortas of adult Fibulin-$4^{R/R}$ animals. Mostly, proteomics data reports on the absence or presence of certain proteins, whereas gene expression profiling data is subjected to pathway analysis. We hypothesized that by performing pathway analysis on our proteomics data, and by comparing gene and protein expression, this would hint us towards new important pathways that additionally play a role in aneurysm formation. Our -omics data point to the fact that altered mitochondrial function and metabolism accompany aneurysm formation in Fibulin-$4^{R/R}$ mice, which we substantiate with functional experiments. These findings offer new mechanistic insights into the complex disease of aneurysm formation.

MATERIALS AND METHODS

Experimental Animals

Fibulin-$4^{+/R}$ animals were bred into in a C57BL6 background to obtain Fibulin-$4^{R/R}$ and Fibulin-$4^{+/+}$ experimental animals (backcross 7). Fibulin-4^{SMKO} animals were kindly provided by Hiromi Yanigasawa[30] and bred into the same C57BL6 background. The numbers of animals used for each experiment are described in the results section, and mentioned in figures and/or figure legends. For each experiment with mutant animals, littermate controls were used unless stated otherwise. Animals were housed at the Animal Resource Centre (Erasmus University Medical Centre), which operates in compliance with the "Animal Welfare Act" of the Dutch government, using the "Guide for the Care and Use of Laboratory Animals" as its standard. As required by Dutch law, formal permission to generate and use genetically modified animals was obtained from the responsible local and national authorities. An independent Animal Ethics Committee consulted by Erasmus Medical Center (Stichting DEC Consult) approved these studies (permit number 140-12-05), in accordance with national and international guidelines. For the described experiments animals were sacrificed by CO_2 inhalation, unless stated otherwise.

Preparation of aorta protein extracts and MS/MS protein identification

Fibulin-$4^{R/R}$ and Fibulin-$4^{+/+}$ littermate control mice (n=2 per group, female) were sacrificed at an age of 80-90 days, and thoracic aortas were collected. Next, aorta protein extracts were made and protein concentration was determined as described[31]. Equal amounts of total protein were loaded and size separated on a gradient (5-20%) SDS gel. Subsequently, gels were stained with Coomassie Brilliant Blue. Lanes were excised from the gel and 5mm slices were subjected to destaining, in-gel reduction with dithiothreitol, alkylation with chloroacetamide and digestion with trypsin (Promega, sequencing grade), essentially as described[32]. For Nanoflow LC-MS/MS details see online supplement. The analysis was performed in duplicate on independent samples (n=2 per genotype). Proteins with a Mascot score of 60 and higher with a unique

peptide count of at least 1, were taken into account for both genotypes separately. To perform an Ingenuity Pathway Analysis, lists of proteins identified in Fibulin-$4^{R/R}$ and Fibulin-$4^{+/+}$ aortas were aligned and assessed for proteins only present in one or the other, or both. Next, proteins only present in Fibulin-$4^{R/R}$ aortas were designated 'up'. Likewise, proteins only present in Fibulin-$4^{+/+}$ aortas, thus absent in Fibulin-$4^{R/R}$ were designated 'down'. Also, for enrichment of the IPA analysis, we took into account proteins present in both genotypes; proteins with a unique peptide count either 2-fold higher or 2-fold lower in Fibulin-$4^{R/R}$ compared to Fibulin-$4^{+/+}$ were designated 'up' and 'down', respectively. For proper IPA analysis arbitrary signs of +2 and -2 were given to a protein designated up or down, respectively. A total of 374 proteins were fed into IPA (80 down, 294 up; also see Table S1 and S2).

GO term analysis

To classify proteins according to GO terms, we used the AgBAse GOretriever for GO-term retrieval, which classifies proteins on the basis of cellular components (http://agbase.msstate.edu/cgi-bin/tools/goretriever_select.pl). For the 374 proteins that were identified as different between Fibulin-$4^{R/R}$ and Fibulin-$4^{+/+}$, 342 could be assigned with a GO-term. These were separated into 12 categories: Nucleus, Cytoplasm, Cytoskeleton, ECM, Mitochondrion, Proteasome, Plasma membrane, Ribosomes, Endoplasmatic Reticulum and Sarcoplasmic Reticulum (ER and SR), Golgi and Other (includes all other cellular components not mentioned before) and Unknown. For each category percentages were calculated by dividing proteins present in such category by all proteins assigned with a GO-term.

Micro array experiments

Total thoracic aorta RNA of 3-month old Fibulin-$4^{+/+}$ (n=3) and Fibulin-$4^{R/R}$ (n=2) was obtained using standard procedures (Qiagen). Labelling, hybridization, and scanning of Affymetrix Mouse Exon 1.0 ST microarrays (Affymetrix, Mountain View, CA) were performed according to standard Affymetrix protocol (http://www.affymetrix.com/support/technical/byproduct.affx?product=moexon-st). Raw intensity values of all samples were normalized by robust multichip analysis normalization (background correction and quantile normalization) using Partek version 6.5 (Partek Inc., St. Louis, MO). Principal Component Analysis showed good separation of the 2 sample sets. Differential expressed genes were identified using ANOVA (Partek). Cut-off values for significantly expressed genes: p-value=<0.03 and -1.5 <= fold change=> +1.5. Functional analysis was performed using IPA (Ingenuity, Redwood City, CA). Upstream regulators were selected by p-value <0.01, Bias-corrected z-score >2 and <-2. For the comparison of adult and newborn Fibulin-$4^{R/R}$ gene expression data, we used the Fibulin-$4^{R/R}$ newborn data previously published by Hanada et al[17]. This comparison resulted in 106 overlapping, significantly regulated genes (FC>1.2; p<0.05), of which 99 were regulated in the same direction. These 106 overlapping genes were used for pathway analysis in IPA. For upstream regulator analysis the same selection criteria were used as mentioned above.

RNA isolation and realtime PCR

Liver and aortic tissue from Fibulin-$4^{+/+}$ and Fibulin-$4^{R/R}$ mice, snap frozen and stored at -80 °C, was used for this experiment. RNA from aortic tissue was isolated with the miRNeasy mini kit (Qiagen) and liver RNA with RNeasy mini kit (Qiagen). cDNA was made with iScript cDNA synthesis kit (Biorad) according to manufacturing protocol. Q-PCR was performed with 200 nM forward and reverse primers and iQ™ SYBR® Green Supermix (biorad) on the CFX96 system (Biorad); denaturation at 95°C for 3 min, 40 cycles denaturation at 95°C for 15 sec, annealing/extension at 55°C for 30 sec.

Table 1. Primer sequences used for realtime PCR

	Fw seq	Rev seq	Size
PPARα	AACATCGAGTGTCGAATATGTGG	CCGAATAGTTCGCCGAAAGAA	99
PPARγ	CACAATGCCATCAGGTTTGG	GCTGGTCGATATCACTGGAGATC	82
PGC1α	CTGCGGGATGATGGAGACAG	TCGTTCGACCTGCGTAAAGT	101
PGC1β	GGGAAAAGGCCATCGGTGAA	CAGCACCTGGCACTCTACAA	122
B2M	CTCACACTGAATTCACCCCCA	GTCTCGATCCCAGTAGACGGT	98

B2M was used as a housekeeping gene. Relative gene expression levels were determined with the comparative Ct method.

Cell culture

Mice (aged 100 days) were euthanized by an overdose of CO_2 and autopsied according to standard protocols. Primary VSMCs were isolated according to the method of Proudfoot and Shanahan[33], from the thoracic aorta of Fibulin-$4^{+/+}$, Fibulin-$4^{R/R}$ and Fibulin-4^{SMKO} mice and cultured on gelatinized dishes in Dulbecco's Modified Eagle's Medium (DMEM) (Lonza BioWhittaker) supplemented with 1% penicillin-streptomycin (PS) and 10% fetal calf serum (FCS) (also see Kobayashi et al., 2004). Tgfbr-$1^{M318R/+}$ and control VSMCs were kindly provided by Hal Dietz and Elena MacFarlane [34]. VSMCs were used until passage 10 for experiments described unless stated otherwise. Human patient fibroblasts with Fibrillin-1 (FBN1 c.4817-1G>A: FBN1 ex 39), TGFβ receptor 2 (TGFBR2 c.1573delA: TGFBR2 ex 07) and Smad3 (SMAD3 c.859C>T, p.R287W: SMAD3 ex 9) mutations were kindly provide by D.F. Majoor-Krakauer, I.B.M.H. van der Laar and J.M.A. Verhagen. All patients provided written informed consent for participation in the study.

For the proliferation assay, cells were used at passage 7 and 8. Fibulin-$4^{+/+}$ and Fibulin-$4^{R/R}$ VSMCs were seeded in triplicate in 6 cm dishes (5000 cells/dish) and allowed to attach. Cells were fixed overnight at 4°C with 10% trichloroacetic acid (TCA, Sigma-Aldrich, T9159) at day 1, 2, 3, 6, and 7 after seeding. A sulforhodamine beta (SRB) assay [35] for proliferation was performed after collection of all time points. The fixed and dried dishes were incubated for 20 minutes with 0.5% SRB solution (Sigma-Aldrich, S9012) in 1% acetic acid and excess SRB was removed by washing with 1% acetic acid. After drying, bound SRB was dissolved in 10mM TRIS (Sigma-Aldrich, T6066). Absorbance was measured at 560nm and the percentage of growth was calculated at each day relative to the number of cells at day 1.

Mitochondrial respiration

Oxygen consumption rates (OCR) and extracellular acidification rate (ECAR) were measured using an XF-24 Extracellular Flux Analyzer (Seahorse Bioscience). Respiration was measured in XF assay media (non-buffered DMEM containing 2mM L-glutamine, 100 mM sodium pyruvate and 5mM glucose), in basal conditions and in response to 1 μM oligomycin (ATP synthase inhibitor), 1 μM fluoro-carbonyl cyanide phenylhydrazone (FCCP, uncoupler), 1 μM rotenone (complex I inhibitor), 1 μM antimycin A (complex III inhibitor). VSMCs and MEFS were seeded at a density of 30,000 cells/well and analysed after 24 hours. Optimal cell densities were determined experimentally to ensure a proportional response to FCCP with cell number. ECAR was measured during the entire experiment. For these experiments three independent cell lines were used per genotype, for which 6-8 wells were measured per time point.

Oxygraph and Mitochondrial complex activity measurements

Tissue homogenates were prepared from frozen muscle in 0.25 M sucrose, 10 mM N-[2-hydroxyethyl] piperazine-N′-[2 ethylsulfonic acid](HEPES) and 1 mM Ethylene Diamine Tetra-acetic Acid (EDTA), pH 7.4. Mitochondrial respiratory activity, measured as oxygen consumption rate (flux in pmol O_2/second/mg mitochondrial protein) was assessed at 37°C by high-resolution respirometry (Oxygraph-2k, Oroboros Instruments). Complex I- and II-dependent respiration were measured in state 2 (respectively, in the presence of 2 mmol/L malate and 10 mmol/L glutamate, and in the presence of 10 mmol/L succinate) and state 3 (in the presence of substrates and 0.25 mmol/L ADP). To prevent retrograde flux of electrons via complex I, complex II-dependent respiration was measured in the presence of 0.5 μmol/L of the complex I inhibitor rotenone. Respiratory adenylate control index (RCI) was calculated by dividing oxygen flux in state 3 by the flux in state 2. For complex activity measurements see online supplement.

Registration of reactive oxygen species with molecular imaging

Mice were anaesthetized (isoflurane 2%, O_2 2 L/min) and visualized using the IVIS spectrum imaging system (Perkin Elmer). L-012 (8-amino-4-chloro-7-phenylpyridol[3,4-d]pyridazine-1,4(2*H*,3*H*)dione, a chemitransluminescent probe and derivative of luminol, was purchased from

Wako Chemical (Neuss, Germany) and dissolved in H_2O. A concentration of 75 mg/kg in a volume of 100 μl was administered intravenously. Images were taken with the IVIS Spectrum imaging system (Perkin Elmer). For molecular imaging, mice were sacrificed after an hour by an overdose of anaesthesia and the chest was opened according to standard necropsy protocols. Data acquisition and analysis was performed using IVIS imaging software Living Image (Caliper). The photon flux was quantified within a region of interest encompassing the thoracic chest region of each mouse. The signal was normalized against an illumination profile for the selected field of view. Also see reference [36].

DHE staining

Cryosections 10 μm thick were stored at −80°C. After thawing the sections, they were stained by 5 μM dihydroethidium (DHE) and 0.5 μg/ml Hoechst 33258 in phosphate buffered saline (PBS) for 30 min at 37°C in a humidified atmosphere. The fluorescence of the superoxide specific reaction product of DHE oxidation was measured using a fluorescence inverted microscope (Olympus IX50) equipped with a 460–490 nm band pass excitation filter and 515 nm emission IF-barrier filter, digitized with an F-view camera (Soft Imaging System, Münster, Germany), and analysed offline (AnalySIS 3.1; Soft Imaging System). To determine the integrated density ratio, we first determined the sum of the fluorescence values of the pixels in the ethidium (red) and 2-OH-ethidium (green) selection separately. Subsequently the integrated intensity ratio was determined by dividing the 2-OH-ethidium (green) values over the ethidium (red) values for the individual samples.

PGC1α luciferase assay

Fibulin-$4^{+/+}$ and Fibulin-$4^{R/R}$ VSMCs were transiently transfected using lipofectamine 2000 (Invitrogen). Cells were dually transfected with PGC1α 2kb firefly luciferase plasmid (Addgene plasmid 8887 [37]) and SV40-renilla luciferase plasmid (10:1). After 24 hours, cells were washed with PBS, replenished with medium containing low serum (0.2% FCS) and cells were either treated overnight with TGFβ1 (5 ng/ml, Biovision) to stimulate TGFβ signalling, SB431542 hydrate (10 μM, Sigma), inhibitor of the TGFβ receptor, forskolin (10 μM, Sigma) for PGC1α activation, or DMSO as a negative control. After 24 hours, cells were lysed and firefly/renilla luciferase ratio was determined with the dual-luciferase assay system (Promega) using Glomax- multi+ detection (Promega) for each cell line. Relative luciferase levels were calculated by using the untreated Fibulin-$4^{+/+}$ VSMCs (control) as reference value.

Statistical analysis

All experiments described were performed blinded by using cell line and mouse numbers without genotypes. Normal distribution of the data was assessed using the Shapiro Wilk test. The unpaired 2-tailed Student t-test was performed to analyse the specific sample groups for significant differences. All results are expressed as mean ± SEM. However, for data with non-

normal distribution, log-transformation of the data, followed by the Student t-test, was performed. A p-value <0.05 was considered to indicate a significant difference between groups. In the figures $p<0.05$ or $p<0.01$ is shown with *, and $p<0.001$ with **. All analyses were performed using IBM SPSS Statistics version 21.0 (SPSS Inc., Chicago, IL, USA) or Graphpad.

RESULTS

Proteomics analysis identifies increased mitochondrial proteins levels in Fibulin-4$^{R/R}$ aortas

For the proteomics analysis, Fibulin-4$^{R/R}$ and Fibulin-4$^{+/+}$ protein extracts isolated from 3 month old thoracic aortas Fibulin-4$^{R/R}$ and Fibulin-4$^{+/+}$ animals were used. Reduction of Fibulin-4 protein was confirmed by western blot (Fig S1 A, left panel). Proteome expression profiles were analysed using a 1D gradient gel of total aorta protein extract. Next, proteins separated on the gel were trypsin digested and identified by an MS/MS method coupled to Mascot database searches (Table S1). A duplicate analysis of the samples identified more than 75% of the proteins in the first analysis. Analysis of an independent set of aorta extracts identified more than 65% of the previously identified proteins.

To determine differences in the proteome of Fibulin-4$^{R/R}$ and Fibulin-4$^{+/+}$ aortas, we used a Mascot score cut-off of 60. This resulted in a total of 695 proteins, of which 494 identified proteins for Fibulin-4$^{+/+}$ and 655 identified proteins for Fibulin-4$^{R/R}$ aorta. Ingenuity Pathway Analysis (IPA) was performed on a selection of proteins that were either present or absent, as well as proteins with a 2-fold higher or lower peptide count, in Fibulin-4$^{R/R}$ versus Fibulin-4$^{+/+}$ aorta, designated over- and underrepresented, respectively. This resulted in 80 proteins that were overrepresented in Fibulin-4$^{+/+}$ compared to Fibulin-4$^{R/R}$ aorta and 294 proteins that were overrepresented in Fibulin-4$^{R/R}$ compared to Fibulin-4$^{+/+}$, leaving 321 proteins designated as 'not changed' between Fibulin-4$^{+/+}$ and Fibulin-4$^{R/R}$ (Table S2 and Fig 1A).

To verify this approach, we subsequently checked whether we could find proteins known to be associated with aneurysm formation based on three important associated factors: the ECM, TGFβ and RAS signalling. We used the AgBAse GOretriever for GO-term retrieval, which classifies proteins on the basis of cellular components (http://agbase.msstate.edu/cgi-bin/tools/goretriever_select.pl). Of the 374 proteins in total that were differentially expressed between Fibulin-4$^{R/R}$ and wildtype mice, 342 GO-terms could be assigned. Here we observed that 14% of these proteins fell into the category 'ECM' (Fig1B). Moreover, compared to wildtype, in the Fibulin-4$^{R/R}$ aorta we observed overrepresentation of the ECM proteins elastin, fibrillin, fibronectin, laminin and different collagen subtypes. We performed confocal 3D imaging on aortic walls of Fibulin-4$^{+/+}$ and Fibulin-4$^{R/R}$ mice, showing expanded and disorganized elastin

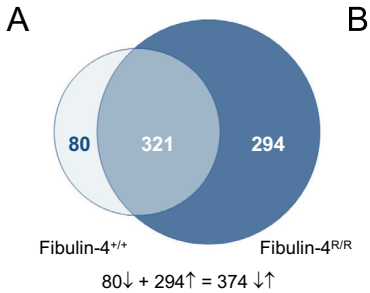

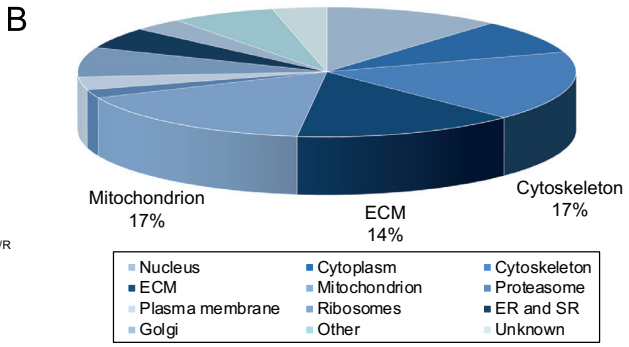

C

Upstream Regulator	Description	Molecule Type	Pred. Act. State	Bias-corr z-score	p-value overlap
TGFB1	Transforming growth factor, beta 1	growth factor	Activated	3,54	2,10E-15
TP53	Tumor protein p53	transcription regulator	Activated	2,31	1,53E-04
AGT	Angiotensinogen	growth factor	Activated	2,10	2,69E-06
SREBF2	Sterol regulatory element binding transcription factor 2	transcription regulator	Inhibited	-3,76	1,79E-04
MLXIPL	MLX interacting protein-like	other	Inhibited	-3,27	3,03E-06
SREBF1	Sterol regulatory element binding transcription factor 1	transcription regulator	Inhibited	-3,22	5,45E-09
HNF4A	Hepatocyte nuclear factor 4, alpha	transcription regulator	Inhibited	-3,00	8,66E-07
T3-TR-RXR	TR/RXR Activation complex	complex	Inhibited	-2,93	4,98E-03
PDGF BB	PDGF complex	complex	Inhibited	-2,19	2,42E-04
ATP7B	ATPase, Cu++ transporting, beta polypeptide	transporter	Inhibited	-2,16	4,15E-03
IRF4	Interferon regulatory factor 4	transcription regulator	Inhibited	-2,05	1,74E-03
PPARA	Peroxisome proliferator-activated receptor alpha	ligand-dependent nuclear receptor	Inhibited	-2,00	1,00E-09

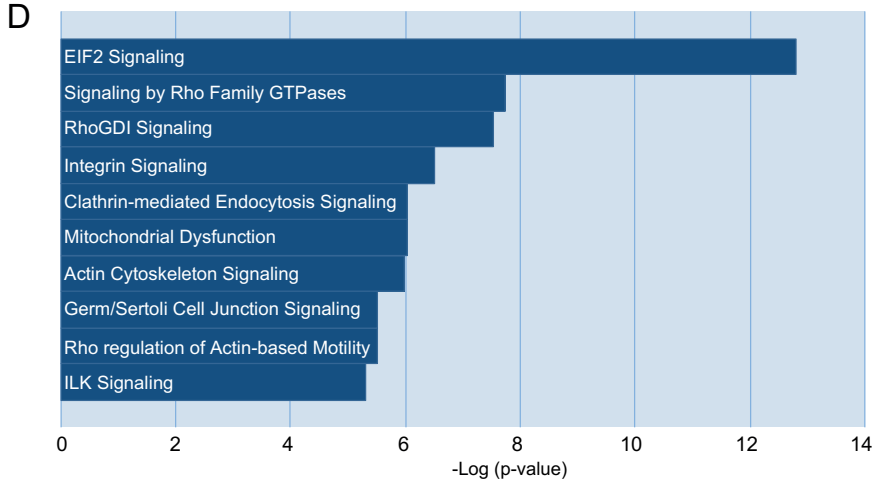

Figure 1. Proteomics analysis of Fibulin-4$^{R/R}$ and Fibulin-4$^{+/+}$ thoracic aortas identifies mitochondrial function as potentially affected.

A) Venn diagram comparison of proteins identified in Fibulin-4$^{+/+}$ (left circle) and Fibulin-4$^{R/R}$ (right circle) aortas; on the left side proteins overrepresented in Fibulin-4$^{+/+}$ aortas (light grey), on the right side proteins overrepresented in Fibulin-4$^{R/R}$ aortas (dark grey). Overlap between the two circles represents proteins that exhibit no chance between the two groups. **B)** Pie graph of GO-term distribution of proteins differentially regulated in Fibulin-4$^{R/R}$ compared to Fibulin-4$^{+/+}$ aorta. Cytoskeleton (17%), extracellular matrix (ECM,

14%) and mitochondria (17%) together comprise 48% of differentially regulated proteins. **C)** Table depicting predicted activation or inhibition of Upstream Regulators (-2> bias-corrected z-score>2, p-value <0.01), derived from an IPA analysis based on differentially regulated proteins in Fibulin-$4^{R/R}$ compared to Fibulin-$4^{+/+}$ aortas. Notably, TGFβ1 and Angiotensinogen (AGT) are predicted to be upregulated, which is known from literature, thus validating this prediction approach. **D)** Graph depicting the top 10 significantly changed ($p<0.01$) canonical pathways, derived from an IPA analysis based on the differentially regulated proteins in Fibulin-$4^{R/R}$ compared to Fibulin-$4^{+/+}$ aortas. Mitochondrial dysfunction is the 6th most significantly changed canonical pathway.

structure in the latter (Fig S1B). In addition, western blot analysis showed increased amounts of elastin protein in Fibulin-$4^{R/R}$ compared to Fibulin-$4^{+/+}$ aortic extracts (Fig S1C). Both results confirm the overrepresentation of the ECM proteins that we observed in proteomics data. Next to this overabundance of ECM proteins, 17% of the proteins fell into the category 'cytoskeleton'. Cytoskeleton proteins are closely connected to the ECM via integrins. Unexpectedly, we also observed that 17% of all proteins with significantly changed expression fell into the category 'mitochondria' (Fig 1B).

Next, the 374 deregulated proteins were loaded into IPA for further analysis. Of these 374 protein IDs, 369 were mapped by IPA. We performed both a pathway and an upstream regulator analysis to get an idea of the changes in processes involved. TGFβ1 itself turned out to be upregulated and was also predicted to be activated (based on 69 deregulated target molecules) as part of the upstream regulator analysis (Fig 1C). Thus, the proteomics data points to involvement of TGFβ signalling in Fibulin-4 associated aneurysms as previously reported[17, 27, 38]. Both ACE as well as Rac1, which are part of the RAS pathway, were upregulated in the protein dataset of Fibulin-$4^{R/R}$ compared to Fibulin-$4^{+/+}$. Moreover, angiotensinogen, a key molecule in the RAS pathway, was predicted to be upregulated (Fig 1C). Indeed, previous analysis of mouse aortas showed that angiotensinogen is increased in Fibulin-$4^{R/R}$ animals compared to Fibulin-$4^{+/+}$ [8, 10]. In conclusion, our proteome analysis reveals deregulation of TGFβ signalling and RAS, processes already known to be changed in Fibulin-$4^{R/R}$ aneurysms, validating our approach.

Canonical pathway analysis (IPA) pointed towards changes in cytoskeleton and integrin signalling (Fig 1D), as did the GO-analysis, which fits with fibulin-4's functions within the ECM. Interestingly, mitochondrial dysfunction was also a significantly changed canonical pathway, which fits with the findings of the GO analysis showing a protein overrepresentation in the category 'mitochondria'. Taken together, next to factors known to be changed in aneurysm formation, our proteomics data analysis suggests changes in mitochondrial function in the aortas of Fibulin-$4^{R/R}$ animals.

Decreased oxygen consumption rate in mutant Fibulin-4 and TGFβ-1 receptor VSMCs

To investigate mitochondrial function, we analysed mitochondrial respiration using a Seahorse XF-24 Extracellular Flux Analyzer, which allows simultaneous measurement of the oxygen consumption rate (OCR) and the extracellular acidification rate (ECAR). While OCR indicates respiration, ECAR reflects lactate production and thus glycolytic flux. OCR and ECAR thus provide a comprehensive estimate of the bioenergetics properties of the studied specimen. We observed a significantly decreased basal respiration (without addition of any inhibitor) in Fibulin-$4^{R/R}$ vascular smooth muscle cells (VSMCs) compared to Fibulin-$4^{+/+}$ controls (Fig 2A-B, phase I, $p<0.01$). While no differences were observed in respiration after injection of the ATP synthase inhibitor oligomycin, the addition of FCCP, an oxidative phosphorylation (OXPHOS) uncoupler eliciting maximal respiration, indicated a significantly lower maximal OCR in Fibulin-$4^{R/R}$ VSMCs (Fig 2A-B, phase III, $p<0.01$). Complete repression of respiration by the combined addition of complex I inhibitor rotenone and complex III inhibitor antimycin A, led to the same OCR in Fibulin-$4^{R/R}$ and Fibulin-$4^{+/+}$ VSMCs, indicating that besides mitochondrial respiration, oxygen consumption differences due to other cellular processes are negligible (Fig 2A). Experiments were repeated three times with two independent cell lines per genotype which gave similar consistent results (Fig 2B). Interestingly, ECAR was consistently higher in Fibulin-$4^{R/R}$ compared to Fibulin-$4^{+/+}$ VSMCs (Fig 2C-D, $p<0.01$), which might be indicative of metabolic rearrangements to compensate for mitochondrial defects in Fibulin-$4^{R/R}$ cells. Interestingly, lower basal and maximum OCR were also observed in mouse embryonic fibroblasts of Fibulin-$4^{R/R}$ mice compared to Fibulin-$4^{+/+}$ control mice, highlighting that decreased oxygen consumption is a general phenomenon in the Fibulin-$4^{R/R}$ mouse model (Fig S2, $p<0.01$).

We next wanted to verify that the observed defect in mitochondrial function is due to reduced Fibulin-4 in Fibulin-$4^{R/R}$ cells, rather than potential secondary effects associated with the engineered allele. To this end we isolated Fibulin-4^{SMKO} VSMCs from the Fibulin-4^{SMKO} mouse, in which Fibulin-4 is knocked out in the smooth muscle cells specifically. Absence of Fibulin-4 in Fibulin-4^{SMKO} aortic extracts was verified by western blot (Fig S1A right panel). We then performed the same Seahorse experiments as described above for the Fibulin-$4^{R/R}$ VSMCs. Interestingly, also these Fibulin-4^{SMKO} VSMCs showed a significant reduction in both basal and maximal OCR compared to Fibulin-$4^{+/+}$ VSMCs (Fig 2E, $p<0.01$), demonstrating that Fibulin-4 deletion results in the observed defects in mitochondrial respiration similar to those in the Fibulin-$4^{R/R}$ VSMCs. We did not observe significant changes in the ECAR compared to Fibulin-$4^{+/+}$ VSMCs (data not shown).

We were interested whether the same decreased oxygen consumption rate was present in VSMCs from other aneurysmal syndromes. This prompted us to first measure mitochondrial respiration in VSMCs obtained from the Tgfbr-$1^{M318R/+}$ mouse, a model for Loeys-Dietz syndrome (LDS)[34]. Similar to Fibulin-$4^{R/R}$ and Fibulin-4^{SMKO} VSMCs, Tgfbr-$1^{M318R/+}$ VSMCs showed a

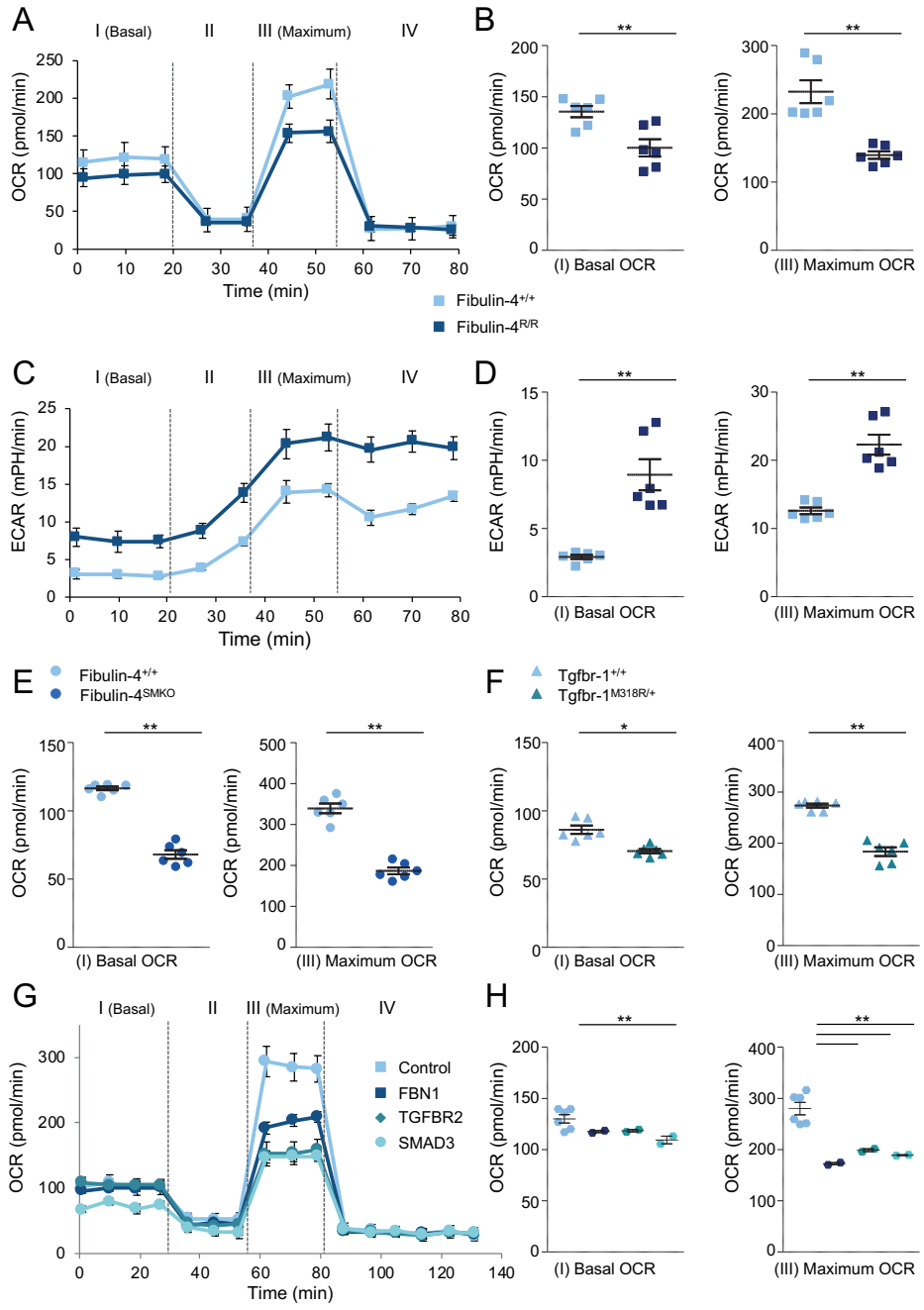

Figure 2. Reduced OCR and increased ECAR in Fibulin-4 deficient VSMCs.

A) Graph depicting the Oxygen Consumption Rate (OCR) in Fibulin-$4^{R/R}$ VSMCs (dark blue squares) and Fibulin-$4^{+/+}$ VSMCs (light blue squares) at basal level (I) and after addition of oligomycin, a complex V

inhibitor (II), FCCP, an OXPHOS uncoupler, for maximum OCR measurement (III), and a combination of rotenone (complex I inhibitor) and antimycin A (complex III inhibitor), showing potential OCR differences not due to mitochondria (IV). **B)** Both at basal level (I) and at maximum oxygen consumption level (III) Fibulin-$4^{R/R}$ VSMCs show a significantly lower OCR compared to Fibulin-$4^{+/+}$ ($p<0.01$, Student t-test), indicating altered mitochondrial function. The scatter plot shows absolute OCR levels from three experiments that were performed in two independent cell lines per genotype. **C)** Graph depicting the Extracellular Acidification Rate (ECAR) in Fibulin-$4^{R/R}$ and Fibulin-$4^{+/+}$ VSMCs. **D)** ECAR is significantly elevated in Fibulin-$4^{R/R}$ compared to Fibulin-$4^{+/+}$ VSMCs ($p<0.01$, Student t-test), quantified at basal (I) and maximum OCR (III). The scatter plot shows ECAR levels from three experiments that were performed in two independent cell lines per genotype. **E)** Scatter plots showing basal (I) and maximum (III) OCR levels in Fibulin-4^{SMKO} VSMCs (dark blue circles), which are knock-out for Fibulin-4 in VSMCs specifically, and Fibulin-$4^{+/+}$ VSMCs (light blue circles), for three experiments that were performed in two independent cell lines per genotype. Fibulin-4^{SMKO} VSMCs show a significantly lower OCR compared to Fibulin-$4^{+/+}$ ($p<0.01$, Student t-test) **F)** Scatter plots showing basal (I) and maximum (III) OCR levels in Tgfbr-$1^{M318R/+}$ (dark blue triangles) and Tgfbr-$1^{+/+}$ VSMCs (light blue triangles), of three experiments that were performed in two independent cell lines per genotype. Both at basal (I) and at maximum OCR level (III) Tgfbr-$1^{M318R/+}$ VSMCs show a significantly lower OCR compared to Tgfbr-$1^{+/+}$ ($p<0.01$, Student t-test) **G)** Graph depicting the Oxygen Consumption Rate (OCR) in three different human fibroblast cell lines derived from aneurysmal patients with a Fibrillin-1 (FBN1, dark blue squares), TGFβ receptor 2 (TGFBR2, blue diamonds) and SMAD3 (light blue circles) mutation, as well as the mean of three control cell lines (light blue squares). **H)** Scatter plots showing basal (I) and maximum (III) OCR levels, which are significantly lower for the human mutant fibroblasts compared to control ($p<0.01$, Student t-test). OCR observations were made in two independent experiments, in case of the controls for three independent cell lines.

reduced basal and maximal OCR compared to Tgfbr-$1^{+/+}$ VSMCs (Fig 2F). We did not observe an obvious decrease in ECAR as seen for Fibulin-$4^{R/R}$ VSMCs (data not shown). To examine whether oxygen consumption is also affected in cells of Marfan and Loeys-Dietz patients, we set out to measure mitochondrial respiration in patient cell lines. Although we did not have access to human VSMCs, we were able to obtain human fibroblasts from aneurysmal patients with Fibrillin-1 (FBN1 c.4817-1G>A: FBN1 ex 39), TGFβ receptor 2 (TGFBR2 c.1573delA: TGFBR2 ex 07) and Smad3 (SMAD3 c.859C>T, p.R287W: SMAD3 ex 9) mutations, as well as 3 control cell lines. We next used the human patient fibroblasts to perform seahorse experiments. Interestingly, all three patient cell lines showed a significantly reduced basal and maximum OCR compared to the control cell lines (Fig 2G and H). From these data we conclude that the altered mitochondrial oxygen consumption in aneurysms is not restricted to Fibulin-4 mutations per se, but is present in VSMCs and fibroblasts of multiple thoracic aneurysmal aorta syndromes.

Complex I, III, IV and V levels and activity in Fibulin-$4^{R/R}$ VSMCs and tissues

To investigate whether mitochondrial localization was affected by Fibulin-4 mutation, we first stained two independent Fibulin-$4^{R/R}$ and Fibulin-$4^{+/+}$ VSMC cell lines used in the Seahorse experiments with Mitotracker CMX Ros and SiR-Actin. We observed no differences in mitochondrial localization or obvious differences in cytoskeletal composition between Fibulin-4

mutant or control cell lines (Fig 3A). We next performed fluorescence-activated cell sorting (FACS) experiments using Fibulin-$4^{R/R}$ and Fibulin-$4^{+/+}$ VSMCs with the Mitotracker CMX Ros probe to determine the number of mitochondria per cell. From this analysis we observed no differences in mitochondrial signals, indicating no change in number of mitochondria per cell (Fig 3B). The observed differences in mitochondrial function in Fibulin-$4^{R/R}$ and Fibulin-$4^{+/+}$ cells prompted us to examine mitochondrial structure in VSMCs of the aorta by electron microscopy (EM). The mitochondrial ultrastructure in Fibulin-$4^{+/+}$ and Fibulin-$4^{R/R}$ cells appeared similar, although the Fibulin-$4^{R/R}$ mitochondria seemed somewhat reduced in size (Fig 3C).

The clear differences in mitochondrial respiration, without affecting the number of mitochondria per cell, could imply an altered mitochondrial mass (i.e. total mitochondrial volume in the cell) in Fibulin-$4^{R/R}$ VSMCs. In turn, this could indicate less mitochondrial complexes per cell, leading to decreases in OCR. However, the proteomics data showed a higher expression of mitochondrial complex proteins involved in oxidative phosphorylation. To investigate expression of mitochondrial complex proteins, we performed Western blot analysis using thoracic aorta tissue with an antibody cocktail directed against five specific OXPHOS I-V complex subunits that are labile when its complex is not assembled. Interestingly, when compared to Fibulin-$4^{+/+}$, the protein level of complexes I through IV was significantly ($p<0.05$) increased in Fibulin-$4^{R/R}$ aortas, whereas complex V showed no significant change (Fig 3D-E). This is in agreement with the results from the proteomics analysis which showed that several individual mitochondrial complex proteins are upregulated. This could indicate a partial compensatory reaction of the respiratory electron transport chain (ETC) to counteract the decrease in mitochondrial mass. We also performed this western blot on Fibulin-4^{SMKO} aortic extracts and littermate controls, to see if deleting Fibulin-4 in VSMCs alone could result in overexpression of these complexes. Indeed, we observed overexpression of Complex I-IV in Fibulin-4^{SMKO} (Fig S1D), however this was not a significant difference, indicating that other cells in the aorta of Fibulin-$4^{R/R}$ animals may also contribute to this effect.

To see if decreased OCR is not limited to the aorta, we measured respiratory capacity in aorta, heart, muscle and liver of Fibulin-$4^{+/+}$ and Fibulin-$4^{R/R}$ animals. Unfortunately, we were unable to determine OCR in aortic extracts, probably due to rigidity of the tissue because of ECM content. Nevertheless, heart and skeletal muscle, containing large amounts of muscle cells and highly dependent on mitochondrial activity, both showed a significantly lower OCR (Fig 3F). The liver did not show a lower, but somewhat higher (non-significant) OCR (Fig 3F), which we would expect if the observed OCR decrease is muscle cell specific. To determine whether the decreased oxygen consumption was due to reduced mitochondrial complex activity, we measured individual Complex I, III, IV and V activities (II is not subject to change), but observed no significant change (Fig 3G). These data fit with the observation that more Complex I-IV proteins are present in the aorta (Fig D-E). Taken together, we can conclude that the reduced oxygen consumption is not due to lower complex activity.

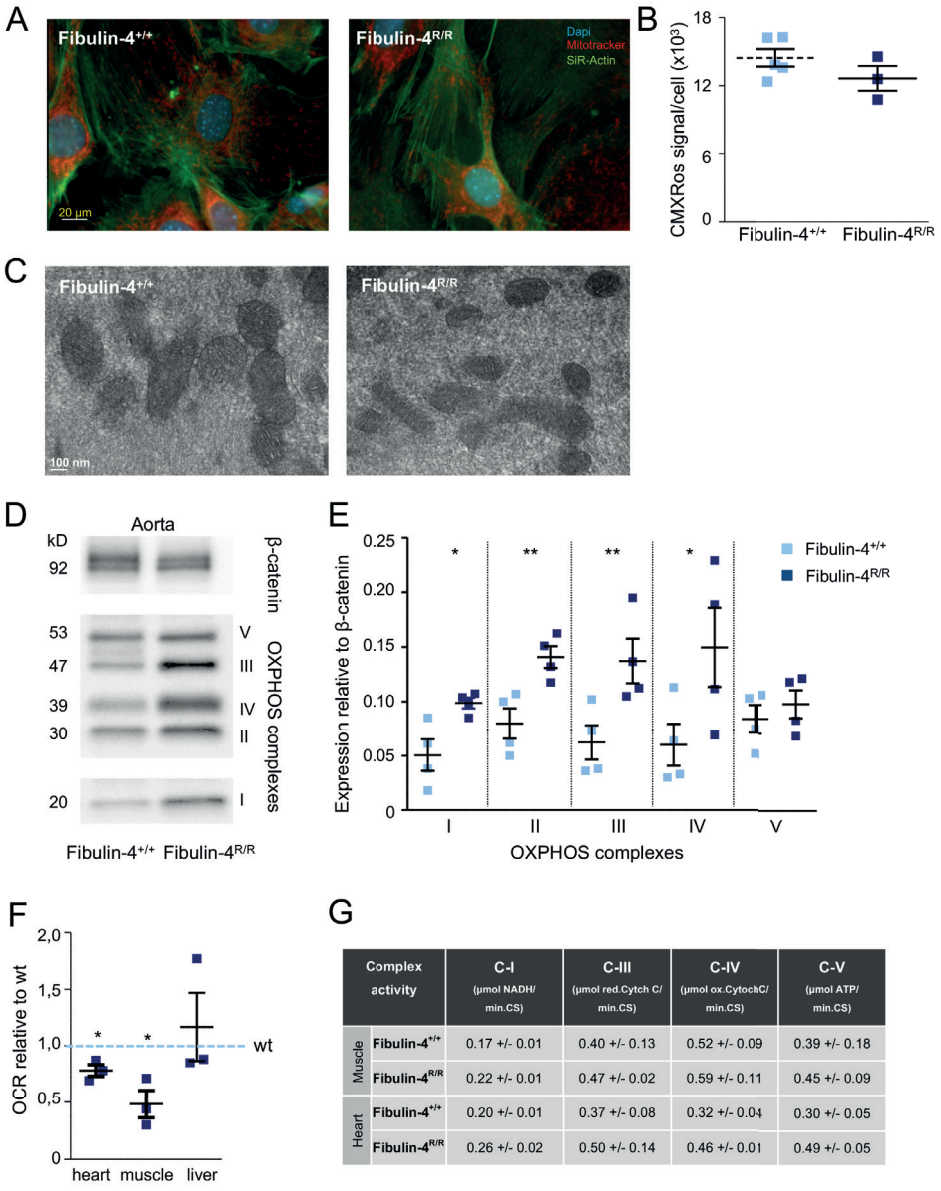

	Complex activity	C-I (µmol NADH/ min.CS)	C-III (µmol red.Cytch C/ min.CS)	C-IV (µmol ox.CytochC/ min.CS)	C-V (µmol ATP/ min.CS)
Muscle	Fibulin-4$^{+/+}$	0.17 +/- 0.01	0.40 +/- 0.13	0.52 +/- 0.09	0.39 +/- 0.18
	Fibulin-4$^{R/R}$	0.22 +/- 0.01	0.47 +/- 0.02	0.59 +/- 0.11	0.45 +/- 0.09
Heart	Fibulin-4$^{+/+}$	0.20 +/- 0.01	0.37 +/- 0.08	0.32 +/- 0.04	0.30 +/- 0.05
	Fibulin-4$^{R/R}$	0.26 +/- 0.02	0.50 +/- 0.14	0.46 +/- 0.01	0.49 +/- 0.05

Figure 3. Mitochondrial size and complexes are affected in the thoracic aorta of Fibulin-4$^{R/R}$ animals.

A) Mitotracker and SiR-Actin staining of Fibulin-4$^{R/R}$ and Fibulin-4$^{+/+}$ VSMCs showing a very similar distribution and pattern. **B)** Scatter plot depicting mitotracker (CMXRos) signal per cell, a measure for mitochondrial number per cell. No significant difference was observed (Student t-test). Mitotracker experiments were performed for n=3 (Fibulin-4$^{R/R}$) and n=5 (Fibulin-4$^{+/+}$) cell lines, with the same result. **C)** Representative electron micrographs of VSMCs in Fibulin-4$^{+/+}$ and Fibulin-4$^{R/R}$ aortas, showing no obvious structural changes, except for smaller mitochondrial size in the latter. **D)** Representative western blot for mitochondrial

complexes I-V proteins in Fibulin-$4^{+/+}$ and Fibulin-$4^{R/R}$ aorta lysates with β-catenin as loading control. Please note that complex IV is lower in size than complex III. Although detection was done on the same Western blot, it is divided into three pieces as the pictures were taken with different exposure times; 1, 2 and 5 minutes for β-catenin, complex II-V and complex I, respectively. **E)** Quantification of the different complexes for wildtype and Fibulin-$4^{R/R}$ aortas, showing significant increases in complexes I-IV in Fibulin-$4^{R/R}$ aortas compared to wildtype (n=4 per genotype, *$p<0.05$. **$p<0.01$, Student t-test on log-transformed data). **F)** OCR measurements in heart, muscle and liver, showing lower OCR in Fibulin-$4^{R/R}$ animals compared to their respective Fibulin-$4^{+/+}$ littermates (n=3 per genotype, $p<0.05$, Student t-test on log-transformed data). **G)** Complex activity measurements in Fibulin-$4^{+/+}$ and Fibulin-$4^{R/R}$ heart and muscle showing no significant difference (n=3 per genotype)

Molecular imaging reveals increased ROS in the aorta of Fibulin-$4^{R/R}$ animals

The observed imbalance between mitochondrial mass and the expression and activity of mitochondrial enzyme complexes may lead to an increase in generation of reactive oxygen species (ROS). In this context, we did observe a somewhat lower ADP ratio in Fibulin-$4^{R/R}$ muscular tissues (data not shown), which would imply less efficient ATP production that could lead to more radical formation. To investigate if indeed more radicals are present, we performed molecular imaging using the L-012 probe. This probe emits a luminescent signal upon interaction with reactive oxygen and nitrogen species that is quantified using an IVIS spectrum imaging system. We injected Fibulin-$4^{R/R}$ and Fibulin-$4^{+/+}$ animals with the L-012 probe and recorded the luminescent signal from the opened chest of mice after 1 hour to determine the signal localization. Experiments were performed three times with each Fibulin-$4^{R/R}$ animal matched to a Fibulin-$4^{+/+}$ littermate control. We observed a significant increase in average L-012-derived luminescence in Fibulin-$4^{R/R}$ aortas compared to Fibulin-$4^{+/+}$ (Fig 4A-B, $p<0.05$). Consistently, staining of Fibulin-$4^{R/R}$ aortic sections with the superoxide indicator DHE showed increased 2-OH-ethidium fluorescence compared to Fibulin-$4^{+/+}$, indicative of increased superoxide levels (Fig 4C, $p<0.05$). Together, these data show that ROS levels are elevated in Fibulin-$4^{R/R}$ aortas.

Systemic metabolic analyses indicate a metabolic switch towards fatty acid oxidation in Fibulin-$4^{R/R}$ animals

Previous gene expression studies performed on young Fibulin-$4^{R/R}$ animals gave insight into the mechanism of aneurysm formation, amongst which were cytoskeleton re-organization and perturbed TGFβ signalling[17]. As we observed many changes at the protein level pointing towards mitochondrial involvement, we wondered whether this would also be reflected at the transcriptional level. Additionally we were interested whether gene expression profiles could point to potential mechanisms and targets involved. Therefore, we performed gene expression analyses on 3-month old Fibulin-$4^{+/+}$ and Fibulin-$4^{R/R}$ thoracic aortas by using GeneChip mouse exon 1.0 ST arrays (Affymetrix). The obtained gene expression differences (p-value of 0.03; Fold Change 1.2) were uploaded and analysed in IPA. Canonical pathway analysis pointed towards numerous pathway changes related to metabolism (see Fig 5A for the top 10); out of the 30 ,

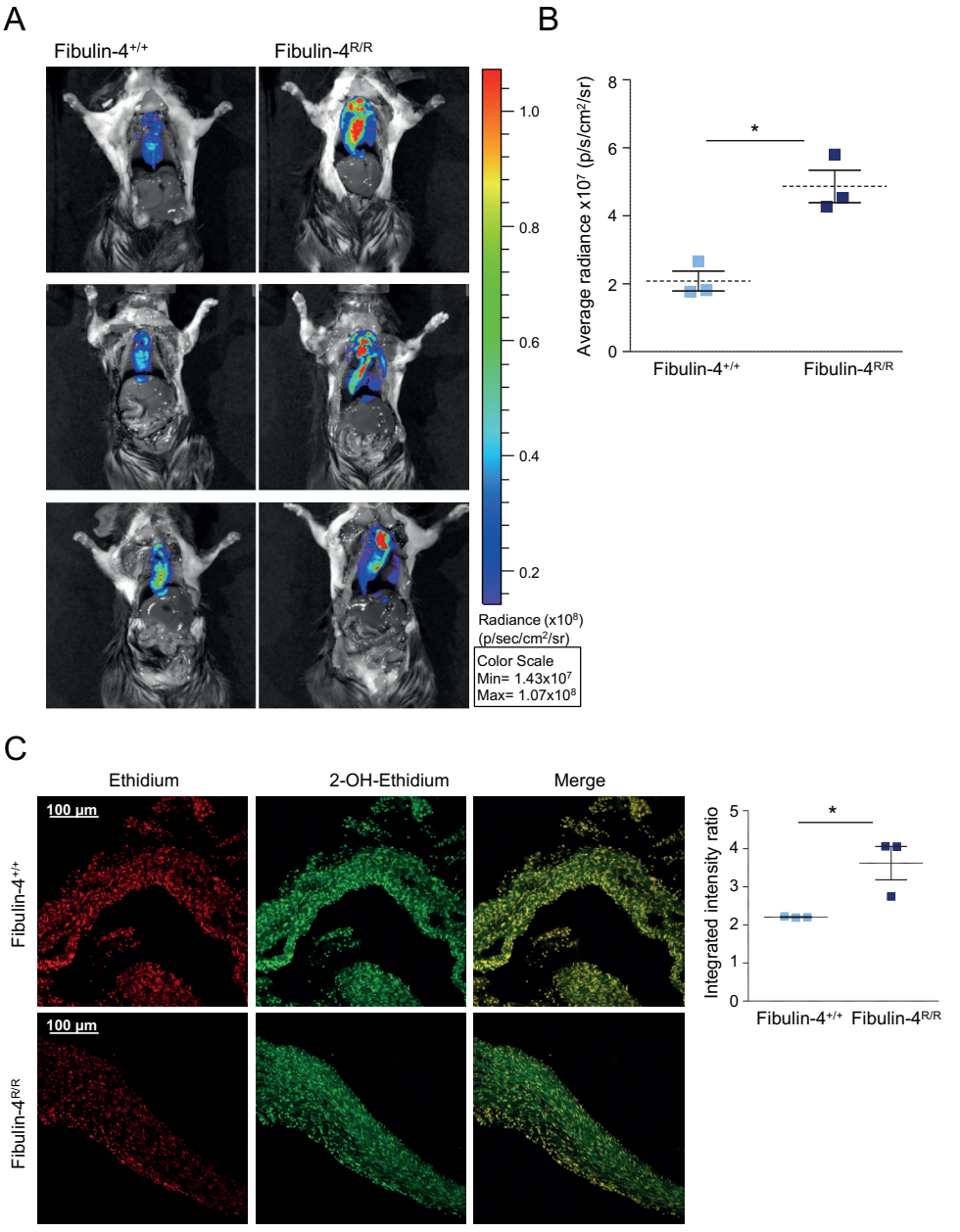

Figure 4. Molecular imaging reveals increased ROS levels in Fibulin-4$^{R/R}$ animals.

A) Representative pictures of 3 independent experiments showing increased LO12 probe signal intensity (emits light after ROS binding) in Fibulin-4$^{R/R}$ (right) animals compared to respective Fibulin-4$^{+/+}$ (left) littermates. **B)** Quantification of the average radiance at the site of the aorta, a measure for the amount of ROS reacting with LO12 probe, shows significantly higher levels in the Fibulin-4$^{R/R}$ compared to Fibulin-4$^{+/+}$

mice (n=3 per genotype, *p=0.01, Student t-test). **C)** Left panel: Representative sections of DHE staining for superoxide anion, in aortic sections from Fibulin-$4^{R/R}$, counterstained with ethidium for DNA content (red), show increased 2-OH-DHE fluorescence (green) compared to Fibulin-$4^{+/+}$ as shown in the merged picture (left, predominantly green in Fibulin-$4^{R/R}$ versus yellow in Fibulin-$4^{+/+}$). The white line indicates a length of 100 μm. Right panel: Scatter plot depicting the integrated intensity ratio for Fibulin-$4^{+/+}$ and Fibulin-$4^{R/R}$, showing an increase in the latter (n=3 per genotype, *p<0.05, Student t-test).

canonical pathways predicted to be significantly changed (p<0.01), 73% are directly involved in metabolic processes (data not shown). Moreover, when we examine the first 10 networks significantly changed based on our gene dataset, at the first position we find 'Energy Production/ Lipid Metabolism/Small Molecule Biochemistry' (Fig S3).

To investigate if metabolic changes observed in the thoracic aorta are also reflected systemically in the mouse, we first analysed body weights of the mice. Indeed, Fibulin-$4^{R/R}$ animals (n=38) had a significantly lower body weight than Fibulin-$4^{+/+}$ animals (Fig 5B, p<0.05). Next, we examined three important metabolic parameters; glucose, lactate and ketones in blood of non-fasted Fibulin-$4^{+/+}$ and Fibulin-$4^{R/R}$ animals. These parameters together shed light on the main metabolic processes used to generate ATP. Both blood glucose levels as well as blood lactate did not show significant differences between the two genotypes (Fig 5C-D). However, blood ketone levels were significantly lower in Fibulin-$4^{R/R}$ compared to Fibulin-$4^{+/+}$ animals (Fig 5E, p<0.01). Interestingly, in our gene expression analysis, we found that the key enzyme responsible for breakdown of ketones, is significantly upregulated in the aorta (3-oxoacid CoA transferase, OXCT1, 1.3 fold, p=0.03, Fig S6A). In addition, IPA analysis revealed many genes involved in the citric acid cycle (tricarboxylic acid cycle, TCA) pathway significantly downregulated in Fibulin-$4^{R/R}$ compared to Fibulin-$4^{+/+}$ aortas (Fig S4A).

The liver is a central organ involved in metabolism and adjusts metabolic processes to energy demands of the different tissues within an organism. Since ketones are products of fatty acid oxidation in the liver, we next performed oil-red-o staining on livers isolated from Fibulin-$4^{+/+}$ and Fibulin-$4^{R/R}$ animals (n=5 per group) that were normally fed. These animals did not show signs of malnutrition, or malabsorption of food in the intestine, and the liver showed no overt abnormalities on H&E-stained sections (data not shown). Yet, livers of Fibulin-$4^{R/R}$ animals clearly showed reduced oil-red-o staining in all five animals examined as compared to their respective Fibulin-$4^{+/+}$ littermates (Fig 5F, p<0.01). In contrast, periodic acid-Schiff (PAS) staining for glycogen showed the exact opposite; all five Fibulin-$4^{R/R}$ animals showed increased glycogen accumulation compared to their respective Fibulin-$4^{+/+}$ littermates (Fig 5G, p<0.01). We found no direct evidence for malfunctioning mitochondria of the liver regarding the process of OXPHOS, since these livers showed normal OCR, and immunoblots of liver lysates from Fibulin-$4^{R/R}$ and

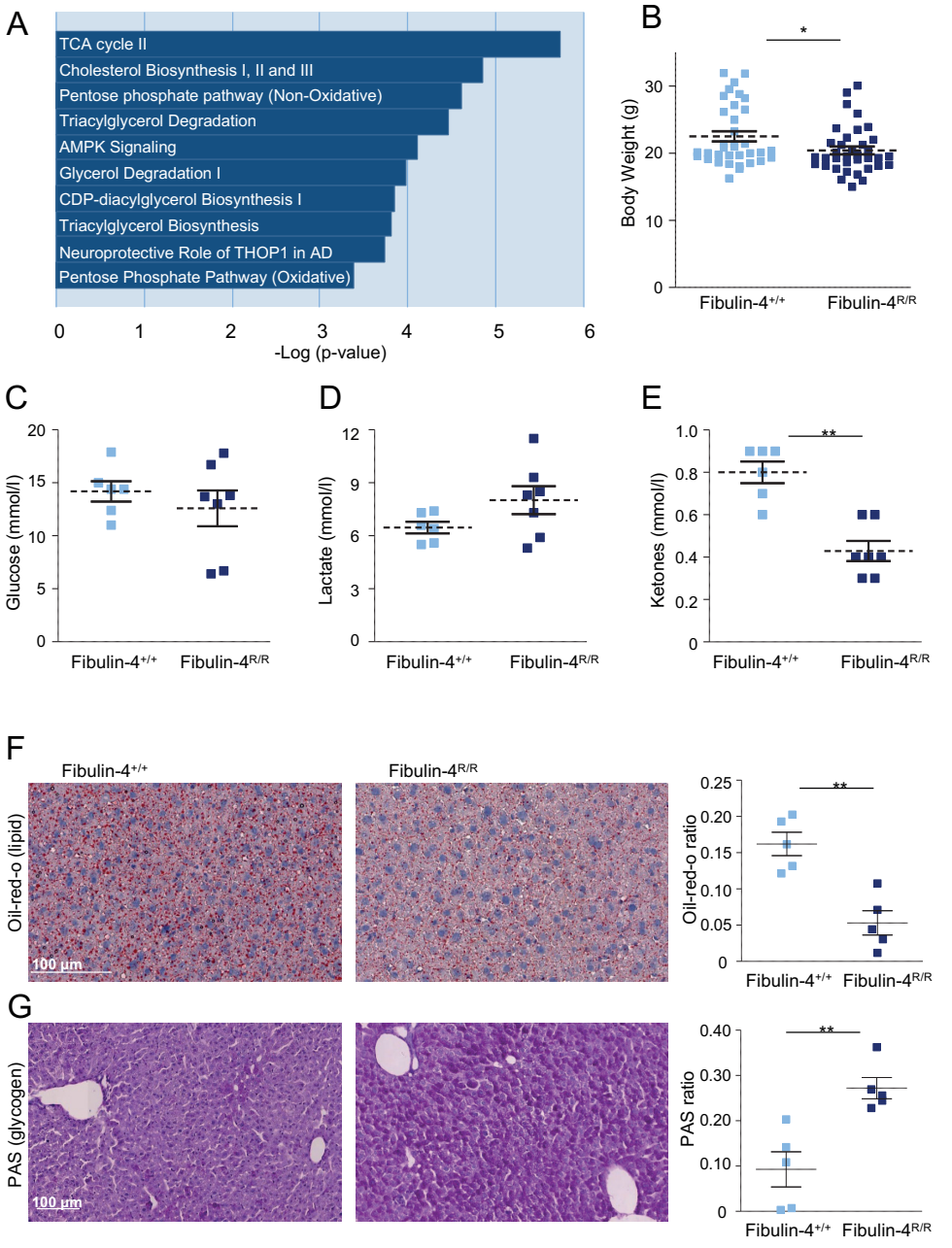

Figure 5. Gene expression analysis and metabolic parameters show altered metabolism in Fibulin-4$^{R/R}$ animals.

A) Graph depicting the top 10 significantly changed ($p<0.01$) canonical pathways, derived from an IPA analysis based on the differentially regulated genes between Fibulin-4$^{R/R}$ and Fibulin-4$^{+/+}$ aortas, showing an overrepresentation of pathways involved in energy metabolism. **B)** Scatter plot depicting body weights

of Fibulin-$4^{R/R}$ and Fibulin-$4^{+/+}$ animals, showing significant reduction in Fibulin-$4^{R/R}$ compared to Fibulin-$4^{+/+}$ animals at 3 months (n=38 and 35, respectively, $p<0.05$, Student t-test). **C), D)** and **E)** Scatter plots depicting glucose (Fibulin-$4^{+/+}$ n=6, Fibulin-$4^{R/R}$ n=7), lactate (Fibulin-$4^{+/+}$ n=6, Fibulin-$4^{R/R}$ n=5) and ketone levels (Fibulin-$4^{+/+}$ n=6, Fibulin-$4^{R/R}$ n=7), respectively, in blood of Fibulin-$4^{R/R}$ and Fibulin-$4^{+/+}$ animals, showing a significant reduction in serum ketone levels for Fibulin-$4^{R/R}$ animals ($p<0.01$, Student t-test). **F)** Representative pictures of oil-red-o staining for lipids in Fibulin-$4^{R/R}$ and Fibulin-$4^{+/+}$ livers (left), and quantification of oil-red-o ratio (right). Compared to their Fibulin-$4^{+/+}$ littermates, Fibulin-$4^{R/R}$ show decreased oil-red-o staining in the liver ($p<0.01$, Student t-test) (n=5 per genotype). **G)** Representative pictures of PAS staining for glycogen in Fibulin-$4^{R/R}$ and Fibulin-$4^{+/+}$ livers (left), and quantification of PAS ratio (right). Compared to their Fibulin-$4^{+/+}$ littermates, Fibulin-$4^{R/R}$ show increased PAS staining in their livers ($p<0.01$) (n=5 per genotype). The white line indicates a length of 100 μm.

Fibulin-$4^{+/+}$ animals did not show differences in the amount of the various OXPHOS complexes (Fig S4B). This could be due to absence or low expression of Fibulin-4 in the liver. Thus, based on the reduction of fatty acids in the liver together with reduction of ketones in the blood, it is likely that metabolism in the liver of Fibulin-$4^{R/R}$ mice has shifted to fatty acid β-oxidation and the production of ketone bodies, to meet the altered demand in energy carrier type (ketone bodies versus glucose) by the aneurysmal aorta.

We next compared the gene expression data of newborn Fibulin-$4^{R/R}$ aortas, previously published by Hanada et al.[17], with the gene expression data of adult Fibulin-$4^{R/R}$ aortas. This comparison resulted in 106 overlapping, significantly regulated genes ($FC>1.2$; $p<0.05$) used for IPA analysis, of which 99 were regulated in the same direction. Canonical pathway analysis showed processes involved in fat and glucose metabolism significantly regulated, such as atherosclerosis signalling, PPARα/RXRα signalling and glycolysis, in common between newborn and adult aortas (Fig S5A), which may hint to processes that are important form an early time point on for aneurysm formation in these animals. Moreover, upstream regulator analysis predicted, amongst others, TGFB1, miR-29b and PPARG to be significantly differentially regulated (Fig S5B). Interestingly, TGFB1 and miR-29b have previously been published to be altered in Fibulin-$4^{R/R}$ aortas [17, 38, 39], and are here also found to be important key regulators. PPARG was not previously identified, but plays an important role in fat metabolism. As we observed changes in fat and glycogen deposition in adult Fibulin-$4^{R/R}$ livers compared to Fibulin-$4^{+/+}$ livers, we performed the same staining on newborn livers. However, we did not observe obvious changes in fat or glycogen deposition between Fibulin-$4^{R/R}$ and Fibulin-$4^{+/+}$ newborn livers (Fig S5C, n=5 per genotype). These data together could indicate that the aneurysmal induced changes in metabolic processes may precede the metabolic changes in the liver.

Reduced PGC1α expression and activity in aortas and VSMCs of Fibulin-$4^{R/R}$ animals

Since we discovered changes in mitochondrial function in thoracic aortas of Fibulin-$4^{R/R}$ animals, it would be interesting to know which process or subset of factors is responsible. To investigate

this, we looked at upstream regulators that are predicted to be significantly changed based on the gene expression data in the thoracic aorta of Fibulin-$4^{R/R}$ animals. Interestingly, PGC1α and PGC1β (peroxisome proliferator-activated receptor gamma, coactivator 1 α and β) as well as PPARα, PPARδ and PPARγ (peroxisome proliferator-activated receptor α, δ and γ) were predicted to be significantly downregulated (Table 1). In addition, we noticed that they were also all significantly downregulated at the gene expression level, except for PPARδ, which showed no significant change (Table 1). Next, we performed real-time PCR analysis to check the mRNA expression levels of PGC1α, PGC1β, PPARα and PPARγ in thoracic aorta extracts of Fibulin-$4^{R/R}$ and Fibulin-$4^{+/+}$ animals. We found that mRNA levels of PGC1α and PGC1β were both significantly downregulated in Fibulin-$4^{R/R}$ compared to Fibulin-$4^{+/+}$ aortas (Fig 6A, $p<0.05$, $n=11$ and $n=7$, respectively), whereas levels of PPARα and PPARγ were lower but not significantly different from Fibulin-$4^{+/+}$ (Fig S4C). Interestingly, in the liver we found that PGC1α was significantly upregulated (Fig S4D, $p<0.05$), which would be consistent with the observed lower lipid content (higher lipid usage) of the liver (Fig 5F) and the somewhat higher OCR (Fig 3G). PGC1α is the master switch between mitochondrial biogenesis and organismal metabolism, and signals to PPARs, essential regulators of lipid metabolism, making these interesting molecules for further investigation. Moreover, when examining the networks predicted to be significantly regulated in our gene expression dataset, the highest significantly regulated network is 'Energy Production/Lipid Metabolism/Small Molecule Biochemistry' (Fig S3). The visual representation of this network, derived from IPA, highlights that PPARα and PPARγ play a central role (Fig S6A).

Next, we performed a gene to protein comparison, where we compared the lists of significantly regulated genes and proteins in adult Fibulin-$4^{R/R}$ aortas to Fibulin-$4^{+/+}$. This comparison revealed 30 molecules that changed both at the gene and protein level (Fig S6B). This list included key genes/proteins involved in metabolism, like glucose-6-phosphate dehydrogenase and fatty acid synthase (Fig S6B). Strikingly, when we asked whether IPA could find a connection between the 30 overlapping molecules (core analysis on the 30 genes/proteins in common), we indeed found the highest network regulated to be Lipid Metabolism, in which again PPARα and PGC1α are involved as key regulators (Fig S6C).

In order to check PGC1α activity in VSMCs, we used a luciferase-based assay. We transfected plasmids containing firefly luciferase under the control of the PGC1α promoter in Fibulin-$4^{R/R}$ and Fibulin-$4^{+/+}$ VSMCs, with plasmids containing renilla luciferase as transfection control. Relative luciferase levels, a measure for PGC1α activity, were significantly lower in Fibulin-$4^{R/R}$ VSMCs (Fig 6B, $p<0.01$). It was reported that TGFβ signalling negatively regulates PGC1α [40-42]. As we previously found TGFβ signalling to be increased in Fibulin-$4^{R/R}$ aortas and cells [17, 38], we next investigate the effect of TGFβ signalling on PGC1α. We performed the PGC1α luciferase-based assay on Fibulin-$4^{+/+}$ and Fibulin-$4^{R/R}$ VSMCs with either TGFβ treatment, TGFβR inhibition (SB431542), or forskolin, a potent inducer of PGC1α activity. In both Fibulin-$4^{+/+}$ and Fibulin-

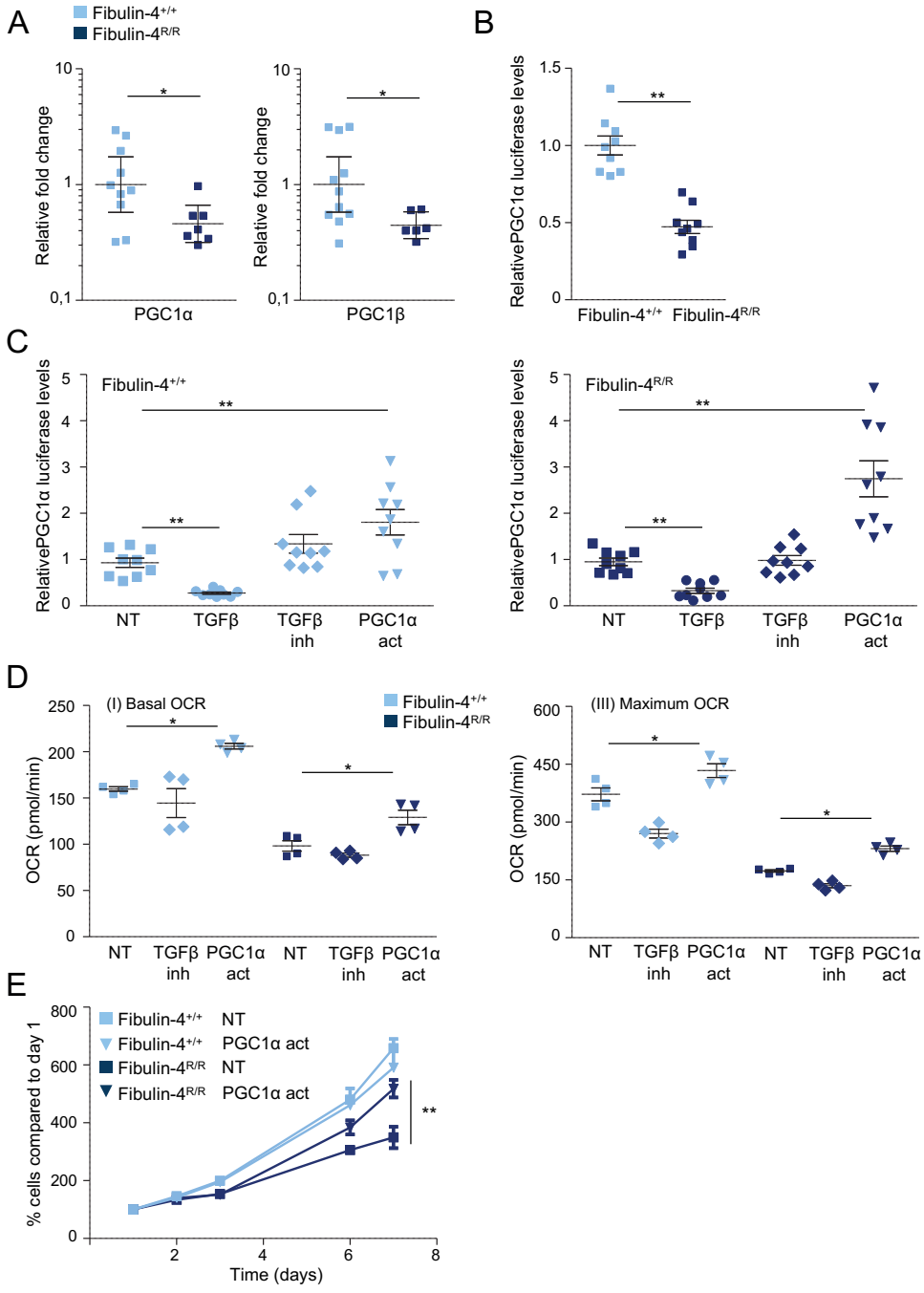

Figure 6. PGC1α expression and activity changes in Fibulin-4$^{R/R}$ aortas and VSMCs

A) Real-time PCR analysis shows significantly downregulated mRNA levels of PGC1α and PGC1β in Fibulin-$4^{R/R}$ compared to Fibulin-$4^{+/+}$ aortas ($p<0.05$, $n=7$ and $n=11$, respectively, Student t-test on log-transformed data). **B)** Relative luciferase levels show decreased PGC1α transcriptional activation in Fibulin-$4^{R/R}$ compared to Fibulin-$4^{+/+}$ VSMCs ($p<0.01$, Student t-test on log-transformed data). **C)** Relative luciferase levels show decreased PGC1α transcriptional activation after TGFβ treatment in both Fibulin-$4^{R/R}$ (right) and Fibulin-$4^{+/+}$ (left) VSMCs compared to the untreated (NT) control. Forskolin, a potent PGC1α activator, significantly increases PGC1α transcriptional activation in both Fibulin-$4^{R/R}$ and Fibulin-$4^{+/+}$ VSMCs to the same extent as compared to the untreated control. Data is shown for 3 independent experiments, $n=3$ cell lines per genotype. TGFβ inhibition does not significantly increase PGC1α activity. **D)** Scatter plots depicting the basal and maximum Oxygen Consumption Rate (OCR) in Fibulin-$4^{+/+}$ and Fibulin-$4^{R/R}$ VSMCs after forskolin treatment, which activates PGC1α, compared to the untreated controls, and TGFβ inhibition. Both Fibulin-$4^{+/+}$ and to Fibulin-$4^{R/R}$ show a significant increase in basal and maximum OCR compared to the untreated controls ($p<0.01$, Student t-test) after forskolin treatment. TGFβ inhibition does not show a significant increase. Experiments were performed twice, $n=2$ cell lines per genotype**. E)** Growth curves of Fibulin-$4^{R/R}$ and Fibulin-$4^{+/+}$ VSMCs showing that activation of PGC1α significantly restores the reduced growth of Fibulin-$4^{R/R}$ VSMCs compared to the untreated situation (NT) ($p<0.01$, non-linear fit of exponential decay). Experiments were performed twice, $n=2$ cell lines per genotype, the mean of two cell lines is shown.

$4^{R/R}$ VSMCs, treatment with TGFβ significantly reduced PGC1α transcription (Fig 6C, $p< 0.01$), showing that also in VSMCs TGFβ signalling negatively regulates PGC1α. Yet, TGFβR inhibition did not significantly increase PGC1α activation, pointing to the involvement of non-canonical TGFβ signalling as SB431542 does not inhibit JNK, p38MAPK or ERK signalling. Forskolin significantly induced PGC1α activity in both Fibulin-$4^{R/R}$ and Fibulin-$4^{+/+}$ VSMCs (Fig 6C, $p<0.01$); in both cases a 3-fold induction compared to the untreated situation. These data point to an active inhibition of PGC1α activity in VSMCs of Fibulin-$4^{R/R}$ aortas. We next performed seahorse experiments in which we either examined the effect of TGFβR inhibition, or PGC1α activation. Interestingly, activation of PGC1α increased basal and maximum oxygen consumption in both Fibulin-$4^{+/+}$ and Fibulin-$4^{R/R}$ VSMCs (Fig 6D, $p<0.05$), whereas TGFβR inhibition did not have the same effect. It was previously found that Fibulin-$4^{R/R}$ VSMCs show low proliferation rates compared to Fibulin-$4^{+/+}$ VSMCs, which can be rescued by inhibiting TGFβ [38]. As TGFβ negatively regulates PGC1α levels, we examined whether increased PGC1α levels would also rescue this low proliferation rate. Indeed, PGC1α activation was able to significantly increase the proliferation rate of Fibulin-$4^{R/R}$ VSMCs specifically (Fig 6E, $p<0.01$). Taken together, these results show that PGC1α, an important molecular switch between mitochondrial biogenesis and organismal metabolism, is downregulated in aortas of Fibulin-$4^{R/R}$ animals due to increased TGFβ signalling. When activated, PGC1α can restore the decrease in oxygen consumption and the decreased proliferation in Fibulin-$4^{R/R}$ VSMCs.

DISCUSSION

In this study we took an integrative approach to better understand the molecular mechanisms involved in aneurysm formation, by using a combination of proteomics, genomics and functional experiments on thoracic aortas of aneurysmal Fibulin-$4^{R/R}$ animals. Interestingly, these data indicated changes in mitochondrial function and energy metabolism. Indeed, we measured a decrease in oxidative phosphorylation in VSMCs derived from the thoracic aorta of Fibulin-$4^{R/R}$ and Fibulin-$4^{+/+}$ animals. In addition, we observed smaller mitochondria, but not less mitochondria or lower activity of mitochondrial complexes. Furthermore, in Fibulin-$4^{R/R}$ compared to Fibulin-$4^{+/+}$ mice, we observed aortic gene expression differences that indicated altered aortic metabolic processes. Upstream regulator analysis on gene and protein expression data indicated PGC1α, PPARα and PPARγ as significant regulators in this process. Moreover, we found that PGC1α transcriptional activation was greatly reduced in VSMCs derived from Fibulin-$4^{R/R}$ aortas, and once PGC1α was activated in these VSMCs, this restored the decreased OCR observed in Fibulin-$4^{R/R}$ VSMCs as well as their reduced growth rate.

We verified that the observed defect in mitochondrial function was due to reduced Fibulin-4 in Fibulin-$4^{R/R}$ cells, rather than potential secondary effects associated with the engineered allele; to this end, we used the Fibulin-4^{SMKO} mouse model as a control, in which the Fibulin-4 gene is completely knocked out in VSMCs specifically. Indeed, these Fibulin-4^{SMKO} VSMCs showed a diminished oxygen consumption rate, as we observed for Fibulin-$4^{R/R}$ VSMCs, showing that complete deletion of Fibulin-4 has a similar effect on mitochondrial respiration as the Fibulin-4 reduced allele.

Although very little data are available on involvement of mitochondria in aneurysm formation and development, some evidence points in this direction. For example, mutations in *SLC2A10* result in Arterial Tortuosity Syndrome (ATS, OMIM#208050,[43]) a connective tissue disorder characterized by elongation and tortuosity of the major arteries including the aorta. *SLC2A10* encodes for GLUT10, a glucose transporter that transports l-dehydro ascorbic acid (DHA) into mitochondria. The absence of GLUT10 leads to decreased DHA recycling and thus to more oxidative damage. In zebrafish, defects in this gene lead to problems in development of the cardiovascular system in parallel to mitochondrial dysfunction[44]. In line with this notion, we demonstrate that VSMCs from the Tgfbr-$1^{M318R/+}$ mouse, a model for LDS[34], similarly show reduced OCR. Moreover, we find that Marfan and Loeys-Dietz patient fibroblasts with mutations in the *FBN1, TGFBR2* and *SMAD3* genes also show reduced OCR. These observations support the concept that altered mitochondrial function plays a role in aneurysmal disease.

An important question is how a deficiency in a protein involved in structural integrity of the ECM can lead to altered mitochondrial function and metabolism. External cues can lead to cytoskeleton

rearrangements since the ECM is connected to the cytoskeleton via integrins. Alternatively, ECM disturbances could invoke alterations in mechanotransduction that lead to modifications in the cytoskeleton or maybe even to its disintegration. Mitochondria depend on the cytoskeleton for their motility and proper function (for review see[45]). Thus, if the ECM disintegrates, this could lead to cytoskeleton disintegration due to loss of connections. In turn, this could lead to structural or functional defects in mitochondria. In fact, several genes that are components of the cytoskeleton are mutated in aneurysmal disease, exemplifying that the cytoskeleton is an important factor. One example is *ACTA2*, encoding αSMA, which is a major constituent of the contractile apparatus, that when mutated, leads to ascending aortic aneurysms and dissection (AAT6, OMIM##611788 [6, 46]). However, although we did observe mitochondrial function changes and a reduction in mitochondrial size, mitochondrial structure and appearance did not seem to be affected. Also, mitochondria are still aligned along the actin cytoskeleton as could be inferred from EM pictures and stainings for actin.

In addition, Fibulin-$4^{R/R}$ mice show increased TGFβ signalling. Notably, several papers recently reported that TGFβ signalling negatively regulates PGC1α levels [40-42]. Interestingly, derived from our -omics data, PGC1α, PPARα and γ were identified as key components in the mitochondrial biogenesis signalling process. PGC1α is a transcriptional co-activator and is expressed in tissues with high oxidative capacity, where it serves important roles in regulation of mitochondrial functional capacity and cellular energy metabolism[47]. Physiological conditions that demand increased mitochondrial energy production, such as exercise and fasting, induce PGC1α activity. Likewise, low PGC1α levels imply reduced mitochondrial function. Accordingly, studies on PGC1α deficient ($PGC1\alpha^{-/-}$) mice have shown that PGC1α is necessary for regulation of mitochondrial function and cellular metabolism[48, 49]. Both mitochondrial volume density and respiratory capacity are reduced in these mice and there is no normal control of body fat mass, which emphasizes the importance of PGC1α in fatty acid β-oxidation. Furthermore, $PGC1\alpha^{-/-}$ mice do not respond normally to increased demands for energy[49]. PGC1α is involved in the mitochondrial oxidation of fatty acids for energy in the cell through direct co-activation of PPARs[47, 50]. Recently it was shown that PGC1α protein expression is also lowered in aortic material isolated from patients with abdominal aneurysms[51], which indicates that PGC1α expression may play a regulatory role in both thoracic and abdominal aneurysms [51]. Moreover, increasing mitochondrial function via PGC1α activation has a positive effect on aging and longevity[52, 53]. Interestingly, we not only found lower PGC1α expression in Fibulin-$4^{R/R}$ thoracic aortas, but also PGC1α transcriptional activation itself was down in Fibulin-$4^{R/R}$ VSMCs. However, this activation could be enhanced by forskolin, a PGC1α activator, and enhancement of PGC1α activation was able to restore the decreased oxidative respiration observed in Fibulin-$4^{R/R}$ VSMCs.

We also found that TGFβ decreased PGC1α transcriptional levels in Fibulin-$4^{+/+}$ and Fibulin-$4^{R/R}$ VSMCs, implying that the increased TGFβ signalling in Fibulin-$4^{R/R}$ aortas and VSMCs

is responsible for the decreased PGC1α levels, thus impacting mitochondrial respiration. This would also explain why we find reduced mitochondrial respiration in cells derived from other aneurysmal syndromes that show increased TGFβ signalling, such as LDS and Marfan. Ramnath et al showed that lowering of TGFβ levels in Fibulin-4$^{R/R}$ VSMCs restored their reduced proliferation rate [38]. Similarly, we now show that by activating PGC1α, we can also increase this proliferation rate, suggesting that this reduced proliferation phenotype is induced by increased TGFβ levels, possibly via PGC1α reduction.

It is evident that mitochondria are major cellular sources of ROS and changes in metabolism can alter mitochondrial function and the resulting ROS production. Likewise, in Fibulin-4$^{R/R}$ animals, we find evidence for increased ROS in the aorta. In this regard, changes in mitochondrial metabolism could also be an attempt to adapt to increased ROS, or to reduce ROS in response to a potential source of damage, at the organismal level. In line with this, we also find reduced oxygen consumption in other muscle cell containing organs; heart and skeletal muscle, but not in kidney or liver. Furthermore, in Fibulin-4$^{R/R}$ animals we observe a relative shift from glucose utilization to fatty acid usage as evidenced from metabolic parameters in blood and liver, as well as from our aortic gene expression analysis. The accumulation of glycogen in the liver might indicate increased storage of glucose into glycogen, in accordance to a relative increase in fatty acid β-oxidation that provides the energy for gluconeogenesis in the absence of an increased demand for glucose from the liver. Interestingly, newborn livers do not yet show these changes in liver metabolism. However, they do already show aneurysms, which may indicate that the aortic structural and/or signalling changes induce the liver metabolic changes at a later stage. The observed metabolic changes in adult Fibulin-4$^{R/R}$ mice are even more interesting since we did not detect changes in the liver mitochondrial complexes themselves, but did observe upregulation of PGC1α mRNA levels, pointing to a normal response of the liver to a change in demand of energy carrier type. Plasma measurements of Fibulin-4$^{R/R}$ mice show significantly lower levels of ketone bodies compared to their wildtype littermates. Taken together, this could indicate that the thoracic aorta of Fibulin-4$^{R/R}$ mice retrieves its energy from ketone bodies rather than from glucose, which could be the underlying reason for the liver to switch from glucose to fatty acid usage. In fact, adapting organismal metabolism under conditions of stress, such as organ damage, is a well-known survival mechanism in aging that attempts to preserve the organism by allowing time and energy for repair[54-56]. Actually, mitochondrial dysfunction itself is considered an important hallmark of aging[57]. ROS and mitochondrial dysfunction both increase with age, resulting in decreased bioenergetic efficiency. In fact, age-related aneurysms show many vascular aging characteristics such as elastin breakdown, collagen deposition as well as morphological changes in VSMCs [58]. Previously, we identified similar overexpression of miR-29b in Fibulin-4$^{R/R}$ aneurysmal aortas and aging mouse aortas, concomitant with reduced ECM protein expression thereby sensitizing the aorta for aneurysms formation[39]. In line with this, structural ECM changes could induce signalling processes that are partly mediated by

TGFβ, including those involving mitochondrial biogenesis. These signalling responses would then attempt to reduce aortic damage, similar to the organismal response observed in aging.

In this context, it would be interesting to see the effect of PGC1α activators on aneurysm formation in the Fibulin-$4^{R/R}$ mouse. Previously, calorie restriction has been shown to have positive effects on mitochondrial biogenesis as well as many aging characteristics in different species[59-62], and notably also affects PGC1α signalling by increasing PGC1α. In line with this, the results reported here could open up the exciting possibility of nutritional interventions as a possible treatment for aneurysmal disease.

FUNDING

This work was supported by the 'Lijf en Leven' grant (2011) 'DIVERS' (dilaterend versus stenoserend vaatlijden) (IvdP; PvH, JE); The FACS machine was purchased thanks to the ZonMW (91109036) equipment grant (RvdL).

ACKNOWLEDGEMENTS

We would like to thank Julian Benschop for isolating the RNA used in the gene expression experiments, Bibi van Thiel, Susan Ghazi and Sylvia Gabriëls for technical assistance, Daniëlle Majoor-Krakauer, Ingrid van der Laar and Judith Verhagen for providing the human patient fibroblasts, Carmen Halabi for providing us with the Fibulin-4 antibody, and the Biomics core facility at the Erasmus Medical Center for running the mouse exon arrays. We acknowledge Bruce Spiegelman for the use of the Addgene plasmid 8887 in the PGC1αluciferase assay.

CONFLICT OF INTEREST

None declared

References

1. Dietz, H.C., et al., *Marfan syndrome caused by a recurrent de novo missense mutation in the fibrillin gene.* Nature, 1991. **352**(6333): p. 337-9.
2. Longo, G.M., et al., *Matrix metalloproteinases 2 and 9 work in concert to produce aortic aneurysms.* J Clin Invest, 2002. **110**(5): p. 625-32.
3. Neptune, E.R., et al., *Dysregulation of TGF-beta activation contributes to pathogenesis in Marfan syndrome.* Nat Genet, 2003. **33**(3): p. 407-11.
4. Judge, D.P. and H.C. Dietz, *Marfan's syndrome.* Lancet, 2005. **366**(9501): p. 1965-76.
5. Loeys, B.L., et al., *A syndrome of altered cardiovascular, craniofacial, neurocognitive and skeletal development caused by mutations in TGFBR1 or TGFBR2.* Nat Genet, 2005. **37**(3): p. 275-81.
6. Guo, D.C., et al., *Mutations in smooth muscle alpha-actin (ACTA2) lead to thoracic aortic aneurysms and dissections.* Nat Genet, 2007. **39**(12): p. 1488-93.
7. Moltzer, E., et al., *The role of the renin-angiotensin system in thoracic aortic aneurysms: clinical implications.* Pharmacol Ther, 2011. **131**(1): p. 50-60.
8. Moltzer, E., et al., *Impaired vascular contractility and aortic wall degeneration in fibulin-4 deficient mice: effect of angiotensin II type 1 (AT1) receptor blockade.* PLoS One, 2011. **6**(8): p. e23411.
9. Holm, T.M., et al., *Noncanonical TGFbeta signaling contributes to aortic aneurysm progression in Marfan syndrome mice.* Science, 2011. **332**(6027): p. 358-61.
10. Huang, J., et al., *Angiotensin-converting enzyme-induced activation of local angiotensin signaling is required for ascending aortic aneurysms in fibulin-4-deficient mice.* Sci Transl Med, 2013. **5**(183): p. 183ra58, 1-11.
11. Papke, C.L. and H. Yanagisawa, *Fibulin-4 and fibulin-5 in elastogenesis and beyond: Insights from mouse and human studies.* Matrix Biol, 2014.
12. Cook, J.R., et al., *Cardiovascular manifestations in Marfan syndrome and related diseases; multiple genes causing similar phenotypes.* Clin Genet, 2014.
13. Yamashiro Y, Y.H., *Crossing Bridges between Extra- and Intra-Cellular Events in Thoracic Aortic Aneurysms.* J Atheroscler Thromb. , 2017: p. 1-12.
14. Brooke, B.S., et al., *Angiotensin II blockade and aortic-root dilation in Marfan's syndrome.* N Engl J Med, 2008. **358**(26): p. 2787-95.
15. Habashi, J.P., et al., *Angiotensin II type 2 receptor signaling attenuates aortic aneurysm in mice through ERK antagonism.* Science, 2011. **332**(6027): p. 361-5.
16. Habashi, J.P., et al., *Losartan, an AT1 antagonist, prevents aortic aneurysm in a mouse model of Marfan syndrome.* Science, 2006. **312**(5770): p. 117-21.
17. Hanada, K., et al., *Perturbations of vascular homeostasis and aortic valve abnormalities in fibulin-4 deficient mice.* Circ Res, 2007. **100**(5): p. 738-46.
18. Kaijzel, E.L., et al., *Multimodality imaging reveals a gradual increase in matrix metalloproteinase activity at aneurysmal lesions in live fibulin-4 mice.* Circ Cardiovasc Imaging, 2010. **3**(5): p. 567-77.

19. Ramnath, N.W., et al., *Extracellular matrix defects in aneurysmal Fibulin-4 mice predispose to lung emphysema.* PLoS One, 2014. **9**(9): p. e106054.
20. Argraves, W.S., et al., *Fibulins: physiological and disease perspectives.* EMBO Reports, 2003. **4**(12): p. 1127-31.
21. Chen, Q., et al., *Fibulin-4 regulates expression of the tropoelastin gene and consequent elastic-fibre formation by human fibroblasts.* Biochem J, 2009. **423**(1): p. 79-89.
22. Giltay, R., R. Timpl, and G. Kostka, *Sequence, recombinant expression and tissue localization of two novel extracellular matrix proteins, fibulin-3 and fibulin-4.* Matrix Biol, 1999. **18**(5): p. 469-80.
23. Davis, E.C., *Smooth muscle cell to elastic lamina connections in developing mouse aorta. Role in aortic medial organization.* Lab Invest, 1993. **68**(1): p. 89-99.
24. Dasouki, M., et al., *Compound heterozygous mutations in fibulin-4 causing neonatal lethal pulmonary artery occlusion, aortic aneurysm, arachnodactyly, and mild cutis laxa.* American Journal of Medical Genetics Part A, 2007. **143**(22): p. 2635-41.
25. Hoyer, J., et al., *Lethal cutis laxa with contractural arachnodactyly, overgrowth and soft tissue bleeding due to a novel homozygous fibulin-4 gene mutation.* Clin Genet, 2009. **76**(3): p. 276-81.
26. Hucthagowder, V., et al., *Fibulin-4: a novel gene for an autosomal recessive cutis laxa syndrome.* Am J Hum Genet, 2006. **78**(6): p. 1075-80.
27. Renard, M., et al., *Altered TGFbeta signaling and cardiovascular manifestations in patients with autosomal recessive cutis laxa type I caused by fibulin-4 deficiency.* Eur J Hum Genet, 2010. **18**(8): p. 895-901.
28. Horiguchi, M., et al., *Fibulin-4 conducts proper elastogenesis via interaction with cross-linking enzyme lysyl oxidase.* Proc Natl Acad Sci U S A, 2009. **106**(45): p. 19029-34.
29. McLaughlin, P.J., et al., *Targeted disruption of fibulin-4 abolishes elastogenesis and causes perinatal lethality in mice.* Mol Cell Biol, 2006. **26**(5): p. 1700-9.
30. Huang, J., et al., *Fibulin-4 deficiency results in ascending aortic aneurysms: a potential link between abnormal smooth muscle cell phenotype and aneurysm progression.* Circ Res, 2010. **106**(3): p. 583-92.
31. Cox, B. and A. Emili, *Tissue subcellular fractionation and protein extraction for use in mass-spectrometry-based proteomics.* Nat Protoc, 2006. **1**(4): p. 1872-8.
32. van den Berg, D.L., et al., *An Oct4-centered protein interaction network in embryonic stem cells.* Cell Stem Cell, 2010. **6**(4): p. 369-81.
33. Proudfoot, D.a.S., C., *Human vascular smooth muscle cell culture*, in *Human Cell Culture Protocols (methods in Molecular Biology)*, R.R. Mitry, Hughes, Robin D. , Editor. 2012, Springer. p. 251-263.
34. Gallo, E.M., et al., *Angiotensin II-dependent TGF-beta signaling contributes to Loeys-Dietz syndrome vascular pathogenesis.* J Clin Invest, 2014. **124**(1): p. 448-60.
35. Orellana, E.A. and A.L. Kasinski, *Sulforhodamine B (SRB) Assay in Cell Culture to Investigate Cell Proliferation.* Bio Protoc, 2016. **6**(21).
36. Kielland, A., et al., *In vivo imaging of reactive oxygen and nitrogen species in inflammation using the luminescent probe L-012.* Free Radic Biol Med, 2009. **47**(6): p. 760-6.

37. Handschin, C., et al., *An autoregulatory loop controls peroxisome proliferator-activated receptor gamma coactivator 1alpha expression in muscle.* Proc Natl Acad Sci U S A, 2003. **100**(12): p. 7111-6.
38. Ramnath, N.W., et al., *Fibulin-4 deficiency increases TGF-beta signalling in aortic smooth muscle cells due to elevated TGF-beta2 levels.* Sci Rep, 2015. **5**: p. 16872.
39. Boon, R.A., et al., *MicroRNA-29 in aortic dilation: implications for aneurysm formation.* Circ Res, 2011. **109**(10): p. 1115-9.
40. Fournier, B., et al., *Blockade of the activin receptor IIb activates functional brown adipogenesis and thermogenesis by inducing mitochondrial oxidative metabolism.* Mol Cell Biol, 2012. **32**(14): p. 2871-9.
41. Tiano, J.P., D.A. Springer, and S.G. Rane, *SMAD3 negatively regulates serum irisin and skeletal muscle FNDC5 and peroxisome proliferator-activated receptor gamma coactivator 1-alpha (PGC-1alpha) during exercise.* J Biol Chem, 2015. **290**(18): p. 11431.
42. Yadav, H., et al., *Protection from obesity and diabetes by blockade of TGF-beta/Smad3 signaling.* Cell Metab, 2011. **14**(1): p. 67-79.
43. Coucke, P.J., et al., *Mutations in the facilitative glucose transporter GLUT10 alter angiogenesis and cause arterial tortuosity syndrome.* Nat Genet, 2006. **38**(4): p. 452-7.
44. Willaert, A., et al., *GLUT10 is required for the development of the cardiovascular system and the notochord and connects mitochondrial function to TGFbeta signaling.* Hum Mol Genet, 2012. **21**(6): p. 1248-59.
45. de Cavanagh, E.M., et al., *Angiotensin II, mitochondria, cytoskeletal, and extracellular matrix connections: an integrating viewpoint.* Am J Physiol Heart Circ Physiol, 2009. **296**(3): p. H550-8.
46. Renard, M., et al., *Novel MYH11 and ACTA2 mutations reveal a role for enhanced TGFbeta signaling in FTAAD.* Int J Cardiol, 2013. **165**(2): p. 314-21.
47. Finck, B.N. and D.P. Kelly, *PGC-1 coactivators: inducible regulators of energy metabolism in health and disease.* J Clin Invest, 2006. **116**(3): p. 615-22.
48. Lehman, J.J., et al., *Peroxisome proliferator-activated receptor gamma coactivator-1 promotes cardiac mitochondrial biogenesis.* J Clin Invest, 2000. **106**(7): p. 847-56.
49. Leone, T.C., et al., *PGC-1alpha deficiency causes multi-system energy metabolic derangements: muscle dysfunction, abnormal weight control and hepatic steatosis.* PLoS Biol, 2005. **3**(4): p. e101.
50. Wenz, T., *Mitochondria and PGC-1alpha in Aging and Age-Associated Diseases.* J Aging Res, 2011. **2011**: p. 810619.
51. Gabrielson, M., et al., *Altered PPARgamma Coactivator-1 Alpha Expression in Abdominal Aortic Aneurysm: Possible Effects on Mitochondrial Biogenesis.* J Vasc Res, 2016. **53**(1-2): p. 17-26.
52. Feige, J.N., et al., *Specific SIRT1 activation mimics low energy levels and protects against diet-induced metabolic disorders by enhancing fat oxidation.* Cell Metab, 2008. **8**(5): p. 347-58.
53. Rera, M., et al., *Modulation of longevity and tissue homeostasis by the Drosophila PGC-1 homolog.* Cell Metab, 2011. **14**(5): p. 623-34.
54. Garinis, G.A., et al., *Persistent transcription-blocking DNA lesions trigger somatic growth attenuation associated with longevity.* Nat Cell Biol, 2009. **11**(5): p. 604-15.

55. Schumacher, B., et al., *Delayed and accelerated aging share common longevity assurance mechanisms.* PLoS Genet, 2008. **4**(8): p. e1000161.
56. van der Pluijm, I., et al., *Impaired genome maintenance suppresses the growth hormone--insulin-like growth factor 1 axis in mice with Cockayne syndrome.* PLoS Biol, 2007. **5**(1): p. e2.
57. Lopez-Otin, C., et al., *The hallmarks of aging.* Cell, 2013. **153**(6): p. 1194-217.
58. Collins, J.A., et al., *The anatomy of the aging aorta.* Clin Anat, 2014. **27**(3): p. 463-6.
59. Colman, R.J., et al., *Caloric restriction delays disease onset and mortality in rhesus monkeys.* Science, 2009. **325**(5937): p. 201-4.
60. de Cavanagh, E.M., F. Inserra, and L. Ferder, *Angiotensin II blockade: a strategy to slow ageing by protecting mitochondria?* Cardiovasc Res, 2011. **89**(1): p. 31-40.
61. Piper, M.D., et al., *Dietary restriction and aging: a unifying perspective.* Cell Metab, 2011. **14**(2): p. 154-60.
62. Vermeij, W.P., et al., *Restricted diet delays accelerated ageing and genomic stress in DNA-repair-deficient mice.* Nature, 2016. **537**(7620): p. 427-431.

SUPPLEMENTAL METHODS

Preparation of aorta protein extracts and MS/MS protein identification continued

Nanoflow LC-MS/MS was performed on an 1100 series capillary LC system (Agilent Technologies) coupled to an LTQ mass spectrometer (Thermo) operating in positive mode and equipped with a nanospray source. Peptide mixtures were trapped on a ReproSil C18 reversed-phase column (Dr Maisch GmbH; column dimensions 2 cm × 100 μm, packed in-house) at a flow rate of 8 μl min^{-1}. Peptide separation was performed on a ReproSil C18 reversed-phase column (Dr Maisch GmbH; column dimensions 20 cm × 75 μm, packed in-house) using a linear gradient from 0% to 80% B (A = 0.1% formic acid; B = 80% (v/v) acetonitrile, 0.1% formic acid) in 90 min and at a constant flow rate of 200 nl min^{-1}. The column eluent was directly sprayed into the ESI source of the mass spectrometer. Mass spectra were acquired in continuum mode; fragmentation of the peptides was performed in data-dependent mode by CID. Peak lists were created from raw data files using the Mascot Distiller software (version 2.4; MatrixScience). The Mascot algorithm (version 2.3; MatrixScience) was used for searching against a Uniprot database (release 2012_02.fasta, taxonomy: Mus musculus (mouse)). Peptide tolerance was set to 2Da. and fragment ion tolerance was set to 0.8 Da. A maximum number of two missed cleavages by trypsin was allowed and carbamidomethylated cysteine and oxidized methionine were set as fixed and variable modifications, respectively.

Immunofluorescent stainings

VSMC cultured on collagenized glass slides were stained with Mitotracker CMX Ros for 30 min at 37°C. After incubation cells were washed with PBS and fixed with 2% paraformaldehyde for 15 min at room temperature. Excess Mitotracker staining was removed by 5 min incubation with 80% ice cold acetone. Slides were mounted with vecthashield including dapi.

Mitotracker experiments

Single cells were prepared by trypsinization and spinning at 1000 rpm (corresponding to 18g) for 5 minutes. Resulting pellets were replenished with DMEM culture medium without phenol red, supplemented with 5% FCS. Per experiment 400.000 cells were stained with Hoechst 33342 (10μg) and Mitotracker CMX Ros (25nM) for 30 min at 37°C. Single and double stained FL cells were used for the setup of gaitings and as controls. All analysis and sorting experiments were performed on a BD SORP FACS Aria II cell sorter (BD Biosciences). For the combined mitotracker and SiR-Actin staining, VSMCs were seeded on collagen coated coverslips in a concentration of 2x10^4 cells/ml. After 2 days 0.1nM SiR-Actin was added to the cells for 19h, after which cells were washed with PBS and replenished with medium containing 200nM of mitotracker for 30 min of pulse labeling. Then, cells where washed with PBS, fixated with 2% paraformaldehyde for 10 minutes. Coverslips containing the cells were mounted with vectashield containing dapi. Fluorescence imaging was done on a Axio Imager.D2 (Zeiss) equipped with a CoolSNAP MYO

CCD camera (Photometrics) and a PhotoFluor LM-75 Long FL Lamp (89north). Images were recorded using a 63x 1.4NA Plan Apochromat objective and the following filtercubes (Chroma Technology Corp.): 49000 ET_DAPI, 49008 ET-mCherry/Texas Red, and 49009 ET-Cy5.

Electron microscopy

Following cardiac perfusion thoracic aortas were harvested, dissected into small segments and left in fixative (3% in glutaraldehyde in 0.1 M sodium cacodylate buffer (pH 7.4)) overnight at 4°C. After extensive washing in 0.1 M sodium cacodylate buffer, the tissues were sequentially treated with osmium tetroxide, tannic acid and uranyl acetate, then dehydrated and embedded in Epon as previously described. Thin sections (60 nm) were counterstained with methanolic uranyl acetate and lead citrate and viewed using a Tecnai 12 transmission electron microscope at 120 kV. ImageJ was used to quantify the perimeter and area of 30 mitochondria from two different animals of each genotype obtained by TEM. A Student *t*-test was used to calculate the p-values. To ensure that the mitochondria were oriented in the right direction (following the orientation of the actin filaments); cross sections and longitudinal sections of aorta were viewed by TEM.

Western Blots

Liver and thoracic aortic tissue from Fibulin-$4^{+/+}$ and Fibulin-$4^{R/R}$ mice, snap frozen and stored at -80 °C, was used for this experiment. Tissue was lysed in radioimmunoprecipitation assay (RIPA) buffer (50 mM Tris-HCl pH 8, 1% NP-40, 0.5% Na-deoxycholate, 0.1% SDS, 150 mM NaCl) containing complete protease inhibitor cocktail (1:100) (Roche applied science), to exclude degradation of proteins within the tissue. Lysates were sheared and denatured at 50 ^{0}C. To detect ECM proteins Fibulin-4 and Elastin aortic lysates were obtained via the urea extraction method. In short, 250ul of 8M urea in 16 mM Na_2HPO_4 at pH7 with 1x protease inhibitor and a metal bead was added to each aorta. Samples were homogenized for 3 min. Supernatant was incubated at 4°C overnight on rocker. Next, supernatant was centrifuged 14000 rpm for 3 min. to remove debris. The resulting supernatant was diluted with 16mM Na_2HPO_4 for a final concentration of 2M urea. Then,10% TCA solution at 1/4th volume of protein supernatant volume, was added to each sample and incubated on ice for 1 hr, after which an equal volume of cold acetone was added and incubated on ice for 1 hr. Samples were then centrifuged at 14k rpm for 10 min 4 °C, pellets were washed with 750 uL of cold acetone, again centrifuge at 14k rpm for 10 min 4 °C. The washing step was repeated twice. Protein concentration in tissue lysates was determined by Lowry protein assay. 15μg of total protein lysate was fractionated on 4-20% mini-protean TGX gel (Biorad) by SDS-PAGE. The fractionated proteins were transferred to a PVDF membrane (Immobilon) by western blot procedure (1hour, 100V). To block nonspecific binding of the antibodies, the membrane was incubated in 5% nonfat milk|0.1% Tween in PBS for 1 hour at room temperature. The protein of interest was detected by primary antibody incubation in 1% nonfat milk, 0.1% Tween in PBS (overnight at 4 ^{0}C). See Table 3 for primary antibodies. The membrane was washed 4 times with 0.1% Tween in PBS for 8 minutes after which the membrane

was incubated with the horseradish peroxidase-labeled secondary antibody: sheep anti-mouse IgG (1:2500) or goat anti-rabbit IgG (1:2500) (Jackson ImmunoResearch Laboratories). The secondary antibody was detected through autoradiography (Alliance 2.7 UVItec) using a chemiluminescence (ECL) system (Amersham Pharmacia Biotech). The expression of the bands was quantified with the Fiji image analyzing software Quantity-One.

Table 3: Primary antibodies used for Western Blot analysis

Primary antibody	Protein	Predicted mol. weight (kDa)	Antibody dilution	Host	Sources
Mitoprofile total OXPHOS Rodent WB antibody Cocktail	Complex I: NDUFB8 Complex II: SDHB Complex III: UQCRC2 Complex IV: MTCO1 Complex V: ATP5A	20 30 47 39 53	1:500	Mouse	MitoSciences, Eugene
Mouse anti-β-catenin IgG	β-Catenin Clone 14	92	1:2000	Mouse	BD Transduction laboratories
Rabbit anti-Fibulin-4 IgG	Fibulin-4	50	1:1000	Rabbit	Gift from Carmen Halabi
Rabbit anti-Elastin IgG	Elastin	68	1:1000	Rabbit	Abcam

Oxygraph and Mitochondrial complex activity measurements continued

Enzyme activities were measured in the homogenates. Citrate synthase, an indicator of the mitochondrial number was measured according to [1]. Mitochondrial complex activities were determined in muscle homogenates by spectrophotometric methods as described before [2, 3]. Complex I or NADH-Coenzyme Q reductase was determined kinetically by following the rotenon sensitive decrease in NADH amount. Complex III or Ubiquinol-cytochrome c reductase was determined by following the Antimycin A sensitive reduction of cytochrome c by reduced decylubiquinol as described [4]. Complex IV or cytochrome c oxidase was measured by following the formation of oxidized cytochrome c. Complex V or ATP synthase was determined as the oligomycin sensitive Mg-ATPase [2, 3]. For objective comparison between genotypes, complex activities were compared relative to amount of protein and based on the amount of CS.

Histology and mouse metabolic parameters

Livers of Fibulin-$4^{+/+}$ and Fibulin-$4^{R/R}$ mice were histologically examined for general pathology and metabolic state. Liver tissue from the same animals was either formalin fixated in 4% formalin or snap frozen in liquid nitrogen. Formalin-fixated tissue was embedded in paraffin wax, 5 mm of paraffin sections were stained with Haematoxylin and Eosin (HE) for general pathology and Periodic Acid-Schiff (PAS) for glycogen storage. 5 mm of frozen sections were used for oil-red-o (ORO) staining to determine the accumulation of neutral fats in the liver. ORO ratio was determined by measuring the ORO stained area, and dividing this by the total area measured. PAS ratio was determined by measuring the PAS stained area, and dividing this by the total

area measured. Blood glucose and β-ketone ketone levels were measured using a Freestyle mini blood glucose or the Freestyle Precision β-ketone measurement device (Abbott Diabetes Care), respectively, on a drop of freshly retrieved whole blood. Lactate levels were measured in a heparin coated capillary filled with 125 μl freshly retrieved whole blood, using the ABL800 FLEX analyzer (Radiometer Medical ApS).

REFERENCES BELONGING TO SUPPLEMENTAL METHODS

1. Srere, P.A., *Citrate Synthase*, in *Methods in Enzymology*. 1969, Academic Press: London. p. 3-11.
2. Scholte, H.R., et al., *Riboflavin-responsive complex I deficiency.* Biochim Biophys Acta, 1995. **1271**(1): p. 75-83.
3. Scholte, H.R., et al., *Defects in oxidative phosphorylation. Biochemical investigations in skeletal muscle and expression of the lesion in other cells.* J Inherit Metab Dis, 1987. **10 Suppl 1**: p. 81-97.
4. Trounce, I.A., et al., *Assessment of mitochondrial oxidative phosphorylation in patient muscle biopsies, lymphoblasts, and transmitochondrial cell lines.* Methods Enzymol, 1996. **264**: p. 484-509.

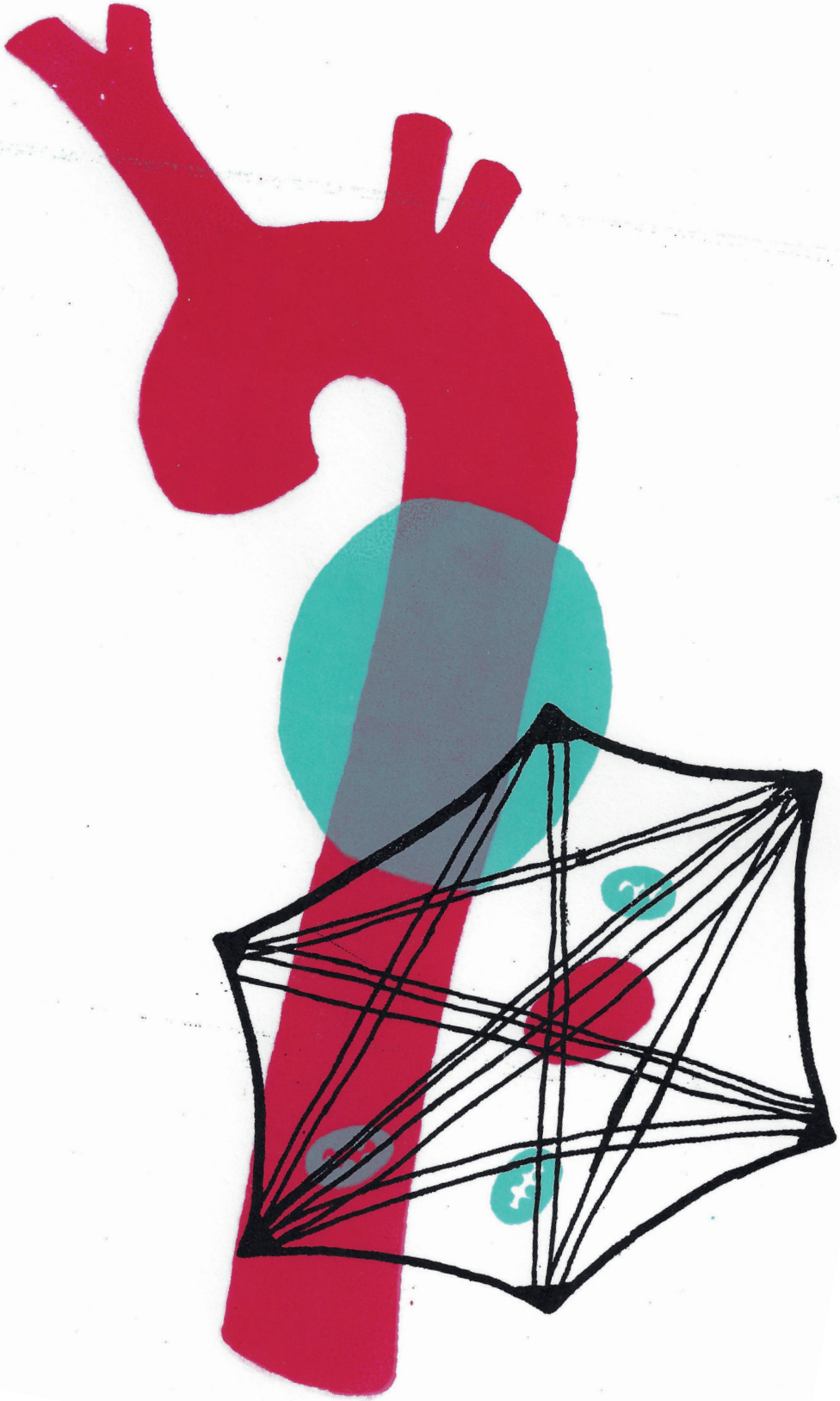

CHAPTER 6

GENE EXPRESSION PROFILING IN SYNDROMIC AND NON-SYNDROMIC HERITABLE THORACIC AORTIC DISEASE: FURTHER EVIDENCE ON THE ROLE OF INFLAMMATION AND MITOCHONDRIAL DYSFUNCTION

Judith M.A. Verhagen[1], Joyce Burger[1,2], Jos A. Bekkers[3], Rutger W.W. Brouwer[4], Marianne L.T. van der Sterre[1], Jan H. von der Thüsen[5], Hennie T. Brüggenwirth[1], Myrthe van den Born[1], Jeroen Essers[2,6,7], Wilfred F.J. van IJcken[4], Marja W. Wessels[1], Ingrid van der Pluijm[2,6], Jolien W. Roos-Hesselink[8], Robert M.W. Hofstra[1], Ingrid M.B.H. van de Laar[1*] and Erwin Brosens[1*]

Departments of [1]Clinical Genetics, [2]Molecular Genetics, [3]Cardiothoracic Surgery, [4]Center for Biomics, [5]Pathology, [6]Vascular Surgery, [7]Radiation Oncology, [8]Cardiology, Erasmus MC, University Medical Center Rotterdam, Rotterdam, the Netherlands.

**These authors contributed equally to this work.*

Manuscript in preparation.

ABSTRACT

Objectives

Thoracic aortic aneurysm is a potentially devastating disorder with a strong genetic predisposition. Despite the identification of multiple disease-causing genes in the past decade, still little is known about the exact underlying mechanisms that drive the pathological changes in the aortic wall. The aim of our study was to compare gene expression profiles of patients with syndromic and non-syndromic heritable thoracic aortic disease (HTAD), in order to identify the underlying molecular pathways that play a role in aneurysm formation.

Methods

We collected aortic wall samples from patients with *FBN1*-positive Marfan syndrome (MFS, n=6) and mutation-negative HTAD (n=15). Control samples were obtained from healthy donor hearts (n=5). mRNA expression levels were measured by RNA sequencing and compared between patients and controls.

Results

FBN1 mRNA expression levels were highly variable in MFS patients and not significantly different from HTAD and controls. Moreover, we did not identify a distinctive TGF-β gene expression signature in MFS patients. Interestingly, in both MFS and HTAD, differential gene expression analysis pointed toward inflammation and mitochondrial dysfunction. In HTAD, we also identified several pathways related to cell adhesion and motility.

Conclusions

Our findings suggest great overlap in the pathophysiological processes underlying MFS and HTAD. More importantly, our results reveal that mitochondrial and inflammatory pathways play important roles in the pathogenesis of HTAD, opening the possibilities for new therapeutic approaches.

INTRODUCTION

Thoracic aortic aneurysms, typically involving the aortic root and/or proximal ascending aorta, are often asymptomatic. However, if left untreated, thoracic aortic aneurysms can result in aortic dissection, rupture or sudden death. Approximately 20% of individuals with thoracic aortic aneurysms and dissections have a positive family history [1], and thus may have a genetic predisposition, now generally referred to as heritable thoracic aortic disease (HTAD) [2].

A major breakthrough in our understanding of HTAD came in 1991, when Dietz et al. identified *FBN1*, encoding the extracellular matrix protein fibrillin-1, as the causal gene for Marfan syndrome (MFS) [3]. Though initially considered a mere structural disorder of the connective tissue caused by fibrillin-1 deficiency, dysregulation of the transforming growth factor-beta (TGF-β) signaling pathway has emerged as the key mechanism in the pathogenesis of MFS. In addition to aortic root dilatation, patients with MFS typically present with ectopia lentis and skeletal features. In over 90% of patients that meet the diagnostic criteria for MFS (Ghent nosology) a pathogenic variant in *FBN1* can be identified [4, 5].

In the past decade, variants in genes encoding other components of the TGF-β signaling pathway and extracellular matrix have emerged as major drivers in the pathogenesis of other syndromic forms of HTAD, such as Loeys-Dietz syndrome and vascular Ehlers-Danlos syndrome [6]. Despite overlapping etiologies, these syndromes display important distinguishing features [7]. In addition, genes that encode components of the vascular smooth muscle cell (VSMC) contractility apparatus have been linked to non-syndromic forms of HTAD [8]. However, despite advancing knowledge and sequencing technologies, only ~30% of families with non-syndromic HTAD receive a molecular diagnosis [9]. The diagnostic yield decreases if sporadic cases are included [10], suggesting that other (genetic) factors remain to be identified in both familial and sporadic thoracic aortic disease. Finding a molecular cause enables predictive testing in relatives and contributes to personalized medical and surgical management [11].

Differential gene expression analysis may provide valuable information regarding the molecular mechanisms underlying thoracic aortic disease. Previous studies have mainly focused on patients with acute ascending aortic (Stanford type A) dissection, suggesting a key role for extracellular matrix assembly and maintenance, cell adhesion and signaling, inflammation and cytoskeleton proteins [12-16]. These studies were performed using microarrays, which rely on pre-designed complement sequence detection. RNA sequencing (RNA-seq), on the contrary, which was used in the present study, delivers unbiased information about the transcriptome, is more sensitive in detecting low abundant transcripts and has a broader dynamic range, allowing for the detection of a larger number of differentially expressed genes [17]. Here, we apply RNA-seq to investigate gene expression profiles in aortic tissue from patients with MFS and to compare these findings with

profiles from patients with mutation-negative HTAD. We hypothesize that (i) patients with MFS have a distinctive TGF-β specific gene expression signature, and (ii) patients without a molecular diagnosis will have a different gene expression signature compared to controls. Moreover, we expect that (iii) the expression signature of patients without a molecular diagnosis can be subdivided into specific clusters; either based on affected biological pathway (e.g. VSMC contractility, TGF-β signaling or other) or specific phenotypic features (e.g. aortic valve morphology, histological characteristics or gender). Characterizing the affected biological pathways and/or gene networks could aid in identifying the underlying genetic factors and may enhance the development of more effective therapies for thoracic aortic disease in individuals with a genetic predisposition.

MATERIALS AND METHODS

Study population

Patients with thoracic aortic disease undergoing elective ascending aortic replacement at the Erasmus University Medical Center between January 2015 and May 2018 were included in this study. Patients with acute aortic dissection and traumatic aortic injuries were excluded. Residual aortic tissue from healthy donor hearts, stored on ice and transported to our center for subsequent implantation, were collected as control samples. Full-thickness aortic wall samples were snap-frozen in liquid nitrogen immediately after surgical removal from the patient or donor heart, and stored at -80°C until further processing.

All patients underwent structured clinical evaluation including medical and family history, physical examination, transthoracic echocardiography and preoperative computed tomography angiography of the thoracic aorta. Aortic diameters were determined at the level of the aortic annulus, sinuses of Valsalva, sinotubular junction, proximal and distal ascending aorta, aortic arch, and proximal and distal descending aorta. Aortic valve morphology and function were documented at surgery. Postoperatively, patients with thoracic aortic disease were offered standard genetic counseling and diagnostic testing (copy number analysis using SNP array and/or whole exome sequencing, see Supplemental Methods) at our outpatient clinic. We applied an exome-based virtual gene panel for targeted analysis of 34 known HTAD-related genes (Supplementary Table S1). Further analysis of selected candidate genes was based on individual characteristics. In patients with a strong suspicion of a specific disorder or known pathogenic variant in the family, we performed targeted analysis of the respective gene by Sanger sequencing. Variants in *FBN1* were classified as dominant negative (DN; interference of mutant with non-mutant fibrillin-1 protein) or haploinsufficient (HI; production of only non-mutant fibrillin-1 protein) using the Alamut software, as described previously [18]. First-degree relatives were offered predictive genetic testing (if appropriate) and/or advised to undergo cardiovascular screening. Our study protocol was approved by the Erasmus MC Medical and Ethical Review

Committee (MEC 2014-579, MEC 2017-040 and MEC 2017-097). All participants provided written informed consent.

Sample selection

From the 61 patients included in the study, we selected 21 patients with either confirmed or suspected (i.e. age at diagnosis <40 years and/or positive family history) genetically triggered thoracic aortic disease: 6 patients with MFS, and 15 patients with non-syndromic HTAD without a pathogenic or likely pathogenic variant in any of the known HTAD-related genes (Table 1). In addition, we obtained 5 control samples from healthy donor hearts (HTx). Samples selected for genome-wide transcriptional analysis were derived from the anterior side of the ascending aorta. Statistical analyses were performed to compare the sample groups for significant differences in baseline characteristics. Data were expressed as mean ± standard deviation for continuous variables, and absolute numbers (percentage) for categorical variables. Comparisons were made using the Student's *t*-test and Fisher's exact test, respectively. All statistical tests were two-sided. Differences between groups were considered statistically significant at *p*-values <0.05. Analyses were performed using Microsoft Excel or GraphPad Software.

Table 1. Demographics of the study population.

	MFS (n=6)	HTAD (n=15)	controls (n=5)
Age at operation (years)	30.2 ± 11.8 †	53.2 ± 16.4	37.8 ± 18.1
Males (%)	4 (67%)	10 (67%)	1/4 (25%) ‡
Caucasian (%)	4 (67%)	15 (100%)	N/A
Max. aortic diameter (mm)	51.5 ± 4.0	53.9 ± 5.7	N/A
Aortic z-score	7.03 ± 2.34	7.29 ± 2.44	N/A
Bicuspid aortic valve	0 (0%)	7 (47%)	0 (0%)
Positive family history	3 (50%)	9 (60%)	N/A
Hypertension	1 (17%)	7 (47%)	N/A
Hypercholesterolemia	0 (0%)	2 (13%)	N/A
Diabetes mellitus	0 (0%)	1 (7%)	N/A
Smoking	1 (17%)	2 (13%)	N/A

HTAD, heritable thoracic aortic disease (without disease-causing variant in known genes); MFS, Marfan syndrome; N/A, not available.

† $p<0.005$ compared to HTAD, ‡ unknown gender in one control sample.

Histopathological examination

Available surgical aortic specimens were systematically examined for histopathologic findings of inflammatory and non-inflammatory aortic diseases according to current guidelines [19, 20]. All specimens were stained for hematoxylin-eosin, Verhoeff-van Gieson (elastin), Picrosirius red (collagen), and Alcian blue (proteoglycans). Additional stains were performed on indication.

RNA sample preparation and sequencing

Frozen tissue samples were ground using a pre-chilled mortar and pestle, and subsequently disrupted and homogenized using a bead mill. Total RNA was extracted with the RNeasy Fibrous Tissue Mini Kit (QIAGEN). Residual genomic DNA was removed using the RNase-Free DNase Set (QIAGEN). RNA concentration, purity and integrity were assessed on the 2100 Bioanalyzer using the RNA 6000 Nano Kit (Agilent Technologies). Only samples with a RNA integrity number (RIN) >7 were eligible for RNA-seq. Libraries were prepared using the TruSeq Stranded mRNA Library Prep Kit (Illumina, San Diego, CA, USA). The resulting DNA libraries were sequenced according to the Illumina TruSeq Rapid v2 protocol on an Illumina HiSeq2500 machine. Paired-end reads were generated of 100 base pairs in length.

Differential expression analysis

Raw RNA-seq data was processed in two ways: using (A) HISAT2 and htseq-count, and (B) CLC Genomics Workbench (see Supplemental Methods for further details). Subsequent normalization and differential expression analysis was performed using three different algorithms. After step A, normalization and differential expression analysis was performed on the public Galaxy server using either DESeq2 version 2.11.40.2 [21] or edgeR version 3.20.7.2 [22]. In approach B, further analysis was performed using the tools provided within CLC Genomics Workbench version 10.0.1 (QIAGEN Bioinformatics). Read counts were normalized for transcript length and total number of mapped reads (RPKM) [23]. Genes with a fold change (FC) ≥ 1.5 and a false discovery rate (FDR) adjusted p-value <0.05 were considered differentially expressed. Data were visualized using the Integrative Genomics Viewer (IGV).

Pathway analysis

Differentially expressed genes were uploaded into the Ingenuity Pathway Analysis (IPA) software, Summer Release 2018 (QIAGEN Bioinformatics). We performed a Core Analysis for each group, using default parameters, to predict effects on pathways and biological functions, and discover plausible upstream regulators and mechanistic networks [24]. Pathways with a negative log10(p-value) greater than 1.3 were considered significant. In addition, gene lists were uploaded to ToppGene to perform gene set enrichment analysis [25].

RESULTS

Patient characteristics

Patients with MFS were significantly younger (mean age 30.2 $\pm$ 11.8 years) than those with mutation-negative HTAD (mean age 53.2 $\pm$ 16.4 years, $p=0.0057$) (Table 1). No significant age difference was found between the patient groups and controls. The majority of MFS and HTAD patients (67%) were male; whereas at least 3 out of 5 controls were female. The maximal aortic

diameters prior to surgical intervention and corresponding z-scores did not significantly differ between patients with MFS and HTAD. There were no significant differences in the presence or absence of cardiovascular risk factors (i.e. hypertension, hypercholesterolemia, diabetes mellitus and smoking) between these groups. The clinical and genetic features of patients with MFS are presented in Table 2.

Histopathological findings

Aortic wall specimens were available for histologic examination in 5/6 MFS patients and 12/15 mutation-negative HTAD patients. Specimens from all MFS patients and five HTAD patients (mean age 36.5 ± 14.2 years) had histopathologic features of moderate to severe overall medial degeneration, i.e. disorganization and fragmentation of elastic fibers, smooth muscle cell nuclei loss, and mucoid extracellular matrix accumulation [20, 26]. Two of these HTAD specimens also showed atherosclerotic lesions with calcification, and (chronic) dissection of the medical layer. In three other HTAD patients (mean age 62.7 ± 6.7 years), aortic specimens showed moderate atherosclerosis. This was associated with inflammation in two patients. In the remaining four HTAD patients (mean age 52.0 ± 20.9 years), histological examination of aortic wall specimens revealed no abnormalities.

RNA-seq data alignment

We generated in excess of 34 million reads per sample (mean 43.5 ± 15.5 million reads). Of these reads, 92 to 99% aligned to the human reference genome. A total of 10,096 transcripts showed detectable expression (defined as mean expression of ≥2 reads per kilobase per million) in the ascending aorta of the control group. Twenty-six transcripts were highly expressed (≥1000 reads per kilobase per million) (Supplemental Table S2), including the known HTAD genes *ACTA2* (aortic smooth muscle actin) [27] and *BGN* (biglycan) [28]. The list further includes several genes that code for calcium-binding and cytoskeletal proteins, such as *MYL9* (myosin light chain 9), *TAGLN* (transgelin), *S100A6* (S100 calcium binding protein A6) and *TMSB4X* (thymosin beta 4 X-linked), that represent good candidate genes for HTAD. Of note, we did not find rare, potentially deleterious variants in these four genes in our in-house cohort of 179 patients with unexplained thoracic aortic disease.

Correlation of transcriptome samples

Principal component analysis (PCA) of gene expression data in CLC Genomics Workbench showed wide scattering of the HTAD samples, which partially overlap with the clustering of MFS samples (Figure 1A). Unsupervised hierarchical clustering showed that the HTAD samples could be subdivided into three separate groups (Figure 1B). This clustering was not related to aortic valve morphology (i.e. bicuspid vs. tricuspid aortic valve) nor the presence or absence of atherosclerotic lesions at histologic examination. The HTAD subgroups will be investigated in more detail in future studies.

Table 2. Clinical and genetic features of patients with MFS.

cDNA change	c..2368_2369insC	c.3506G>T	c.3646G>T	c.4954T>C	c.7003C>T	15q21 deletion (including *FBN1*)
Protein change	p.Cys790Serfs*12	p.Gly1169Val	p.Glu1216*	p.Cys1652Arg	p.Arg2335Trp	
Zygosity	Heterozygous	Heterozygous	Heterozygous	Heterozygous	Homozygous	Heterozygous
Effect	HI	DN	HI	DN	DN	HI
Mutant allele	0/141 (0%)	78/199 (39%)	5/82 (6%)	52/120 (43%)	400/400 (100%)	Absent (0%)
FBN1 mRNA level †	57%	93%	46%	59%	150%	38%
Ectopia lentis	+	+	+	+	+	-
Myopia	Unknown	+	+	+	-	+
Pectus deformity	+	-	-	+	-	-
Scoliosis	-	-	+	+	-	+
Joint hypermobility	+	-	Unknown	+	-	+
Reduced elbow extension	-	-	Unknown	+	-	+
Pes planus	+	-	+	-	+	+
Striae atrophicae	Unknown	+	+	+	+	-
Other		Migraine	Allergic rhinitis	Inguinal hernia	Dural ectasia	Inguinal hernia, intellectual disability

DN, dominant negative; HI, haploinsufficient.

† *FBN1* mRNA expression level compared with controls (n=5). The mean level in controls was set at 100%.

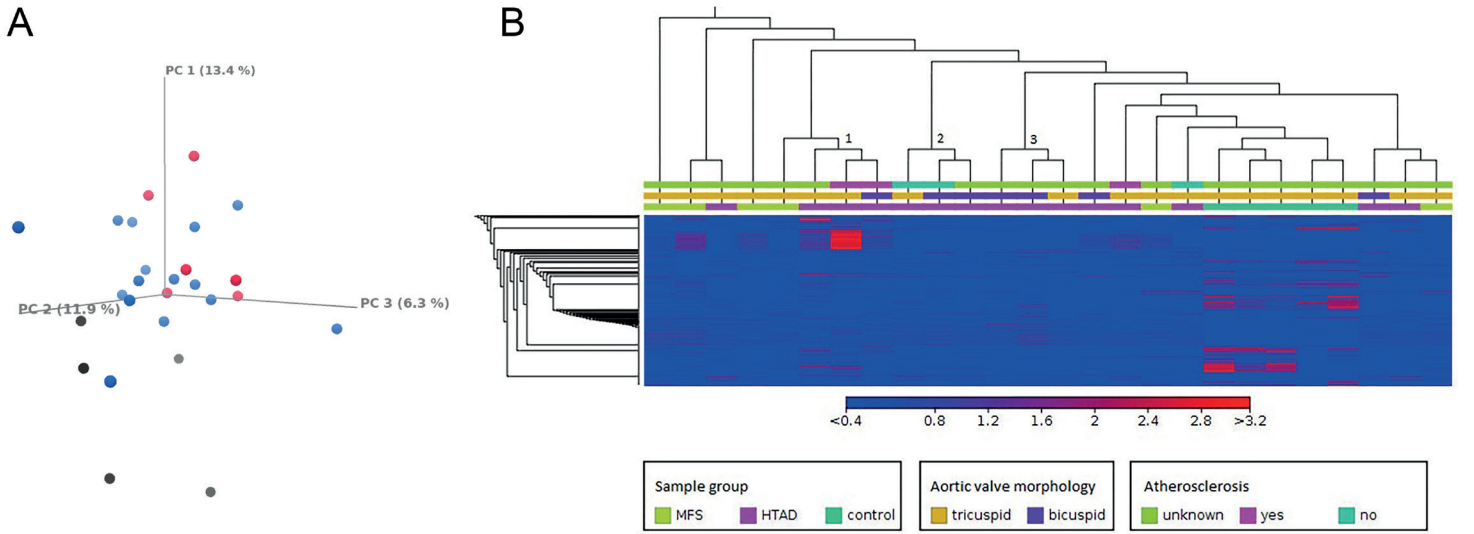

Figure 1. Principal component analysis (PCA) and hierarchical clustering of gene expression data.

A) Three-dimensional scatter plots of PCA on gene expression data. Colors represent the different sample groups: MFS = red, HTAD = blue, controls = black. The numbers in brackets correspond to the proportion of variance explained by the respective principal component. **B)** Heat map generated from gene expression data. HTAD samples clustered into three separate groups (indicated by 1-3). This clustering was not related to aortic valve morphology nor the presence or absence of atherosclerosis.

Differential expression and pathway analysis

We used three algorithms (DESeq2, edgeR and CLC Genomics Workbench) to identify differentially expressed genes in pairwise comparisons between MFS, HTAD and controls. The number of differentially expressed genes per tool is shown in Figure 2 and Table 3. Lists of differentially expressed genes were uploaded into IPA and ToppGene for further analysis. The DESeq2 algorithm, which yielded the highest numbers of differentially expressed genes, was used for exploratory data analysis. The edgeR and CLC Genomics Workbench (CLC-GW) algorithms were used to confirm our findings.

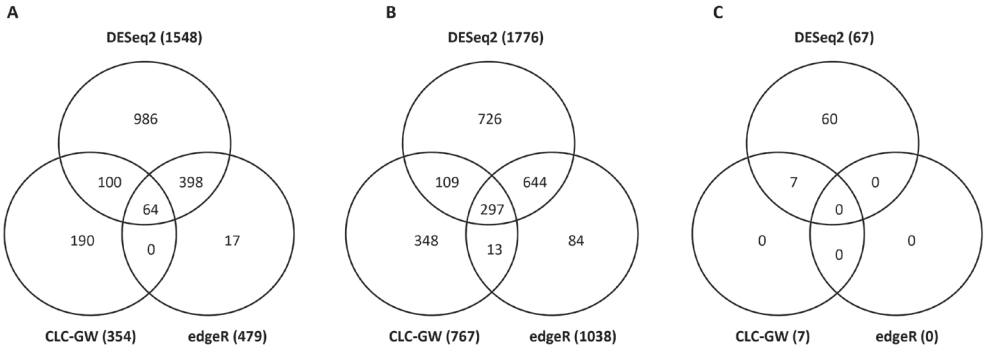

Figure 2. Venn diagrams showing the number and distribution of differentially expressed genes (fold change ≥1.5, false discovery rate adjusted p-value <0.05) among the three algorithms used for differential expression analysis.

A) Marfan syndrome (MFS) vs. controls, **B)** hereditary thoracic aortic disease (HTAD) vs. controls, **C)** MFS vs. HTAD.

Table 3. Number of differentially expressed genes in different comparisons

	DESeq2			edgeR			CLC-GW		
	Total	**Up**	**Down**	**Total**	**Up**	**Down**	**Total**	**Up**	**Down**
MFS vs. controls	1548	743	805	479	193	286	354	212	142
HTAD vs. controls	1776	888	888	1038	414	624	767	452	315
MFS vs. HTAD	67	42	25	0	0	0	7	7	0

HTAD, heritable thoracic aortic disease; MFS, Marfan syndrome.

Apparent lack of TGF-β signature in ascending aorta from MFS patients

The DESeq2 algorithm yielded a total of 1548 differentially expressed genes between MFS samples and controls: 743 genes were upregulated and 805 were downregulated (Figure 2A and Table 3). Sixty-four genes (4%) were also discovered by the edgeR and CLC-GW algorithms (Figure 2A and Supplemental Table S3). The top 10 up- en downregulated genes is displayed in Table 4. Four of the top dysregulated genes code for extracellular matrix proteins (indicated

by an asterisk). *OGN* (osteoglycin) and *ASPN* (asporin), that both encode members of the small leucine-rich proteoglycan family, have been reported to interact with the TGF-β signaling pathway [29, 30]. Pathway analysis identified 62 canonical pathways significantly enriched by genes that were differentially expressed between MFS and controls (Supplemental Table S4).

Table 4. Top 10 up- en downregulated genes in MFS compared with controls.

Symbol	Description	Location	FC	FDR
Upregulated genes				
PRND	Prion like protein doppel	Plasma membrane	5.85	4.96E-07
LAMP5	Lysosomal associated membrane protein family member 5	Cytoplasm	4.98	4.63E-07
LINC00865	Long intergenic non-protein coding RNA 865	Other	3.42	2.24E-05
*OGN**	Osteoglycin	Extracellular space	2.87	5.77E-07
*ASPN**	Asporin	Extracellular space	2.69	1.10E-06
SCG5	Secretogranin V	Extracellular space	2.66	5.22E-04
*ECM2**	Extracellular matrix protein 2	Extracellular space	2.54	8.68E-09
ANGPT2	Angiopoietin 2	Extracellular space	2.17	6.12E-05
PLD1	Phospholipidase D1	Cytoplasm	2.08	8.54E-17
PRSS35	Serine protease 35	Extracellular space	2.06	7.49E-04
Downregulated genes				
PCSK1N	Proprotein convertase subtilisin/ kexin type 1 inhibitor	Extracellular space	-4.54	4.07E-05
RP11-124N14.3	[Undefined]	Other	-3.94	8.52E-05
RNF122	Ring finger protein 122	Other	-3.91	3.14E-13
RP5-977B1.11	[Undefined]	Other	-3.86	4.58E-07
RP5-940J5.9	[Undefined]	Other	-3.46	2.71E-05
AC010761.8	[Undefined]	Other	-3.45	1.69E-03
ACTA2-AS1	ACTA2 antisense RNA 1	Other	-3.10	5.44E-04
TPGS1	Tubulin polyglutamylase complex subunit 1	Cytoplasm	-2.66	1.32E-04
CCDC85B	Coiled-coil domain containing 85B	Cytoplasm	-2.66	2.09E-05
*FGFR2**	Fibroblast growth factor receptor 2	Plasma membrane	-2.59	4.69E-06

FC, fold change; FDR, false discovery rate (Benjamini-Hochberg procedure); MFS, Marfan syndrome.

Complete list of differentially expressed genes is provided in Supplemental Table S3. Genes marked with an asterisk (*) code for extracellular matrix proteins.

Surprisingly, the canonical TGF-β signaling pathway was not among them. The top 10 enriched pathways is displayed in Figure 3. Pathways indicative of inflammation and mitochondrial dysfunction were overrepresented. Targeted assessment of the canonical TGF-β signaling pathway revealed significantly increased expression of the ligand TGFB2 (fold change 2.3, FDR adjusted *p*-value 0.03). Expression of the TGF-β receptors and intracellular signaling molecules was not significantly altered. Top ranked network functions identified by IPA were associated with lipid metabolism and inflammatory response. Gene Ontology (GO) Enrichment Analysis revealed no statistically significant results.

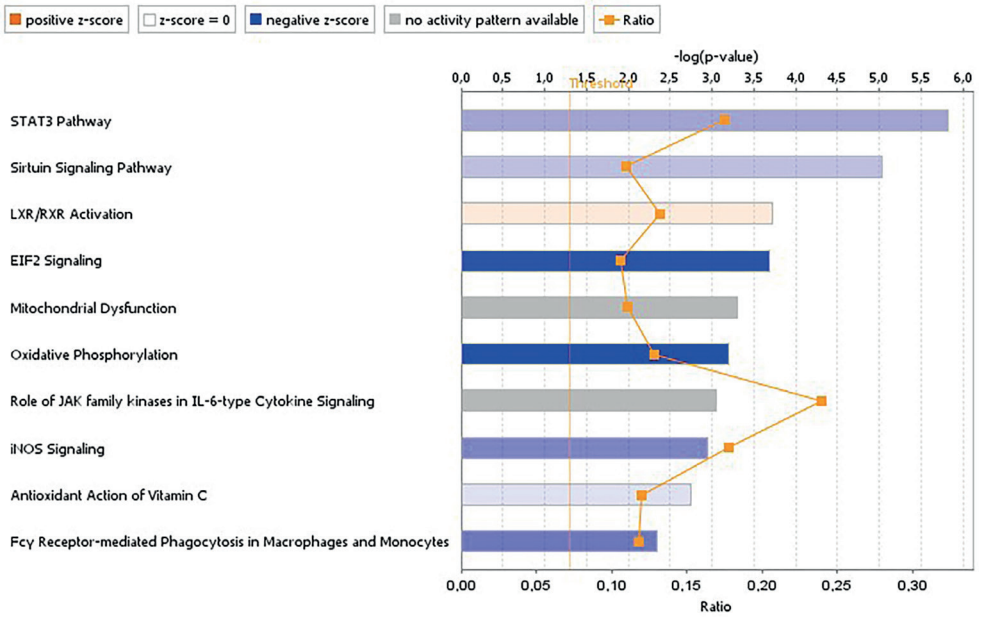

Figure 3. Top 10 pathways enriched for differentially expressed genes (DESeq2) in MFS compared with controls.

FBN1 expression in highly variable and not significantly different from non-Marfan aortas

We subdivided the MFS patients in those with dominant negative (DN, n=3) and haploinsufficient (HI, n=3) *FBN1* variants (Table 2). As expected, gene expression profiles of these subgroups did not differ substantially. *FBN1* mRNA expression levels were lower in MFS patients with HI variants (mean 360 ± 74 counts per million) compared to MFS patients with DN variants (mean 772 ± 351 counts per million) (Table 2). However, this difference was not statistically significant (p=0.1178). Inter-individual variability was high, with *FBN1* mRNA levels ranging from 38% to

150% of the mean expression level in controls. The mean *FBN1* mRNA levels in aortic tissue from patients with MFS did not significantly differ from patients with HTAD ($p=0.7165$) and controls ($p=0.2963$).

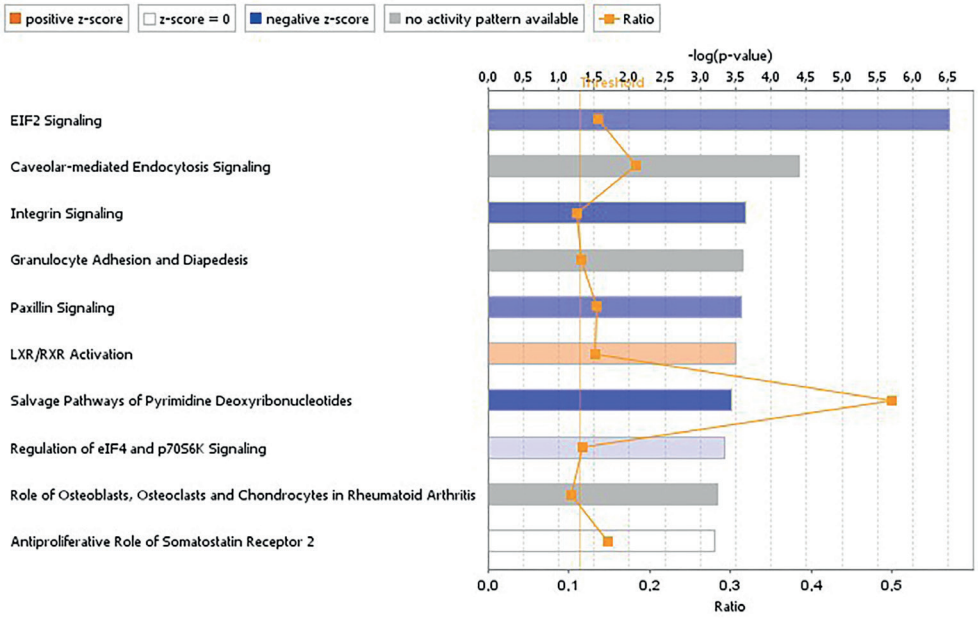

Figure 4. Top 10 pathways enriched for differentially expressed genes (DESeq2) in HTAD compared with controls.

No distinct clustering of gene expression profiles in HTAD

The DESeq2 algorithm yielded a total of 1776 genes differentially expressed between HTAD and controls: 888 genes were upregulated and 888 genes were downregulated (Figure 2B and Table 3). Two hundred ninety-seven genes (17%) were also discovered by edgeR and CLC-GW (Figure 2B and Supplemental Table S5). The top 10 up- en downregulated genes is displayed in Table 5. One of the top dysregulated genes, *S100A12* (S100 calcium binding protein A12), has previously been associated with thoracic aortic aneurysm and dissection, albeit in an opposite direction [31]. Pathway analysis identified 79 canonical pathways significantly enriched by genes that were differentially expressed between HTAD and controls (Supplemental Table S6). The top 10 enriched pathways is displayed in Figure 3. Similar to the pairwise comparison between MFS and controls, pathways indicative of inflammation and mitochondrial dysfunction were overrepresented. In addition, we identified several pathways related to cell adhesion and motility, including integrin, paxillin and focal adhesion kinase (FAK) signaling and regulation of actin-based motility by Rho family GTPases. This latter observation was supported by GO Enrichment

Analysis: the top enriched GO Biological Processes (Table 6) are mostly related to locomotion [GO:0040011] (7/25, 28%) and circulatory system development [GO:0072359] (5/25, 20%), both including factors involved in cytoskeletal organization and remodeling. The complete list of enriched GO Biological Processes can be found in Supplemental Table S7. Of the 269 genes assigned to a GO Cellular Component category, 42 (16%) are active in the extracellular space [GO:0005615].

Table 5. Top 10 up- en downregulated genes in HTAD compared with controls.

Symbol	Description	Location	FC	FDR
Upregulated genes				
LINC00996	Long intergenic non-protein coding RNA 996	Other	3.82	3.96E-06
PRND	Prion like protein doppel	Plasma membrane	3.44	1.98E-04
DAPL1	Death associated protein like 1	Other	3.32	2.09E-05
WARS2-IT1	WARS intronic transcript 1	Other	3.15	2.31E-04
CCL17	C-C motif chemokine ligand 17	Extracellular space	3.05	7.23E-04
FRMD1	FERM domain containing 1	Other	2.99	1.41E-03
CD1C	CD1c molecule	Plasma membrane	2.86	4.70E-05
GPR82	G protein-coupled receptor 82	Plasma membrane	2.86	5.51E-04
MGAT4C	MGAT4 family member C	Cytoplasm	2.85	2.53E-04
ANO4	Anoctamin 4	Plasma membrane	2.82	8.88E-04
Downregulated genes				
MCEMP1	Mast cell expressed membrane protein 1	Cytoplasm	-6.91	1.64E-10
CBARP	CACN beta subunit associated regulatory protein	Other	-5.99	1.67E-12
LINC00473	Long intergenic non-protein coding RNA 473	Other	-4.46	3.13E-06
S100A12	S100 calcium binding protein A12	Cytoplasm	-4.36	4.13E-06
ERFE	Erythroferrone	Extracellular space	-4.36	1.37E-07
AC010761.8	[Undefined]	Other	-4.31	4.16E-06
PROK2	Prokineticin 2	Extracellular space	-4.26	7.25E-06
FOSL1	FOS like 1, AP-1 transcription factor subunit	Nucleus	-4.24	2.58E-08
LILRA5	Leukocyte immunoglobulin like receptor 5	Plasma membrane	-4.15	3.04E-06
RP11-124N14.3	[Undefined]	Other	-4.10	6.45E-07

FC, fold change; FDR, false discovery rate (Benjamini-Hochberg procedure); HTAD, hereditary thoracic aortic disease.
Complete list of differentially expressed genes is provided in Supplemental Table S5.

Table 6. Top 25 GO Biological Processes enriched in HTAD versus controls.

	ID	Name	*p*-value	FDR	Molecules †
1	GO:0016477	cell migration	6.61E-08	1.46E-04	44 / 1300
2	GO:0040011	locomotion	7.11E-08	1.46E-04	53 / 1735
3	GO:0090130	tissue migration	4.54E-07	6.24E-04	16 / 244
4	GO:0048870	cell motility	8.99E-07	7.41E-04	44 / 1428
5	GO:0051674	localization of cell	8.99E-07	7.41E-04	44 / 1428
6	GO:0048646	anatomical structure formation involved in morphogenesis	1.22E-06	8.41E-04	41 / 1299
7	GO:0009967	positive regulation of signal transduction	2.68E-06	1.58E-03	44 / 1488
8	GO:0030198	extracellular matrix organization	3.46E-06	1.65E-03	18 / 354
9	GO:0043062	extracellular structure organization	3.60E-06	1.65E-03	18 / 355
10	GO:0090287	regulation of cellular response to growth factor stimulus	4.22E-06	1.72E-03	15 / 256
11	GO:0001944	vasculature development	4.60E-06	1.72E-03	26 / 677
12	GO:0001568	blood vessel development	7.09E-06	2.32E-03	25 / 651
13	GO:0010631	epithelial cell migration	7.31E-06	2.32E-03	14 / 235
14	GO:0030334	regulation of cell migration	8.03E-06	2.32E-03	27 / 742
15	GO:0090132	epithelium migration	8.45E-06	2.32E-03	14 / 238
16	GO:0048514	blood vessel morphogenesis	1.42E-05	3.65E-03	22 / 551
17	GO:0071363	cellular response to growth factor stimulus	1.74E-05	3.82E-03	24 / 643
18	GO:0040012	regulation of locomotion	1.76E-05	3.82E-03	29 / 866
19	GO:0072358	cardiovascular system development	1.92E-05	3.82E-03	33 / 1058
20	GO:0072359	circulatory system development	1.92E-05	3.82E-03	33 / 1058
21	GO:0034097	response to cytokine	1.95E-05	3.82E-03	28 / 825
22	GO:0006928	movement of cell or subcellular component	2.21E-05	4.14E-03	49 / 1882
23	GO:2000145	regulation of cell motility	2.61E-05	4.68E-03	27 / 793
24	GO:0071345	cellular response to cytokine stimulus	3.27E-05	5.61E-03	25 / 713
25	GO:0070848	response to growth factor	3.45E-05	5.63E-03	24 / 671

FDR, false discovery rate (Benjamini-Hochberg procedure); HTAD, hereditary thoracic aortic disease.
† Number of molecules in dataset / number of annotated molecules in genome. Complete list of enriched biological processes including hits in query list is provided in Supplemental Table S7.

Aortic samples show similar gene expression profiles irrespective of their genetic make-up

The DESeq2 algorithm yielded only 67 differentially expressed genes between MFS and HTAD samples, indicating great overlap between the pathophysiological processes underlying these disorders (Figure 2C and Table 3), that may reflect a 'final common pathway'. Indeed, the majority of genes differentially expressed between MFS and controls were also found in the pairwise comparison between HTAD and controls (Figure 5). Seven genes (10%) were also discovered by CLC-GW, including the collagen genes *COL1A1*, *COL3A1* and *COL4A1* (Supplementary Table S8); none were picked up by edgeR.

An overview of the main findings in our study is displayed in Table 7.

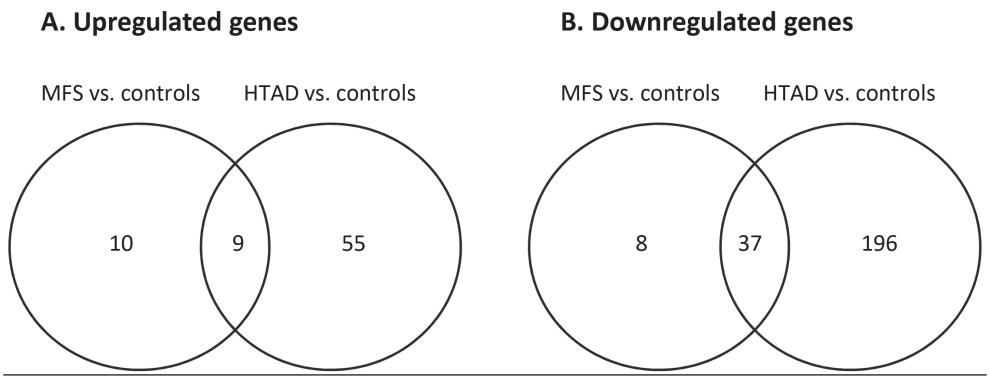

Figure 5. Venn diagrams showing the number of differentially expressed genes in common between Marfan syndrome (MFS) vs. controls and hereditary thoracic aortic disease (HTAD) vs. controls.

Table 7. Summary of the main results of this study.

	MFS vs. controls	HTAD vs. controls	MFS vs. HTAD
# DEG	↑19 ↓45	↑64 ↓233	0
# DEG in common	↑9 ↓37		
Top upregulated genes	*OGN*, *ASPN*, *ECM2*		*COL1A1*, *COL3A1*, *COL4A1*†
Top downregulated genes	*FGFR2*	*S100A12*	
Top enriched pathways	mitochondrial dysfunction and inflammation		
Top enriched functions		locomotion	
Top enriched components		extracellular space	

DEG, differentially expressed genes; HTAD, hereditary thoracic aortic disease; MFS, Marfan syndrome.

† Genes detected using DESeq2 and CLC-GW algorithm (but not edgeR).

DISCUSSION

In aortic samples from both MFS and HTAD patients, we identified a gene expression signature indicative of inflammation and mitochondrial dysfunction. Inflammation is a well-known contributor to atherosclerotic vascular disease, such as coronary artery disease [32]. In addition, chronic inflammation of the aortic wall is a typical histological feature of aneurysms located in the abdominal aorta [33]. Recent studies have demonstrated that inflammation is also involved in the pathogenesis of thoracic aortic disease, irrespective of genetic predisposition [34-36]. Though initially described as a non-inflammatory condition, these studies suggest that inflammatory cells, cytokines and metalloproteinases contribute to medial degeneration in both familial and sporadic thoracic aortic disease.

Mitochondrial dysfunction, leading to enhanced production of reactive oxygen species (ROS), reduced ATP production, and activation of cell death programs, has also been established as an important factor in various cardiovascular diseases [37]. The role of mitochondrial dysfunction in thoracic aortic disease, however, is less well studied. In VSMCs, ROS have been implicated in several physiological and pathophysiological processes such as growth, differentiation and migration [38], suggesting a direct link between the mitochondrial dysfunction and locomotion-related gene expression signature that were observed in the HTAD samples. Impaired mitochondrial function, reflected by decreased oxygen consumption and increased acidification rates, have recently been observed in aneurysmal aortas from *Fibulin-4*$^{R/R}$ mice [39]. These authors also demonstrated decreased oxygen consumption rates in VSMCs from *Tgfbr1*$^{M318R/+}$ mice, a mouse model for Loeys-Dietz syndrome (LDS) [40], and skin fibroblasts from patients with MFS and LDS. Our findings support their concept that altered mitochondrial function plays a role in aneurysm formation. Further studies are pending to validate our findings and investigate the different components of the electron transport chain using patient-derived VSMCs.

We observed high inter-individual variability in *FBN1* mRNA expression levels in aortic tissue from MFS patients (Supplemental Table S2). In patients with *FBN1* variants that are predicted to lead to haploinsuffiency, mutant *FBN1* transcript was indeed absent or present at a very low level (0-6%), therefore excluding large variations in nonsense mediated mRNA decay as a cause of the variable expression in these patients. As suggested previously, variable expression of the normal allele likely contributes to the variability in *FBN1* mRNA expression, and may depend on functional polymorphisms in the promotor region or trans-acting regulators [41, 42].

The top differentially expressed genes between MFS samples and controls encompassed several extracellular matrix genes. This might result from disorganization of extracellular matrix due to dysfunctional fibrillin-1, or reduced aortic wall strength due to reduced levels of normal fibrillin-1 [43]. Surprisingly, we did not find a distinctive TGF-β gene expression signature in MFS patients.

This might be related to the advanced stage of disease, i.e. severe aortic dilatation requiring surgical intervention. Hence, our expression profiles likely reflect the effect rather than the cause of the disease. Alternatively, the use of full thickness aortic biopsies might have "diluted" the effect and masked relevant results. The use of VSMCs alone, however, would have excluded potentially important extracellular processes. Third, levels of mRNA may poorly correlate with the abundances of their corresponding proteins [44]. To distinguish between different scenarios, we will perform further studies (e.g. immunohistochemical and functional analyses) of various components of the TGF-β pathway.

Gene expression profiles may alter with disease progression and medical treatment [45]. As a consequence, we likely have missed relevant changes in gene expression that occurred early in the disease process. Our dataset does, however, provide important insight into the molecular mechanisms involved in disease *progression*. This knowledge may help to develop new therapeutic approaches to delay or prevent vascular complications and/or the need for surgical intervention. In fact, anti-inflammatory drugs may be effective in reducing aneurysm progression. Interestingly, 3-hydroxy-3-methylglutaryl-coenzyme A reductase inhibitors, commonly called statins, which are widely prescribed for their lipid-lowering effect, also possess anti-inflammatory properties [46]. A systematic review and meta-analysis involving more than 80,000 patients with abdominal aortic aneurysms (AAA) recently confirmed that statin therapy is associated with reduced AAA growth, rupture rate and elective perioperative mortality [47]. Ex vivo experiments in human AAA tissues suggest that statins inhibit of the Rac1/NF-κB pathway, with subsequent suppression of matrix metalloproteinase (MMP)-9 and cytokine secretion [48]. To date, only two studies have investigated the effect of statins in thoracic aortic aneurysms [49, 50]. Both studies suggested better outcomes (e.g. improved survival free from dissection and rupture or increased interval to surgery) among patients receiving statins. Our data support the idea that anti-inflammatory therapy should be considered as an additive treatment in patients with thoracic aortic disease. Future studies should investigate whether serologic markers for inflammation can help guide treatment decisions.

At present, there is no effective treatment for mitochondrial disorders. Therapeutic approaches mainly focus on maintaining optimal health, by preventing worsening of symptoms during illness and physiological stress (e.g. dehydration and prolonged fasting) and avoiding mitochondrial toxins. In general, measures aim to increase energy production and reduce reactive oxygen species. Scientific evidence that current interventions, such as the use of vitamins supplements, pharmacological agents and exercise therapy, do alleviate mitochondrial disease manifestations is limited [51, 52]. Nevertheless, as serious adverse events are uncommon, it would be interesting to investigate the effect of these interventions on the course of thoracic aortic disease. Such trials should be adequately designed and monitored to ascertain the efficacy of specific therapeutic agents in particular subtypes and stages of disease at a time.

Technical limitations

RNA library preparation and sequencing procedures include a number of steps that might introduce biases in the resulting data [53]. The TruSeq Stranded mRNA Library Prep kit, for example, uses poly(A) selection for mRNA enrichment, which significantly reduces the proportion of unwanted ribosomal RNA, thereby improving the sequencing depth of mRNA. However, this procedure also removes other non-polyadenylated transcripts, including multiple histone-encoding transcripts, which are therefore discarded from further analysis. Second, due to limited resources, we did not include technical replicates in our experimental design. Therefore, we could not control for technical variation.

Biological limitations

Our control group contained more females than males, whereas the majority of MFS and HTAD patients was male. This might have had an effect on our study, considering the marked gender differences observed in thoracic aortic disease [54]. Principal component analysis, however, did not indicate a gender-dependent effect (Supplemental Figure 1). Second, HTAD exhibits extreme genetic heterogeneity. Therefore, we might not have been able to measure effects of individuals cases at the group level, and discriminate them from MFS and controls.

CONCLUSION

Our results indicate that different types of HTAD share common molecular pathways. Both inflammation and mitochondrial dysfunction seem to play important roles in the pathogenesis of MFS and mutation-negative HTAD. These pathways should be further explored as potential therapeutic targets for preventing disease progression.

ACKNOWLEDGEMENTS

We are indebted to the patients and families that participated in this study. A special thanks goes to Liesbeth Duininck, Aimee Rijntjes and other colleagues in the Department of Cardiothoracic Surgery for their assistance in sample collection.

Disclosure: The authors report no conflicts of interest.

Funding resources: This work was supported by funding from the Dutch Heart Foundation (2014T007) and an Erasmus University Rotterdam Fellowship to Ingrid M.B.H. van de Laar.

REFERENCES

1. Albornoz, G., M.A. Coady, M. Roberts, R.R. Davies, M. Tranquilli, J.A. Rizzo, and J.A. Elefteriades, *Familial thoracic aortic aneurysms and dissections--incidence, modes of inheritance, and phenotypic patterns.* Ann Thorac Surg, 2006. **82**(4): p. 1400-5.
2. Milewicz, D.M. and E. Regalado, *Heritable Thoracic Aortic Disease Overview.* 1993.
3. Dietz, H.C., G.R. Cutting, R.E. Pyeritz, C.L. Maslen, L.Y. Sakai, G.M. Corson, et al., *Marfan syndrome caused by a recurrent de novo missense mutation in the fibrillin gene.* Nature, 1991. **352**(6333): p. 337-9.
4. Loeys, B.L., H.C. Dietz, A.C. Braverman, B.L. Callewaert, J. De Backer, R.B. Devereux, et al., *The revised Ghent nosology for the Marfan syndrome.* J Med Genet, 2010. **47**(7): p. 476-85.
5. Baetens, M., L. Van Laer, K. De Leeneer, J. Hellemans, J. De Schrijver, H. Van De Voorde, et al., *Applying massive parallel sequencing to molecular diagnosis of Marfan and Loeys-Dietz syndromes.* Hum Mutat, 2011. **32**(9): p. 1053-62.
6. Gillis, E., L. Van Laer, and B.L. Loeys, *Genetics of thoracic aortic aneurysm: at the crossroad of transforming growth factor-beta signaling and vascular smooth muscle cell contractility.* Circ Res, 2013. **113**(3): p. 327-40.
7. Meester, J.A.N., A. Verstraeten, D. Schepers, M. Alaerts, L. Van Laer, and B.L. Loeys, *Differences in manifestations of Marfan syndrome, Ehlers-Danlos syndrome, and Loeys-Dietz syndrome.* Ann Cardiothorac Surg, 2017. **6**(6): p. 582-594.
8. Luyckx, I. and B.L. Loeys, *The genetic architecture of non-syndromic thoracic aortic aneurysm.* Heart, 2015. **101**(20): p. 1678-84.
9. Brownstein, A.J., V. Kostiuk, B.A. Ziganshin, M.A. Zafar, H. Kuivaniemi, S.C. Body, et al., *Genes Associated with Thoracic Aortic Aneurysm and Dissection: 2018 Update and Clinical Implications.* Aorta (Stamford), 2018. **6**(1): p. 13-20.
10. Weerakkody, R., D. Ross, D.A. Parry, B. Ziganshin, J. Vandrovcova, P. Gampawar, et al., *Targeted genetic analysis in a large cohort of familial and sporadic cases of aneurysm or dissection of the thoracic aorta.* Genet Med, 2018.
11. Milewicz, D.M. and E.S. Regalado, *Use of genetics for personalized management of heritable thoracic aortic disease: how do we get there?* J Thorac Cardiovasc Surg, 2015. **149**(2 Suppl): p. S3-5.
12. Mohamed, S.A., H.H. Sievers, T. Hanke, D. Richardt, C. Schmidtke, E.I. Charitos, et al., *Pathway analysis of differentially expressed genes in patients with acute aortic dissection.* Biomark Insights, 2009. **4**: p. 81-90.
13. Cheuk, B.L. and S.W. Cheng, *Differential expression of elastin assembly genes in patients with Stanford Type A aortic dissection using microarray analysis.* J Vasc Surg, 2011. **53**(4): p. 1071-1078 e2.
14. Sulkava, M., E. Raitoharju, A. Mennander, M. Levula, I. Seppala, L.P. Lyytikainen, et al., *Differentially expressed genes and canonical pathways in the ascending thoracic aortic aneurysm - The Tampere Vascular Study.* Sci Rep, 2017. **7**(1): p. 12127.

15. Weis-Müller, B.T., O. Modlich, I. Drobinskaya, D. Unay, R. Huber, H. Bojar, et al., *Gene expression in acute Stanford type A dissection: a comparative microarray study.* J Transl Med, 2006. **4**: p. 29.
16. Müller, B.T., O. Modlich, H.B. Prisack, H. Bojar, J.D. Schipke, T. Goecke, et al., *Gene expression profiles in the acutely dissected human aorta.* Eur J Vasc Endovasc Surg, 2002. **24**(4): p. 356-64.
17. Zhao, S., W.P. Fung-Leung, A. Bittner, K. Ngo, and X. Liu, *Comparison of RNA-Seq and microarray in transcriptome profiling of activated T cells.* PLoS One, 2014. **9**(1): p. e78644.
18. Franken, R., A.W. den Hartog, T. Radonic, D. Micha, A. Maugeri, F.S. van Dijk, et al., *Beneficial Outcome of Losartan Therapy Depends on Type of FBN1 Mutation in Marfan Syndrome.* Circ Cardiovasc Genet, 2015. **8**(2): p. 383-8.
19. Stone, J.R., P. Bruneval, A. Angelini, G. Bartoloni, C. Basso, L. Batoroeva, et al., *Consensus statement on surgical pathology of the aorta from the Society for Cardiovascular Pathology and the Association for European Cardiovascular Pathology: I. Inflammatory diseases.* Cardiovasc Pathol, 2015. **24**(5): p. 267-78.
20. Halushka, M.K., A. Angelini, G. Bartoloni, C. Basso, L. Batoroeva, P. Bruneval, et al., *Consensus statement on surgical pathology of the aorta from the Society for Cardiovascular Pathology and the Association For European Cardiovascular Pathology: II. Noninflammatory degenerative diseases - nomenclature and diagnostic criteria.* Cardiovasc Pathol, 2016. **25**(3): p. 247-57.
21. Love, M.I., W. Huber, and S. Anders, *Moderated estimation of fold change and dispersion for RNA-seq data with DESeq2.* Genome Biol, 2014. **15**(12): p. 550.
22. Robinson, M.D., D.J. McCarthy, and G.K. Smyth, *edgeR: a Bioconductor package for differential expression analysis of digital gene expression data.* Bioinformatics, 2010. **26**(1): p. 139-40.
23. Mortazavi, A., B.A. Williams, K. McCue, L. Schaeffer, and B. Wold, *Mapping and quantifying mammalian transcriptomes by RNA-Seq.* Nat Methods, 2008. **5**(7): p. 621-8.
24. Kramer, A., J. Green, J. Pollard, Jr., and S. Tugendreich, *Causal analysis approaches in Ingenuity Pathway Analysis.* Bioinformatics, 2014. **30**(4): p. 523-30.
25. Chen, J., E.E. Bardes, B.J. Aronow, and A.G. Jegga, *ToppGene Suite for gene list enrichment analysis and candidate gene prioritization.* Nucleic Acids Res, 2009. **37**(Web Server issue): p. W305-11.
26. Waters, K.M., L.M. Rooper, A. Guajardo, and M.K. Halushka, *Histopathologic differences partially distinguish syndromic aortic diseases.* Cardiovasc Pathol, 2017. **30**: p. 6-11.
27. Guo, D.C., H. Pannu, V. Tran-Fadulu, C.L. Papke, R.K. Yu, N. Avidan, et al., *Mutations in smooth muscle alpha-actin (ACTA2) lead to thoracic aortic aneurysms and dissections.* Nat Genet, 2007. **39**(12): p. 1488-93.
28. Meester, J.A., G. Vandeweyer, I. Pintelon, M. Lammens, L. Van Hoorick, S. De Belder, et al., *Loss-of-function mutations in the X-linked biglycan gene cause a severe syndromic form of thoracic aortic aneurysms and dissections.* Genet Med, 2017. **19**(4): p. 386-395.
29. Shanahan, C.M., N.R. Cary, J.K. Osbourn, and P.L. Weissberg, *Identification of osteoglycin as a component of the vascular matrix. Differential expression by vascular smooth muscle cells during*

neointima formation and in atherosclerotic plaques. Arterioscler Thromb Vasc Biol, 1997. **17**(11): p. 2437-47.

30. Nakajima, M., H. Kizawa, M. Saitoh, I. Kou, K. Miyazono, and S. Ikegawa, *Mechanisms for asporin function and regulation in articular cartilage.* J Biol Chem, 2007. **282**(44): p. 32185-92.
31. Hofmann Bowman, M., J. Wilk, A. Heydemann, G. Kim, J. Rehman, J.A. Lodato, et al., *S100A12 mediates aortic wall remodeling and aortic aneurysm.* Circ Res, 2010. **106**(1): p. 145-54.
32. Ross, R., *Atherosclerosis--an inflammatory disease.* N Engl J Med, 1999. **340**(2): p. 115-26.
33. Kuivaniemi, H., E.J. Ryer, J.R. Elmore, and G. Tromp, *Understanding the pathogenesis of abdominal aortic aneurysms.* Expert Rev Cardiovasc Ther, 2015. **13**(9): p. 975-87.
34. He, R., D.C. Guo, W. Sun, C.L. Papke, S. Duraisamy, A.L. Estrera, et al., *Characterization of the inflammatory cells in ascending thoracic aortic aneurysms in patients with Marfan syndrome, familial thoracic aortic aneurysms, and sporadic aneurysms.* J Thorac Cardiovasc Surg, 2008. **136**(4): p. 922-9, 929 e1.
35. Cifani, N., M. Proietta, L. Tritapepe, C. Di Gioia, L. Ferri, M. Taurino, and F. Del Porto, *Stanford-A acute aortic dissection, inflammation, and metalloproteinases: a review.* Ann Med, 2015. **47**(6): p. 441-6.
36. Pisano, C., C.R. Balistreri, A. Ricasoli, and G. Ruvolo, *Cardiovascular Disease in Ageing: An Overview on Thoracic Aortic Aneurysm as an Emerging Inflammatory Disease.* Mediators Inflamm, 2017. **2017**: p. 1274034.
37. Chistiakov, D.A., T.P. Shkurat, A.A. Melnichenko, A.V. Grechko, and A.N. Orekhov, *The role of mitochondrial dysfunction in cardiovascular disease: a brief review.* Ann Med, 2018. **50**(2): p. 121-127.
38. Clempus, R.E. and K.K. Griendling, *Reactive oxygen species signaling in vascular smooth muscle cells.* Cardiovasc Res, 2006. **71**(2): p. 216-25.
39. van der Pluijm, I., J. Burger, P.M. van Heijningen, I.J. A, N. van Vliet, C. Milanese, et al., *Decreased mitochondrial respiration in aneurysmal aortas of Fibulin-4 mutant mice is linked to PGC1A regulation.* Cardiovasc Res, 2018. **114**(13): p. 1776-1793.
40. Gallo, E.M., D.C. Loch, J.P. Habashi, J.F. Calderon, Y. Chen, D. Bedja, et al., *Angiotensin II-dependent TGF-beta signaling contributes to Loeys-Dietz syndrome vascular pathogenesis.* J Clin Invest, 2014. **124**(1): p. 448-60.
41. Tjeldhorn, L., S.S. Amundsen, T. Baroy, S. Rand-Hendriksen, O. Geiran, E. Frengen, and B. Paus, *Qualitative and quantitative analysis of FBN1 mRNA from 16 patients with Marfan Syndrome.* BMC Med Genet, 2015. **16**: p. 113.
42. Aubart, M., S. Gazal, P. Arnaud, L. Benarroch, M.S. Gross, J. Buratti, et al., *Association of modifiers and other genetic factors explain Marfan syndrome clinical variability.* Eur J Hum Genet, 2018. **26**(12): p. 1759-1772.
43. Hollister, D.W., M. Godfrey, L.Y. Sakai, and R.E. Pyeritz, *Immunohistologic abnormalities of the microfibrillar-fiber system in the Marfan syndrome.* N Engl J Med, 1990. **323**(3): p. 152-9.
44. Vogel, C. and E.M. Marcotte, *Insights into the regulation of protein abundance from proteomic and transcriptomic analyses.* Nat Rev Genet, 2012. **13**(4): p. 227-32.

45. Kim, K.L., C. Choi, and W. Suh, *Analysis of disease progression-associated gene expression profile in fibrillin-1 mutant mice: new insight into molecular pathogenesis of marfan syndrome.* Biomol Ther (Seoul), 2014. **22**(2): p. 143-8.
46. Golia, E., G. Limongelli, F. Natale, F. Fimiani, V. Maddaloni, I. Pariggiano, et al., *Inflammation and cardiovascular disease: from pathogenesis to therapeutic target.* Curr Atheroscler Rep, 2014. **16**(9): p. 435.
47. Salata, K., M. Syed, M.A. Hussain, C. de Mestral, E. Greco, M. Mamdani, et al., *Statins Reduce Abdominal Aortic Aneurysm Growth, Rupture, and Perioperative Mortality: A Systematic Review and Meta-Analysis.* J Am Heart Assoc, 2018. **7**(19): p. e008657.
48. Yoshimura, K., A. Nagasawa, J. Kudo, M. Onoda, N. Morikage, A. Furutani, et al., *Inhibitory effect of statins on inflammation-related pathways in human abdominal aortic aneurysm tissue.* Int J Mol Sci, 2015. **16**(5): p. 11213-28.
49. Stein, L.H., J. Berger, M. Tranquilli, and J.A. Elefteraides, *Effect of statin drugs on thoracic aortic aneurysms.* Am J Cardiol, 2013. **112**(8): p. 1240-5.
50. Angeloni, E., A. Vitaterna, M. Pirelli, and S. Refice, *Effects of statin therapy on ascending aorta aneurysms growth: A propensity-matched analysis.* Int J Cardiol, 2015. **191**: p. 52-5.
51. Pfeffer, G., K. Majamaa, D.M. Turnbull, D. Thorburn, and P.F. Chinnery, *Treatment for mitochondrial disorders.* Cochrane Database Syst Rev, 2012(4): p. CD004426.
52. Hirano, M., V. Emmanuele, and C.M. Quinzii, *Emerging therapies for mitochondrial diseases.* Essays Biochem, 2018. **62**(3): p. 467-481.
53. Conesa, A., P. Madrigal, S. Tarazona, D. Gomez-Cabrero, A. Cervera, A. McPherson, et al., *Erratum to: A survey of best practices for RNA-seq data analysis.* Genome Biol, 2016. **17**(1): p. 181.
54. Nicolini, F., A. Vezzani, F. Corradi, R. Gherli, F. Benassi, T. Manca, and T. Gherli, *Gender differences in outcomes after aortic aneurysm surgery should foster further research to improve screening and prevention programmes.* Eur J Prev Cardiol, 2018. **25**(1_suppl): p. 32-41.

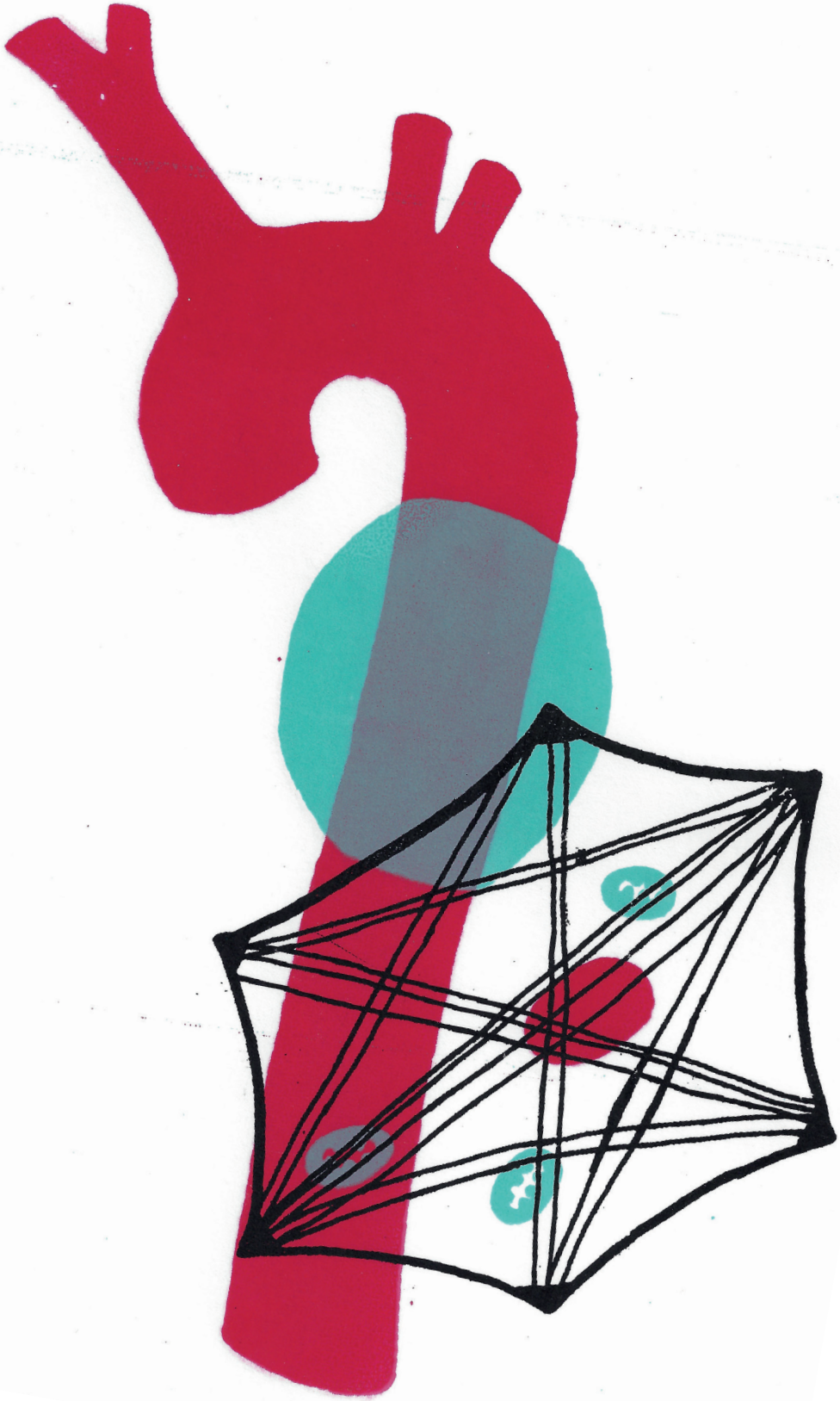

SUMMARY AND CONCLUSIONS

Cardiovascular diseases are one of the leading causes of mortality. They include aortic diseases such as aortic aneurysms, dilatations of the aorta that result in thinning of the aortic wall which eventually leads to aortic dissections or rupture of the aorta. Aortic aneurysms often remain asymptotic and are usually detected in late stages of the disease. Currently the only treatments are surgical repair of the aneurysm by placement of a stent or by placement of a stent that bridges the aneurysmal region. Aortic aneurysms can occur in different regions of the aorta; above the diaphragm they are categorized as thoracic aortic aneurysms (TAA) and below the diaphragm as abdominal aortic aneurysms (AAA). While multiple genetic causes have been identified for TAA, the genetic causes for AAA have not been very well established. Although genetic causes have been found for TAA, the availability of pharmaceutical treatments to prevent or delay aneurysm formation is still limited. Therefore, a better understanding of the molecular mechanisms that play a role in aneurysm development is needed to eventually develop new treatments for aortic aneurysms.

In this thesis, we aimed to characterize causative aneurysm genes and elucidate the molecular mechanisms that underlie aortic aneurysm formation. We aspired to create a better understanding of aneurysm formation and study the effect of different potential causative mutations on cellular function. The main findings of this thesis are summarized below.

In **chapter 2** we characterized fibroblasts cell lines derived from aneurysm patients bearing *ACTA2*, *MYH11*, *SMAD3* and *FBN1* mutations and control fibroblasts. The cells were analyzed for transdifferentiation, TGFβ responsiveness and functional parameters such as migration and contractility to determine whether these features can be distinguished from controls. Our study showed that molecular phenotyping can distinguish aneurysm causing mutations from controls. Molecular phenotyping further proved to be an efficient method to investigate the functional consequences of identified variants of unknown significance. Additionally, in the future, these data can be used to select functional assays to identify the effects of potential novel aneurysm gene variants and thereby determine their pathogenicity.

A new *SLC2A10* knockout mouse model is analyzed in **chapter 3** to investigate whether this model is suitable to characterize the role of *SLC2A10* in arterial tortuosity syndrome (ATS). Characterization of the *Gulo*$^{tm1mae/tm1mae}$;*Slc2a10*$^{-/-}$ (double knock-out) mice revealed only some mild cardiovascular phenotypic manifestations compared to controls. Interestingly, *SLC2A10* double knock-out VSMCs showed a reduced maximum oxygen consumption rate and aberrant extracellular matrix deposition compared to controls. Analysis of the TGFβ signaling pathway did not display any differences between *Gulo*$^{tm1mae/tm1mae}$;*Slc2a10*$^{-/-}$ and wild-type VSMCs. Although the mouse model did not show most of the typical ATS symptoms, e.g. arterial tortuosity and

aneurysm formation, the cellular phenotype did resemble the cellular findings of ATS patients, such as reduced maximum oxygen consumption rate and aberrant extracellular matrix deposition. This model could therefore be useful to further investigate the molecular mechanisms involved in ATS at the cellular level.

Chapter 4 evaluates two *Fibulin-4* mouse models for cytoskeleton aberration, cellular movement and TGFβ signaling activity. During this study we aimed to determine the effects of reduced fibulin-4 (Fibulin-$4^{R/R}$) and total ablation of fibulin-4 specifically in VSMCs (Fibulin-$4^{f/-}$/SM22Cre^{+}) on cellular function. Analysis of the cytoskeleton revealed that Fibulin-$4^{f/-}$/SM22Cre^{+} VSMCs were unable to form smooth muscle actin (SMA) fibers, while Fibulin-$4^{R/R}$ VSMCs were able to form SMA fibers. However, both Fibulin-4 models showed decreased migration compared to their controls. Increased activation of the TGFβ signaling pathway was found in Fibulin-$4^{R/R}$ VSMCs. Yet, this increase was not present in Fibulin-$4^{f/-}$/SM22Cre^{+} VSMCs. Since both mouse models show aneurysm formation, we concluded that not only dysregulation of the TGFβ signaling pathways, but also SMA cytoskeleton dynamics play a role in aneurysm formation.

In **chapter 5** we aimed to identify novel pathways involved in aneurysm formation. Proteomics and genomics data revealed alterations in the mitochondrial protein composition in Fibulin-$4^{R/R}$ aortas. Functional analysis of Fibulin-$4^{R/R}$ VSMCs showed lower oxygen consumption rates. Additionally, reduced mitochondrial respiration was found in VSMCs of the Tgfbr-$1^{M318R/+}$ Loeys-Dietz mouse model and fibroblasts of patients with Marfan (*FBN1*) and Loeys-Dietz syndrome (*TGFBR2* and *SMAD3*). Furthermore, gene expression analysis revealed dysregulation of metabolic pathways and the predicted key regulator between mitochondrial function and metabolism, PGC1α, was found to be downregulated in Fibulin-$4^{R/R}$ VSMCs. Increased TGFβ levels led to a reduction of PGC1α, suggesting a link between TGFβ signaling and PGC1α regulation. We were able to restore PGC1α activity in Fibulin-$4^{R/R}$ VSMCs and improve the mitochondrial respiration by treatment with forskolin, a PGC1α activator. Our data uncovers a novel pathway that is involved in aneurysm formation and could serve as a potential new target for treatments of aneurysms.

Chapter 6 evaluates RNA expression of aortic tissue derived from Marfan and non-syndromic heritable thoracic aortic disease (HTAD) patients compared to control aortic tissue derived from healthy donors. Interestingly differential gene and protein expression analysis pointed towards mitochondrial dysfunction and increased inflammation in Marfan and HTAD patients, while lacking a distinct TGFβ gene expression signature. These findings show that inflammatory and mitochondrial pathways play an important role in the pathophysiological processes that underlie aortic aneurysmal disease.

The results presented in this thesis illustrate that, although much research has been performed, novel pathways that are involved in aortic aneurysm formation are still identified. Our findings show

that not only defective TGFβ signaling is involved in aneurysm formation, but also cytoskeleton dysfunction, aberrant extracellular matrix deposition and altered mitochondrial respiration.

Future perspectives

The presented functional assays and novel identified pathways in this thesis could be used for several advancements in the diagnosis and treatment of aneurysms in the future.

The described functional assays could in the future be used in a clinical setting. Functional outcomes that are determined for confirmed pathogenic variants and controls can be used to compare to functional outcomes of a variant of unknown significance (VUS). If the outcomes of the VUS suggest altered functionality this can indicate that the VUS is pathogenic. Reclassification of a VUS will lead to better diagnosis in families and provides them with clarity on the effects of the identified variant. Additionally these functional assays can be used to pinpoint potential new causative aneurysm genes. Dermal fibroblasts of aneurysm patients with an unknown variant can be transdifferentiated and compared to known pathogenic variants with regard to differentiation potential, migration and contractility. By comparing their outcomes, resemblances could be found that can suggest which processes are altered in the patient fibroblasts, pointing to a set of genes in which a variant might be present.

These two potential uses promote more accurate genetic diagnosis of aneurysm patients and family screening. To implement these functional assays, future research should include further analysis of pathogenic variants and their functional readouts in addition to analysis of VUS. The selection of these VUS would ideally be done in close collaboration with clinical geneticists to also link the clinical background of the patients to the functional readouts.

There is still a great need for a better understanding of the molecular mechanisms that are involved in aneurysm formation. This need is for instance illustrated by the minimal options for treatment for aneurysm patients. The novel pathways involved in aneurysm formation described in this thesis could give an impulse to the identification of therapeutic targets. These targets could lead to the development of medication that delays or prevents aneurysm formation. To ensure this development, future research should be focused on further identifying and specifying the pathways that are involved in aneurysm formation. By identifying the proteins and their interactors, the potential targets become further specified for drug development. Additionally, currently available medication that affects these novel pathways could be screened to determine if it positively affects the functionality of patient cells.

To take these next steps in the diagnosis and treatment of aneurysm formation it is important to have close collaboration between clinical geneticists, vascular surgeons, fundamental and translational scientists. A multidisciplinary approach will be essential in the diagnosis and treatment of aneurysm patients.

NEDERLANDSE SAMENVATTING

Hart- en vaatziekten zijn een van de meest voorkomende doodsoorzaken, hieronder vallen ook aandoeningen aan de aorta zoals aorta aneurysmata. Aorta aneurysmata zijn verwijdingen van de aorta die leiden tot het dunner worden van de aortawand. Wanneer de aortawand te dun wordt kunnen aorta dissecties (scheuring van de binnenste laag van de aorta) ontstaan of de aorta wand kan helemaal scheuren, met fatale bloedingen tot gevolg. Aorta aneurysmata worden vaak per toeval ontdekt en patiënten ervaren vaak geen klachten vanwege het aneurysma totdat de ziekte al ver gevorderd is en het risico op scheuringen erg groot is geworden. Momenteel is het opereren van een aneurysma de enige behandelmogelijkheid. Tijdens deze operatie wordt een prothese geplaatst in de aorta waarna het aneurysma er strak om heen wordt gevouwen, of er wordt via de lies een opgevouwen prothese naar het aneurysma gebracht en die de verwijding afdekt. Aorta aneurysmata kunnen op verschillende plaatsen voorkomen; boven het diafragma noemen we deze thoracale aorta aneurysma (TAA) en onder het diafragma worden het abdominale aorta aneurysma (AAA) genoemd. Inmiddels zijn er verschillende genetische oorzaken gevonden voor TAA, terwijl voor AAA deze genetische oorzaken nog minder duidelijk zijn. Ondanks dat de genetische oorzaken voor TAA deels bekend zijn, zijn de behandelingen die aneurysmata kunnen voorkomen of kan zorgen dat ze minder snel groeien nog maar beperkt voorhanden. Om in de toekomst medicijnen te kunnen ontwikkelen voor de behandeling van een aneurysma is het belangrijk om te begrijpen wat er gebeurt tijdens aneurysmavorming op cellulair en moleculair niveau.

Het doel van dit proefschrift is om aneurysmavorming beter te begrijpen en dit doen we door het karakteriseren van de genetische oorzaken van aorta aneurysmata en het onderzoeken van processen op moleculair niveau in cellen uit de aorta. Ons onderzoek heeft meer inzicht gegeven in welke effecten genetische mutaties hebben op het functioneren van een cel en hoe dit bijdraagt aan aneurysma vorming. In dit hoofdstuk worden de belangrijkste bevindingen van dit proefschrift samengevat.

In **hoofdstuk 2** karakteriseren we huidcellen afkomstig van aneurysma patiënten met mutaties in *ACTA2*, *MYH11*, *SMAD3* en *FBN1,* en controle huidcellen. Het doel is om te bepalen of de patiëntcellen te onderscheiden zijn van de controle cellen aan de hand van transdifferentiatie, gevoeligheid voor TGFβ en functionele parameters, waaronder migratie en contractie. Ons onderzoek laat zien dat de patiëntcellen op verschillende manieren te onderscheiden zijn van de controle cellen. Onze resultaten laten ook zien dat de toegepaste testen effectieve methodes zijn om functionele consequenties van genetische mutaties te onderzoeken. In de toekomst zouden deze methodes gebruikt kunnen worden om de schadelijkheid van nieuw ontdekte mutaties te bepalen.

Een nieuw ontwikkeld muismodel voor *SLC2A10* wordt geanalyseerd in **hoofdstuk 3** om te bepalen of dit model geschikt is om de rol van *SLC2A10* in het arterial tortuosity syndroom (ATS) te onderzoeken. Karakterisering van de dubbel knock-out muizen (*Gulo*$^{tm1mae/tm1mae}$;*Slc2a10*$^{-/-}$) onthulde een aantal milde cardiovasculaire afwijkingen in vergelijking met de controle muizen. Opmerkelijk was dat gladde spiercellen uit de aorta van de dubbel knock-out muizen een verlaagd maximaal zuurstofverbruik hadden in hun mitochondriën en dat deze cellen een afwijkende extracellulaire matrix produceerden in vergelijking met controle cellen. Analyse van de TGFβ signaleringsroute liet geen verschil zien tussen de dubbel knock-out en de controle cellen. Onze resultaten laten zien dat hoewel het nieuwe *SLC2A10* muis model geen typische ATS symptomen zoals kronkeling van de arteriën en aneurysma vorming heeft, het fenotype van de cellen wel lijkt op dat van cellen van ATS patiënten. Daarom is dit model wel geschikt voor het onderzoek naar de rol van *SLC2A10* in ATS op cellulair niveau.

Hoofdstuk 4 evalueert twee *Fibuline-4* muis modellen aan de hand van cytoskelet afwijkingen, cellulaire beweging en TGFβ signalering. Het doel van dit onderzoek is om te bepalen wat de effecten zijn van verminderde hoeveelheden (Fibulin-4$^{R/R}$) en totale afwezigheid (Fibulin-4$^{f/-}$/SM22Cre^{+}) van fibuline-4 op het functioneren van een gladde spiercel uit de aorta. Analyse van het cytoskelet onthulde dat Fibulin-4$^{f/-}$/SM22Cre^{+} gladde spiercellen geen gladde spiercel actine (SMA) vezels konden maken, terwijl Fibulin-4$^{R/R}$ gladde spiercellen dit wel konden. Echter lieten beide modellen verminderde migratie zien ten opzichte van de controles. In het Fibulin-4$^{R/R}$ model werd verhoogde activatie van de TGFβ signaaltransductie gevonden, terwijl dit niet aanwezig was in Fibulin-4$^{f/-}$/SM22Cre^{+} gladde spiercellen. Aangezien beide muis modellen aneurysma vorming laten zien concludeerden wij dat niet alleen ontregeling van de TGFβ signaaltransductie, maar ook verstoring van de cytoskelet dynamiek een rol spelen in aneurysma vorming.

Het doel van **hoofdstuk 5** was het identificeren van nieuwe signaleringsroutes die betrokken zijn bij aneurysmavorming. Eiwit (proteomics) en genexpressie analyse onthulden afwijkingen in de mitochondriële eiwitten in Fibulin-4$^{R/R}$ muizen aorta's. Functionele analyse van Fibulin-4$^{R/R}$ gladde spiercellen liet een verlaagd zuurstofverbruik van de mitochondriën zien. Verlaagd zuurstofverbruik werd verder gevonden in gladde spiercellen van een Loeys-Dietz muis model (Tgfbr-1$^{M318R/+}$) en in huidcellen van Marfan (*FBN1*) en Loeys-Dietz (*TGFBR2* en *SMAD3*) syndroom patiënten. Analyse van genexpressie onthulde een ontregeling van het metabolisme in Fibulin-4$^{R/R}$ aorta's en daarnaast werd gevonden dat de regelaar (PGC1α) tussen mitochondrieel functioneren en metabolisme verlaagd was. Verhoogde TGFβ niveaus leiden tot een verlaging van PGC1α en dit suggereert een link tussen de TGFβ signalering en PGC1α regulatie. In onze experimenten konden we de PGC1α activiteit in Fibulin-4$^{R/R}$ gladde spiercellen herstellen door middel van behandeling met forskolin, een PGC1α activator, en dit herstelde ook het mitochondriële zuurstofverbruik. Ons onderzoek legt een nieuwe signaleringsroute bloot die betrokken is bij aneurysma vorming en dit zou kunnen leiden tot nieuwe aangrijppunten voor medicijnen.

Hoofdstuk 6 evalueert de expressie van RNA in aorta weefsel van Marfan syndroom patiënten, aorta weefsel van niet-syndromale erfelijke aorta aneurysmata en aorta weefsel van gezonde donoren. Het doel van dit onderzoek was het ontrafelen van de moleculaire processen die ten grondslag liggen aan aneurysmavorming. Opmerkelijk genoeg duidde differentiële gen- en eiwitexpressie analyse op ontsteking en mitochondriële dysfunctie in zowel Marfan patiënten als niet-syndromale aneurysma patiënten. Verder viel op dat er geen dysregulatie van TGFβ genexpressie te vinden was in de aorta's van Marfan patiënten niet-syndromale aneurysma patiënten. Deze resultaten laten zien dat ontsteking en mitochondriële signaleringsroutes een belangrijke rol spelen in de pathofysiologische processen die betrokken zijn bij aneurysmavorming.

De resultaten die gepresenteerd worden in dit proefschrift illustreren dat, hoewel er al veel onderzoek gedaan is, er nog steeds nieuwe signaleringsroutes geïdentificeerd worden die betrokken zijn bij aneurysmavorming. Onze bevindingen laten zien dat niet alleen afwijkingen in de TGFβ signaaltransductie betrokken zijn bij aneurysmavorming maar ook afwijkingen aan het cytoskelet, de extracellulaire matrix en mitochondrieel zuurstofverbruik. In de toekomst kunnen deze nieuw inzichten dienen als mogelijke aangrijpingspunten voor de ontwikkeling van medicijnen die aorta aneurysmavorming kunnen voorkomen of afremmen.

LIST OF ABBREVIATIONS

AA	Aortic aneurysm
AA	Ascorbic acid (chapter 3)
AAA	Abdominal aortic aneurysms
ADP	Actin depolymerizing factor
ATP	Adenosine triphosphate
ATS	Arterial tortuosity syndrome
BAPN	β-aminopropionitrile monofumarate
BMPs	Bone morphogenetic proteins
CIMT	Carotid intima-media thickness
CTGF	Connective tissue growth factor
DHA	Dehydroascorbic acid
DKO	Double knock-out
DN	Dominant negative
ECAR	Extracellular acidification rate
ECM	Extracellular matrix
EDS	Ehlers-Danlos syndrome
EM	Electron microscopy
ER	Endoplasmic reticulum
EVAR	Endovascular aneurysm repair
F-actin	Filamentous actin
FC	Fold change
FCCP	Fluoro-carbonyl cyanide phenylhydrazone
FDR	False discovery rate
Fibulin-4^{-}	Mouse with Fibulin-4 knock-out
Fibulin-4^{+}	Mouse carrying wildtype allele
Fibulin-4$^{+/+}$	Wildtype mouse (wt)
Fibulin-4^{f}	Mouse carrying floxed Fibulin-4 allele that can be deleted by Cre recombinase
Fibulin-4^{R}	Mouse carrying Fibulin-4 mutant allele with reduced Fibulin-4 expression
Fibulin-4$^{R/R}$	Mutant mouse with 4-fold reduction in the Fibulin-4 gene transcript
Fibulin-4^{SMKO}	Wildtype mouse with Fibulin-4 deleted in vascular smooth muscle cells specifically
G-actin	Globular actin or monomeric actin
GDFs	Growth and differentiation factors
GO	Gene ontology
GWAS	Genome-wide association studies
HI	Haploinsufficient
HLA	Human leukocyte antigen

HTAD	Heritable thoracic aortic disease
IPA	Ingenuity Pathway Analysis
KO	Knock-out
LAP	Latency associated peptide
LDS	Loeys-Dietz syndrome
LLC	Large latent complex
LOX	Lysyl oxidase
LTBPs	Latent TGFβ binding proteins
MAGPs	Microfibril-associated glycoproteins
MEF	Mouse embryonic fibroblast
MFS	Marfan syndrome
MMPs	Matrix metalloproteases
MYH11	Myosin heavy chain
MYLK	Myosin light chain kinase
OCR	Oxygen consumption rate
OXPHOS	Oxidative phosphorylation
PGC1	Peroxisome proliferator-activated receptor gamma, coactivator 1
PPAR	Peroxisome proliferator activated receptor
RAS	Renin-angiotensin system
ROS	Reactive oxygen species
SLC	Small latent complex
SM22 Cre+	Mouse expressing Cre recombinase under SM22 promoter, Smooth muscle cell specific
SMA	Smooth muscle actin
TAA	Thoracic aortic aneurysms
TCA	Tricarboxylic acid cycle
TEM	Transmission Electron Microscopy
TGFβ	Transforming growth factor β
VSMCs	Vascular smooth muscle cells
VUS	Variant of unknown significance
WES	Whole exome sequencing
WGS	Whole genome sequencing
WT	Wildtype

CURRICULUM VITAE

Personal details

Full name:	Joyce Burger
Date of birth:	August 25th 1990
Place of birth:	Alkmaar, The Netherlands
Nationality:	Dutch

Research experience

2015 – 2019	PhD student Erasmus Medical Centre – Rotterdam, The Netherlands Department of Molecular Genetics and Department of Clinical Genetics 'Molecular mechanisms of aortic aneurysms'
2013-2014	Major research internship Leiden University Medical Center – Leiden, The Netherlands Department of Molecular Cell Biology 'The role of p73 and Hdmx in Ewing sarcomas'
2012-2013	Minor research internship Leiden University Medical Center – Leiden, The Netherlands Department of Radiology 'The effect of BMP2 and BMP4 on PPAR gamma activated adipogenesis'
2012	Bachelor internship Leiden University Medical Center – Leiden, The Netherlands Department of Anatomy and Embryology 'The role of endothelial cilia in the initiation and/or progression of atherosclerosis in a Fibulin-4 knockdown mouse model'

Education

2015-2019	Doctor of Philosophy (PhD), Medical Genetics Centre (MGC) Erasmus Medical Centre Rotterdam – Rotterdam, The Netherlands
2012-2014	MSc, Biomedical Sciences, research specialization Leiden University - Leiden, The Netherlands
2009 - 2012	BSc, Biomedical Sciences Leiden University - Leiden, The Netherlands

LIST OF PUBLICATIONS

Molecular phenotyping and quantitative functional assessment of pathogenic variants in aneurysm genes ACTA2, MYH11, SMAD3 and FBN1

Manuscript in preparation

Joyce Burger*, Natalija Bogunovic*, Hiu Liu, Arne IJpma, Alessandra Maugeri, Dimitra Micha, Timo ten Hagen, Danielle Majoor-Krakauer, Ingrid van der Pluijm, Jeroen Essers#, Kak Khee Yeung#

* Authors contributed equally, # Corresponding authors

Gene expression profiling in syndromic and non-syndromic heritable thoracic aortic disease: further evidence on the role of inflammation and mitochondrial dysfunction

Manuscript in preparation

J.M.A. Verhagen, J. Burger, J.A. Bekkers, A.T. den Dekker, M.L.T. van der Sterre, J.H. von der Thüsen, H.T. Brüggenwirth, M. van den Born, J. Essers, W.F.J. van IJcken, M.W. Wessels, I. van der Pluijm, J.W. Roos-Hesselink, R.M.W. Hofstra, I.M.B.H. van de Laar, E. Brosens

Slc2a10 knock-out mice deficient in ascorbic acid synthesis recapitulate aspects of arterial tortuosity syndrome and display mitochondrial respiration defects

Accepted Human Molecular Genetics 2020 Apr

A. Boel, J. Burger, M. Vanhomwegen, M. Renard, S. Barnhoorn, B. Descamps, C. Vanhove, C. Casteleyn, B. Callewaert, A. Willaert, I. van der Pluijm, J. Essers, P. Coucke

Inflammation and TGF-β signaling differ between abdominal aneurysms and occlusive disease

J Cardiovasc Dev Dis. 2019 Dec; 6(4): 38.

A. IJpma, L te Riet, K.M. van de Luijtgaarden, P.M. van Heijningen, J. Burger, D Majoor-Krakauer, E. Rouwet, J. Essers, H.J.M. Verhagen, I. van der Pluijm

Fibulin-4 deficiency differentially affects cytoskeleton structure and dynamics as well as TGFβ signaling

Cell Signal. 2019 Jun;58:65-78

J. Burger, N. van Vliet, P.M. van Heijningen, H. Kumra, G.J. Kremers, M. Alves, G. van Cappellen, H. Yanagisawa, D.P. Reinhardt, R. Kanaar, I. van der Pluijm, J. Essers

Decreased mitochondrial respiration in aneurysmal aortas of Fibulin-4 mice is linked to PGC1A regulation

Cardiovasc Res. 2018 Nov 1;114(13):1776-1793

I. van der Pluijm, J. Burger*, P.M. van Heijningen*, A. IJpma, N. van Vliet, C. Milanese, K. Schoonderwoerd, W. Sluiter, L.J. Ringuette, D.H.W. Dekkers, I. Que, E.L. Kaijzel, L. te Riet, E. MacFarlane, D. Das, R. van der Linden, M. Vermeij, J.A. Demmers, P.G. Mastroberardino, E.C. Davis, H. Yanagisawa, H. Dietz, R. Kanaar, J. Essers

* Authors contributed equally

PHD PORTFOLIO

Summary of PhD training and teaching

Name PhD student:	Joyce Burger
Erasmus MC department:	Molecular Genetics Clinical Genetics
Research school:	Medical Genetics Centre (MGC)
Promotor:	Prof.dr. R. Kanaar and Prof.dr. R.M.W. Hofstra
Copromotor:	Dr. J. Essers and Dr. I. van der Pluijm
PhD period:	2015-2019

1. PhD training

General academic skills (6 ECTS)	Year
- Safe Laboratory Techniques – MGC	2015
- Research Integrity	2017
- Statistics	2017
- Biomedical English Writing and Communication	2018

In-depth courses (12 ECTS)	Year
- Genetics – MGC	2015
- Atherosclerosis and aneurysmal disease, from bed to bench and back (COEUR)	2015
- Vascular Biology – Dutch Heart Foundation	2015
- Chromatin day 2015	2015
- Epigenetic regulation in health and disease – MGC	2016
- Crispr Course – Biochemistry	2017
- Image J analysis - Optical Imaging Centre Erasmus MC	2017

Research seminars and lectures (4 ECTS)	Year
Various – COEUR, MGC and Biomedical science cluster	2015-2019

Symposia and conferences (15 ECTS)	Year
Oral presentations	
- Wetenschapsdag Heelkunde, Rotterdam, The Netherlands	2017
- Rolduc Genetics Meeting, Kerkrade, The Netherlands	2017
- COEUR PhD day, Rotterdam, The Netherlands	2017
- 24th MGC PhD workshop, Leuven, Belgium	2017
- Wetenschapsdag Heelkunde, Rotterdam, The Netherlands	2018
- European Elastin Meeting, Nijmegen, The Netherlands	2018
- Sector meetings, work discussions and journal clubs	2015-2019
Poster presentations	
- 23rd MGC PhD workshop, Dortmund, Germany	2016
- European society of vascular surgery, Leiden, The Netherlands	2017
- American Heart Association research meeting 2017, Anaheim, California, USA	2017

Attendance

- Symposium aortapathologie - te wijd of te nauw? Rotterdam, The Netherlands	2015
- 22nd MGC PhD workshop, Maastricht	2015
- Wetenschapsdag Heelkunde, Rotterdam, The Netherlands	2015
- Symposium Heritable Thoracic Aortic Disease, Ghent, Belgium	2016
- Mechanobiology, Amsterdam, The Netherlands	2016
- 1st Translational cardiovascular research meeting (Hartstichting), Utrecht, The Netherlands	2017

Awards

- 2nd prize poster presentations, 23rd MGC PhD workshop	2016
- 2nd prize presentations, 24th MGC PhD workshop	2017
- Best presentation, Wetenschapsdag Heelkunde	2018
- Best presentation, European Elastin Meeting	2018

2. Teaching activities

Teaching (1 ECTS)	Year
BSc Nanobiology, seminars Molecular Biology	2015
	2016
	2017
	2018

Supervision students (9 ECTS)	Year
Supervision Bachelor student during minor BRiP	2015
Supervision of HLO graduation internship (9 months)	2016-2017
Supervision Bachelor student during minor BRiP	2017
Supervision HLO student (5 months)	2018
Supervision HLO graduation internship (9 months)	2018-2019

Total 2015-2019	**(47 ECTS)**

DANKWOORD

Het is nu echt zo ver, mijn proefschrift is klaar. Een paar hele mooie, fijne, leuke jaren sluit ik hiermee af. Met dit dankwoord wil ik iedereen bedanken die ik tijdens mijn PhD heb mogen ontmoeten voor de fijne samenwerkingen, adviezen, hulp en steun. In mijn eentje had ik het niet kunnen doen!

Allereerst mijn co-promotoren: dr. Jeroen Essers en dr. Ingrid van der Pluijm. Beste Jeroen en Ingrid, bedankt dat jullie mij de kans geboden hebben om mijn PhD project bij jullie in de groep te doen! Jeroen, al jaren voor ik op zoek ging naar een PhD project was jouw naam al bekend voor mij. Tijdens mijn Bachelor stage mocht ik aan het Fibulin-4$^{R/R}$ muis model werken, bedankt dat ik verder kon werken aan dit mooie model! Daarnaast wil ik je bedanken voor je vertrouwen, steun, optimisme, enthousiasme en kennis. Ik heb dit altijd enorm gewaardeerd. Ingrid, dankjewel dat jij altijd het overzicht hield als ik dat soms niet meer had. Dankjewel voor je optimisme, humor, suggesties en hulp tijdens het schrijven! Ik wil jullie allebei bedanken voor alles wat ik heb geleerd tijdens mijn PhD, zonder jullie steun, adviezen en inzet zou dit minder soepel verlopen zijn.

Mijn promotoren: prof. dr. Roland Kanaar en prof. dr. Robert Hofstra. Graag wil ik jullie bedanken voor de begeleiding de afgelopen jaren. De jaarlijkse update meeting was altijd fijn om te bespreken of we op de juiste weg zaten met het project. Beste Roland, bedankt voor je vertrouwen, je oog voor detail en input tijdens de werkbesprekingen. Beste Robert, bedankt voor je vertrouwen en input tijdens onze besprekingen.

Ik wil graag de leden van de grote en kleine commissie bedanken voor het kritisch lezen van mijn proefschrift en het zitting nemen in mijn promotiecommissie.

Lieve paranimfen, Kirsten en Nicole (en stiekem ook Bibi), bedankt dat jullie mijn paranimfen wilde zijn. Ik vind het heel fijn dat jullie naast mij zullen staan op de dag van mijn promotie! Kirsten, we kennen elkaar nu al sinds de basisschool en we hebben al ontzettend veel meegemaakt samen. Van schaatsen en dagjes weg tot uitgaan en concerten en festivals bezoeken. Ik hoop dit nog vele jaren samen met jou te mogen doen! Dankjewel voor al je steun en vertrouwen tijdens mijn promotietraject en natuurlijk ook voor de creatieve hulp bij het ontwerp van mijn boekje! Bibi en Nicole, vanaf dag 1 was het al gezellig op het lab en gedurende de jaren zijn we steeds meer gaan ondernemen samen. Nicole, dankjewel voor al je hulp op het lab en dat ik altijd bij je terecht kan om even te kletsen of klagen. Bibi, dankjewel dat we altijd konden praten op kantoor over zowel werk als privé, maar ook lekker konden kletsen over van alles. Ik wil jullie allebei bedanken voor de dansjes tijdens Het Foute Uur (natuurlijk ook daar buiten) en de geweldige zangpartijen

die daarbij horen. Ik kan niet wachten tot we de volgende Disney/kinderfilm gaan kijken waarbij de thee en chocola niet kan ontbreken!

Voor mij zijn leuke collega's enorm belangrijk voor een plezierige werkervaring en wat heb ik het met jullie getroffen.

Ik wil het Fibulin-4 groepje bedanken voor alle gezelligheid en hulp op het lab en tijdens de werkbesprekingen. Yanto, het was altijd leuk om alle mooie plaatjes die jij maakt te zien en samen te lunchen, vergeet niet soms uit de bunker te komen ;). Nathalie, het is mooi om te zien hoeveel motivatie en doorzettingsvermogen jij hebt met je projecten. Heel veel succes met de rest van je PhD, je kan het! Janette, heel veel succes de komende jaren met je PhD project, maar dat zal vast goed komen. Hamid, bedankt voor je bijdrages in de werkbespreking. Paula, je zit al even niet meer bij ons op het lab maar ik wil je bedanken voor je hulp bij mijn projecten en de gezellige tijd!

Cecile, dankjewel dat je iedereen wegwijs maakt in de systemen en je altijd wilt helpen! Stefan het was altijd gezellig met jou in het lab en als we allebei op zoek waren naar Jeroen! Nathalie, ook jij bent al even weg maar je blijft altijd onderdeel van ons lab voor mij! Dankjewel dat ik je legpuzzels kon lenen en daar eeuwen over kon doen :p. Ik vond het ontzettend leuk om jou, Bastiaan en de kleine Joris op te zoeken in Groningen!

Hanny, onze western blotting koningin! Fijn dat ik altijd bij jou terecht kon als ik iets niet wist qua blotten en natuurlijk ook voor een kletspraatje. Nicole, Anja, Titia, Danny Marjolein, Danny en Marta, ik heb ontzettend genoten van alle lunches (waar het niveau soms ver te zoeken was), de sinterklaas surprises en natuurlijk de karaoke!

Arshdeep, Maarten, Nick, Claire and Dejan, thank you for all the fun conversations we had in the office. Alex, Charlie, Martine, Joyce, Sari, Marcel, Whenhao, Giorgia, Natasa, Maaike, Ben and all other lab members: Thank you for sharing the good and the bad times with me in our corridor.

Ayestha, van naast elkaar in de klas tijdens wiskunde tot naast elkaar op de 6e verdieping van de Ee toren in het Erasmus MC, dankjewel voor je humor en je steun. Lennart, ongeveer tegelijk begonnen we aan onze PhD projecten. Dankjewel voor de gesprekken, samen met Ayestha, in de gang op weg naar het koffiezetapparaat. Allebei heel veel succes met het afronden van jullie PhD en ik zie jullie op je verdediging! Marit en Sandra, fijn dat jullie mijn trein buddies waren op de vroege ochtend of aan het eind van de dag. Het treinen naar Leiden werd zo een stuk leuker.

Naast alle lab collega's wil ik ook graag onze ICT'ers en de dames van de keuken bedanken voor alle hulp om het onderzoekwerk heen. Sonja en Jasperina, ontzettend bedankt voor alle hulp en adviezen!

Onderzoek doe je niet alleen en daarom gaat mijn dank ook uit naar alle co-auteurs en verdere samenwerkingen. Mede door jullie bijdrage hebben we een aantal mooie publicaties en manuscripten kunnen maken. Arne en Danielle, bedankt voor jullie input tijdens de aneurysma besprekingen. Ingrid en Judith bedankt voor de fijne samenwerking en de leuke besprekingen. Judith, ik heb het ontzettend gezellig gehad met je op het lab, Het Foute Uur op de achtergrond en heel veel droogijs en vloeibare stikstof in de buurt om de aorta's koud te houden! Annekatrien, Paul en Bert, bedankt voor de prettige samenwerking en de gezellige skype gesprekken! Sander, bedankt voor al je hulp met de Seahorse! Natalija and Kakkhee, thank you for the collaboration on the functional assay manuscript. Dieter and Heena, I really appreciate your input on the Fibulin-4 cytoskeleton manuscript and your help with the ECM stainings. Maria, thank you for your enthusiasm and your help with the F/G-actin! Gert en Gert-Jan, bedankt voor alle instructies en hulp met de microscopen. Daarnaast wil ik ook graag mijn studenten, Lleroy, Nicole en Ihsane, bedanken voor al hun harde werk in het lab.

Inmiddels weet ik dat ik het bij NWO ook getroffen heb met mijn collega's. Team Leven ontzettend bedankt voor het warme welkom, jullie hulp en natuurlijk de wandelingen tijdens de lunch. Team Veni mag natuurlijk niet ontbreken, fijn dat ik deel ben het leukste ronde team!

Het organiseren van het wetenschapscafé Rotterdam heeft mij veel geleerd buiten mijn eigen werkveld en ik heb dit mogen doen met ontzettend leuke mensen. Luuk, Florence, Mylene, Jasmijn, Eric en Evelien, dankjewel!

Vrije tijd en ontspanning zijn de afgelopen jaren heel erg belangrijk voor mij geweest. Christa, Linda en Froukje, lieve oud huisgenootjes, ontzettend bedankt voor alle etentjes, kopjes thee en gezellige momenten.

Alex, Wouter, Matthijs, Linda, Manouk, Laura, Casper en Hugo bedankt voor alle gezellige momenten, kopjes thee/gin-tonics/glaasjes port/biertjes/wijntjes, weekendjes weg, etentjes, het altijd gezellige en licht competitieve voetbal kijken, hulp bij het klussen en alle andere leuke activiteiten. Bedankt voor alles, ik kijk uit naar alle volgende ontmoetingen!

Lieve Maarten en Kirsten (nu ook nog als koppel), dankjewel voor alle spelletjes avonden, concerten, etentjes en leuke gesprekken! Het is altijd onwijs gezellig met jullie, bedankt voor alle leuke momenten.

Lieve families, Burger, Bakker, van Os en Laan, hoewel het voor jullie misschien niet altijd duidelijk was wat mijn onderzoek precies inhield, wil ik jullie bedanken voor jullie interesse, jullie steun en natuurlijk ook voor alle feestdagen, familiedagen, familieweek in de Katjeskelder, sinterklaas vieringen en Efteling bezoekjes die ik met jullie heb mogen beleven. Lieve opa en oma, dankjewel voor alle knuffels en dat jullie altijd voor mij klaar staan. Eén dropje voor naar huis en één dropje voor onderweg!

Karin, Diederik, Laura en Ashwin, mijn lieve schoonfamilie, heel erg bedankt voor alle gezellige avonden, etentjes, spelletjes, hulp bij het klussen en klusadviezen, bezoekjes aan Antwerpen en bovenal jullie steun en betrokkenheid.

Gaby en Britt, mijn allerliefste zusjes! Dankjewel dat jullie er altijd voor mij zijn, met advies, humor en veel gezelligheid. Dankjewel dat jullie zo betrokken waren bij wat ik nou precies deed op het lab en hoe het met mij ging.

Lieve papa en mama, jullie steun, adviezen en liefde zijn erg belangrijk voor mij. Bedankt dat jullie er altijd voor me waren en mij vertrouwen gaven als ik aan mezelf twijfelde. Jullie betrokkenheid bij mijn leven en interesses waardeer ik enorm, jullie zijn geweldig!

Lieve Saartje, dankjewel dat je altijd op mijn toetsenbord wilde zitten tijdens het schrijven van dit boekje, je bent wel een schattig katje.

Lieve Bram, dankjewel voor je vertrouwen, steun, geduld, schop onder m'n kont en bovenal liefde tijdens de afgelopen jaren. Jij weet altijd hoe je me kan helpen, gerust kan stellen en ook enorm aan het lachen kan maken. Ik kijk uit naar alle mooie jaren die voor ons liggen. Dankjewel voor alles, ik hou van je!